

Universidade do Minho
Escola de Engenharia

Ruben Brandão Freitas

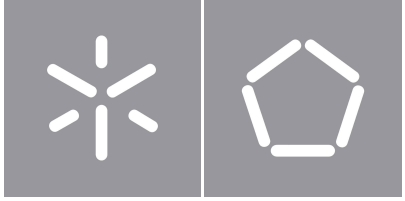
Multiphoton Microscopy for Label-Free Colorectal Cancer Diagnosis: Towards an Endoscopic Application

August 2026

Multiphoton Microscopy for Label-Free Colorectal Cancer Diagnosis: Towards an Endoscopic Application

Ruben Brandão Freitas

UMinho | 2026



University of Minho
School of Engineering

Ruben Brandão Freitas

Multiphoton Microscopy for Label-Free Colorectal Cancer Diagnosis: Towards an Endoscopic Application

Doctoral Thesis
Doctoral Program in Biomedical Engineering

Work carried out under the supervision of
Professor Dr. José Higino Gomes Correia
Dr. Marino de Jesus Correia Maciel

August 2026

Copyright and Terms of Use for Third Party Work

This is an academic work that may be used by third parties provided that internationally accepted rules and good practices regarding copyright and related rights are respected.
Accordingly, this work may be used under the license provided below.
If the user needs permission to use the work under conditions not provided for in the indicated licensing, they should contact the author through the University of Minho RepositoriUM.

License granted to users of this work:



Attribution-NonCommercial 4.0 International

CC BY-NC 4.0

`https://creativecommons.org/licenses/by-nc/4.0/`

Acknowledgements

This journey was, at times, extremely challenging, and without the support and influence of many people, it would not have been possible to take it to the end. A part of this thesis belongs to all of you, and I would like to express my sincere gratitude.

To Beatriz, for being my companion throughout this path, for always being strong enough to listen to me on the worst days, and for helping me get back on track when I felt lost. You are a true inspiration of strength and focus. I am very lucky to have you by my side. Thank you for never letting me forget that "Nada é pior que o Freixo !!!".

To my father and mother, thank you for all the values you have given me over the years. This work is also yours, built on the strength, focus, belief, and love that you have always given me.

To all my grandparents, thank you for instilling in me the values of hard work and perseverance. You will always be in my memory.

To my family, thank you for your constant support, for your care, and for teaching me what a family should be. You showed me that I will never be alone.

To my childhood friends, thank you for all the adventures over the last 20 years, from afternoons by the river to long nights together. You are an essential part of who I am. Thank you for always being there.

To all the friends I made throughout this academic journey, thank you for all the days and nights partying or just talking, the barbecues, the adventures exploring the world, and the shared experiences. Life would be much more boring without you. And never forget: "Ao Eusebio! À Amália! E ao Tinoco!!!".

To Bruno, for walking this path alongside me, for all the shared adventures, and for teaching me never to trust someone who says "it's not that spicy." Your ideas and your (sometimes exaggerated) focus were a constant source of inspiration.

To Hugo, thank you for all the time spent in dark rooms, for the ideas and inspiration, and for your companionship during the freezing winter in Sweden. Without you, that experience would have been much harder, and the best lasagna in Sweden would never have been achieved.

To Bórlido, my gym partner, thank you for being there after work, for helping me release the frustrations of the day, and for always listening. Your support meant a lot during the toughest moments.

To Per Lundgren, thank you for welcoming me to Chalmers, where I was able to grow both professionally and personally. It was one of the best experiences of this journey. To Maria Asplund, thank you for accepting me in your lab, I learned so much there.

To Lukas, thank you for your friendship, companionship, and invaluable knowledge of cleanroom work,

you were the best teacher I could have asked for. To Hanna, my office and DWL mate, thank you for making the days in the office and the cleanroom much more enjoyable. To Mazahrul, thank you for all the coffees and life advice, you helped me grow, and I will carry your strength and focus with me. You are an Ironman to me.

To Raul, Azega, Sherry, Markus, Hassan, and Charlie, thank you for all the lunches, afterworks, and advice; you made my time in Sweden much richer. I hope Lukas can teach us a few more dance moves in the future. To everyone at EMSL, thank you for the discussions, the support, the fikas, and for welcoming me.

To Professor Mike, thank you for everything. Even without being my official supervisor, you guided me as if you were. You taught me what I know about optics, and without you, this would not have been possible. To Manuel, thank you for teaching me what it means to build an optical setup and for showing me the value of hard work. To Nelssom, thank you for all your help with signal acquisition. To everyone in the lab, thank you for the conversations, the debates, and for teaching me what a femtosecond truly is.

To Florival and Rui, thank you for all the time spent together in the lab, for your companionship, and for being part of this journey. To everyone at MNFab Lab, past and present, thank you for your support, ideas, and collaboration.

To Sara, even without being my official supervisor, thank you for your dedication and guidance, your help was essential.

To Marino and Professor Higino, thank you for your guidance, your support, and for believing in me and accepting me as a PhD candidate.

To all the partners, thank you for your collaboration, which made this work possible.

To Chalmers UT, thank you for welcoming me and providing the conditions that allowed me to grow. These experiences were essential to my development.

To the University of Minho, thank you for providing not only the conditions to improve myself but also unforgettable experiences.

To Fundação para a Ciência e Tecnologia (FCT), thank you for supporting my research. This work was funded under the grant reference 2021.06966.BD (https://doi.org/10.54499/2021.06966.BD) and by MPhotonBiopsy, PTDC/FISOTI/1259/202 (https://doi.org/10.54499/PTDC/FIS-OTI/1259/2020).

This PhD was the greatest professional challenge I have ever faced. There were many obstacles that felt like the end of the road, moments of doubt, and a constant feeling of not being enough, often combined with a lack of time to rest. There were many moments when I thought this was not achievable, but it was thanks to all of you that I made it through.

Statement of Integrity

I hereby declare having conducted this academic work with integrity.

I confirm that I have not used plagiarism or any form of undue use of information or falsification of results along the process leading to its elaboration.

I further declare that I have fully acknowledged the Code of Ethical Conduct of the University of Minho.

University of Minho, Braga, August 2026

Ruben Brandão Freitas

Resumo

O cancro colorretal (CRC) mantém-se como uma das principais causas de mortalidade associada ao cancro a nível mundial, sendo que os protocolos de diagnóstico atuais dependem de procedimentos invasivos e de análises histopatológicas demoradas. Neste contexto, técnicas de imagiologia ótica capazes de caracterizar tecidos *in vivo* têm emergido como alternativas promissoras à biópsia convencional. Esta tese investiga o potencial da tomografia de coerência ótica (OCT) e da microscopia multifotónica (MPM) no diagnóstico do CRC, com foco na sua futura integração em sistemas endoscópicos.

De forma a possibilitar estudos controlados e reprodutíveis, foram desenvolvidos modelos biológicos e fantomas. O ensaio da membrana corioalantóica (CAM) foi utilizado como plataforma *in vivo* para o crescimento de tecidos colorretais não malignos e malignos. Os fantomas foram usados para replicar as propriedades óticas e bioquímicas dos tecidos biológicos.

No âmbito da OCT, foi implementada uma análise quantitativa baseada no coeficiente de atenuação de tecidos em modelos CAM, utilizando uma máquina de vetores de suporte (SVM) treinada com características extraídas de duas regiões a diferentes profundidades. A validação cruzada aninhada produziu um desempenho ótimo, com valores de exatidão, sensibilidade, precisão e AUC iguais a 1.0.

Simultaneamente, a MPM foi explorada para imagiologia funcional através da deteção de fluoróforos endógenos (NAD(P)H e FAD), permitindo a caracterização metabólica através do rácio redox. Foram fabricados filtros óticos altamente seletivos (centrados em 485 nm e 530 nm) que permitiram uma análise metabólica fiável mesmo em fantomas complexos, revelando diferenças estatisticamente significativas entre amostras normais e tumorais (teste de Mann-Whitney U, $P < 0.05$). Apesar destes avanços, diversos desafios, como a capacidade de deteção de sinal, foram identificados, evidenciando a necessidade de otimizações futuras.

A viabilidade da miniaturização dos sistemas OCT e MPM para integração em colonoscópios foi também avaliada, delineando os principais requisitos para a sua aplicação clínica.

No geral, este trabalho estabelece um enquadramento experimental e tecnológico abrangente para sistemas de imagiologia ótica integrados contribuindo para o desenvolvimento da biópsia ótica em tempo real e sem marcadores no diagnóstico do CRC.

Palavras-chave Biópsia ótica; Cancro colorrectal; Fantomas de tecido colorrectal; Microscopia multifotónica; Tomografia de coerência óptica

Abstract

Colorectal cancer (CRC) remains one of the leading causes of cancer-related mortality worldwide, with current diagnostic approaches relying on invasive and time-consuming histopathological analysis. In this context, optical imaging techniques capable of *in vivo* tissue characterization have emerged as promising alternatives to traditional biopsy. This thesis investigates the potential of optical coherence tomography (OCT) and multiphoton microscopy (MPM) for CRC diagnosis, with a focus on their future integration into endoscopic platforms.

To enable controlled and reproducible experimentation, both biological and tissue-mimicking phantoms were developed. The chorioallantoic membrane (CAM) assay served as an *in vivo* platform for the growth of non-malignant and malignant colorectal tissues. The phantoms were designed to replicate the optical and biochemical properties of biological samples.

For OCT, a quantitative analysis based on the attenuation coefficients of tissues in CAM assays was conducted using a support vector machine (SVM) classifier trained on features extracted from two distinct depth regions. Nested cross-validation achieved optimal performance, with accuracy, recall, precision, and AUC all reaching 1.0.

In parallel, MPM was investigated for functional imaging through the detection of endogenous fluorophores (reduced nicotinamide adenine dinucleotide (phosphate) (NAD(P)H) and flavin adenine dinucleotide (FAD)), enabling metabolic characterization via the redox ratio. Highly selective optical filters (centered at 485 nm and 530 nm) were fabricated, allowing reliable metabolic analysis even in complex phantoms and revealing statistically significant differences between normal and tumoral samples (Mann-Whitney U test, $P < 0.05$). Despite these advances, several challenges, such as signal detection efficiency, were identified, highlighting the need for further optimization.

The feasibility of miniaturizing OCT and MPM systems for integration into conventional colonoscopes was also assessed, outlining key requirements for clinical translation.

Overall, this work establishes a comprehensive experimental and technological framework for integrated optical imaging systems, contributing toward real-time, label-free optical biopsy for CRC diagnosis.

Keywords Colorectal cancer; Colorectal tissue phantoms; Multiphoton microscopy; Optical biopsy; Optical coherence tomography

Contents

PART I Conceptualization **1**

1 Introduction **2**

1.1 Thesis Overview . . . 2

1.2 Author's Contribution . . . 4

1.3 Biological Tissues . . . 5

1.4 Cancer Tissues . . . 9

1.5 Colorectal Cancer . . . 11

1.6 Colorectal Cancer Diagnosis Techniques . . . 15

1.6.1 Traditional Diagnosis Techniques . . . 15

1.6.2 Emerging Techniques . . . 18

1.7 Motivation and Objectives . . . 20

1.8 Thesis Organization . . . 22

2 Light-matter Interaction **24**

2.1 General Overview . . . 24

2.1.1 Linear Phenomena . . . 26

2.1.2 Nonlinear Phenomena . . . 29

2.2 Effects of Light on Biological Tissues . . . 31

PART II Tissue models **33**

3 CAM Assays **34**

3.1 Context . . . 34

3.2 Experimental Methods . . . 36

3.3 Results and Samples Analysis . . . 37

3.4 Outlook . . . 40

4 Colorectal Tissue Phantoms **41**

4.1 Context . . . 41

4.2 Theoretical Framework . . . 46
4.2.1 Phantoms Fabrication . . . 47
4.2.2 Phantoms Characterization . . . 48
4.3 Experimental Methods . . . 50
4.3.1 Phantoms Fabrication . . . 50
4.3.2 Phantoms Characterization . . . 56
4.4 Results and Samples Analysis . . . 61
4.4.1 One-Photon Absorption Spectra of NAD(P)H and FAD . . . 61
4.4.2 One-photon Fluorescence Spectra of NAD(P)H and FAD . . . 62
4.4.3 Two-photon Fluorescence Spectra of NAD(P)H and FAD . . . 63
4.4.4 Absorbance Spectra of Hemoglobin, Polystyrene Beads, and Gelatin . . . 66
4.4.5 Refractive Index of Gelatin . . . 67
4.4.6 Gelatin Thickness . . . 69
4.5 Outlook . . . 71

PART III Optical Filters 72

5 Fabry-Perot Optical Filters 73

5.1 Context . . . 73
5.2 Theoretical Framework . . . 74
5.3 Experimental Methods . . . 81
5.3.1 Optical Filters Design and Simulation . . . 81
5.3.2 Optical Filters Fabrication . . . 83
5.3.3 Optical Filters Characterization . . . 84
5.4 Results and Samples Analysis . . . 85
5.4.1 Optical Filters Design Calculation . . . 85
5.4.2 Experimental Refractive Indices and Optical Filters Optimization . . . 87
5.4.3 Optical Filters Design Simplification . . . 91
5.4.4 Second-order Resonant Cavity . . . 94
5.4.5 Expected Optical Filters Performance in Fluorescence Measurements . . . 97
5.4.6 Optical Filters Fabrication and Characterization . . . 102
5.5 Outlook . . . 107

PART IV Tissue Models Analysis with Optical Coherence Tomography and Multiphoton Microscopy 109

6 Optical Coherence Tomography of CAM Assays 110

6.1 Context . . . 110
6.2 Theoretical Framework . . . 111
6.3 Optical Coherence Tomography Setup . . . 117
6.4 Experimental Methods . . . 118
6.4.1 Data Acquisition and Processing . . . 118
6.4.2 Data Analysis . . . 119
6.5 Results and Samples Analysis . . . 121
6.6 Outlook . . . 124

7 Multiphoton Microscopy of Tissue Phantoms 126

7.1 Context . . . 126
7.2 Theoretical Framework . . . 130
7.2.1 Second Harmonic Generation . . . 132
7.2.2 Two-photon Excitation Fluorescence . . . 134
7.3 Multiphoton Microscopy Setup . . . 136
7.3.1 Setup Description . . . 136
7.3.2 Setup Characterization . . . 140
7.4 Experimental Methods . . . 146
7.4.1 Data Acquisition and Processing . . . 146
7.4.2 Data Analysis . . . 149
7.4.3 Preliminary SHG Measurements with Biological Tissues . . . 150
7.5 Results and Samples Analysis . . . 151
7.5.1 Liquid Phantoms with a Fluorophore (NAD(P)H or FAD) . . . 151
7.5.2 Liquid Phantoms with Both Fluorophores (NAD(P)H and FAD) . . . 152
7.5.3 Liquid Phantoms with Hemoglobin, Polystyrene Beads, and Fluorophores (NAD(P)H and FAD) . . . 157
7.5.4 Solid Phantoms with Both Fluorophores (NAD(P)H and FAD) . . . 160
7.5.5 Solid Phantom with Hemoglobin, Polystyrene Beads, and Fluorophores (NAD(P)H and FAD) . . . 166

7.5.6 Preliminary SHG Measurements with Biological Tissues 170
7.6 Outlook 171

PART V Systems Miniaturization **173**

8 Colonoscope Integration **174**
8.1 Context 174
8.2 Optical Coherence Tomography Miniaturization 175
8.3 Multiphoton Microscopy Miniaturization 177
8.3.1 Current Miniaturized Systems 178
8.3.2 Proposed System 179
8.3.3 Preliminary Experimental Results 181
8.4 Outlook 182

PART VI Final Remarks **184**

9 Conclusions **185**

10 Future work **187**

Bibliography **187**

List of Figures

1.1 Fluorescence emission ranges of the main endogenous fluorophores in biological tissues [1]. 7

1.2 Wavelength-dependent absorption coefficients of key biological chromophores (oxyhemoglobin (HbO_2), deoxyhemoglobin (Hb), lipids, and water (H_2O)) [2]. 9

1.3 Number of new cancer cases worldwide in 2022 [3]. 12

1.4 Death rate of colon and rectum cancer in the United States from 1999 to 2023 (per $100{,}000$ population) [4]. 13

1.5 Rate of new cancer cases worldwide in 2020, by type of cancer (per $100{,}000$ population) [5]. 13

1.6 Rate of cancer deaths worldwide in 2022 (per $100{,}000$ population) [6]. 14

1.7 Predicted number of cancer-related deaths worldwide from 2022 to 2050 [7]. 14

1.8 (a) Flexible endoscope used for conventional gastrointestinal imaging (Pentax FC-38FW2); (b) distal tip of the endoscope (Pentax FC-38FW2), showing the imaging lens, illumination system, and instrumentation channel; and (c) wireless capsule endoscopy device (PillCam SB2). 17

2.1 Jablonski diagram illustrating key photophysical processes, including single-, two-, and three-photon absorption, fluorescence emission, nonradiative relaxation, intersystem crossing to the triplet state, and photochemical pathways. 25

2.2 Potential energy diagram illustrating electronic states (S_0, S_1) and their associated vibrational levels, highlighting vibronic transitions and the Franck–Condon principle governing optical absorption and emission. 28

2.3 Energy-level diagrams of nonlinear optical processes, according to their dependence on the incident power. 29

3.1 CAM assay implementation stages. 37

3.2 CAM assay samples. Digital camera images inside the egg of (a) NCM460-derived tissue grown on the CAM, and (b) RKO-derived tissue grown on the CAM. Images inside the egg using a Leica M80 stereomicroscope of (c) NCM460-derived tissue, and (d) RKO-derived tissue. Excised CAM membrane containing (e) NCM460-derived tissue, and (f) RKO-derived tissue, imaged with a Nikon L200N microscope (10× objective). 38

4.1 Representation of the Brewster angle at the interface between two media. 49
4.2 Polystyrene beads commercial suspension dilution to obtain a solution with $2.5\,\%(\mathrm{w/V})$. 50
4.3 Fabrication workflow of the liquid optical phantoms containing only NAD(P)H or FAD. . . 51
4.4 Fabrication workflow of the liquid optical phantoms containing NAD(P)H and FAD. 52
4.5 Fabrication workflow of the liquid optical phantoms containing NAD(P)H, FAD, hemoglobin, and polystyrene beads. 54
4.6 Custom-built mold for gelatin phantom fabrication, consisting of two microscope glass slides separated by calibrated spacer strips (yellow strips) and sealed with parafilm on three sides, leaving one side open for solution injection (upper side). 55
4.7 Fabrication workflow of the solid optical phantoms. 56
4.8 Custom-built optical setup for absorbance measurements. 58
4.9 Custom-built setup for refraction index measuring. 60
4.10 One-photon absorbance spectra of NAD(P)H and FAD: (a) full spectral range; (b) region of interest (ROI) (300 - 500 nm). 61
4.11 1PEF spectra, under excitation at 375 nm and 400 nm: (a) NAD(P)H emission; (b) FAD emission. 63
4.12 2PEF spectra of NAD(P)H and FAD in liquid phantoms: (a) NAD(P)H at 800 nm excitation; (b) FAD at 800 nm excitation; (c) NAD(P)H at 750 nm excitation; (d) FAD at 750 nm excitation. 64
4.13 Normalized 2PEF spectra acquired under 750 nm excitation and 1PEF spectra acquired under 375 nm excitation for NAD(P)H and FAD. 65
4.14 Integrated fluorescence intensity as a function of the excitation power with the corresponding regression curves at 750 nm excitation for: (a) NAD(P)H; (b) FAD. 65
4.15 Absorbance spectra of hemoglobin (Hb), polystyrene beads (Pb) and gelatin. 66
4.16 Optical microscope images of gelatin phantoms acquired with a Leica M80 microscope, showing representative thickness measurements: (a) sample 1 measured between two glass slides; (b) sample 2, (c) sample 3, and (d) sample 4, each measured with one glass slide removed. 70

5.1 Interference-based optical filter with a Fabry–Perot structure, consisting of two Bragg mirrors acting as reflectors separated by an optical cavity (resonator). 75
5.2 Representation of a thin-film on a substrate, showing partial reflection of the incident light at the air–film and film–substrate interfaces. 77

5.3 Developed optical filters, based on a Fabry–Perot structure. 82
5.4 Refractive index as a function of wavelength for: (a) SiO_2 thin-films (samples S1 and S2, and literature sample [8]); and (b) TiO_2 thin-film (sample T1 and literature sample [9]). . 89
5.5 Simulated transmittance spectra of the Fabry–Perot filters: (a) broadband transmittance of the 485 nm filter; (b) transmittance of the 485 nm filter in the ROI; (c) broadband transmittance of the 530 nm filter; (d) transmittance of the 530 nm filter in the ROI. Black curves correspond to the individually calculated mirror design, while red curves represent the optimized designs using identical mirror thicknesses. 93
5.6 Comparison between the simulated transmittance spectra of the 530 nm filter versions: (a) broadband transmittance comparison between version 1 (first order cavity) and version 2 (second order cavity); (b) detailed view of the transmittance spectra in the ROI. . . 96
5.7 1PEF spectra of NAD(P)H and FAD overlaid with the simulated transmittance spectra of the optical filters: (a) 485 nm filter and version 1 of the 530 nm filter; (b) 485 nm filter and version 2 of the 530 nm filter. 97
5.8 2PEF spectra of NAD(P)H and FAD overlaid with the simulated transmittance spectra of the optical filters: (a) 485 nm filter and version 1 of the 530 nm filter; (b) 485 nm filter and version 2 of the 530 nm filter. 98
5.9 Product between the filter transmittance spectra and the 1PEF spectra of NAD(P)H and FAD, illustrating the effective spectral contribution of each fluorophore after filtering: (a) 485 nm filter; (b) first-order 530 nm filter, v1; (c) second-order 530 nm filter, v2. 100
5.10 Product between the simulated filter transmittance spectra and the 2PEF spectra of NAD(P)H and FAD, illustrating the effective spectral contribution of each fluorophore after filtering: (a) 485 nm filter; (b) first-order 530 nm filter, v1; (c) second-order 530 nm filter, v2. 101
5.11 Transmittance spectra of the fabricated optical filters (485 nm and 530 nm): (a) experimental measured transmittance; (b) comparison between simulated and experimental transmittance over the full spectral range; (c) comparison between simulated and experimental transmittance in the ROI. 104
5.12 Fluorescence spectra resulting from the multiplication of the fabricated filter transmittance with the 2PEF spectra of NAD(P)H and FAD: (a) response with the 485 nm filter; (b) response with the 530 nm filter. 105

5.13 Fluorescence spectra acquired with and without optical filtering, illustrating the effect of spectral selection for: (a) NAD(P)H phantom; and (b) FAD phantom. 106
5.14 Comparison between calculated and experimentally measured 2PEF spectra with optical filtering for: (a) NAD(P)H phantom; and (b) FAD phantom. 106
5.15 Cross-sectional SEM image of a fabricated 485 nm Fabry–Perot filter, showing the multilayer structure and layer interfaces. 107

6.1 Schematic diagram of a Michelson interferometer, illustrating the principal optical components: a light source, beamsplitter, reference mirror, and detector. 112
6.2 The workflow of the OCT image acquisition, processing, and extraction of features [10]. . 119
6.3 Raw B-scan OCT images in dB scale, obtained using the ThorImage OCT software: (a) a non-malignant CAM sample and (d) a malignant CAM sample; attenuation coefficient B-scan images fully processed with the algorithm previously detailed, with the selected two bands highlighted in red of: (b) a non-malignant CAM sample and (e) a malignant CAM sample; zoomed in section of the two highlighted bands of: (c) a nonmalignant CAM sample and (f) a malignant CAM sample, with a compensation for the air-tissue interface border irregularities and further division of each band into four ROI. 120
6.4 Boxplots showing the: (a) and (d) MED; (b) and (e) IQR; (c) and (f) MAX of the attenuation coefficient (μ_{OCT}) for non-malignant (NM) and malignant (M) tumors, in the upper and lower band. Analysis of the SVM classifier accuracy values in function of the distance between the two bands (μm) for: (g) isolated features MED, IQR and MAX; and (h) combined features MED + MAX, MED + IQR, MED + MAX + IQR [10]. 122

7.1 Energy-level diagrams comparing: (a) SHG; and (b) 2PEF. 132
7.2 MPM experimental setup for 2PEF measurements, including excitation beam conditioning, polarization control, auxiliary imaging arm (white-light source and camera), and detection system with spectral filtering and spectrometer acquisition (both transmission and reflection paths). 137
7.3 Experimental multiphoton microscopy setup showing a cuvette containing a Rhodamine B solution positioned at the focal region between the excitation and collection objectives. 139
7.4 Knife-edge measurements of the laser beam (750 nm) at two positions along the optical path: (a) Position 1, located 105 cm before the objective; (b) Position 2, at the entrance of the objective. 141

7.5 Schematic representation of the Gaussian beam propagation along the optical axis, illustrating the variation of the beam diameter from $2w_1$ at position z_1 to $2w_2$ at z_2, and approaching the beam waist $2w_3$ at z_3. 142
7.6 Schematic representation of the Gaussian beam propagation through the objective lens M, illustrating the modification of the beam diameter and wavefront curvature from $2w_2$ and R_2, at the entrance (z_2), to $2w_4$ and R_4, after the objective (z_4). 143
7.7 Schematic representation of the Gaussian beam propagation after the objective lens, showing the evolution of the beam radius from $2w_4$ at position z_4 to the minimum beam waist $2w_5$ at position z_5. The parameter R_4 represents the radius of curvature of the wavefront immediately after the objective, while L denotes the propagation distance required to reach the focal point where the beam waist is formed. 145
7.8 The workflow of 2PEF signal acquisition and processing for a single spatial pixel. 149
7.9 2PEF spectra acquired from liquid phantoms mimicking normal and tumoral tissue conditions: (a) NAD(P)H phantoms; (b) FAD phantoms. Each curve represents the average of three measurements acquired with an excitation wavelength of 750 nm and an incident laser power of 100 mW. 152
7.10 2PEF spectra acquired from mixed NAD(P)H/FAD phantoms under normal and tumoral conditions: (a) NAD(P)H channel, day 1; (b) FAD channel, day 1; (c) NAD(P)H channel, day 2; (d) FAD channel, day 2. 153
7.11 Redox ratio calculated from 2PEF measurements of mixed NAD(P)H/FAD phantoms under normal and tumoral conditions. 155
7.12 Distribution of redox ratio values obtained from 2PEF measurements of mixed NAD(P)H/FAD phantoms fabricated on three different days, comparing normal and tumoral conditions. 156
7.13 2PEF spectra acquired from phantoms containing NAD(P)H, FAD, polystyrene beads and hemoglobin: (a) 485 nm filter channel, test 1; (b) 530 nm filter channel, test 1; (c) 485 nm filter channel, test 2; (d) 530 nm filter channel, test 2. Normal and tumoral phantoms are shown for comparison. Each curve represents the average of three consecutive acquisitions. 158
7.14 Redox ratio calculated from 2PEF measurements of phantoms containing NAD(P)H, FAD, polystyrene beads and hemoglobin. Results are shown in normal and tumoral conditions. 160

7.15 Mean and median fluorescence emission spectra obtained from 2D scans of representative solid gelatin phantoms containing NAD(P)H and FAD: (a) mean and (c) median spectra acquired using the 485 nm filter, highlighting the NAD(P)H emission region; (b) mean and (d) median spectra acquired using the 530 nm filter, corresponding to the FAD emission region. 162

7.16 Spatial distribution maps of the redox ratio for the normal gelatin phantoms containing NAD(P)H and FAD. Each subfigure ((a) to (g)) corresponds to a different acquisitions. The color scale represents the redox ratio value calculated on a pixel-by-pixel basis for the scanned area. 163

7.17 Spatial distribution maps of the redox ratio for the tumoral gelatin phantoms containing NAD(P)H and FAD. Each subfigure ((a) to (g)) corresponds to a different acquisitions. The color scale represents the redox ratio value calculated on a pixel-by-pixel basis for the scanned area. 164

7.18 Boxplot representation of the redox ratio values obtained from all scanned normal and tumoral phantoms. The central line represents the median, the box corresponds to the interquartile range (IQR), the whiskers indicate the data spread, and the points represent outliers. 165

7.19 Mean and median fluorescence emission spectra obtained from 2D scans of representative solid gelatin phantoms containing NAD(P)H, FAD, hemoglobin, and polystyrene beads: (a) mean spectrum using the 485 nm filter; (b) mean spectrum using the 530 nm filter; (c) median spectrum using the 485 nm filter; (d) median spectrum using the 530 nm filter. 167

7.20 Spatial distribution maps of the redox ratio for normal solid phantoms containing NAD(P)H, FAD, hemoglobin, and polystyrene beads. Each subfigure ((a) to (f)) corresponds to a different acquisitions. The color scale represents the redox ratio calculated on a pixel-by-pixel basis. 168

7.21 Spatial distribution maps of the redox ratio for tumoral solid phantoms containing NAD(P)H, FAD, hemoglobin, and polystyrene beads. Each subfigure ((a) to (f)) corresponds to a different acquisitions. The color scale represents the redox ratio calculated on a pixel-by-pixel basis. 169

7.22 Boxplot representation of the redox ratio values obtained from all solid phantoms containing NAD(P)H, FAD, hemoglobin, and polystyrene beads. 170

7.23 Measured SHG signals from: (a) normal CAM sample; (b) tumoral CAM sample. 171

8.1 Illustration of the OCT integration in a conventional colonoscope for optical biopsy of the colorectal tissues. The OCT catheter is connected to the OCT system through an optical fiber [10]. 176

8.2 (a) Schematic representation of the proposed miniaturized MPM system for endoscopic integration. Abbreviations: PMT - photomultiplier tube; PBS - polarizing beam splitter; SPF - short-pass filter; (b) conceptual illustration of the multiphoton probe integration within a conventional colonoscope. The excitation light is guided through an optical fiber along the instrument channel, reaching the distal end where the miniaturized probe interacts with the biological sample (represented by a CAM model). 180

8.3 (a) Schematic representation of the prism-based pulse compressor, adapted from Akturk *et al.* [11]; (b) Experimental implementation of the pulse compressor setup, showing the optical components mounted on a translation stage. 182

8.4 FWHM of the output pulse as a function of the distance between the prism and the corner cube. 182

List of Tables

4.1 Summary of excitation and emission wavelength ranges, and imaging techniques for NAD(P)H autofluorescence. 45

4.2 Summary of excitation and emission wavelength ranges, and imaging techniques for FAD autofluorescence. 46

4.3 Brewster angle measurements and refractive indices for gelatin at $\lambda = 445$ nm. 67

4.4 Brewster angle measurements and refractive indices at $\lambda = 515$ nm. 68

4.5 Brewster angle measurements and refractive indices for gelatin at $\lambda = 638$ nm. 69

5.1 Thicknesses of the SiO_2/TiO_2 thin-film multilayer for the optical filter with 485 nm transmittance peak. 86

5.2 Thicknesses of the SiO_2/TiO_2 thin-film multilayer for the optical filter with 530 nm transmittance peak. 87

5.3 RF sputtering deposition conditions for SiO_2 thin-films (sample S1 (with ± 170 nm; sample S2 with ± 80 nm) and TiO_2 thin-film (sample T1 with ± 47 nm). 88

5.4 Experimental thicknesses of SiO_2 thin-films (samples S1 and S2), and TiO_2 thin-film (sample T1), obtained using different characterization techniques. 88

5.5 Thicknesses of the SiO_2/TiO_2 thin-films multilayer, for the 485 nm transmittance peak optical filter, with the experimental refractive index values. 90

5.6 Thicknesses of the SiO_2/TiO_2 thin-films multilayer, for the 530 nm transmittance peak optical filter, with the experimental refractive index values. 91

5.7 Thicknesses of the SiO_2/TiO_2 thin-films multilayer, for the optical filter with 485 nm transmission peak, after design optimization and simplification. 92

5.8 Thicknesses of the SiO_2/TiO_2 thin-films multilayer, for the 530 nm transmittance peak optical filter, after design optimization and simplification. 92

5.9 FWHM values for the designed optical filters, considering the individually calculated mirror design and optimized design using identical mirror thicknesses. 94

5.10 Thicknesses of the SiO_2/TiO_2 thin-films multilayer, for the 530 nm transmittance peak optical filter with a second-order resonance cavity after design optimization, and simplification. 96

5.11 RF sputtering deposition conditions for the fabrication of the 485 nm filter. 102

5.12 RF sputtering deposition conditions for thin-film for the fabrication of the 530 nm filter. . 102

5.13 Experimental FWHM values for the fabricated filters. 103

6.1 Accuracy, recall, precision, and AUC of the SVM classifier for the different combination of features, at a distance between bands of 51.5 µm in the attenuation coefficient B-scans (AC) and in the raw OCT B-scans images (RAW). 124

Acronyms

1PEF one-photon excited fluorescence

2PEF two-photon excited fluorescence

A absorbance

AC alternating current

Ar argon

ATP adenosine triphosphate

CAM chorioallantoic membrane

CCD charge coupled device

CRC colorectal cancer

CT computed tomography

CW continuous-wave

DRC depth-resolved confocal

FAD flavin adenine dinucleotide

FD-OCT frequency domain optical coherence tomography

FFT fast fourier transform

FIT fecal immunochemical test

FLIM fluorescence lifetime imaging

FMN flavin mononucleotide

FSR free spectral range

FWHM full width at half maximum

gFOBT guaiac-based fecal occult blood test

GRIN gradient refractive index

Hb deoxyhemoglobin

HbO_2 oxyhemoglobin

IPA isopropyl alcohol

MEMS micro-electro-mechanical systems

MOEMS micro-opto-electro-mechanical systems

MPM multiphoton microscopy

mt-sDNA multitarget stool DNA tests

n refractive index

NAD coenzyme nicotinamide adenine dinucleotide

NAD(P)H reduced nicotinamide adenine dinucleotide (phosphate)

NAD+ oxidized nicotinamide adenine dinucleotide

NADH reduced nicotinamide adenine dinucleotide

NADP nicotinamide adenine dinucleotide phosphate

NADPH reduced nicotinamide adenine dinucleotide phosphate

NaOH sodium hydroxide

NIR near-infrared

O_2 oxygen

OCT optical coherence tomography

OXPHOS oxidative phosphorylation

PBS phosphate-buffered saline

PDMS polydimethylsiloxane

PMT photomultiplier tube

RAE rotating-analyzer ellipsometer

RF radio frequency

ROC AUC area under the receiver operating characteristic curve

ROI region of interest

SD-OCT spectral domain optical coherence tomography

SEM scanning electron microscopy

SHG second harmonic generation

SiO_2 silicon dioxide

SLD superluminescent diode

SRS stimulated raman scattering

SS-OCT swept-source optical coherence tomography

SVM support vector machine

T transmittance

TACS tumor-associated collagen signatures

TD-OCT temporal domain optical coherence tomography

Ti titanium

TiO_2 titanium dioxide

Part I

Conceptualization

Chapter 1

Introduction

This chapter introduces the main context and scope of the thesis. It outlines the fundamental concepts related to colorectal cancer (CRC), relevant biological tissue properties, and current diagnostic approaches, highlighting their limitations. In addition, it presents the motivation and objectives that guide this work, as well as an overview of the contributions developed throughout the thesis.

1.1 Thesis Overview

CRC represents a major global health challenge, being one of the most prevalent and deadly forms of cancer. Early detection plays a crucial role in improving patient survival rates. However, current diagnostic workflows rely heavily on conventional colonoscopy followed by histopathological analysis of biopsied tissue. While effective, this approach is inherently invasive, time-consuming, and dependent on *ex situ* analysis, often delaying clinical decisions and required treatments.

In recent years, significant efforts have been directed toward the development of advanced optical imaging techniques capable of enabling real-time*, in vivo* tissue characterization. These approaches aim to provide what is commonly referred to as optical biopsy, allowing clinicians to assess tissue morphology and biochemical properties directly during endoscopic procedures, without the need for physical tissue removal. Such capabilities have the potential to transform current clinical practices by improving diagnostic speed, reducing patient risk, and enabling more accurate and immediate therapeutic decisions.

Among the various optical imaging modalities, optical coherence tomography (OCT) and multiphoton microscopy (MPM) have emerged as particularly promising techniques. OCT provides high-resolution, depth-resolved structural imaging of biological tissues, enabling the visualization of microstructural features associated with pathological changes. Its compatibility with optical fiber technology makes it especially suitable for integration into endoscopic systems, allowing access to internal organs such as the colon. MPM offers complementary functional information by exploiting nonlinear light–matter interactions and intrinsic tissue contrast mechanisms. In particular, endogenous fluorophores such as reduced nicotinamide adenine dinucleotide (phosphate) (NAD(P)H) and flavin adenine dinucleotide (FAD) can be used to analyze cellular metabolism, providing valuable biomarkers for distinguishing between normal and malignant tissues.

Despite their significant potential, the use of OCT and MPM in routine clinical practice remains lim-

ited by several technological challenges. Although OCT systems are inherently more compact than MPM, their implementation in endoscopic environments requires careful optimization to maintain imaging performance under strict size constraints. In particular, the limited diameter of the instrument channel in standard colonoscopes imposes severe restrictions on the design and integration of optical systems. On the other hand, conventional MPM systems are typically bulky and complex, requiring sophisticated laser sources and optical components, which hinder their integration into compact and flexible medical devices.

In this context, the present thesis aims to explore and advance the use of OCT and MPM for CRC diagnosis, with a particular focus on their adaptation to conditions compatible with future endoscopic integration. The work combines fundamental studies on light–tissue interaction with the development of experimental models, optical components, and imaging methodologies, addressing both structural and functional aspects of tissue characterization.

A central aspect of this research is the use of tissue models to enable controlled and reproducible experimentation. The chorioallantoic membrane (CAM) assay is employed as an *in vivo* platform for the growth of both non-malignant and malignant colorectal tissues, providing a biologically relevant environment for optical imaging studies. In parallel, tissue-mimicking phantoms are developed to reproduce the optical and biochemical properties of biological tissues, allowing systematic validation and optimization of imaging techniques under well-defined conditions. These models play a crucial role in bridging the gap between simplified experimental setups and complex biological systems.

Another focus of this thesis lies in the development of specialized optical components required for multiphoton imaging, particularly highly selective optical filters based on a Fabry-Perot structure. These components are essential for isolating fluorescence signals from endogenous biomarkers and enabling efficient detection in complex biological environments. Their design, fabrication, and characterization represent an important step toward improving the performance and feasibility of MPM systems for biomedical applications.

The thesis also addresses the analysis of optical data obtained from both OCT and MPM techniques. For OCT, particular emphasis is placed on the extraction of quantitative features, such as the attenuation coefficient, to enable discrimination between non-malignant and malignant tissues. The use of machine learning approaches further enhances the ability to classify tissue types based on optical signatures, demonstrating the potential of OCT as a diagnostic tool for CRC. For MPM, the analysis focuses on the detection of endogenous fluorescence signals and the evaluation of metabolic indicators, such as the redox ratio, which provide insights into tissue physiology and pathological state.

Finally, this work explores the challenges and feasibility of miniaturizing OCT and MPM systems for

integration into conventional colonoscopes. The development of compact optical architectures, fiber-based light delivery systems, and miniaturized components is investigated as a pathway toward the realization of clinically viable devices. Although full integration is not achieved within the scope of this thesis, the results obtained demonstrate important progress and establish a solid foundation for future developments in this field.

In summary, this thesis contributes to the advancement of optical imaging technologies for CRC diagnosis by combining experimental, technological, and analytical approaches. By addressing key challenges related to tissue modeling, signal detection, data analysis, and system miniaturization, this work supports the long-term goal of enabling real-time, *in vivo* optical biopsy during endoscopic procedures. Such advancements have the potential to significantly improve early detection, enhance diagnostic accuracy, and ultimately contribute to better clinical outcomes for patients with CRC.

1.2 Author's Contribution

This thesis presents original contributions in the development and application of optical imaging techniques for CRC diagnosis, with a particular focus on OCT and MPM.

The main contributions of the author are summarized as follows:

- **Design, fabrication, and characterization of optical filters:** development of Fabry–Perot filters, including design, microfabrication, characterization, and application in a custom-built MPM optical setup.
- **Development of tissue-mimicking phantoms:** definition and implementation of fabrication protocols, including the selection and optimization of all relevant components to replicate colorectal tissue properties.
- **MPM setup development and optimization:** implementation and iterative optimization of an MPM custom-built system, improving signal detection and overall performance.
- **Development of a refractive index measurement setup:** design and implementation of an experimental setup for refractive index characterization of materials and fabricated samples.
- **OCT image database (CAM assays):** acquisition and organization of an OCT dataset from CAM models, made publicly available to support further data analysis and research [12].

- **OCT data processing and analysis:** development of image processing pipelines and Python code, and implementation of machine learning methods (support vector machine (SVM)) for tissue classification.
- **MPM data processing and analysis:** development of Python code for fluorescence signal analysis, including metabolic characterization through redox ratio evaluation.
- **Scientific publications:** contribution to three peer-reviewed publications arising from the work developed in this thesis [10, 13, 14], as well as an additional publication [15] that, although not directly part of this work, utilizes the MPM setup developed within its scope.
- **Conceptual development of miniaturized MPM systems:** initial design and identification of key requirements for future integration into endoscopic platforms.

1.3 Biological Tissues

Biological tissues can be broadly classified into three major types: epithelial, connective, and glandular. Epithelial tissue covers organ surfaces and lines internal structures, such as the inner lining of the digestive tract. It consists of sheets of tightly packed cells held together by intercellular junctions and supported by a thin layer of connective tissue known as the basement membrane. Epithelial tissue performs several essential biological functions, including protection, absorption, and secretion. Connective tissue consists of cells embedded in a nonliving material known as the extracellular matrix and includes several subtypes, such as loose connective, dense connective, elastic, reticular, and adipose tissue. Generally, the connective tissue is composed of cells and structural fibers, mainly collagen, elastin, and reticulin. Finally, glandular tissue is specialized for secretion and is typically derived from epithelial tissue [16].

Biological tissues can also be classified according to their structural organization. For example, fibrous tissues are mainly composed of collagen and elastin fibers arranged in lamellar bundles or fascicles. Collagen is a fibrous protein whose fundamental structural unit is tropocollagen, composed of three polypeptide strands arranged in a triple helix. Covalent cross-linking occurs both within the triple helix and between adjacent tropocollagen molecules, contributing to the formation of different types of collagen. Among these, collagen types I to V are the most abundant, with type III commonly found in the dermis, intestine, heart valves, and vessel walls. The refractive index of collagen type I is approximately 1.43 in the fully hydrated state and 1.53 in the dry state at $850\,\text{nm}$. Collagen molecules assemble into organized and partially overlapping bundles called fibrils, which further associate to form larger collagen fibers. The structural or-

ganization of fibrous proteins can produce optical anisotropy. For example, myocardial fibers are oriented along different axes and exhibit birefringence because the refractive index along the fiber axis differs from that in the transverse direction [16].

Biological tissues may also be classified by the organ or system to which they belong, such as mucosal, muscular, nervous, cervical, or adipose tissues. They can also be categorized according to their pathological state, for example, as scar or malignant tissue [16].

Mucous membranes (mucosa) consist of a moist epithelial layer and an underlying connective tissue. They are usually formed by simple epithelium, although stratified epithelium is found in areas subject to abrasion, such as near body openings. Mucous membranes are found in the gastrointestinal and respiratory tracts, as well as in the urogenital ducts, and are kept moist by glandular secretions [16].

Biological cells are the fundamental structural units of tissues. They consist of protoplasm surrounded by a plasma membrane and typically contain a nucleus. Cells vary considerably in size and shape, but most mammalian cells have diameters from 5 to $75\,\mu$m. Several intracellular structures contribute to the optical scattering properties of tissues, including cell nuclei (5–$10\,\mu$m), mitochondria (1–$2\,\mu$m), lysosomes (1–$2\,\mu$m), and ribosomes (20 nm) [16].

Tissue aging and pathological processes may significantly alter tissue structure and optical properties. For instance, scar tissue replaces normal tissue after injury and typically contains a higher proportion of collagen type III compared with normal tissue, which is richer in collagen type I. In addition, collagen fibers in scar tissue are generally less organized and less oriented than in healthy tissue [16]. Tumors, whether benign or malignant, are characterized by abnormal tissue growth, often associated with increased vascularization and structural heterogeneity [1, 16].

Biological tissues can be described, to a first approximation, as dielectric media with an average refractive index higher than that of air. In the near-infrared (NIR) spectral range, the refractive index of human tissue typically varies between 1.350 and 1.620 [2]. In the visible region, it ranges between 1.335 and 1.620 [2].

The effective refractive index of tissue can be estimated as a weighted average of the refractive indices of its constituents, namely the scattering centers (e.g., cells and organelles) and the surrounding medium. When the refractive indices of these components are closely matched, light scattering is significantly reduced. Since water is a major constituent of biological tissues, their refractive index is strongly dependent on water content [2].

At the cellular level, the refractive index varies across different structures in the NIR region. Typical values include 1.350–1.360 for extracellular fluid, 1.360–1.375 for cytoplasm, 1.460 for the cell membrane,

1.380–1.410 for the nucleus, 1.380–1.400 for mitochondria and other organelles, and 1.600–1.700 for melanin granules [2].

For bulk tissues, the refractive index at 663 nm ranges from approximately 1.368 for liver tissue to 1.455 for adipose (fatty) tissue [2]. Additionally, the refractive index of biological tissues generally decreases with increasing wavelength over the visible range (390–700 nm), reflecting normal dispersion behavior [2].

Biological tissues also contain several endogenous fluorophores that emit fluorescence when excited by light at specific wavelengths. When tissues are excited with ultraviolet light ($\lambda \leq 370$ nm), fluorescence from proteins and nucleic acids can be observed. Structural proteins such as collagen and elastin are typically excited from 300 nm to 400 nm, producing broad emission bands between 400 nm and 600 nm. Metabolic cofactors such as NADH, which are primarily located in mitochondria, are selectively excited between 330 nm and 370 nm. Other endogenous fluorophores, including flavin mononucleotide (FMN) and FAD, with excitation maxima around 380 nm and 450 nm, also contribute to intrinsic cellular fluorescence [1]. The fluorescence emission spectral ranges of the main endogenous fluorophores present in biological tissues are illustrated in Figure 1.1 [1].

These endogenous fluorophores play an important role in optical diagnostics, since their fluorescence signals are closely related to cellular metabolism. In particular, the reduced (NADH) and oxidized (NAD+)

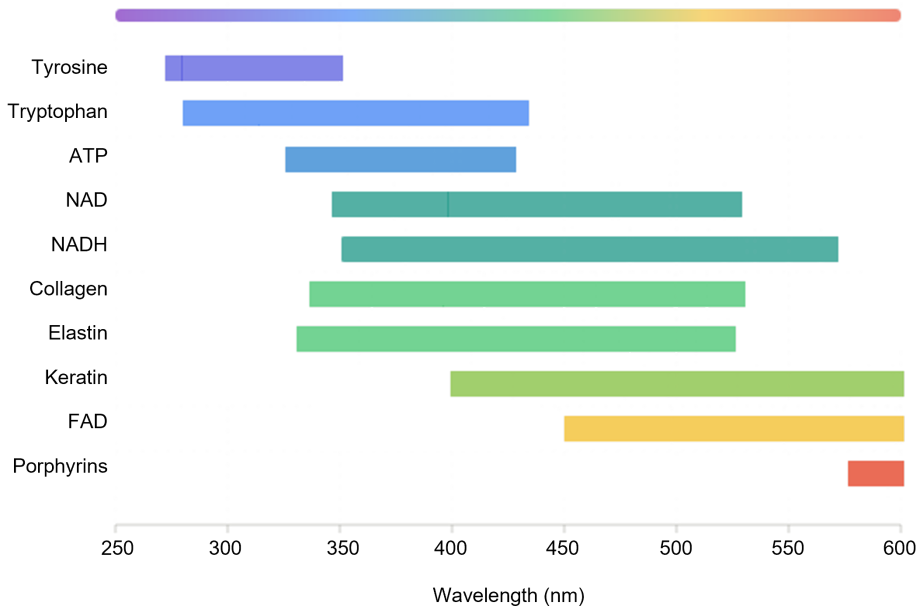


Figure 1.1: Fluorescence emission ranges of the main endogenous fluorophores in biological tissues [1].

forms of coenzyme nicotinamide adenine dinucleotide (NAD) participate in cellular metabolic pathways, and variations in NADH fluorescence intensity can be used to detect metabolic alterations associated with pathological conditions.

In addition to endogenous fluorophores, exogenous fluorescent dyes can be used to probe cellular anatomy and physiology. Recent developments include receptor-targeted dye–peptide conjugates and fluorescent protein platforms for *in vivo* optical imaging of tumors [1].

Another important phenomenon to consider in the analysis of biological tissues is absorbance (A). This phenomenon describes how light is attenuated as it propagates through a medium and is defined as the logarithmic ratio between the incident and transmitted light intensities. According to the Beer–Lambert law [2, 17], it can be expressed as:

$$A(\lambda) = \epsilon(\lambda) \cdot c \cdot d \tag{1.1}$$

where $\epsilon(\lambda)$ is the wavelength-dependent extinction coefficient, c is the concentration of the absorbing species, and d is the optical path length. The extinction coefficient, in the classical Beer-Lambert law, is associated with molecular absorption and whereas tissue attenuation generally results from the combined effects of absorption and scattering. [2].

Biological tissues contain several chromophores, such as hemoglobin and melanin, that exhibit strong optical absorption. Although these molecules typically have low fluorescence quantum yields, their relatively high concentrations enable them to reabsorb the fluorescence emitted by tissue fluorophores to a significant extent. This results in a filtering effect that alters the observed fluorescence spectra [1]. Figure 1.2 shows the absorption coefficient spectrum of some biological tissue compounds.

Oxyhemoglobin (HbO_2) exhibits a strong absorption peak at 415 nm, known as the Soret band, along with two weaker absorption peaks at 542 nm and 577 nm (Q-bands) [2]. In contrast, deoxyhemoglobin (Hb) presents a primary absorption peak at 430 nm and a secondary peak at 555 nm [2]. Both forms of hemoglobin show significantly reduced absorption at wavelengths longer than 620 nm [2]. Due to the wavelength-dependent absorption properties of tissue chromophores, it is possible to define an optical window in biological tissues, commonly referred to as the therapeutic or diagnostic window, typically spanning from 700 nm to 1100 nm, where absorption is minimized, and photon penetration is maximized. Additionally, narrower transparency windows are also observed around 1300 nm and 1600 nm. In the infrared region, the absorption coefficient is predominantly governed by water content in the tissue [1, 2].

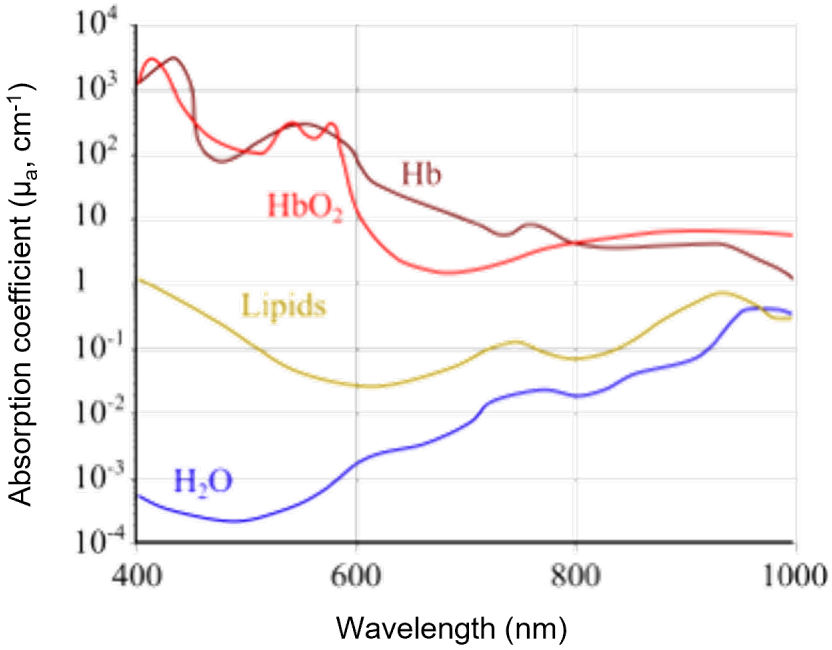


Figure 1.2: Wavelength-dependent absorption coefficients of key biological chromophores $(\text{oxyhemoglobin}\ (HbO_2)$, deoxyhemoglobin (Hb), lipids, and water $(H_2O))$ [2].

1.4 Cancer Tissues

The relationship between cellular metabolism and cancer was first described by Otto Warburg in the early 1920s, who observed that tumor cells produce significantly more lactic acid than normal cells, even in the presence of oxygen (O_2). This phenomenon, known as the Warburg effect, reflects the enhanced reliance of cancer cells on cytosolic glycolysis rather than mitochondrial oxidative phosphorylation (OXPHOS) for energy production. Although aerobic glycolysis remains a hallmark of cancer metabolism, mitochondria continue to play a crucial role in maintaining cellular homeostasis and supporting tumor growth. The coexistence of increased glycolysis and partially suppressed mitochondrial metabolism characterizes what is known as the Warburg phenotype [18].

Both OXPHOS in mitochondria and cytosolic glycolysis are essential metabolic pathways that drive the survival and proliferation of cancer cells. The balance between these two pathways is influenced by several factors, including O_2 availability, nutrient supply, and the tumor microenvironment. In rapidly proliferating tumors, inadequate vascularization often leads to hypoxia and reduced nutrient availability. Under these conditions, cancer cells frequently increase glycolytic activity to sustain energy production. In many tumors, cytosolic glycolysis contributes between 10 and $90\,\%$ of the total cellular adenosine triphosphate (ATP), while the remaining energy is generated through mitochondrial OXPHOS [18]. However, recent studies

have shown that cancer metabolism is highly heterogeneous, with significant variability in the relative contributions of glycolysis and mitochondrial respiration across different tumor types and physiological conditions [19, 20].

Within mitochondria, the Krebs cycle plays a central role in cellular metabolism by generating reducing equivalents such as NADH, which serves as the primary electron donor to the mitochondrial electron transport chain. Flavin cofactors, including FAD, also participate in redox reactions within mitochondrial enzymes. In addition to its role in energy production, NADH contributes to cellular defense mechanisms against oxidative stress and supports several metabolic processes that promote cell survival. The reduced form of nicotinamide adenine dinucleotide phosphate (NADP), NADPH, is particularly important for anabolic pathways, such as fatty acid, amino acid, and nucleotide synthesis. Furthermore, NADPH acts as a cofactor for antioxidant systems helping to maintain cellular redox balance and protect cells from oxidative damage [18, 21]. Changes in the concentration and intracellular distribution of NADPH have been associated with the development and progression of several diseases, including aging-related disorders, diabetes, neurodegenerative diseases, and cancer [22, 23]. In proliferating cancer cells, NADPH-dependent metabolic pathways play an essential role in sustaining cell growth and preventing apoptosis [18]. This way, the elevated concentration of NADH provides the required energy for cancer cells' growth through aggravated glycolysis.

Importantly, several metabolic cofactors involved in cellular respiration exhibit intrinsic autofluorescence. Among these, NADH, NADPH, and FAD are particularly relevant for optical metabolic imaging. The NADH and NADPH share nearly identical excitation and emission spectra. Therefore, their combined autofluorescence signal is commonly referred to as NAD(P)H [18, 21, 24].

The concentrations of NAD(P)H and FAD vary inversely depending on the metabolic state of the cell. While NAD(P)H fluorescence increases during more reduced metabolic states associated with glycolytic activity, FAD fluorescence increases under more oxidized conditions related to mitochondrial respiration. The ratio between the fluorescence intensities of these cofactors, commonly referred to as the metabolic or redox ratio (NAD(P)H/FAD), provides an important indicator of cellular metabolic activity. This ratio has been widely used to differentiate proliferating, quiescent, and apoptotic cells, as well as to characterize metabolic alterations associated with cancer progression [18]. This optical metabolic imaging approach enables the study of cancer heterogeneity, the identification of cancerous versus non-cancerous cells *in situ*, and the monitoring of treatment responses, including responses to chemotherapy [18, 21, 23, 25–27].

From a spectroscopic perspective (Figure 1.1), NADH exhibits one-photon absorption peaks near 260 nm and around 340 nm. When excited at approximately 340 nm, NADH emits fluorescence with a maximum

around 440-465 nm with a fluorescence lifetime of about 0.4 ns in aqueous solution, depending on the cellular environment [18]. In contrast, FAD exhibit one-photon absorption maxima near 370 nm and 440 nm, with fluorescence emission typically observed around 520-530 nm and a fluorescence lifetime of approximately 2.3 ns [18, 24, 26–32].

Collagen also plays an important role in cancer development. Imaging collagen can facilitate the identification of tumor-associated collagen signatures (TACS), which can help to determine the cancer stage and even the direction of the cell invasion that the tumor will take. TACS is a characterization of collagen signatures during defined levels of tumor progression [33]. TACS-1 describes the dense collagen surrounding a tumor at early-stage, where the collagen fibers show no specific alignment. As the tumor develops, the TACS-2 phenotype emerges, characterized by collagen fibers that wrap around the developing tumor and are oriented parallel to the tumor-stromal boundary. Finally, in later-stage tumors, the TACS-3 pattern is observed where collagen fibers are oriented perpendicular to the tumor–stromal boundary. In this stage, collagen fibers are often aligned along the direction of tumor cell invasion [33].

It is also important to note that normal and malignant tissues present distinct structural organization and cellular heterogeneity. In non-malignant tissues, the vascular network is typically well-organized and hierarchical, allowing low–molecular-weight agents to distribute relatively homogeneously throughout the tissue. In contrast, several factors in malignant tissues hinder the uniform distribution of these agents, particularly in the deeper and central regions of tumors. The tumor microenvironment is therefore often characterized by hypoxia, accumulation of metabolic by-products, acidic pH, and elevated concentrations of growth factors. As a result, cancerous tissues frequently exhibit a gradient of tissue density from the surface toward the tumor core. Conversely, normal tissues tend to maintain a higher degree of structural and metabolic homogeneity. This gradient arises because, in malignant tumors, cells in the deeper and central regions tend to aggregate and adapt to reduced O_2 and nutrient availability, as described in previous sections [34–36].

1.5 Colorectal Cancer

Cancer is one of the leading causes of death worldwide [37]. According to the World Health Organization, cancers of the colon and rectum are among the most prevalent malignancies. In 2020, CRC was the third most commonly diagnosed cancer worldwide and the second leading cause of cancer-related deaths, representing a significant global public health challenge [37, 38].

The stage of cancer development at the time of diagnosis has a strong impact on treatment outcomes

and patient survival. Consequently, early detection plays a critical role in preventing metastasis, reducing mortality, and improving both prognosis and quality of life. However, epidemiological studies indicate that more than one-third of CRC patients are diagnosed only after the disease has already spread to the lymph nodes, which significantly compromises survival rates [38–40].

Globally, CRC diagnosis, tumor complications, and therapeutic strategies have therefore become major topics of medical and biomedical research. In 2022, approximately $1{,}926{,}425$ new cases of CRC were reported worldwide. Figure 1.3 presents the six cancers with the highest number of new cases in 2022 [3].

In the United States, the CRC mortality rate was approximately 12.7 deaths per $100{,}000$ population in 2023. As shown in Figure 1.4, mortality rates have gradually decreased between 1999 and 2023. However, reduction has occurred at a relatively slow rate, and in the last five years, it has been relatively stable [4].

Globally, the incidence rate of CRC reached 18.35 cases per $100{,}000$ population in 2022, ranking among the cancers with the highest incidence rates worldwide [5]. Figure 1.5 illustrates the incidence rates of the six most common cancers in 2022.

Similarly, CRC accounted for one of the highest global cancer mortality rates in 2022, with approximately 8.1 deaths per $100{,}000$ population, ranking third among cancer-related causes of death [6]. This distribution is illustrated in Figure 1.6.

Future projections also indicate a substantial increase in the global burden of cancer. The predicted number of cancer-related deaths worldwide is expected to rise from approximately $9{,}743{,}832$ deaths in

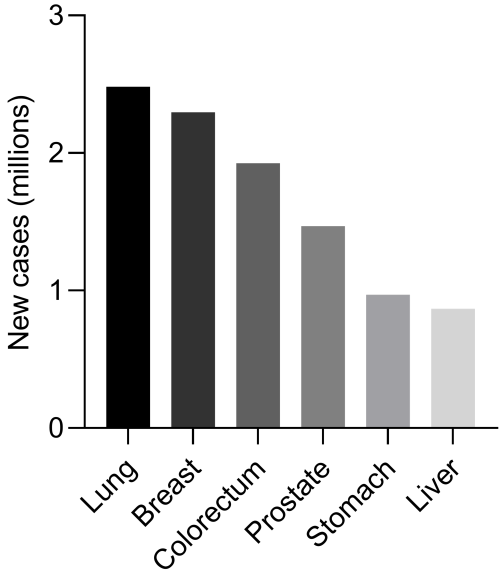


Figure 1.3: Number of new cancer cases worldwide in 2022 [3].

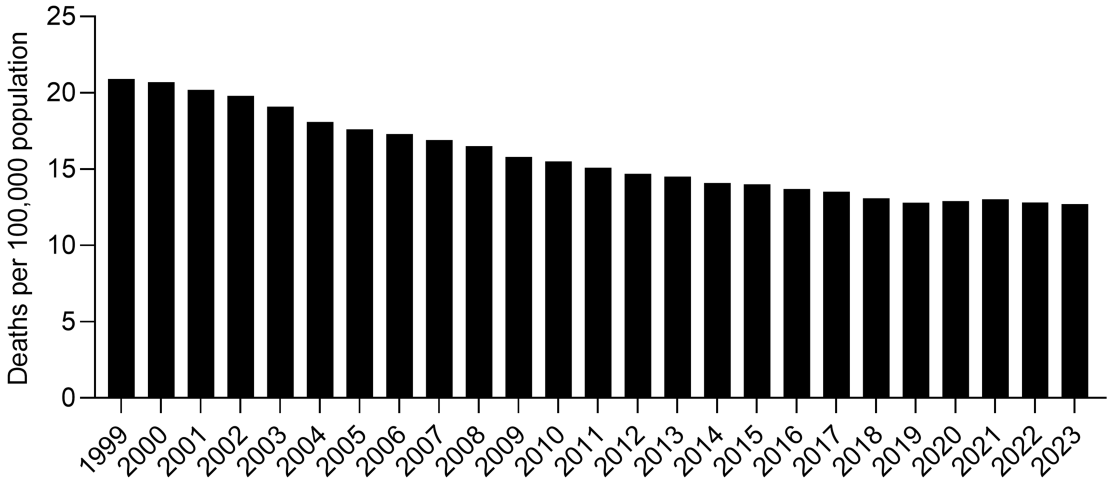


Figure 1.4: Death rate of colon and rectum cancer in the United States from 1999 to 2023 (per $100{,}000$ population) [4].

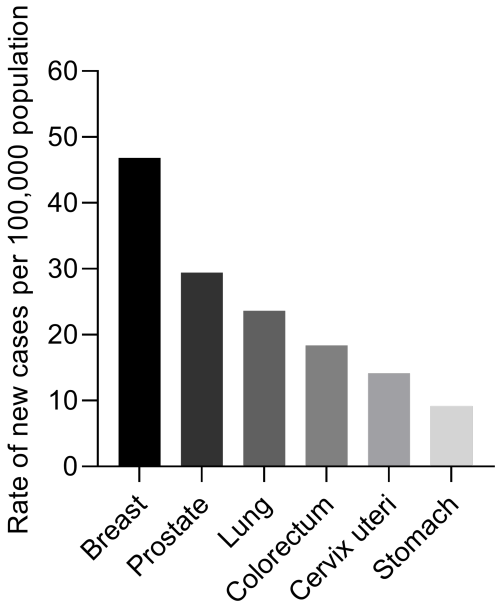


Figure 1.5: Rate of new cancer cases worldwide in 2020, by type of cancer (per $100{,}000$ population) [5].

2022 to about $18{,}480{,}300$ deaths by 2050 [7]. As shown in Figure 1.7, these projections highlight the continued growth in global cancer mortality over the coming decades.

All these data highlight the importance of improving both the accuracy and timeliness of cancer diagnosis, particularly for several types of cancer, with a special emphasis on CRC.

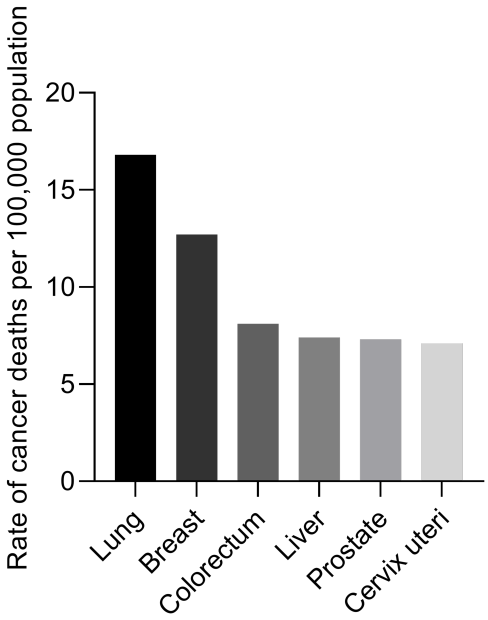


Figure 1.6: Rate of cancer deaths worldwide in 2022 (per $100{,}000$ population) [6].

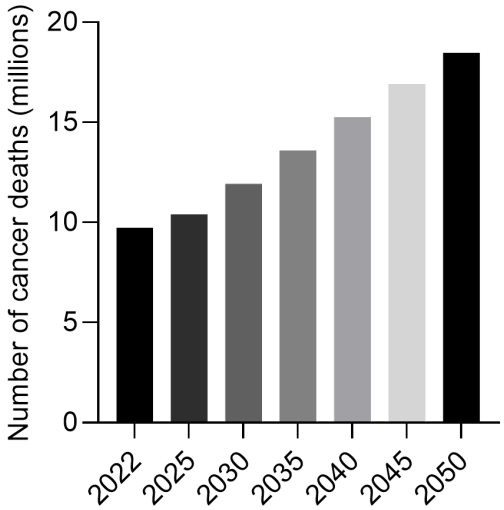


Figure 1.7: Predicted number of cancer-related deaths worldwide from 2022 to 2050 [7].

1.6 Colorectal Cancer Diagnosis Techniques

Early diagnosis of CRC remains the most effective strategy for reducing the impact of the disease. Early detection enables timely treatment and significantly improves long-term survival while reducing the physical and therapeutic burden on patients [41]. According to the American Cancer Society, data from patients diagnosed between 2014 and 2020 show that the five-year survival rate for localized CRC is approximately $91\,\%$ for colon cancer and $90\,\%$ for rectal cancer. These values decrease to $73\,\%$ and $74\,\%$, respectively, for regionally advanced disease, and drop markedly in the presence of distant metastases, reaching $13\,\%$ for colon cancer and $18\,\%$ for rectal cancer [42].

Current guidelines for CRC screening vary across healthcare systems. Nevertheless, most recommendations suggest initiating screening between the ages of 45 and 50, with strategies adapted to individual risk factors, including diet, smoking, obesity, family history, and age [43–47].

In Europe, the Council of the European Union recommends the use of the fecal immunochemical test (FIT) as the primary screening method to identify individuals who should be referred for follow-up colonoscopy, particularly in the age group between 50 and 74 years. Screening programs may adjust FIT thresholds considering individual risk factors and previous test results, enabling a more personalized approach. In addition, endoscopic techniques may be incorporated as primary diagnostic tools within combined screening strategies, especially for higher-risk populations [48].

The following subsection presents an overview of the most commonly used techniques for the diagnosis of suspicious lesions.

1.6.1 Traditional Diagnosis Techniques

There are several established screening and diagnostic methods for CRC, which differ in terms of invasiveness, sensitivity, specificity, cost, and suitability for large-scale implementation. These methods can be broadly divided into two main categories: stool-based tests and imaging-based examinations.

Stool-based tests are the least invasive, relatively inexpensive, require little to no preparation, and are therefore well-suited for population-wide screening programs. These tests detect biomarkers associated with CRC in stool samples. The most used methods include:

- Guaiac-based fecal occult blood test (gFOBT), which detects small amounts of blood in the stool. Since colorectal tumors may bleed into the gastrointestinal tract, this test can indirectly indicate the presence of disease. It demonstrates moderate to high sensitivity and specificity [49];

- FIT, a more recent variation that uses specific antibodies to human hemoglobin. This method improves both sensitivity and specificity compared to gFOBT, while eliminating the need for dietary restrictions [50];

- Multitarget stool DNA tests (mt-sDNA), which combine hemoglobin detection (as in FIT) with the analysis of DNA mutations commonly associated with CRC. This approach significantly increases sensitivity, albeit with reduced specificity and higher cost [51].

In contrast, imaging-based diagnostic techniques provide direct visualization of the colon and allow for more accurate detection and characterization of lesions. The main methods include:

- Computed tomography (CT) colonography, a minimally invasive technique that uses CT imaging to reconstruct a three-dimensional model of the colon. It does not require sedation and is highly sensitive for detecting large polyps. However, it requires bowel preparation and air insufflation, exposes the patient to ionizing radiation, and does not allow biopsy or polyp removal during the procedure [52];

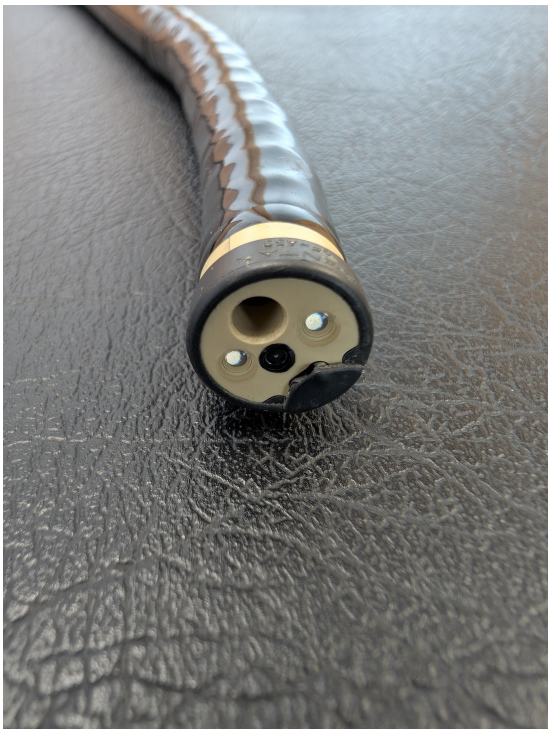
- Colonoscopy is the gold standard for CRC screening. This technique involves the insertion of a flexible endoscope equipped with a camera to visualize the entire colon. It enables the detection of polyps and tumors, as well as tissue sampling and polyp removal through the instrument channel. Suspected lesions are typically biopsied for histopathological analysis. Due to its high sensitivity and specificity, as well as its therapeutic capabilities, colonoscopy remains the most widely used diagnostic method [53]. Figure 1.8(a) and 1.8(b) illustrate a typical colonoscope and associated instrumentation. Despite its advantages, colonoscopy is invasive, requires bowel preparation and often sedation, and may cause complications such as bleeding, perforation, infection, or post-polypectomy syndrome. Additionally, it requires specialized equipment and trained personnel, which can limit its accessibility [54–57];

- Flexible sigmoidoscopy examines only the distal portion of the colon. It is less invasive than a colonoscopy, typically does not require sedation, and involves reduced preparation. However, its diagnostic scope is limited, and it is often used as a complementary screening tool or for investigating specific symptoms [58];

- Capsule endoscopy, a non-invasive technique in which the patient swallows a capsule containing a miniature camera. As the device travels through the gastrointestinal tract, it captures images that can be analyzed for abnormalities, including signs of CRC. This method is well tolerated and



(a)



(b)



(c)

Figure 1.8: (a) Flexible endoscope used for conventional gastrointestinal imaging (Pentax FC-38FW2); (b) distal tip of the endoscope (Pentax FC-38FW2), showing the imaging lens, illumination system, and instrumentation channel; and (c) wireless capsule endoscopy device (PillCam SB2).

does not require sedation. However, it does not allow tissue sampling or therapeutic intervention, provides no control over device movement, and generally exhibits lower sensitivity and specificity compared to colonoscopy. Its cost is also relatively high, and it is mainly used when conventional endoscopy is contraindicated [59, 60]. Figure 1.8(c) shows an example of an endoscopic capsule.

From the discussion above, it can be concluded that conventional clinical evaluation of patients with suspected CRC typically includes medical history review, fecal occult blood tests, colonoscopy, and tissue biopsy [61, 62].

Thus, the definitive diagnosis of suspicious tissue relies on histopathological analysis, in which tissue samples are examined to confirm the presence of CRC. Histopathology, which involves tissue preparation, staining, microscopic visualization, and expert interpretation, is widely regarded as the gold standard for disease diagnosis. Despite its long-standing clinical use and reliability, this process is inherently time and labor-intensive [63, 64].

Histopathological evaluation is typically performed by trained pathologists following histochemical processing carried out by specialized technicians. The most used approach is hematoxylin and eosin staining, a technique introduced in the late 19th century that remains the cornerstone of diagnostic pathology [64].

Thus, it is possible to affirm that the main current diagnostic techniques present several limitations. Conventional white-light colonoscopy is primarily limited to the identification of macroscopic morphological alterations and to tissue excision for subsequent histopathological examination. It may fail to detect diminutive lesions or subtle microscopic abnormalities, particularly in cases involving diffuse disease over large areas. In such situations, targeted biopsy becomes challenging, time-consuming, and potentially prone to sampling errors [65, 66].

Histopathology itself presents significant limitations, as indicated before. The overall process is time-consuming, which restricts its use in scenarios requiring real-time or intraoperative decision-making. In addition, tissue processing can introduce artifacts, such as distortion or loss of biological structures, which may complicate or bias image interpretation. Importantly, the initial fixation step alters or eliminates metabolic, functional, and dynamic information, preventing the assessment of living tissue physiology [63].

1.6.2 Emerging Techniques

There is an increasing demand for non-invasive, objective diagnostic tools to enhance early cancer detection. A major goal in biomedical engineering is the development of techniques for real-time, *in vivo* molecular imaging of tissues without the need for staining, sectioning, or exogenous contrast agents, while maintaining high spatial resolution and three-dimensional capability. In this context, the precise

risk stratification of colorectal polyps through endoscopic evaluation is essential to improve the quality and safety of patient care. This approach reduces unnecessary tissue removal for biopsy and shortens procedure time, thereby minimizing patient risk [67]. Consequently, the concept of optical biopsy, which enables real-time, *in vivo* assessment of colorectal tissues, has gained significant attention in recent years, driven by advances in imaging technologies [67–69].

To address these challenges, several label-free optical imaging approaches have been developed that rely on intrinsic tissue contrast generated by light-matter interactions, rather than conventional histological processing. Examples include stimulated raman scattering (SRS) microscopy, which exploits molecular vibrational contrast by tuning the optical frequency difference between excitation and emission beams [70], photoacoustic microscopy, which provides absorption based contrast by varying the excitation wavelength [71], and multimodal nonlinear optical microscopy, which enables the generation of multiple contrast mechanisms through controlled excitation and detection schemes [72]. Rapid advances in laser technologies and microscopy, combined with the increasing integration of artificial intelligence for image analysis, are making real-time imaging and automated diagnosis increasingly feasible [73, 74].

Among these techniques, label-free nonlinear optical microscopy, and in particular MPM, has emerged as a highly promising approach for addressing current diagnostic limitations. This technique offers high spatial and temporal resolution, together with an intrinsic contrast mechanism based on endogenous tissue properties. By exploiting non-perturbative light–tissue interactions, MPM enables high-resolution imaging of both structural and functional features without the need for exogenous labels [63]. Importantly, such modality can be integrated into conventional endoscopic systems, enabling real-time *in vivo* optical biopsy during colonoscopy procedures [75, 76]. Nevertheless, its implementation still faces challenges, including limited contrast, reduced signal efficiency, and the requirement for a complex and costly laser system, which hinder widespread clinical adoption [63].

A key advantage of optical techniques lies in their ability to probe intrinsic biochemical properties of tissues, particularly cellular metabolism. Endogenous metabolic cofactors such as NAD(P)H and FAD, which play central roles in cellular respiration, can be exploited as label-free biomarkers. Metabolic alterations are a hallmark of cancer; thus changes in the fluorescence signals of these molecules provide valuable information for distinguishing between normal and malignant tissues [22, 25, 26, 77].

Based on this principle, the ratio between NAD(P)H and FAD fluorescence intensities, commonly referred to as the metabolic or redox ratio, has been widely used as an indicator of cellular metabolic state. This ratio is particularly relevant for cancer characterization. For example, Hong *et al.* [26] reported an increased redox ratio in human CRC tissues, characterized by higher NAD(P)H fluorescence and lower FAD

fluorescence in tumor regions compared to non-tumor tissues. In that study, both signals were detected using two-photon excited fluorescence (2PEF). Similar trends have been observed in other cancer types, including breast and bladder cancers, further supporting the potential of NAD(P)H/FAD analysis for cancer diagnosis and characterization [78].

Another relevant technique for cancer diagnosis is OCT, an optical imaging modality capable of producing high-resolution cross-sectional images of inhomogeneous samples, enabling 3D visualization of internal biological microstructures. With axial resolution typically ranging from 1 to $15\,\mu$m, OCT enables optical biopsy of biological tissues [79–82]. The development of optical fiber–based OCT systems has significantly expanded the range of applications of OCT [83, 84], particularly in the field of cancer research [85]. Since OCT systems can be fully implemented using optical fibers, they are inherently compact and well-suited for integration into endoscopic platforms. This makes OCT especially advantageous for accessing internal organs, including the human colon.

Extensive research has demonstrated the strong potential of OCT in oncology, particularly for tumor detection and characterization [86–90]. In gastroenterology, multiple studies have evaluated the performance of OCT for imaging the gastrointestinal tract [91–93], including applications in the upper gastrointestinal system [94, 95].

1.7 Motivation and Objectives

CRC remains one of the leading causes of mortality related to cancer worldwide, highlighting the critical need for early detection and accurate diagnosis. Conventional diagnostic approaches rely on histopathological analysis, which requires tissue extraction, fixation, staining, and microscopic evaluation. Although this methodology is considered the gold standard, it is inherently time-consuming, labor-intensive, and destructive, often requiring several hours to days to produce results. Furthermore, these processes may introduce artifacts that can compromise the accuracy of tissue interpretation.

In this context, there is a growing demand for alternative diagnostic techniques capable of providing real-time, *in vivo*, and label-free assessment of biological tissues, enabling what is commonly referred to as optical biopsy. Such approaches aim to eliminate the need for physical tissue removal and *ex situ* analysis, significantly reducing diagnostic time and improving clinical decision making during procedures such as colonoscopy.

Among the available optical imaging techniques, OCT and MPM have emerged as particularly promising modalities. OCT enables high-resolution, depth-resolved structural imaging of tissues, making it suitable for

identifying morphological alterations associated with cancer. In contrast, MPM provides complementary functional information by probing intrinsic biochemical properties of tissues, particularly through endogenous fluorophores such as NAD(P)H and FAD, which are directly related to cellular metabolism. Since metabolic alterations are a hallmark of cancer, these signals can be used to distinguish between healthy and cancer tissues.

Despite their potential, the clinical translation of these techniques faces significant challenges. Current OCT and MPM systems are typically bulky, complex, and dependent on sophisticated laser sources, and they need to be significantly miniaturized to be compatible with the limited dimensions of standard endoscopic instruments, such as colonoscopes with channel diameters on the order of a few millimeters. Additionally, issues related to signal efficiency, contrast, and integration of optical components must be addressed to ensure reliable performance in biological environments.

Therefore, the main motivation of this thesis is to contribute to the development of optical technologies capable of enabling real-time, *in vivo* optical biopsy for CRC detection, by exploring and advancing the use of OCT and MPM techniques under conditions compatible with future clinical implementation.

To address this motivation, the main objectives of this work are:

- Develop and validate tissue models, including CAM assays and tissue-mimicking phantoms, enabling controlled and reproducible evaluation of optical imaging techniques;
- Design, fabricate, and characterize key optical components, such as highly selective Fabry–Perot filters, required for efficient signal detection in multiphoton imaging systems;
- Study and optimize data acquisition, processing, and analysis methodologies for both OCT and MPM, including the extraction of quantitative features for tissue classification;
- Investigate the capability of OCT for structural characterization and discrimination between non-malignant and malignant colorectal tissues, including the evaluation of its performance under miniaturization constraints;
- Explore MPM as a tool for functional and metabolic imaging of tissues, with particular emphasis on the detection of endogenous fluorophores and the analysis of the redox ratio;
- Assess the feasibility of integrating OCT and MPM into miniaturized platforms compatible with conventional colonoscopy, addressing the main technological constraints associated with system size, signal delivery, and detection.

Ultimately, this work aims to establish a technological and methodological foundation for the future development of integrated optical systems capable of providing simultaneous structural and functional information in real-time. Such systems have the potential to significantly improve the early detection and diagnosis of CRC, contributing to better patient outcomes and more efficient clinical workflows.

1.8 Thesis Organization

This thesis is structured into six main parts, each addressing a specific aspect of the research and contributing to the overall objective of advancing optical techniques for CRC analysis.

The first part provides the general background and theoretical framework that supports the work developed throughout the thesis and is divided into two chapters. The first chapter begins with an overview of the thesis, highlighting its main contributions. This is followed by a discussion of biological tissues, with particular emphasis on cancerous tissues and, more specifically, CRC. Topics such as tissue organization and optical properties, including autofluorescence, scattering, and absorption, are introduced, with a focus on the differences between healthy and cancerous tissues. Additionally, statistical data on CRC and an overview of conventional and emerging diagnostic techniques are presented. The chapter concludes with the motivation and objectives of the thesis. The second chapter of this part introduces the fundamental principles of light–matter interaction, which are essential for understanding the phenomena explored in this work.

The second part focuses on the development of tissue models that mimic human biological tissues. The first chapter presents the CAM assay, including the experimental methodology, obtained results, and main conclusions. The second chapter is dedicated to tissue phantoms, where the theoretical background for their fabrication and characterization is described, along with the developed fabrication methods and comprehensive characterization results.

The third part addresses one of the key technological developments of this work, the Fabry–Perot optical filters for the MPM setup. This section includes the theoretical principles of these filters, as well as the methods used for their design, fabrication, and characterization. The obtained results throughout different phases of design and fabrication of the filters are presented and discussed, together with the main conclusions and future perspectives.

The fourth part is dedicated to the analysis of the developed tissue models. The first chapter focuses on OCT analysis of CAM assays, including the theoretical background of the technique, the experimental setup, and the methods used for data acquisition, processing, and analysis. The main results and conclusions are

then discussed. The second chapter presents the analysis, using MPM of a variety of tissue phantoms and one biological sample derived from CAM assays. It includes the theoretical background of the nonlinear optical processes involved, a detailed description of the developed multiphoton microscopy (MPM) setup and its characterization, and the methodologies used for data acquisition and analysis, followed by the corresponding results, discussion, and main conclusions.

The fifth part explores the miniaturization of OCT and MPM systems for integration into a colonoscope. It presents the conceptual approaches, technical challenges, and preliminary results achieved toward the development of a compact and clinically applicable system.

Finally, the sixth part summarizes the main conclusions of the thesis and outlines directions for future work, particularly focusing on the integration of OCT and MPM technologies into endoscopic platforms for CRC diagnosis.

Chapter 2

Light-matter Interaction

This chapter introduces the fundamental principles of light-matter interaction. It provides an overview of linear and nonlinear optical phenomena, as well as the key physical parameters that describe light propagation and energy transference. In addition, the effects of optical radiation on biological tissues are discussed, establishing the theoretical framework required for the imaging techniques explored in this thesis.

2.1 General Overview

The interaction of light with condensed matter gives rise to a wide range of optical phenomena, which can be broadly classified as linear and nonlinear processes.

In the linear regime, the optical response of a material is directly proportional to the incident electromagnetic field. The main linear phenomena include [96–99]:

- reflection, refraction, and diffraction at surfaces and interfaces of condensed matter systems;
- absorption within the material;
- light scattering, which may be elastic (e.g., Rayleigh scattering), arising from structural inhomogeneities, or inelastic (e.g., Raman or Brillouin scattering), involving interactions with optical or acoustic phonons;
- phosphorescence or fluorescence, corresponding to the re-emission of absorbed energy as electromagnetic radiation, typically at longer wavelengths than the excitation light.

In addition to these linear processes, nonlinear optical effects arise when the interaction between light and matter becomes intensity dependent. These include phenomena such as sum- and difference-frequency generation, harmonic generation, multiphoton fluorescence, self- and cross-phase modulation, and four-wave mixing [100].

Figure 2.1 presents a Jablonski diagram illustrating several of linear and nonlinear processes, including absorption, fluorescence, intersystem crossing, and multiphoton excitation pathways.

To characterize light–tissue interactions, consideration must be given not only to the wavelength but also to the energy and power of the radiation. Energy is defined as the ability to perform work and is

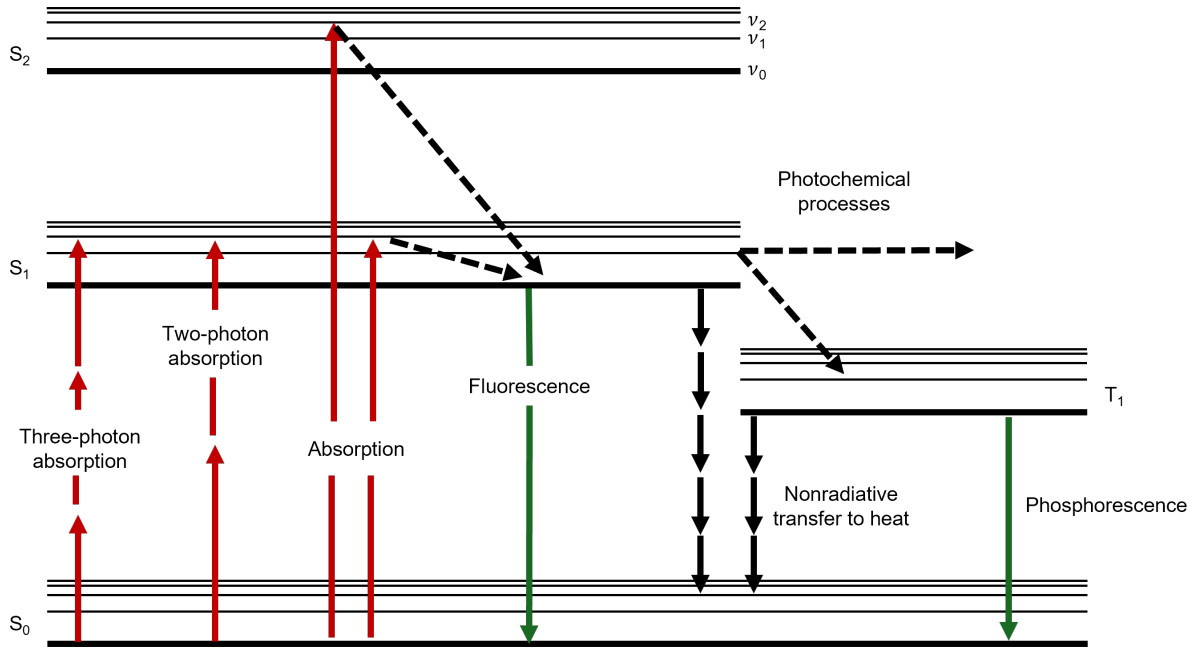


Figure 2.1: Jablonski diagram illustrating key photophysical processes, including single-, two-, and three-photon absorption, fluorescence emission, nonradiative relaxation, intersystem crossing to the triplet state, and photochemical pathways.

measured in joules (J), while power corresponds to the rate of energy delivery, expressed in watts (W) [16]. The power density, or intensity, is defined as the power per unit area perpendicular to the direction of propagation (W/m^2 or W/cm^2) [16].

Fluence (F) is defined as the time-integrated intensity over the duration of the pulse or exposure, given by $F = I \cdot \tau_p$, where τ_p is the pulse duration or pulse width [16]. Radiance describes the angular distribution of intensity, and in biological tissues, it is common to use the fluence rate, which represents the integral of radiance over all propagation directions [16].

Light–tissue interaction also depends on whether the light source operates in continuous-wave (CW) or pulsed [16]. Pulsed light consists of discrete pulses with a duration defined by the pulse width (τ_p) and a repetition rate (f_p) [16].

Laser sources can generate pulses with durations ranging from picoseconds (10^{-12} s) to femtoseconds (10^{-15} s), with repetition rates up to 100 MHz [16]. These systems are typically characterized by the pulse energy (E_p), peak power $(P_p = E_p/\tau_p)$, and average power $(P_{\text{ave}} = E_p \cdot f_p)$ [16].

The lasers generally produce coherent light, meaning that the emitted waves maintain a fixed phase relationship over time. The coherence length (l_c) quantifies the temporal coherence of the source and is given by $l_c = c \cdot \tau_c$, where c is the speed of light and τ_c is the coherence time [16]. For pulsed sources,

the coherence time is typically on the order of the pulse duration, whereas for CW sources, it is inversely proportional to the spectral bandwidth ($\tau_c \sim \lambda^2/(c \cdot \Delta\lambda)$) [16].

The coherence length is a key parameter in OCT, as shorter coherence lengths lead to improved axial resolution. This is because the coherence length defines the maximum optical path difference between the reference and sample arms for which interference can still occur [16].

2.1.1 Linear Phenomena

Linear optical phenomena are the most common light–matter interactions and occur when the incident light intensity is sufficiently low. Under these conditions, the optical response of a material is directly proportional to the applied electromagnetic field. These processes form the basis of most conventional optical components and systems [101].

A linear optical system is characterized by three fundamental properties [101]:

- it obeys the principle of superposition, such that the response to multiple input waves is equal to the sum of the individual responses;
- the output signal scales linearly with the input intensity;
- the frequency of the output remains unchanged when monochromatic light is incident on the system.

However, some phenomena are often treated within the linear framework even though the last condition is not strictly satisfied. This includes spontaneous inelastic scattering processes, such as Raman and Brillouin scattering, where the frequency of the scattered light differs from that of the incident radiation [102, 103]. At high optical intensities, these linear assumptions break down, and nonlinear optical effects emerge [104–107].

The dominant first-order optical processes in condensed matter include reflection, refraction, absorption, and elastic scattering. In contrast, inelastic scattering processes are often classified as high-order interactions [100].

Light propagation in biological tissues is strongly influenced by multiple scattering and absorption events, leading to beam broadening and attenuation. The extent of these effects depends on the size, shape, and density of tissue structures, their refractive index mismatch, and the polarization and wavelength of the incident light [2].

Within the framework of classical optics, these processes can be described in terms of intrinsic material parameters [96, 101]. For normal incidence on a planar interface, the electric field of a monochromatic

wave inside the medium can be written as [101]:

$$\vec{E}(z,t) = \vec{E}_0 e^{i(kz-\omega t)}, \tag{2.1}$$

where ω is the angular frequency, $\vec{E}_0$ is the field amplitude, and k is the wave number in the medium. The wave number is given by [101]:

$$k = \frac{\omega}{c}\tilde{n}, \tag{2.2}$$

where $\tilde{n}$ is the complex refractive index [101]:

$$\tilde{n} = n + i\kappa = \sqrt{\varepsilon}, \tag{2.3}$$

with n the real refractive index, κ the extinction coefficient, and ε the complex dielectric function.

For absorbing media $(\kappa > 0)$, the intensity decays exponentially with propagation distance [101]:

$$I(z) \propto e^{-\alpha z}, \tag{2.4}$$

where the absorption coefficient is [101]:

$$\alpha = \frac{2\kappa\omega}{c}. \tag{2.5}$$

The absorption coefficient can also be interpreted as $\alpha = 1/d$, where d is the distance over which the intensity decreases to $I = I_0/e \approx 0.37 I_0$ [2]. At the microscopic level, absorption is governed by the absorption cross section:

$$\alpha = \rho_M \sigma_{\text{abs}}, \tag{2.6}$$

where ρ_M is the number density of absorbing molecules and σ_{abs} is the absorption cross section.

The reflectance (R) and transmittance (T) of a material of thickness d under normal incidence are then given by [101]:

$$R = \left|\frac{\tilde{n}-1}{\tilde{n}+1}\right|^2, \tag{2.7}$$

$$T = (1-R)e^{-\alpha d}. \tag{2.8}$$

In the absence of absorption $(\alpha = 0)$, energy conservation leads to $R + T = 1$.

In inhomogeneous media such as biological tissues, light can also change direction due to interactions with microscopic structures that act as scattering centers [2]. The scattering coefficient (μ_s) quantifies the probability of scattering events and is defined analogously to absorption as the inverse of the mean free path. The total attenuation coefficient is given by:

$$\mu_t = \alpha + \mu_s \tag{2.9}$$

In most biological tissues, particularly in the visible and NIR regions, scattering dominates over absorption, and light transport is largely governed by μ_s [2]. Scattering primarily arises from refractive index mismatches between cellular components, so when the surrounding media have similar refractive indices, intracellular structures such as organelles become the dominant scattering centers [2].

The luminescence processes can be broadly divided into fluorescence and phosphorescence. Fluorescence corresponds to radiative transitions from excited singlet states with high quantum yield and short lifetimes (nanoseconds), whereas phosphorescence involves transitions from triplet states, typically characterized by lower quantum yield and longer lifetimes (microseconds to milliseconds) [1].

The energies of molecular electronic states depend on nuclear configurations, as illustrated by potential energy curves (Figure 2.2). Each electronic state contains multiple vibrational levels (v_i), which are further split into rotational sublevels. According to the Franck–Condon principle, electronic transitions occur vertically, as nuclear positions remain effectively unchanged during the transition.

As can be seen in Figures 2.1 and 2.2, absorption typically occurs from the ground electronic state (S_0) to higher vibronic levels of excited states (S_n). Rapid vibrational relaxation then leads to population of the lowest vibrational level of the first excited singlet state (S_1). From this state, several competing processes may occur: fluorescence emission back to S_0, internal conversion, intersystem crossing to the triplet state (T_1), and nonradiative energy transfer.

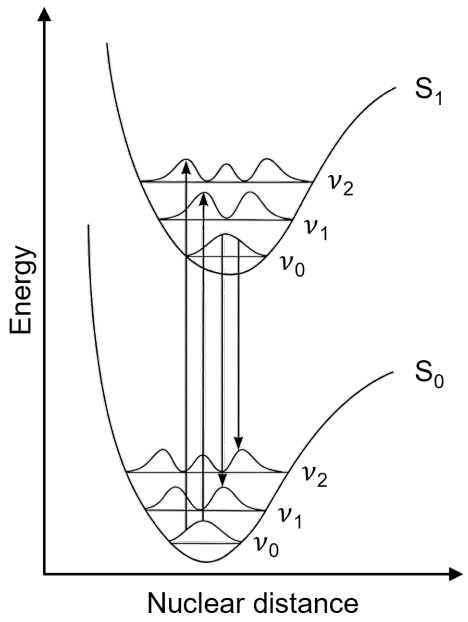


Figure 2.2: Potential energy diagram illustrating electronic states (S_0, S_1) and their associated vibrational levels, highlighting vibronic transitions and the Franck–Condon principle governing optical absorption and emission.

Because fluorescence emission occurs from relaxed excited states, it is generally shifted to lower energies (longer wavelengths) than absorption, a phenomenon known as the Stokes shift. This arises from the reduced overlap between vibrational wavefunctions of the ground and excited states.

Typical timescales for these processes are: absorption ($\sim 10^{-15}$ s), vibrational relaxation ($\sim 10^{-12}$ to 10^{-10} s), fluorescence lifetime ($\sim 10^{-10}$ to 10^{-7} s), intersystem crossing ($\sim 10^{-10}$ to 10^{-8} s), internal conversion ($\sim 10^{-11}$ to 10^{-9} s), and phosphorescence ($> 10^{-6}$ s) [1].

Finally, transition dipole moments have well-defined orientations within molecules. When excited with linearly polarized light, molecules whose dipole moments are aligned with the electric field are preferentially excited, resulting in partially polarized fluorescence emission [1].

2.1.2 Nonlinear Phenomena

Nonlinear optical effect emerge when an intense electromagnetic wave propagates through a material. These processes are termed nonlinear because the material response depends nonlinearly on the applied electromagnetic field (Figure 2.3) [63].

As light propagates through a medium, it interacts with charged particles, inducing oscillations about their equilibrium positions. The resulting separation between positive and negative charges forms electric dipoles, and the dipole moment per unit volume is defined as the induced polarization, $\vec{P}$ [105].

For weak electric fields, the induced polarization is proportional to the applied field, resulting in a linear optical response. However, at sufficiently high field strengths, this proportionality no longer holds, and the

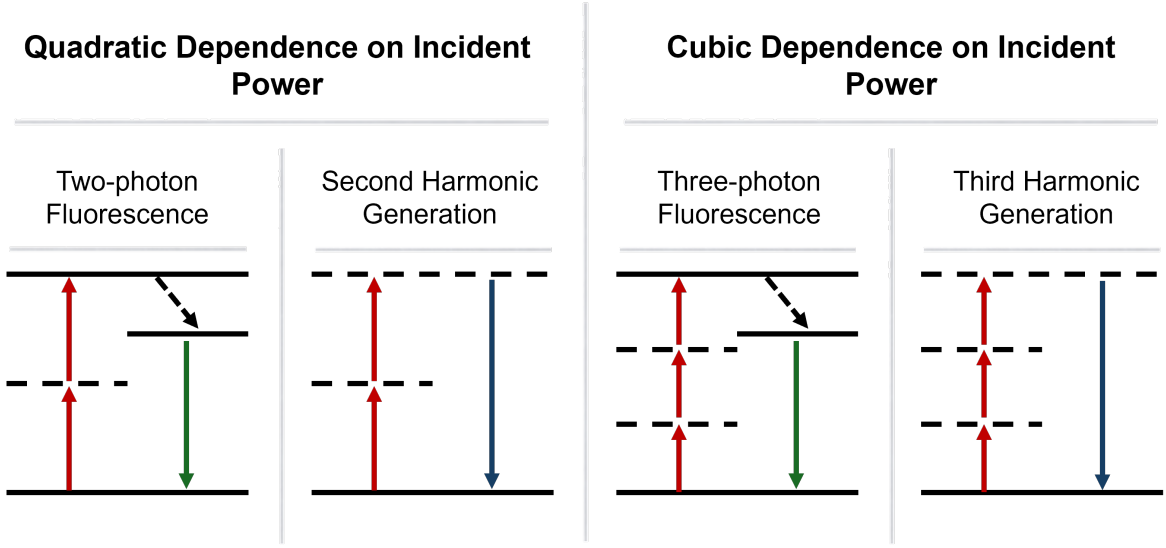


Figure 2.3: Energy-level diagrams of nonlinear optical processes, according to their dependence on the incident power.

material exhibits a nonlinear response, giving rise to new optical phenomena [100].

The macroscopic description of these effects follows from Maxwell's equations. In material media, they can be written as [101, 108]:

$$\vec{D} = \varepsilon_0 \vec{E} + \vec{P}, \tag{2.10}$$

$$\vec{B} = \mu_0 \left(\vec{H} + \vec{M} \right), \tag{2.11}$$

where $\vec{D}$ is the electric displacement field, $\vec{B}$ is the magnetic flux density, ε_0 and μ_0 are the vacuum permittivity and permeability, respectively, $\vec{P}$ is the electric polarization, and $\vec{M}$ is the magnetization.

In the linear regime, the polarization is expressed as:

$$\vec{P} = \varepsilon_0 \chi(\omega) \vec{E}, \tag{2.12}$$

where $\chi(\omega)$ is the linear electric susceptibility, related to the relative permittivity $(\epsilon_r(\omega))$ by:

$$\chi(\omega) = \varepsilon_r(\omega) - 1 \tag{2.13}$$

At high electric field intensities, the material response becomes dependent on the field amplitude, and the polarization must be expressed as a power series in the electric field [105, 109]:

$$P_i = \varepsilon_0 \left(\sum \chi_{ij}^{(1)} E_j + \sum \chi_{ijk}^{(2)} E_j E_k + \sum \chi_{ijkl}^{(3)} E_j E_k E_l \right), \tag{2.14}$$

where $\chi^{(n)}$ are the n-th order nonlinear susceptibility tensors.

Accordingly, the total polarization can also be decomposed as:

$$\vec{P} = \vec{P}^{(1)} + \vec{P}^{(2)} + \vec{P}^{(3)} + \cdots \tag{2.15}$$

where each contribution corresponds to a specific order of the electric field interaction. The $\tilde{P}^{(1)}$ corresponds to linear optical phenomena such as reflection, refraction, and single-photon absorption. Higher-order terms describe nonlinear effects. So, second-order term $\tilde{P}^{(2)}$ gives rise to processes such as second harmonic generation (SHG) and frequency mixing, while the third-order term $\tilde{P}^{(3)}$ is responsible for effects including third-harmonic generation, 2PEF, and coherent Raman scattering. Higher-order terms, such as $\tilde{P}^{(5)}$, are associated with phenomena like three-photon autofluorescence [63, 105, 109].

Although multiple frequency components may be generated in the nonlinear polarization, efficient signal generation requires phase-matching conditions to be satisfied. In practice, these conditions are typically fulfilled for only one (or a limited number of) frequency components, resulting in selective and efficient nonlinear signal generation. This inherent selectivity contributes to the molecular specificity of label-free nonlinear optical microscopy techniques [63].

2.2 Effects of Light on Biological Tissues

The interaction of light with biological tissues can give rise to photophysical, photochemical, and photobiological effects. These include temperature increase, evaporation, and thermomechanical disruption, and depend primarily on the local power density of the incident radiation [16].

When photons are absorbed by tissue, part of the energy is converted into heat, leading to a rise in temperature. This temperature increase may induce both reversible and irreversible structural changes. Irreversible damage occurs when the temperature exceeds a critical threshold (T_{crit}). Depending on the temperature range, different types of thermal damage can be identified, such as [1]:

- Coagulation (protein denaturation, cell necrosis, and dehydration) typically occurs between $45\,^{\circ}\text{C}$ and $75\,^{\circ}\text{C}$;
- Vaporization (tissue dehydration and formation of vapor bubbles) occurs above $100\,^{\circ}\text{C}$ and is associated with mechanical tissue disruption;
- Pyrolysis, involving thermal decomposition, occurs in the range of $350\,^{\circ}\text{C}$ to $450\,^{\circ}\text{C}$.

These processes are collectively referred to as photothermal mechanisms of tissue damage. Importantly, thermal damage depends not only on temperature but also on the duration of exposure [1].

So, in noninvasive optical diagnostics, it is essential to maintain tissue temperature below the critical threshold. The critical temperature is defined as the temperature at which the rate of damage accumulation equals unity, and can be estimated as [1]:

$$T_{\text{crit}} = \frac{E_a}{R \cdot \ln(A)}, \tag{2.16}$$

where E_a is the activation energy, A is a pre-exponential factor, and R is the universal gas constant $(8.32\,\text{J}/(\text{mol}\,\text{K}))$. For example, in porcine skin, $T_{\text{crit}} \approx 59.7\,^{\circ}\text{C}$ [1].

The thermal response of tissue also depends on the temporal characteristics of the light source. For CW irradiation, heat diffusion becomes significant as the temperature gradient between the irradiated region and the surrounding tissue increases, leading to broader thermal damage or heat dissipation. In contrast, for pulsed irradiation, heat conduction is negligible during the pulse duration, since energy deposition occurs on timescales much shorter than thermal diffusion. As a result, pulsed lasers enable more localized and precise tissue modification [1].

The optothermal effect refers to the generation of heat in tissue due to optical absorption over time. When the laser wavelength matches an absorption band of a specific tissue component, the optical energy is preferentially absorbed and efficiently converted into heat, enabling selective targeting [1].

Photochemical interactions depend on several factors, including the type of chromophore (endogenous or exogenous), O_2 concentration, and the wavelength, intensity, and duration of irradiation. Most photochemical reactions are induced by short-wavelength radiation (typically $\lambda < 320$ nm). Common processes include photodissociation (breaking molecules into radicals or ions), photo-association (formation of molecular complexes), and photodecomposition. Additional reactions such as photodimerization, photoisomerization, photohydration, and photooxidation may also occur. Photooxidation involves light-induced electron-transfer reactions, often mediated by O_2, while photoreduction corresponds to electron gain under irradiation. These processes can lead to significant structural and chemical modifications in tissues, including photo-destruction [1].

Part II

Tissue models

Chapter 3

CAM Assays

This chapter presents the development and evaluation of biological tissue models based on the CAM assay. It introduces the experimental framework used to generate both non-malignant and malignant colorectal tissues, followed by a description of the methods, and the obtained experimental results. The capabilities and limitations of the CAM model are discussed, highlighting its role within this work.

3.1 Context

The accurate evaluation of tumor development and progression remains a significant challenge in cancer research. To address this, a wide range of *in vitro* and *in vivo* models have been developed to investigate tumor growth, angiogenesis, and metastatic dissemination [110]. Among these, *in vivo* models of human tumors are essential for studying cancer diagnosis, progression, identification of therapeutic targets, and the evaluation of anti-tumor treatments [111]. Within this context, the CAM assay has emerged as a versatile *in vivo* platform for implanting different cancer cell lines and studying their angiogenic and metastatic potential [110–118].

The CAM is a highly vascularized extraembryonic membrane connected to the developing chick embryo through an accessible circulatory system, providing a rapidly accessible, highly vascularized environment that supports the growth of human tissue xenografts [111, 115]. As such, it has gained increasing recognition as a high-fidelity intermediate model, bridging the gap between *in vitro* systems and more complex animal models. It enables the study of tumor growth dynamics, vascularization, and response to therapy, while also serving as a platform for the development and validation of novel biomedical technologies, including optical diagnostic techniques [115].

Compared to other *in vivo* models, the CAM assay offers several advantages:

- reduced ethical concerns, as the chick embryo does not perceive pain in the CAM tissue before the 17^{th} day of incubation, due to the late development of the nervous system [114, 119, 120];
- ease of handling and low experimental cost;
- a nutrient-rich environment that supports rapid tissue growth;
- an immature immune system at early developmental stages, allowing engraftment without the need

for immunosuppression.

In addition, the CAM model aligns with the principles of the 3Rs (reduction, refinement, and replacement) in animal research [112]. For all these reasons, the CAM model was used in this work as a platform for modeling both healthy and CRC tissue growth.

The CAM enables the successful engraftment of a wide range of tumor models, including both established cancer cell lines and patient-derived tissues [111]. Consequently, numerous studies have employed the CAM model to investigate tumor progression and angiogenesis, processes that are essential for supplying tumors with nutrients and O_2 and facilitating metastatic dissemination. A broad spectrum of cancer cell lines has been reported in the literature, including colorectal (SW480, HCT-116) [121, 122], ovarian (A2780) [123], sarcoma (Saos-2, SW1353, HOS, MG63, MNNG-HOS, SJSA1, U2OS, ZK58) [124, 125], renal carcinoma [126], patient-derived myeloma [127], head and neck squamous cell carcinoma [128], and murine melanoma (B16-F10) [129]. In parallel, successful engraftment has also been demonstrated using tumor tissue fragments, including Walker 256 carcinosarcoma [130], ovarian adenocarcinoma [131, 132], sarcoma [124], meningioma and glioblastoma [133, 134], hepatocellular carcinoma [135], melanoma [136], murine teratoma and melanoma [137], and leporine V2 carcinoma [137]. These examples highlight the broad applicability of the CAM assay as a versatile platform that supports both established cell lines and patient-derived tumor samples.

Although the CAM model has been known for over a century, it has recently gained renewed interest, particularly in the context of precision medicine. Patient-derived tumor models grown on the CAM provide a promising platform for developing personalized therapeutic strategies [138].

Furthermore, the application of advanced optical imaging techniques, such as OCT and MPM, to the CAM model is still emerging but has already demonstrated significant potential. In 2022, Kunze *et al.* [139] used MPM to investigate the remodeling of collagen-rich extracellular matrix by colorectal tumor cells grown on the CAM, enabling 3D visualization of tumor invasion beyond the limitations of conventional histology. More recently, Tsimpaki *et al.* [140] demonstrated the use of spectral domain optical coherence tomography (SD-OCT) for non-invasive monitoring of patient-derived tumor xenografts, including tumor size quantification and vascular assessment by OCT-angiography. Earlier work by Dsouza *et al.* [141] further highlighted the capability of phase-sensitive OCT to detect microvascular blood flow in CAM tissue.

Together, these studies demonstrate the growing interest in combining the CAM model with advanced optical imaging techniques, underscoring its potential as a platform for cancer diagnostics, particularly in CRC.

Regarding the tissue growing in this assay, and as discussed in Part I, non-malignant and malignant

tissues exhibit distinct structural organization and cellular heterogeneity. These differences can be effectively investigated using the CAM model, particularly in the context of tumor microenvironment analysis. Non-malignant tissues are characterized by an organized, hierarchical vascular network that enables homogeneous distribution of nutrients and small molecules. In contrast, malignant tissues exhibit abnormal angiogenesis due to imbalances in pro- and anti-angiogenic signaling, leading to disorganized vascular networks. This results in a heterogeneous distribution of nutrients and O_2, with well-perfused regions near the tumor surface and hypoxic conditions in deeper regions. Consequently, tumors develop a dense cellular core and exhibit gradients in oxygenation, pH, and metabolite concentration [34–36].

3.2 Experimental Methods

Two types of samples were generated from the CAM assay, one derived from human colon cancer cells and the other from normal colonic mucosa cells. The human colon cancer cell line RKO was provided by Dr. Raquel Seruca (IPATIMUP, Porto, Portugal), and the normal colon mucosa-derived cell line NCM460 was obtained from INCELL Corporation (LLC, San Antonio, USA) under MTA approval. Both cell lines were cultured under standard conditions [142].

For CAM implantation, cells were expanded in culture flasks until they reached approximately $90\,\%$ confluence. Cells were then harvested by washing with phosphate-buffered saline (PBS) and detached using trypsin (TrypLETM Express, Gibco) at $37\,^{\circ}$C. Complete culture medium was subsequently added to inactivate the trypsin, after which the cells were collected and centrifuged at 900 rpm for 5 min at $4\,^{\circ}$C. The supernatant was discarded, and the cell pellet was resuspended in fresh culture medium. Cell density was determined using trypan blue exclusion (Trypan Blue Solution, $0.4\,\%$, Gibco).

The CAM assay was used to generate both non-malignant (from NCM460 cells) and malignant (from RKO cells) tumor models for subsequent optical analysis. Fertilized chicken eggs were incubated at $37\,^{\circ}$C and $70\,\%$ relative humidity. After three days of incubation, a small window was created in the eggshell, and the eggs were returned to the incubator. On embryonic day 9, RKO or NCM460 cells (2×10^6 cells/egg) were mixed with Matrigel and inoculated onto the CAM ($10\,\mu$L/egg), allowing the formation of three-dimensional micro-tumors. Tumor growth was monitored daily.

On day 16 of embryonic development, the tumors were photographed *in ovo* and subsequently analyzed using the OCT system. A schematic representation of the CAM protocol is shown in Figure 3.1. Following optical measurements, embryos were euthanized by exposure to CO_2 for 20 min, followed by sacrifice at $80\,^{\circ}$C for 20 min.

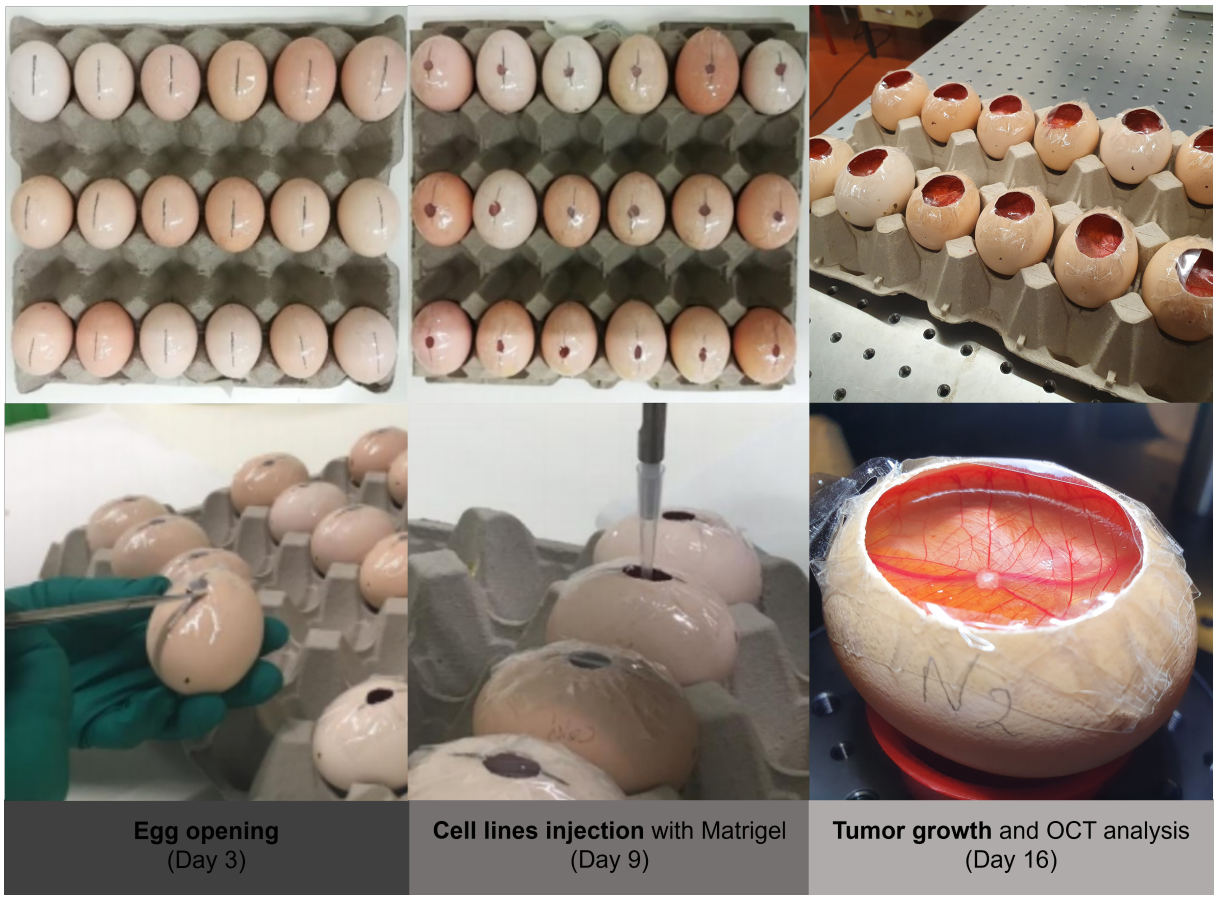


Figure 3.1: CAM assay implementation stages.

For the initial experiments at the 2PEF setup, a simplified approach was adopted to facilitate measurements with the custom-built setup. Unlike the measurements performed on living embryos in OCT imaging, the experiments in 2PEF were conducted on the excised CAM membrane containing the grown tissue. This approach allowed improved stability and handling during optical measurements.

To prepare these samples, embryos were first anesthetized by exposure to CO_2 for 20 min. Subsequently, the eggs were cooled in PBS for 20 min to reduce tissue activity and facilitate manipulation. The CAM membrane was then carefully excised and rinsed three times with PBS to remove residual debris and ensure optimal imaging conditions. The membrane was then placed between two microscope slices and inserted into the 2PEF setup.

3.3 Results and Samples Analysis

Several CAM assay samples were prepared, and representative examples of the obtained tissues are shown in Figure 3.2. Both tissues derived from NCM460 and RKO are presented at different magnifications. Figure 3.2(e) and Figure 3.2(f) were acquired using only the excised CAM membrane rather than the

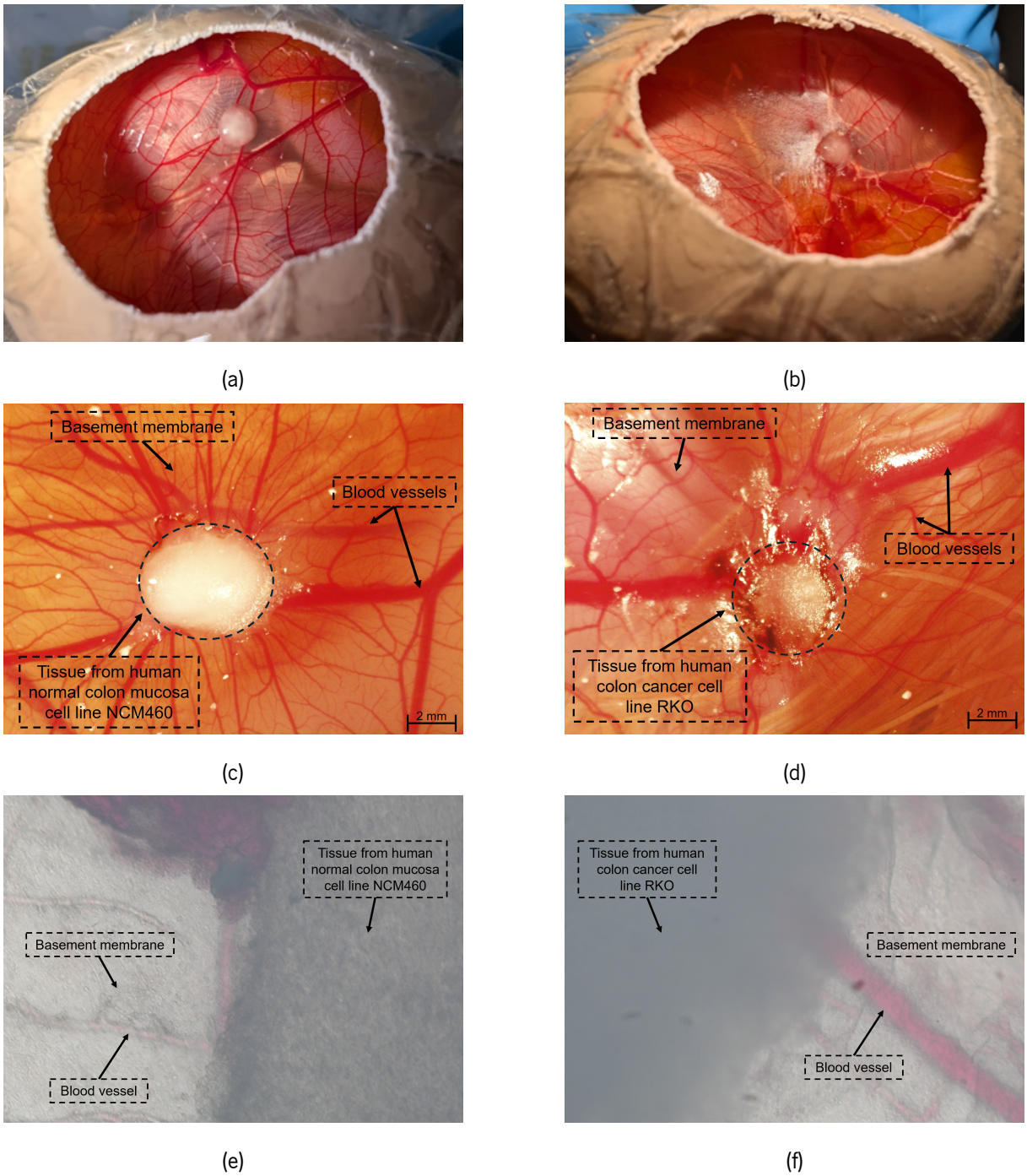


Figure 3.2: CAM assay samples. Digital camera images inside the egg of (a) NCM460-derived tissue grown on the CAM, and (b) RKO-derived tissue grown on the CAM. Images inside the egg using a Leica M80 stereomicroscope of (c) NCM460-derived tissue, and (d) RKO-derived tissue. Excised CAM membrane containing (e) NCM460-derived tissue, and (f) RKO-derived tissue, imaged with a Nikon L200N microscope (10× objective).

intact egg, allowing the use of a high-resolution microscope with back-side illumination.

Regarding tumor growth, NCM460 cells, derived from non-cancerous colon mucosa, were expected

to generate smaller and more homogeneous tissue structures. In contrast, RKO cells, a colorectal carcinoma line with known high proliferative and invasive potential, were expected to form larger and more heterogeneous tumors [143, 144]. Inspection of the microscope images in Figure 3.2(e) and 3.2(f) reveals that RKO-derived tissues appear denser than those formed by NCM460 cells, which is consistent with this expectation. In particular, the lower optical transparency observed in RKO samples suggests a higher tissue density compared to NCM460 samples. However, optical transparency can also be influenced by other factors, including tissue thickness, vascularization, and light scattering properties.

However, contrary to expectations, no clear or consistent differences were observed in tumor dimensions between the two cell lines. Tumors derived from NCM460 and RKO cells often exhibited comparable sizes, and in some cases, NCM460-derived tumors were larger and more morphologically irregular than those formed by RKO cells. These observations suggest that tissue growth under the implemented CAM protocol may not fully reproduce the structural and morphological characteristics typically observed in native healthy and malignant colorectal tissues.

Furthermore, substantial variability in tumor size and morphology was observed even among samples derived from the same cell line, implanted simultaneously, and cultured under identical experimental conditions. This variability was further exacerbated by marked differences between experimental runs, as well as by a high rate of embryo mortality, which frequently reduced the number of samples available for analysis. These factors significantly hindered experimental progression and limited the availability of consistent biological samples.

Although the CAM assay is often presented as a rapid and accessible platform for generating biologically relevant healthy and cancerous tissue models, the challenges encountered in cell culture handling, embryo survivability, and reproducibility of tumor growth have had a considerable impact on this work. These limitations indicate that, despite their ethical and logistical complexities, traditional *ex vivo* tissue samples from animal models or human sources, as well as controlled tissue phantoms, remain essential for the development and validation of optical diagnostic technologies.

Consequently, while CAM-derived samples were selected and successfully employed for the OCT studies, it became evident that relying exclusively on these biological samples was not feasible for the 2PEF measurement and setup validation. This finding motivated and justified the extensive development of tissue-mimicking phantoms, which proved to be a critical component for this work.

Another important consideration in the preparation of the CAM samples is the use of Matrigel to promote cell aggregation. This matrix facilitates the formation of localized 3D tissue structures, preventing the cells' dispersion across the CAM surface. However, Matrigel is a collagen-based material, which introduces an

external source of collagen into the samples. As a result, signals obtained from SHG imaging may be influenced not only by the collagen produced by tumor cells but also by the exogenous collagen present in the Matrigel. This represents a potential limitation for SHG studies.

Therefore, if SHG analysis is to be pursued in future work, alternative sample preparation protocols should be considered. One possible approach is the use of polydimethylsiloxane (PDMS) rings placed on the CAM, within which the cells can be deposited. This strategy would confine the cells to a defined region while avoiding the introduction of external collagen sources. Some preliminary tests have been considered, but this approach remains exploratory and requires further validation.

3.4 Outlook

In summary, the CAM assay was implemented as an *in vivo* platform for the development of biological tissue models derived from both non-malignant (from NCM460 cells) and malignant (from RKO cells) colon cell lines.

The results demonstrated the feasibility of generating tissue-like structures on the CAM, as well as the applicability of this model for optical imaging. Qualitative differences between NCM460 and RKO-derived tissues were observed, particularly in terms of optical density. However, the expected distinctions in tumor size were not consistently reproduced.

Significant variability between samples, along with challenges related to embryo survivability and experimental reproducibility, were identified as major limitations of the implemented protocol. Additionally, the use of Matrigel introduced constraints for nonlinear optical analysis, particularly for SHG imaging.

Overall, while the CAM assay proved to be a valuable and accessible model for OCT studies, it was not sufficient as a fully reliable platform for the validation of the 2PEF system. These limitations motivated the development of tissue-mimicking phantoms, which are presented in the following chapter.

Chapter 4

Colorectal Tissue Phantoms

This chapter presents the development and characterization of tissue-mimicking optical phantoms designed to replicate the optical and biochemical properties of biological tissues. It introduces the theoretical framework, fabrication methodologies, and experimental procedures used to construct both liquid and solid phantoms. The optical properties of the developed phantoms are then analyzed, demonstrating their suitability as controlled and reproducible platforms for the validation of the MPM setup.

4.1 Context

Tissue phantoms, used to simulate light-tissue interactions, are essential for the evaluation of optical techniques, calibration of instrumentation, optimization of experimental procedures, and quality assurance. They are widely used across all fields of optical diagnostics, particularly for testing instrumentation, validating fluorescence spectroscopy techniques, and experimentally assessing theoretical models [145]. Moreover, due to the limited availability of biological tissue samples and the complexity of their preparation, initial measurements using 2PEF were performed with tissue-mimicking phantoms. These phantoms were designed to reproduce both the optical and biochemical properties of normal and tumoral colorectal tissues.

In general, optical phantoms are composed of a scattering medium, an absorbing medium, a diluent, and, when required, fluorophores. Common scattering agents include Intralipid, Nutralipid, Liposyn, and polystyrene microspheres. The latter are particularly advantageous due to their low intrinsic fluorescence and well-defined optical properties, which can be accurately described using Mie theory. Absorbing media typically include trypan blue, Evans blue, indocyanine green, methylene blue, Photofrin II, India ink, and hemoglobin. The diluent is usually deionized water, although isotonic PBS is also frequently employed. By adjusting the relative concentrations of these components, phantoms can be engineered to match specific optical properties of biological tissues, including the absorption coefficient (α), the scattering coefficient (μ_s), and the anisotropy factor (g) [145].

Despite their versatility, liquid phantoms are limited in their ability to reproduce the structural complexity of biological tissues. As a result, solid phantoms using transparent matrices such as polymers, silicone, or gelatin are important. However, these materials also present limitations. Polymer-based phantoms may shrink during polymerization or develop cracks in larger volumes, while gel-based phantoms can suffer

from solvent evaporation, leading to temporal variations in both geometry and optical properties [145].

As such, an ideal tissue phantom should satisfy several key requirements [145]:

- accurately reproduce the geometry and optical parameters relevant to light transport in biological tissues;
- all components must be chemically and physically compatible;
- optical properties should be predictable and reproducible from the composition;
- should exhibit temporal stability and minimal sensitivity to environmental conditions;
- should allow the fabrication of heterogeneous or multilayered structures;
- its preparation should be simple, safe, and reproducible.

Over time, the development of tissue phantoms has evolved from simple homogeneous systems toward increasingly complex, multilayered, and functionally relevant models capable of replicating both endogenous contrast mechanisms and realistic light–tissue interactions. Early approaches primarily focused on reproducing bulk optical properties using calibrated constituents.

In this context, Pimenta [146] employed tissue-mimicking phantoms to validate an optical microsystem for detecting gastrointestinal dysplasia, emphasizing the importance of controlled and reproducible optical responses. However, such phantoms remain simplified representations and do not fully capture tissue heterogeneity or biochemical specificity.

More advanced fabrication strategies have been proposed. Freymüller *et al.* [147] developed fluorescence lifetime phantoms based on quenched coumarin derivatives to mimic endogenous fluorophores such as NAD(P)H and FAD. Their approach enables independent control of fluorescence lifetime and intensity, which is critical for validating fluorescence lifetime imaging (FLIM) systems and represents a transition toward functional biomimicry. Similarly, B. Yu *et al.* [148] and C. Yu *et al.* [149] demonstrated the use of calibrated phantoms for quantitative diffuse reflectance spectroscopy and imaging, typically employing scatterers such as polystyrene microspheres or titanium dioxide (TiO_2) and absorbers such as hemoglobin.

Further developments have focused on improving stability and applicability to imaging systems. Lo *et al.* [150] proposed solid phantoms compatible with LED-based spectroscopic imaging, using silicone or epoxy matrices doped with scattering particles and absorbers. These phantoms provide enhanced mechanical and temporal stability compared to liquid systems and are better suited for clinical translation.

Efforts to incorporate structural realism have led to the development of phantoms that mimic specific tissue components. Kirkpatrick *et al.* [151] introduced *in vitro* collagen-based models capable of reproducing endogenous optical signatures, including SHG, which are particularly relevant for nonlinear microscopy. This represents a significant advancement, as these phantoms reproduce not only linear optical properties but also nonlinear optical responses.

The introduction of multilayered and three-dimensional phantoms further improved physiological relevance. Sokolov *et al.* [152] developed epithelial tissue phantoms with layered architectures representing epithelium and stroma, while Nivetha *et al.* [153] designed bilayer skin phantoms incorporating scattering agents, absorbers, and fluorophores to enable depth-resolved optical studies. More recently, Chen *et al.* [154] reported multilayered phantoms with tunable mechanical, optical, and acoustic properties, addressing the needs of multimodal imaging systems. Additionally, Balu *et al.* [155] highlighted the importance of wavelength-dependent light penetration in nonlinear microscopy, using turbid phantoms to systematically evaluate excitation conditions.

Overall, the state-of-the-art demonstrates a clear progression toward increasingly realistic and application-specific phantoms. Modern fabrication protocols typically involve selecting an appropriate base matrix (liquid or solid), incorporating calibrated scattering agents (e.g., polystyrene microspheres, TiO_2), adding absorbers (e.g., hemoglobin, dyes), and, when necessary, embedding endogenous fluorophores or structural biomolecules such as collagen. The selection of materials and design strategy is strongly dependent on the intended application, whether diffuse reflectance spectroscopy, FLIM, or nonlinear microscopy.

In this work, several tissue phantoms were prepared using fluorophores, absorbers, and scattering agents at physiologically relevant concentrations. To support different stages of the MPM system validation, multiple phantom configurations with increasing complexity were prepared, including both liquid and solid systems, enabling independent assessment of optical contributions and combined tissue-like behavior.

Each component concentration in a tissue phantom was selected based on reported values from the literature. NAD(P)H was included as a key endogenous fluorophore associated with cellular metabolism. In normal colorectal tissue, the reported NAD(P)H concentration is approximately $90\,\mu M$ [31]. In tumoral tissue, NAD(P)H levels are reported to be between 1.4 and 1.6 times higher than in normal tissue, reflecting altered metabolic activity characteristic of cancer cells [26]. Accordingly, NAD(P)H concentrations between $126\,\mu M$ and $144\,\mu M$ should be used in the tumoral phantoms. In this work, a concentration of $126\,\mu M$ was selected for the tumoral phantoms, as it represents the lower bound of the reported tumoral range and remains relatively close to the normal tissue concentration. This conservative choice enables the assessment of the system's sensitivity to subtle metabolic differences. Thus, if smaller concentration

variations can be reliably distinguished, larger differences are expected to be detected with even greater confidence.

FAD, another endogenous metabolic fluorophore, was incorporated to enable redox ratio analysis. In normal tissue, the concentration of NAD(P)H is reported to be approximately 1.82 times higher than that of FAD [27]. Based on the selected NAD(P)H concentration for normal tissue, the corresponding FAD concentration was set to $49.45\,\mu$M. In tumoral tissue, the NAD(P)H concentration is reported to be 3.26 times higher than FAD concentration [27]. Using the previously defined tumoral NAD(P)H range, this resulted in FAD concentrations between $38.65\,\mu$M and $44.17\,\mu$M in the tumoral phantoms. As the approach adopted for NAD(P)H, the lower bound of the reported concentration range was selected for use in the FAD phantoms.

Hemoglobin was added to mimic the absorption properties of tissues. The hemoglobin concentration in normal colorectal tissue is reported to be approximately $1.8\,\mathrm{mg/mL}$ [156]. Tumoral tissues exhibit increased vascularization, leading to higher hemoglobin content. Literature reports indicate that hemoglobin concentration in tumoral tissue is approximately 3.2 times higher than in normal tissue [156]. Consequently, a hemoglobin concentration of approximately $5.8\,\mathrm{mg/mL}$ was used in the tumoral phantoms.

Polystyrene beads were used as scattering centers to replicate the optical scattering properties of biological tissues. According to the literature, normal tissue phantoms typically contain $0.45\,\%(\mathrm{V/V})$ of a polystyrene beads suspension at a concentration of $2.5\,\%(\mathrm{w/V})$ [153]. For tumoral tissue phantoms, the scattering level is generally increased, with reported values of $0.80\,\%(\mathrm{V/V})$ of the same beads suspension, reflecting the higher scattering coefficients commonly observed in tumoral tissues [153].

Gelatin was used as the structural matrix of the solid phantoms. A gelatin concentration of $10\,\%(\mathrm{w/V})$ was selected to achieve a refractive index of approximately 1.4, consistent with that of biological soft tissues [157]. Gelatin also exhibits a melting point of approximately $35\,^{\circ}$C, which allows controlled preparation and solidification of the phantoms under ambient laboratory thermal conditions [158].

To define the thickness of the fabricated solid phantoms, a detailed analysis of the OCT images obtained from tissues cultivated using the CAM assay was performed. As reported by Pereira *et al.* [10], a hypoxic region is typically observed at a depth of approximately $206\,\mu$m in most tumors. Since this hypoxic region is located near the central part of the tumor, it can be inferred that the total tumor thickness is approximately twice this value, corresponding to about $412\,\mu$m. Based on this observation, this thickness was considered a reasonable approximation for tumors grown in this assay, and phantoms with thicknesses close to this value were therefore developed.

Table 4.1 and Table 4.2 summarize the excitation and emission wavelengths used for the acquisition

Table 4.1: Summary of excitation and emission wavelength ranges, and imaging techniques for NAD(P)H autofluorescence.

Excitation (nm)	Emission (nm)	Method	Reference
720	460/50	2PEF microscopy	[159]
810	475	2PEF microscopy	[160]
360/40	455/50	Widefield	[161]
760	300-500 and 500-640	FLIM	[162]
365	465/25	Widefield	[163]
700	460/25	FLIM	[164]
351	460/25	Confocal	[164]
750	410-490 and 510-650	2PEF microscopy	[165]
360	455	Widefield	[166]
800	<490	FLIM	[167]
750	400-480	FLIM	[168]
750		FLIM	[169]
750	440/80	FLIM	[170]
385/15	432/18	Widefield	[171]
820	<490	2PEF microscopy	[172]
755	460/20	2PEF microscopy	[173]
780	447/60	2PEF microscopy	[174]
375	469/35	Endoscopic imaging	[175]
375	445/40	FLIM	[176]

of NAD(P)H and FAD autofluorescence, respectively. There is noticeable variability in the excitation and emission wavelengths. To address this variability, excitation and emission spectra of both fluorophores were experimentally acquired under one-photon and two-photon excitation conditions, in order to select the most suitable wavelengths to be considered in this study.

Additionally, to evaluate the influence of absorption and scattering effects, the transmittance spectra of the absorption and scattering components were analyzed. The transmittance of the bulk base material (gelatin) was also measured to assess its impact on light propagation within the phantom.

Table 4.2: Summary of excitation and emission wavelength ranges, and imaging techniques for FAD autofluorescence.

Excitation (nm)	Emission (nm)	Method	Reference
810	540	2P microscopy	[160]
470/40	520/40	Widefield	[161]
436	530/30	Widefield	[163]
900	510-650	2P microscopy	[165]
454	505-550	Widefield	[166]
890	<490	FLIM	[167]
890	500-600	FLIM	[168]
900		FLIM	[169]
890	550/100	FLIM	[170]
450-488	515/15	Widefield	[171]
910	629/56	2P microscopy	[172]
860	525/25	2P microscopy	[173]
780	>496	2P microscopy	[174]
473	520/35	Endoscopic imaging	[175]

Furthermore, the refractive index of the gelatin was characterized, given its role as the primary solid matrix of the phantom. Finally, the thickness of the fabricated solid phantom was also evaluated, in order to verify that the adopted fabrication technique ensures the desired geometrical specifications.

4.2 Theoretical Framework

Tissue phantoms preparation requires several theoretical concepts and preliminary calculations. Additionally, key principles must be addressed to support the characterization procedures that will be performed on those phantoms.

4.2.1 Phantoms Fabrication

Polystyrene beads concentration

The commercially available polystyrene bead suspension (Polysciences, 07310) was supplied at a concentration of $10\,\%(\mathrm{w/V})$. Therefore, a dilution step was required to obtain the desired working concentration of $2.5\,\%(\mathrm{w/V})$. For this purpose, the standard concentration–volume relationship was used [177]:

$$C_i \cdot V_i = C_f \cdot V_f \Longleftrightarrow \frac{V_f}{V_i} = \frac{C_i}{C_f}, \tag{4.1}$$

where C_i and V_i represent the initial concentration and volume, and C_f and V_f correspond to the final concentration and volume, respectively. The detailed dilution calculations are presented in the Experimental Methods section.

NAD(P)H concentration

For phantom preparation, physiologically relevant concentrations corresponding to normal and tumoral colorectal tissue were used, as previously described. For NAD(P)H, the target concentration for normal tissue was $C_{\mathrm{NAD(P)H}} = 90\,\mu\mathrm{M} = 0.090\,\mu\mathrm{mol/mL}$. Since this concentration is expressed in molar units, it must be converted to mg/mL to enable practical phantom preparation.

To perform this conversion, the relationship between mass and amount of substance was used [178]:

$$m = M \cdot n \tag{4.2}$$

where m is the mass, M is the molar mass, and n is the amount of substance. Considering the molar mass of NAD(P)H $(M = 709.40\,\mathrm{g/mol})$ [179], the required mass per milliliter is given by:

$$m = 709.40 \times 10^{-6}\,\mathrm{g/\mu mol} \times 0.090\,\mu\mathrm{mol} = 0.0638\,\mathrm{mg}, \tag{4.3}$$

resulting in a concentration of $C_{\mathrm{NAD(P)H}} = 0.0638\,\mathrm{mg/mL}$ for normal tissue phantoms.

For tumoral tissue phantoms, the selected NAD(P)H concentration was $C_{\mathrm{NAD(P)H}} = 126\,\mu\mathrm{M}$, corresponding to $0.126\,\mu\mathrm{mol/mL}$. Using the same approach and molar mass, the required mass per milliliter was calculated as:

$$m = 709.40 \times 10^{-6}\,\mathrm{g/\mu mol} \times 0.126\,\mu\mathrm{mol} = 0.0894\,\mathrm{mg}, \tag{4.4}$$

yielding a concentration of $C_{\mathrm{NAD(P)H}} = 0.0894\,\mathrm{mg/mL}$ for tumoral phantoms.

FAD concentration

For FAD, the target concentration for normal tissue phantoms was $C_{\text{FAD}} = 49.45$ µM = 0.0495 µmol/mL. Considering the molar mass of FAD ($M = 829.51$ g/mol) [180], and using Equation 4.2, the corresponding mass per milliliter was calculated as:

$$m = 829.51 \times 10^{-6}\,\text{g/µmol} \times 0.0495\,\text{µmol} = 0.0411\,\text{mg} \tag{4.5}$$

Thus, the final target concentration for normal tissue phantoms was $C_{\text{FAD}} = 0.0411$ mg/mL.

For tumoral tissue phantoms, the selected FAD concentration was $C_{\text{FAD}} = 38.65$ µM = 0.0387 µmol/mL. Using the same approach and molar mass, the required mass per milliliter was:

$$m = 829.51 \times 10^{-6}\,\text{g/µmol} \times 0.0387\,\text{µmol} = 0.0321\,\text{mg} \tag{4.6}$$

resulting in a concentration of $C_{\text{FAD}} = 0.0321$ mg/mL for tumoral phantoms.

Solute mass calculation

The fluorophores and the hemoglobin will be dissolved in water, and thus, it is necessary to consider the mass–concentration relationship that is defined as [177]:

$$m = C \times V \tag{4.7}$$

Following this relation, it will be possible to determine the necessary solute mass to obtain the desired concentration in each phantom.

4.2.2 Phantoms Characterization

Transmittance/ absorbance

To characterize the transmittance of the absorption and scattering components and of the gelatin, the optical transmittance relation was used [181]:

$$T = \frac{I_{\text{sample}}}{I_{\text{reference}}} \tag{4.8}$$

The transmittance (T) is therefore a quantification of the fraction of incident light that passes through the sample. It is defined as the ratio between the detected signal after interaction with the sample and the reference signal measured without the sample.

The absorbance (A) can be easily obtained from the transmittance using the following relation [181]:

$$A = -\log_{10}(T) \tag{4.9}$$

Refractive index

The Brewster angle concept was considered to determine the refractive index of the gelatin.

The Brewster angle is defined as the angle of incidence at which p-polarized light is fully transmitted across the interface between two media, resulting in zero reflected intensity for that polarization (Figure 4.1) [2].

The relationship between the Brewster angle and the refractive indices of the two media is given by [182]:

$$\tan(\theta_B) = \frac{n_1}{n_2}, \tag{4.10}$$

where θ_B is the Brewster angle, n_1 is the refractive index of the incident medium, and n_2 is the refractive index of the sample.

It should be noted that this formulation assumes homogeneous media with a smooth and well-defined interface. However, most biological tissues are optically inhomogeneous, absorptive, and present rough interfaces. Consequently, the direct application of this model to tissue-mimicking phantoms may introduce deviations, and experimental measurements should be interpreted accordingly.

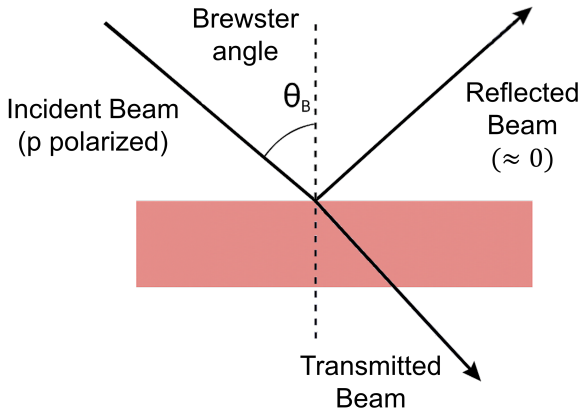


Figure 4.1: Representation of the Brewster angle at the interface between two media.

4.3 Experimental Methods

4.3.1 Phantoms Fabrication

To the future development of phantoms containing a scattering component, an initial step was required to obtain a final polystyrene beads suspension with a concentration of $2.5\,\%(\mathrm{w/V})$. As previously referred, the commercially available polystyrene beads suspension (Polysciences, 07310) has a concentration of $10\,\%(\mathrm{w/V})$. The dilution was calculated using Equation 4.1 and knowing that C_i = $10\,\%(\mathrm{w/V})$=$0.1\,\mathrm{g/mL}$ and C_f = $2.5\,\%(\mathrm{w/V})$ = $0.025\,\mathrm{g/mL}$, obtaining [177]:

$$\frac{V_f}{V_i} = \frac{0.1}{0.025} \Longleftrightarrow V_f = 4 \times V_i \tag{4.11}$$

Accordingly, for 1 mL of the original solution with $10\,\%(\mathrm{w/V})$, 3 mL of distilled water was added to obtain 4 mL of polystyrene bead suspension with $2.5\,\%(\mathrm{w/V})$, following the steps presented in Figure 4.2.

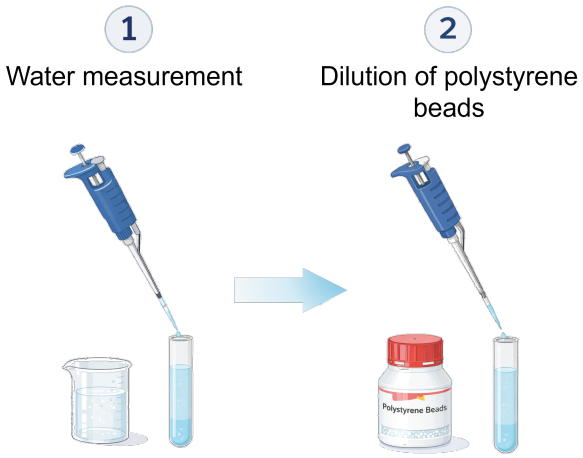


Figure 4.2: Polystyrene beads commercial suspension dilution to obtain a solution with $2.5\,\%(\mathrm{w/V})$.

Liquid phantoms containing NAD(P)H

As explained before, liquid phantoms containing only the NAD(P)H fluorophore (Merck N6005), were prepared using physiologically relevant concentrations corresponding to normal and tumoral colorectal tissue.

For normal tissue phantoms, the target NAD(P)H concentration was $C_{\mathrm{NAD(P)H}}$ = $90\,\mu\mathrm{M}$, which is equal to $C_{\mathrm{NAD(P)H}}$ =$0.0638\,\mathrm{mg/mL}$. Thus, using Equation 4.7 and considering 3 mL of solution (cuvette volume), it was possible to calculate the total mass required:

$$m = 0.0638\,\mathrm{mg/mL} \times 3\,\mathrm{mL} = 0.191\,\mathrm{mg} \tag{4.12}$$

This mass was then dissolved in 3 mL of a 0.01 N sodium hydroxide (NaOH) solution (Merck 160309), which was used as a solvent to improve solubility and stability [179].

For tumoral tissue phantoms, the selected NAD(P)H concentration was $C_{\text{NAD(P)H}} = 126$ µM, which is equal to $C_{\text{NAD(P)H}} = 0.0894$ mg/mL. Using Equation 4.7 and considering 3 mL of solution (cuvette volume), it was possible to conclude the total mass required:

$$m = 0.0894\,\text{mg/mL} \times 3\,\text{mL} = 0.268\,\text{mg}, \tag{4.13}$$

This mass was then dissolved in 3 mL of a 0.01 N NaOH solution (Merck 160309).

Liquid phantoms containing FAD

For the preparation of liquid phantoms containing only FAD fluorophore (Merck F6625), the same procedures described previously for NAD(P)H were followed. For normal tissue phantoms, the target FAD concentration was $C_{\text{FAD}} = 49.45$ µM, corresponding to $C_{\text{FAD}} = 0.0411$ mg/mL. Thus, using Equation 4.7 and considering 3 mL of solution (cuvette volume), it was possible to calculate the total mass required:

$$m = 0.0411\,\text{mg/mL} \times 3\,\text{mL} = 0.123\,\text{mg} \tag{4.14}$$

This mass was then dissolved in 3 mL of ultrapure water.

For tumoral tissue phantoms, the selected FAD concentration was $C_{\text{FAD}} = 38.65$ µM, corresponding to $C_{\text{FAD}} = 0.0321$ mg/mL. Using Equation 4.7 and considering 3 mL of solution (cuvette volume), it was possible to calculate the total mass required:

$$m = 0.0321\,\text{mg/mL} \times 3\,\text{mL} = 0.096\,\text{mg}, \tag{4.15}$$

This mass was then dissolved in 3 mL of ultrapure water.

Figure 4.3 summarizes the fabrication steps of the liquid phantoms containing only NAD(P)H or FAD.

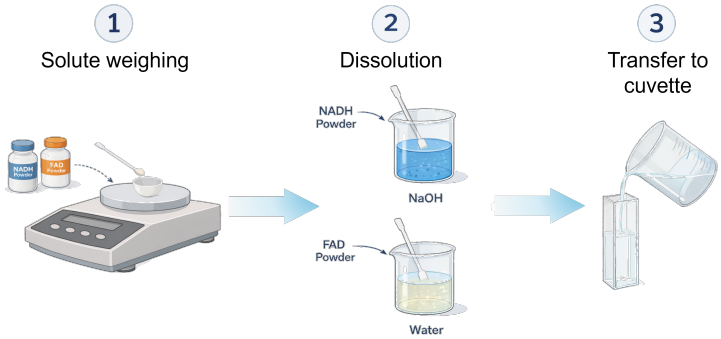


Figure 4.3: Fabrication workflow of the liquid optical phantoms containing only NAD(P)H or FAD.

Liquid phantoms containing NAD(P)H and FAD

For the preparation of liquid phantoms containing both NAD(P)H and FAD, the process schematized in Figure 4.4 was followed. The target concentration for NAD(P)H in phantoms representative of normal tissue was $C_{\text{NAD(P)H}} = 90\,\mu\text{M} = 0.0638\,\text{mg/mL}$, and for FAD was $C_{\text{FAD}} = 49.45\,\mu\text{M} = 0.0411\,\text{mg/mL}$. A final solution volume of $3\,\text{mL}$ was required; therefore, two intermediate solutions of $0.5\,\text{mL}$ were initially prepared for each fluorophore.

Using the concentration-volume relationship presented in Equation 4.1, for NAD(P)H:

$$C_i \times 0.5\,\text{mL} = 0.0638\,\text{mg/mL} \times 3\,\text{mL} \iff C_i = 0.383\,\text{mg/mL} \tag{4.16}$$

So, following Equation 4.7:

$$m = 0.383\,\text{mg/mL} \times 0.5\,\text{mL} = 0.191\,\text{mg} \tag{4.17}$$

For FAD:

$$C_i \times 0.5\,\text{mL} = 0.0411\,\text{mg/mL} \times 3\,\text{mL} \iff C_i = 0.247\,\text{mg/mL} \tag{4.18}$$

Thus,

$$m = 0.247\,\text{mg/mL} \times 0.5\,\text{mL} = 0.123\,\text{mg} \tag{4.19}$$

Accordingly, $0.191\,\text{mg}$ of NAD(P)H was dissolved in $0.5\,\text{mL}$ of 0.01 N NaOH solution, and $0.123\,\text{mg}$ of FAD was dissolved in $0.5\,\text{mL}$ of ultrapure water. The two solutions were then combined, and $2\,\text{mL}$ of ultrapure water was added to obtain the final $3\,\text{mL}$ solution.

For phantoms representative of tumoral tissue, the target NAD(P)H concentration was $C_{\text{NAD(P)H}} = 126\,\mu\text{M} = 0.0894\,\text{mg/mL}$ and the target FAD concentration was $C_{\text{FAD}} = 38.65\,\mu\text{M} = 0.0321\,\text{mg/mL}$. By applying the same procedures used for the normal tissue phantom, for NAD(P)H:

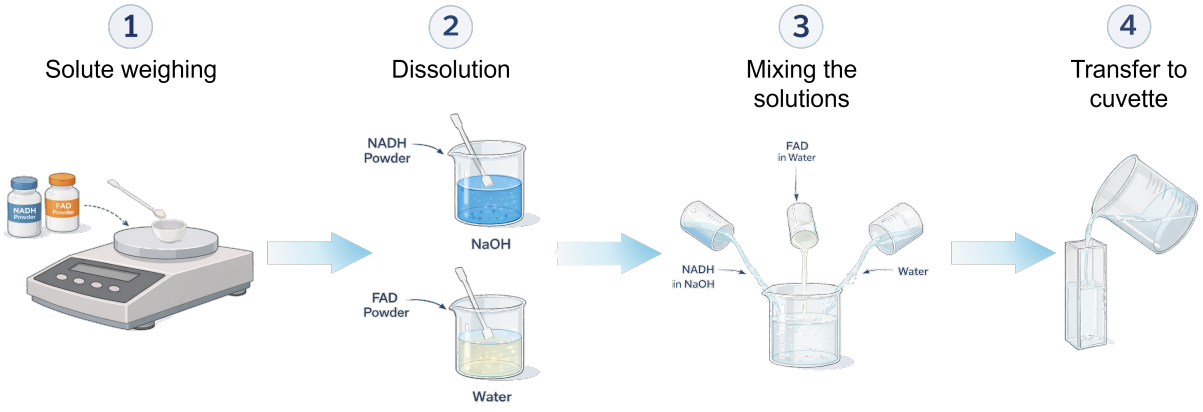


Figure 4.4: Fabrication workflow of the liquid optical phantoms containing NAD(P)H and FAD.

$$C_i \times 0.5\,\text{mL} = 0.0894\,\text{mg/mL} \times 3\,\text{mL} \Longleftrightarrow C_i = 0.536\,\text{mg/mL} \tag{4.20}$$

$$m = 0.536\,\text{mg/mL} \times 0.5\,\text{mL} = 0.268\,\text{mg} \tag{4.21}$$

and for FAD:

$$C_i \times 0.5\,\text{mL} = 0.0321\,\text{mg/mL} \times 3\,\text{mL} \Longleftrightarrow C_i = 0.193\,\text{mg/mL} \tag{4.22}$$

$$m = 0.193\,\text{mg/mL} \times 0.5\,\text{mL} = 0.096\,\text{mg} \tag{4.23}$$

Thus, 0.268 mg of NAD(P)H was dissolved in 0.5 mL of 0.01 N NaOH solution, and 0.096 mg of FAD was dissolved in 0.5 mL of ultrapure water. The two solution were then combined, and 2 mL of ultrapure water was added to obtain the final 3 mL solution.

Liquid phantoms containing NAD(P)H, FAD, hemoglobin, and polystyrene beads

To develop complete liquid phantoms containing NAD(P)H, FAD, hemoglobin (Merck H0267), and polystyrene beads, which mimic biological tissues, several considerations are required. For normal tissues, the target concentrations for NAD(P)H and FAD were the same as those used in the liquid phantoms containing NAD(P)H and FAD. The target concentration for hemoglobin is $1.8\,\text{mg/mL}$, and the target concentration of polystyrene beads is $0.45\,\%(\text{V/V})$.

Using Equation 4.1, the hemoglobin concentration in an initial solution of 0.5 mL:

$$C_i \times 0.5\,\text{mL} = 1.8\,\text{mg/mL} \times 3\,\text{mL} \Longleftrightarrow C_i = 10.8\,\text{mg/mL} \tag{4.24}$$

corresponding to a mass of:

$$m = 10.8\,\text{mg/mL} \times 0.5\,\text{mL} = 5.4\,\text{mg} \tag{4.25}$$

For a final solution volume of 3 mL, the volume of the polystyrene beads solution with $2.5\,\%(\text{w/V})$ is:

$$V = \frac{3 \times 0.45}{100} = 0.014\,\text{mL} \tag{4.26}$$

Thus, 0.191 mg of NAD(P)H, 0.123 mg of FAD, and 5.4 mg of hemoglobin were dissolved separately in three different solutions with 0.5 mL each. The three solutions were then combined, and 0.014 mL of polystyrene bead suspension with $2.5\,\%(\text{w/V})$ and 1.487 mL of ultrapure water were added, yielding a final solution of 3 mL.

For phantoms mimicking tumoral tissue, the same concentrations of NAD(P)H and FAD used previously in the liquid phantoms containing NAD(P)H and FAD were maintained. The target concentration for hemoglobin is $5.8\,\mathrm{mg/mL}$, and the target concentration of polystyrene beads is $0.8\,\%(\mathrm{V/V})$.

Using Equation 4.1, the hemoglobin concentration in an initial solution of $0.5\,\mathrm{mL}$:

$$C_i \times 0.5\,\mathrm{mL} = 5.8\,\mathrm{mg/mL} \times 3\,\mathrm{mL} \iff C_i = 34.8\,\mathrm{mg/mL} \tag{4.27}$$

corresponding to a mass of:

$$m = 34.8\,\mathrm{mg/mL} \times 0.5\,\mathrm{mL} = 17.4\,\mathrm{mg} \tag{4.28}$$

For a final solution volume of $3\,\mathrm{mL}$, the volume of polystyrene bead suspension with $2.5\,\%(\mathrm{w/V})$ that should be added is:

$$V = \frac{3 \times 0.8}{100} = 0.024\,\mathrm{mL} \tag{4.29}$$

Thus, $0.268\,\mathrm{mg}$ of NAD(P)H, $0.096\,\mathrm{mg}$ of FAD, and $17.4\,\mathrm{mg}$ of hemoglobin were each dissolved in a separate $0.5\,\mathrm{mL}$ solution. The three solutions were then combined, and $0.024\,\mathrm{mL}$ of polystyrene beads suspension with $2.5\,\%(\mathrm{w/V})$ and $1.476\,\mathrm{mL}$ of ultrapure water were added, yielding a final volume of $3\,\mathrm{mL}$.

The entire fabrication process of a complete liquid phantom is schematized in Figure 4.5.

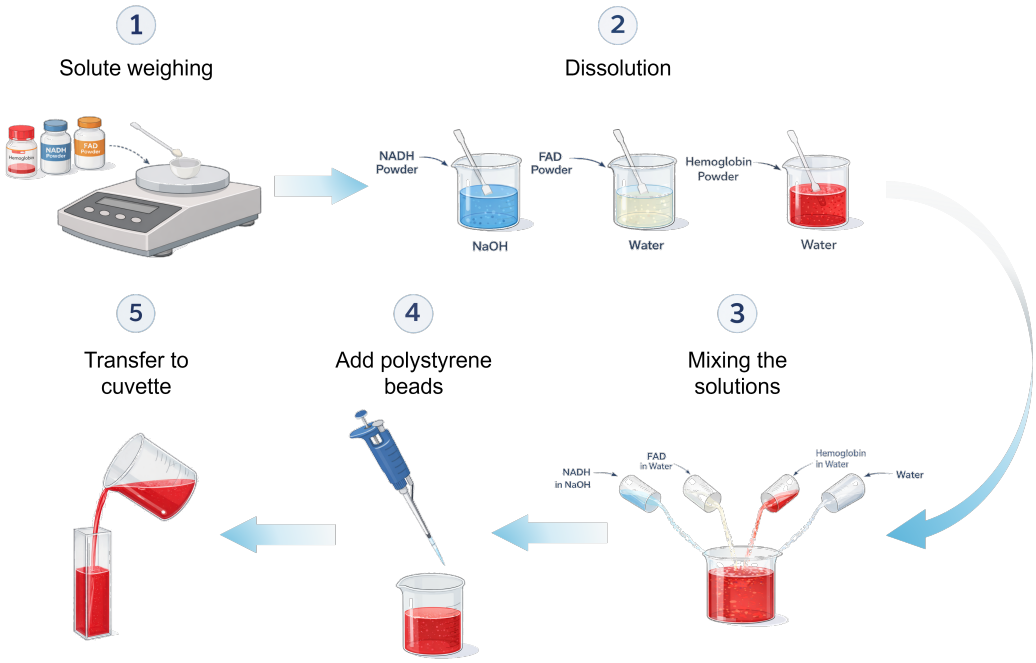


Figure 4.5: Fabrication workflow of the liquid optical phantoms containing NAD(P)H, FAD, hemoglobin, and polystyrene beads.

Solid phantoms containing NAD(P)H and FAD

For solid phantoms representative of normal and tumoral tissues with NAD(P)H and FAD, the same target concentrations described previously for the liquid phantoms were used. After combining the intermediate NAD(P)H and FAD solutions for each type of phantom (normal and tumoral) and adjusting the total volume to 3 mL (as illustrated in Figure 4.4), gelatin powder (Merck C3867) was added to the solution to obtain a final concentration of $C_{\text{gelatine}} = 10\,\%(\text{w/V}) = 100\,\text{mg/mL}$. The gelatin mass used to obtain this concentration in a 3 mL solution was:

$$m = 100\,\text{mg/mL} \times 3\,\text{mL} = 300\,\text{mg} \tag{4.30}$$

The gelatin was dissolved in the 3 mL solution using a magnetic mixer with an integrated hotplate at 600 rpm for 10 min and maintained at $37\,^{\circ}$C, which was sufficient to fully dissolve the gelatin and ensure homogeneous distribution of all components. The temperature was kept below $37\,^{\circ}$C to prevent fluorophores degradation [158, 183]. Then, the solution was introduced into molds (Figure 4.6) specifically designed for phantom fabrication. The molds were constructed using two microscope glass slides separated by three calibrated spacer strips. The spacers were positioned along three sides of the slides, leaving one side open to allow injection of the solution using a syringe equipped with a needle. All sides of the slides were sealed with parafilm to prevent leakage of the liquid solution during filling and solidification. After the solution was left for 2 h at room temperature to form gelatin.

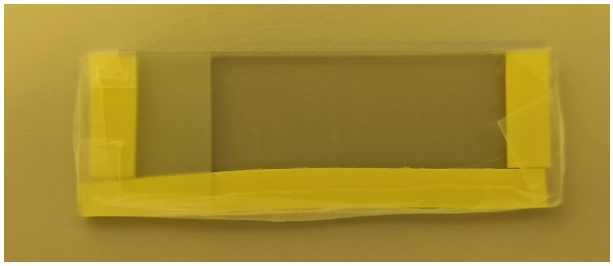


Figure 4.6: Custom-built mold for gelatin phantom fabrication, consisting of two microscope glass slides separated by calibrated spacer strips (yellow strips) and sealed with parafilm on three sides, leaving one side open for solution injection (upper side).

Solid phantoms containing NAD(P)H, FAD, hemoglobin, and polystyrene beads

Solid phantoms containing NAD(P)H, FAD, hemoglobin, and polystyrene beads were prepared to reproduce the combined fluorescence, absorption, and scattering properties of biological tissue. The process is a combination of the procedures represented in Figures 4.5 and 4.7, considering all the target concentrations of NAD(P)H, FAD, hemoglobin, and polystyrene beads used for the preparation of liquid phantoms.

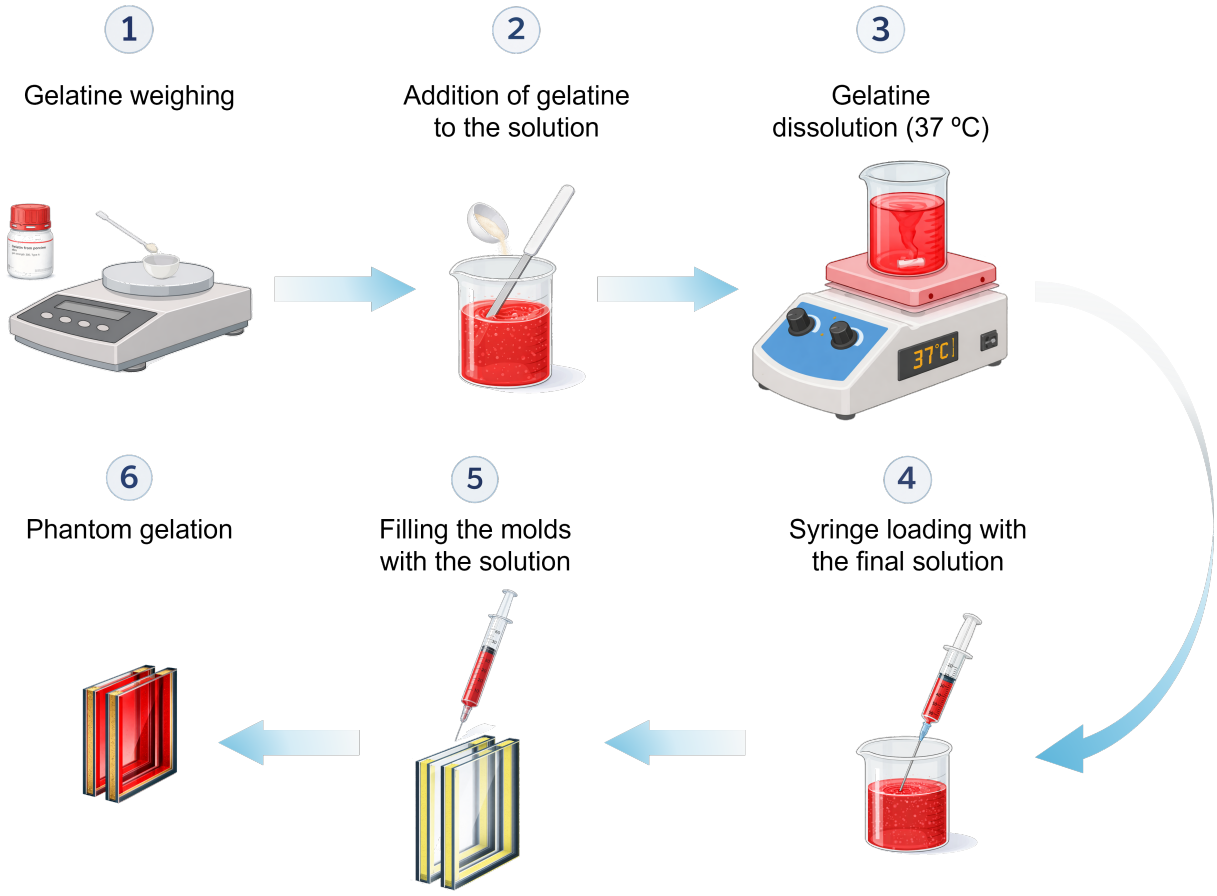


Figure 4.7: Fabrication workflow of the solid optical phantoms.

4.3.2 Phantoms Characterization

A comprehensive optical and physical characterization of all phantom components was carried out to assess their compliance with the intended design specifications. This included one-photon absorption and one-photon excited fluorescence (1PEF) and 2PEF measurements of NAD(P)H and FAD, absorbance characterization of hemoglobin, polystyrene beads, and gelatin, and the determination of the refractive index and thickness of the gelatin.

NAD(P)H and FAD one-photon absorption spectra

To characterize the one-photon absorption spectra of NAD(P)H and FAD, two liquid phantoms were prepared, one containing NAD(P)H and the other containing FAD. The fabrication procedure for these liquid phantoms was described in the previous section. The experimental concentrations used were $128.28\,\mu M$ for NAD(P)H and $323.08\,\mu M$ for FAD. The absorption spectral shape is independent of concentration. The absorption spectra were recorded using a commercial spectrophotometer (Shimadzu UV-3101PC) over the

wavelength range from 200 nm to 600 nm, with a step size of 1 nm. Baseline correction was performed using a reference cuvette filled with the corresponding solvent (0.01 N NaOH solution for NAD(P)H and ultrapure water for FAD).

NAD(P)H and FAD one-photon fluorescence spectra

Following the absorption measurements, the 1PEF spectra of NAD(P)H and FAD were acquired using the same liquid phantoms. Fluorescence measurements were performed using a commercial spectrofluorometer (SPEX Fluorolog-2). Two excitation wavelengths were used, yielding two emission spectra for each phantom, with excitation at 375 nm and 400 nm. Emission spectra were recorded over the wavelength range from 400 nm to 700 nm with a spectral resolution of 1 nm. Background correction was performed using a reference cuvette filled with the corresponding solvent (0.01 N NaOH solution for NAD(P)H and ultrapure water for FAD).

NAD(P)H and FAD two-photon fluorescence spectra

The 2PEF response of NAD(P)H and FAD was characterized using a custom-developed experimental system, the configuration of which is described in a subsequent section. For this characterization, four liquid phantoms were prepared, two containing NAD(P)H and two containing FAD. The target concentrations corresponded to those reported for normal tissues. The obtained experimental concentrations were 93.50 µM for the NAD(P)H phantoms, and 57.47 µM for the FAD phantoms.

Two different excitation wavelengths were used, 750 nm and 800 nm, yielding two spectra for each phantom. The mean laser power at the sample (excitation power) was selected to ensure a detectable signal with sufficient intensity and an adequate signal-to-noise ratio. This power ranged between 50 mW, 100 mW, 115 mW, 150 mW, and 200 mW, depending on the alignment of the optical setup, which influenced both the maximum achievable power and the detected signal intensity. For each measurement, three different excitation powers were selected to verify the nonlinear origin of the signal by analyzing the relationship between the mean excitation power and the resulting fluorescence intensity.

The emitted signal was collected using a commercial imaging spectrometer (Shamrock 300i, Andor Technology) coupled to a cooled charge coupled device (CCD) array (Newton DU920 UVB, Andor Technology). For each excitation power, the CCD signal was integrated for 60 s. The spectral acquisition window was set to 430-568 nm for the NAD(P)H phantoms and 480-600 nm for the FAD phantoms. The acquisition windows were selected such that the peak emission wavelength of each fluorophore was centered within the detection range.

Hemoglobin absorbance spectra

To measure the absorbance of hemoglobin, an experimental setup was used (Figure 4.8). For this analysis, a liquid phantom consisting of hemoglobin dissolved in ultrapure water at a concentration of $1.8\,\mathrm{mg/mL}$ was prepared. A volume of $3\,\mathrm{mL}$ of the solution was placed in a cuvette and measured using the described optical setup.

The absorbance measurements were acquired over the same wavelength range and using the same averaging strategy as those applied for the polystyrene bead measurements. The setup consisted of a $200\,\mathrm{W}$ quartz tungsten halogen lamp as the broadband light source, providing emission over the spectral range $200\,\mathrm{nm}$ to $2400\,\mathrm{nm}$, a monochromator (Newport 74125) for wavelength selection, and an optical fiber to guide the light to the sample and subsequently to the detector. The transmitted light was detected using a photodiode (Hamamatsu S1336-5BQ), and the resulting current was measured with a picoammeter (Keithley 487).

The absorbance measurements were performed over the wavelength range $450\text{-}950\,\mathrm{nm}$, which is relevant for the present study, with a wavelength step of $1\,\mathrm{nm}$. For each wavelength, three measurements were recorded and averaged. A reference spectrum was acquired using an identical cuvette filled with ultrapure water. This process was repeated two times, and the final absorbance spectrum was obtained by averaging the two scans. The detected signal for both the sample and the reference consisted of a wavelength-dependent photocurrent.

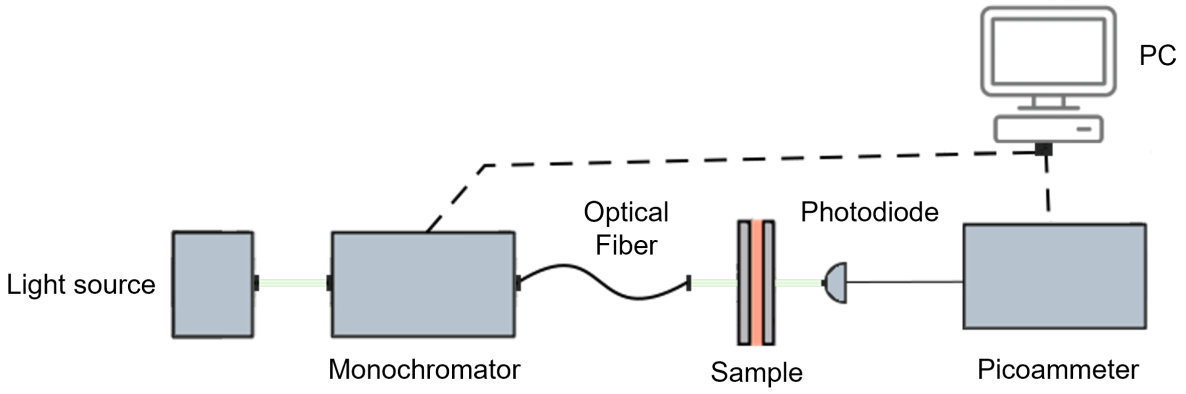


Figure 4.8: Custom-built optical setup for absorbance measurements.

Polystyrene beads absorbance spectra

To characterize the absorbance of the polystyrene beads, a $3\,\mathrm{mL}$ solution with a concentration representative of normal tissue ($0.45\,\%(\mathrm{V/V})$) was used. The solution was placed in a cuvette and measured using a custom-built optical setup, which is illustrated in Figure 4.8. The absorbance measurements were

acquired over the same wavelength range and using the same averaging strategy as those applied for the hemoglobin absorbance measurements.

Gelatin absorbance spectra

Using the same procedure employed for the hemoglobin and polystyrene beads analysis, the gelatin absorbance was measured. For this purpose, a 3D-printed mold in the shape of a cube with an edge length of 1 cm was used. One face of the mold was left open to allow the introduction of the gelatin solution.

Gelatin was dissolved in ultrapure water at a concentration of $10\,\%(\mathrm{w/V})$, using a magnetic stirrer maintained at $37\,^{\circ}$C. After complete dissolution, the solution was poured into the mold and allowed to solidify at room temperature for 24 h prior to the absorbance measurements. After solidification, the gelatin sample was carefully removed from the mold. To avoid damaging the phantom, one side of the mold was intentionally broken to facilitate sample extraction.

Gelatin refractive index

To measure the refractive index (n) of gelatin, a phantom was prepared following the same fabrication procedure described for the gelatin absorbance measurements. The refractive index of gelatin was determined using a method based on the Brewster angle, already explained in a previous section. A dedicated experimental setup (Figure 4.9) was developed to measure the Brewster angle of the fabricated gelatin samples. The setup consisted of a laser source (Oxxius combiner integrating three laser diodes: LBX-638, LBX-515, and LBX-445) a polarizer used to set the incident light to p-polarization, and a rotational stage on which the sample was mounted. The rotational stage was adjusted until the reflected beam disappeared, indicating that the incident light was fully transmitted through the sample, and the angle of the stage recorded. Since the incident medium was air $(n_1 \approx 1)$, the refractive index of the gelatin sample (n_2) could be directly calculated by Equation 4.10.

Using the setup, the Brewster angle was measured for several gelatin phantoms. From these measurements, the refractive index of each sample was calculated. Although the excitation wavelength used in the 2PEF imaging experiments was 750 nm, the refractive index measurement setup at this wavelength was not possible to implement. Consequently, a laser source providing three selectable visible wavelengths in the visible range (638 nm, 515 nm, and 445 nm) was used instead. This approach is justified because the objective of the study was to verify whether the refractive index of gelatin lies within the typical range reported for biological tissues. Moreover, the literature reports refractive index values for biological tissues across the visible and NIR spectral regions.

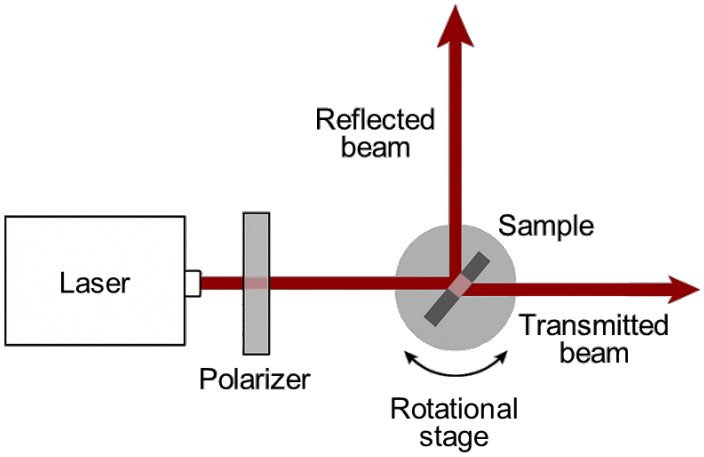


Figure 4.9: Custom-built setup for refraction index measuring.

In this way, the refractive index was measured at three different laser wavelengths. After complete gelatin dissolution, the solution was poured into the 3D-printed mold for solidification. Each phantom sample consisted of a cube with a side length of 10 mm. The mold was designed to ensure minimal surface roughness and to maintain parallelism between opposing faces. For each wavelength, measurements were repeated three to four times. Each reported value corresponds to the average of three consecutive measurements.

Gelatin thickness

Finally, to measure the gelatin thickness, solid phantoms containing both NAD(P)H and FAD were used, following the same fabrication procedure described in the previous section. For some measurements, one of the microscope glass slides was removed after gelation, while for others, both slides were kept in place. The samples were then mounted vertically using a 3D-printed support and placed under an optical microscope (Leica M80). This configuration allowed direct measurement of the distance between the two opposite surfaces of the phantom, corresponding to its thickness. Measurements were performed on four different samples, and for each sample, thickness was measured at two different locations to determine the mean thickness value and assess its spatial variability within and between samples.

4.4 Results and Samples Analysis

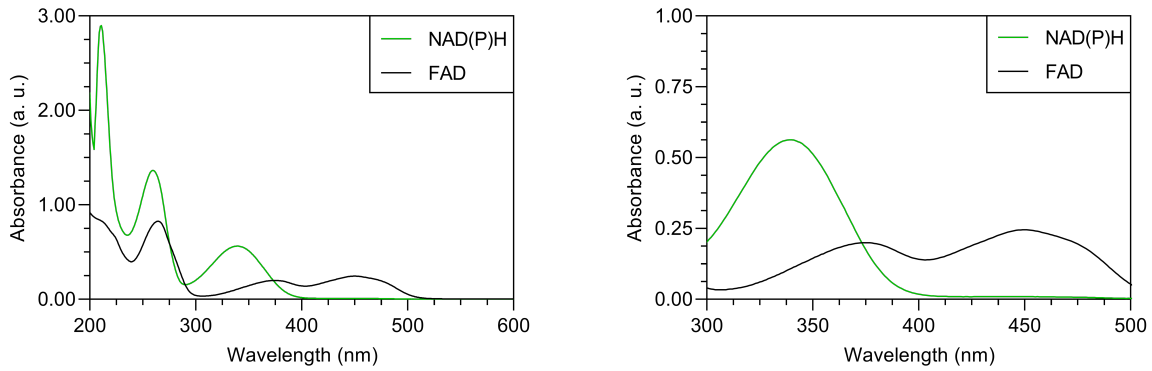
4.4.1 One-Photon Absorption Spectra of NAD(P)H and FAD

The one-photon absorption spectra of NAD(P)H and FAD fluorophores were first characterized. These measurements provided essential information about the main absorption bands of each fluorophore, guiding the selection of appropriate excitation wavelengths.

The obtained absorption spectra of NAD(P)H and FAD are presented in Figure 4.10. The laser source used in the multiphoton setup has a tunable wavelength range between 700 nm and 1000 nm. Thus, the most relevant region of the one-photon absorption spectra corresponds to approximately half of this range, between 350 nm and 500 nm. For this reason, Figure 4.10(b) shows a view of this spectral interval.

As expected from the literature [30], NAD(P)H exhibits a pronounced absorption peak between 300 nm and 400 nm, whereas FAD displays a broader absorption band with a peak around 450 nm. Considering that the goal of this work is the simultaneous excitation of both fluorophores, an excitation wavelength of approximately 375 nm emerges as a suitable compromise for 1PEF. At this wavelength, the absorption of NAD(P)H and FAD is comparable, enabling efficient excitation of both species. At shorter wavelengths, the significantly higher absorption of NAD(P)H would dominate the response and hinder the detection of FAD fluorescence. Conversely, at longer wavelengths, the absorption of NAD(P)H becomes too weak, making it difficult to generate a detectable fluorescence signal. Therefore, the selected excitation wavelength represents an optimal balance for the simultaneous investigation of both fluorophores.

For the prepared solutions, the NAD(P)H concentration was 0.091 mg/mL, corresponding to 128.28 µM



(a) (b)

Figure 4.10: One-photon absorbance spectra of NAD(P)H and FAD: (a) full spectral range; (b) region of interest (ROI) (300 - 500 nm).

($M_{\text{NAD(P)H}}$=709.40 g/mol [179]), while the FAD concentration was 0.268 mg/mL, equal to 323.48 µM (M_{FAD}=829.51 g/mol [180]).

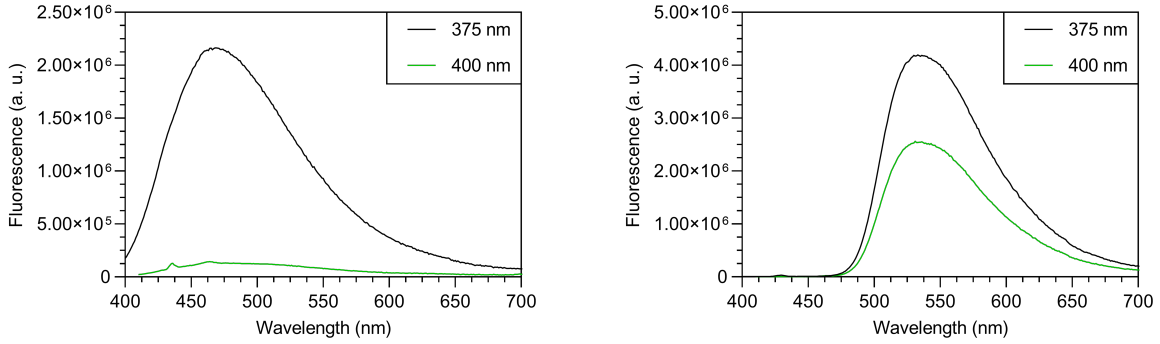
Considering the NAD(P)H and FAD concentration used in the phantoms, $C_{\text{NAD(P)H}} = 128.28$ µM $= 0.091$ mg/mL and $C_{\text{FAD}} = 323.48$ µM $= 0.268$ mg/mL, the molar extinction coefficients of NAD(P)H (6.2×10^3 M^{-1} cm^{-1} at 340 nm [184]) and FAD (1.1×10^4 M^{-1} cm^{-1} at 450 nm [184]), and using the Beer-Lambert law (Equation 1.1), the expected maximum absorbance values for a 1 cm optical path (cuvette dimension) are therefore $A_{\text{NAD(P)H}} \approx 0.79$ and $A_{\text{FAD}} \approx 3.55$. Thus, both fluorophores exhibit smaller absorbance values than expected, particularly FAD. The FAD spectrum shows a substantially reduced absorbance in the visible region. This deviation is attributed to the chemical instability of FAD when dissolved in pure water, where partial reduction, photoreduction, or the formation of semiquinone species readily occurs, leading to a significant attenuation of the characteristic 450 nm absorption band. Since only the oxidized form of FAD exhibits strong visible absorption, buffered and oxygenated conditions are required to preserve its optical properties. Consequently, the observed lower absorbance of FAD relative to NAD(P)H does not reflect an error in concentration or instrumentation, but rather a change in the oxidation state of FAD under the chosen solvent conditions. The small discrepancy observed in the absorbance peaks of NAD(P)H can be attributed to minor errors in solute weighing and incomplete dissolution, which may alter effective concentration, and to potential instrumental uncertainties. It should be noted that these factors also have an impact on the FAD response, but not in a manner that justifies the big difference between the experimental and the expected absorbance values.

4.4.2 One-photon Fluorescence Spectra of NAD(P)H and FAD

After characterizing the one-photon absorption spectra of NAD(P)H and FAD, their corresponding 1PEF fluorescence spectra were acquired. Fluorescence measurements were performed using excitation wavelengths of 375 nm and 400 nm. The 375 nm excitation was selected based on the previous absorption spectra analysis. The excitation at 400 nm was additionally investigated as it corresponds to half of the 800 nm, the optimal emission wavelength of the Ti:sapphire laser employed in the multiphoton setup.

The NAD(P)H spectra (Figure 4.11(a)) show emission peaks centered at 469 nm and 464 nm for excitation at 375 nm and 400 nm, respectively. The FAD fluorescence spectra (Figure 4.11(b)) exhibit an emission maximum at approximately 533 nm for 375 nm excitation and 531 nm for 400 nm excitation. In both cases, the emission profiles and peak positions are in accordance with the characteristic fluorescence signatures reported in the literature [30, 185].

As expected from the absorption spectra, excitation at 400 nm produced lower fluorescence intensity



(a) (b)

Figure 4.11: 1PEF spectra, under excitation at 375 nm and 400 nm: (a) NAD(P)H emission; (b) FAD emission.

for NAD(P)H and FAD. This reduced efficiency reflects the smaller absorption cross-sections of both fluorophores at this wavelength. Consequently, excitation at 400 nm, equivalent to two-photon excitation at 800 nm, is not optimal for the simultaneous excitation of both species in this system, despite its frequent use in MPM [21].

These measurements provide important guidance for defining the spectral detection windows and for designing the optical filters used in the detection pathway. Nevertheless, it has been reported that 2PEF emission spectra may exhibit slight spectral shifts relative to 1PEF excitation [186]. Although the present results are suitable for initial wavelength selection, direct characterization under two-photon excitation remains necessary to accurately determine the optimal detection bands for subsequent experiments.

4.4.3 Two-photon Fluorescence Spectra of NAD(P)H and FAD

As previously indicated, it is important to analyze the 2PEF spectra of NAD(P)H and FAD, since differences between 1PEF and 2PEF spectra may occur. To this end, two liquid phantoms were prepared for each fluorophore. One phantom was excited at 750 nm and the other at 800 nm.

The NAD(P)H phantoms had an experimental concentration of 93.50 µM, and the FAD phantoms an experimental concentration of 57.47 µM. The obtained 2PEF spectra are presented in Figure 4.12. The 2PEF results are consistent with the trends observed under 1PEF. When excitation is performed at 800 nm, the NAD(P)H fluorescence emission is residual, and the FAD fluorescence intensity is reduced by approximately a factor of eight compared to excitation at 750 nm, for the same laser power. These results indicate that 750 nm is the most suitable excitation wavelength for efficient two-photon excitation of both fluorophores.

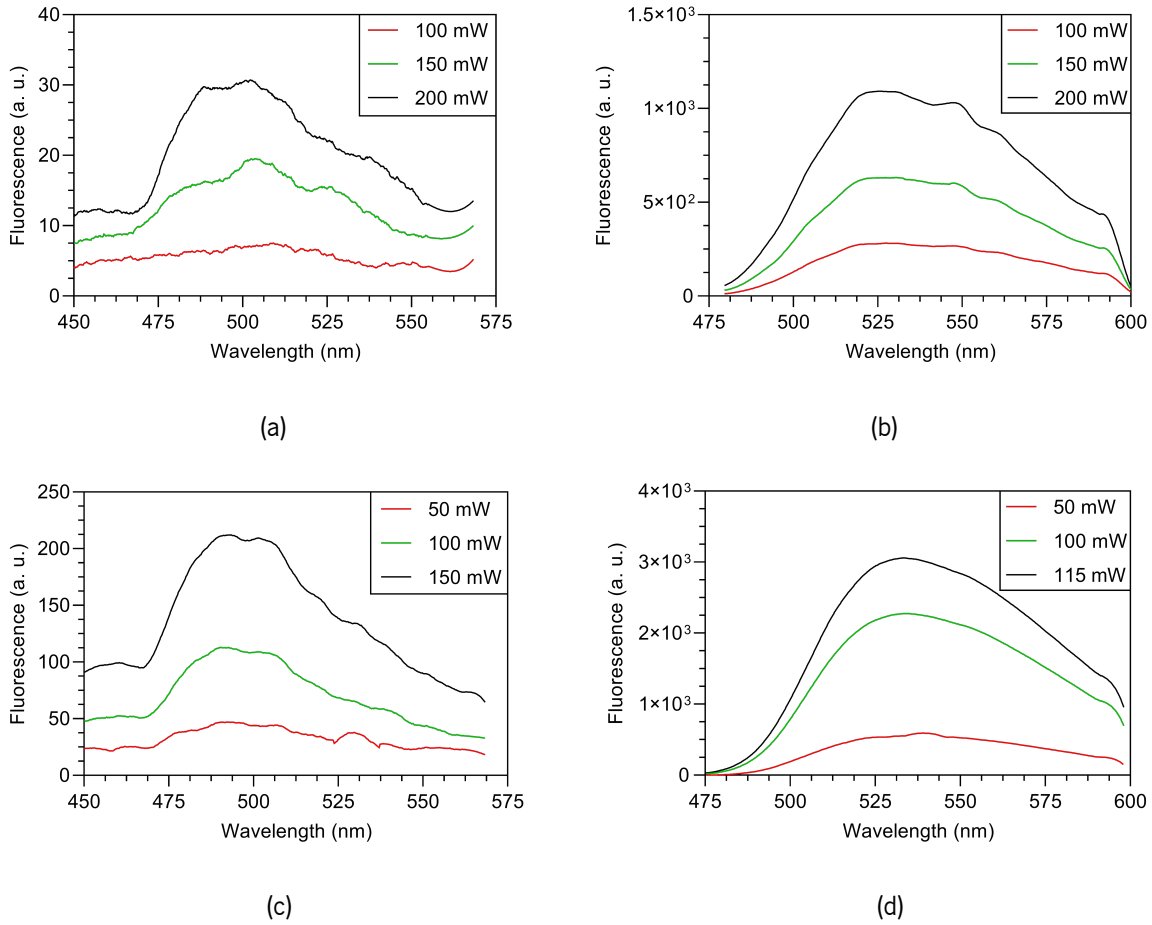


Figure 4.12: 2PEF spectra of NAD(P)H and FAD in liquid phantoms: (a) NAD(P)H at 800 nm excitation; (b) FAD at 800 nm excitation; (c) NAD(P)H at 750 nm excitation; (d) FAD at 750 nm excitation.

For comparison between one and two-photon excitation, the spectra shown in Figure 4.12(c) and Figure 4.12(d) were normalized and plotted together with the 1PEF spectra obtained under 375 nm excitation, as shown in Figure 4.13. This representation allows a direct comparison between 1PEF and 2PEF emission characteristics. For NAD(P)H, a slight red shift of the emission spectrum is observed under two-photon excitation compared to one-photon excitation. Since the measurements were performed in a solution without proteins, this shift cannot be attributed to binding effects and is instead likely related to differences in vibronic state populations arising from the distinct selection rules governing one and two-photon excitation. Importantly, the overall spectral shape remains comparable, indicating that the fundamental emission mechanism is unchanged [30, 187]. This red-shift phenomenon aligns with the findings of Bestvater *et al.*, who conducted a comprehensive study comparing 2PEF and 1PEF from various fluorophores. Their study concluded that the emission spectra of most fluorophores shift towards longer wavelengths [188], corroborating the observations reported in the current study. The FAD emission spectra obtained under

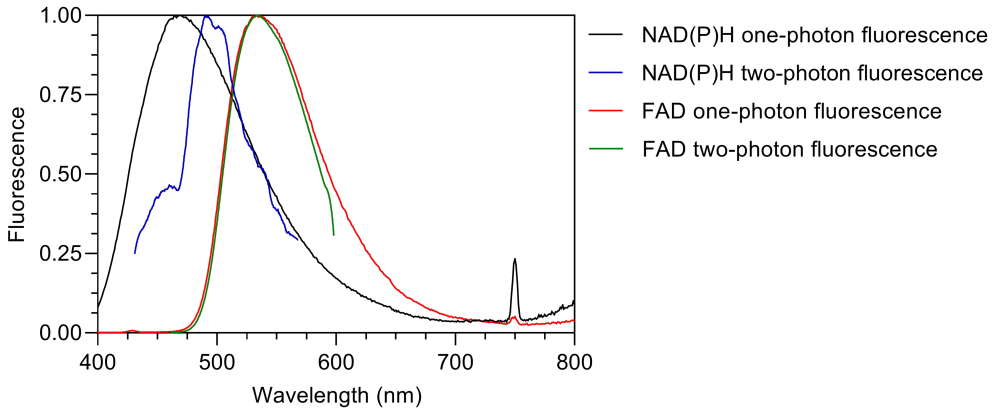
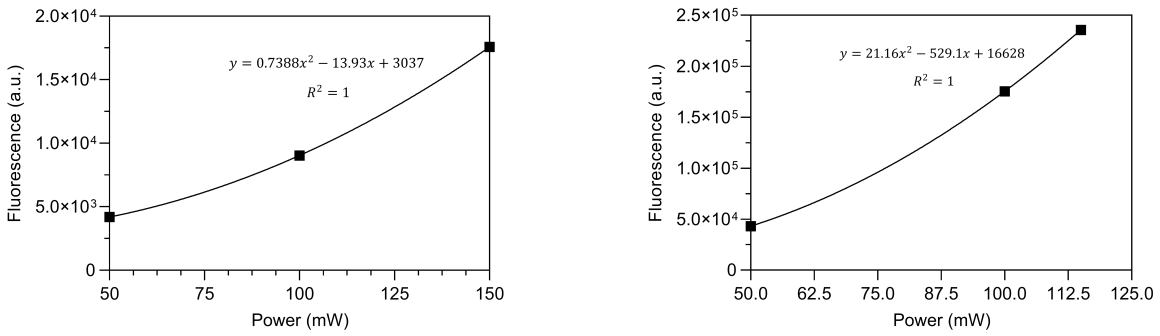


Figure 4.13: Normalized 2PEF spectra acquired under 750 nm excitation and 1PEF spectra acquired under 375 nm excitation for NAD(P)H and FAD.

one and two-photon excitation are nearly identical, consistent with fluorescence emission originating from the same relaxed excited singlet state.

For each excitation wavelength, 2PEF measurements were performed using three different excitation powers. The selected power levels were determined by the laser wavelength, the optical alignment of the system, the maximum achievable output power, and the excitation power required to obtain an adequate signal-to-noise ratio. The use of multiple power levels allows verification of the nonlinear nature of the fluorescence process by analyzing the relationship between excitation power and fluorescence intensity.

To facilitate this analysis, the emission spectra obtained at 750 nm excitation were integrated, and the resulting integrated intensities were plotted as a function of excitation power, as shown in Figure 4.14. The observed quadratic dependence of fluorescence intensity on excitation power confirms that the detected



(a) (b)

Figure 4.14: Integrated fluorescence intensity as a function of the excitation power with the corresponding regression curves at 750 nm excitation for: (a) NAD(P)H; (b) FAD.

signal originates from a nonlinear optical process, consistent with 2PEF.

4.4.4 Absorbance Spectra of Hemoglobin, Polystyrene Beads, and Gelatin

After the characterization of NAD(P)H and FAD, the absorbance of the remaining phantom constituents was also evaluated and is represented in Figure 4.15. This analysis aimed to determine their individual contributions to the overall optical response of a phantom and to verify whether their behavior mimics biological tissues.

Hemoglobin exhibits high absorbance values for wavelengths below approximately 575 nm, and its spectral features closely match those reported in the literature [189]. This confirms that hemoglobin is the primary absorber in a phantom and significantly influences optical measurements, particularly because its absorption overlaps with the fluorescence emission of endogenous fluorophores. Consequently, these results further support the use of 2PEF, since at longer wavelengths (above 650 nm) absorption is reduced, allowing a greater fraction of the excitation light to reach the fluorophores.

It should be noted that, for some components, the recorded signal does not arise solely from absorption. For instance, polystyrene beads predominantly scatter incident light rather than absorb it, and gelatin also introduces a non-negligible scattering contribution. In these cases, the measured quantity represents attenuation (loss of transmitted light) rather than true absorption. Nevertheless, for consistency, this attenuation is reported in absorbance units, providing a practical and comparable metric across all samples.

The polystyrene beads display the expected behavior, with stronger scattering at shorter wavelengths, consistent with Mie scattering trends reported in the literature, which indicate the scattering coefficient decreases with increasing wavelength [190]. This confirms their role as the dominant scattering component of a phantom. Moreover, it reinforces the advantages of 2PEF, as longer excitation wavelengths (such

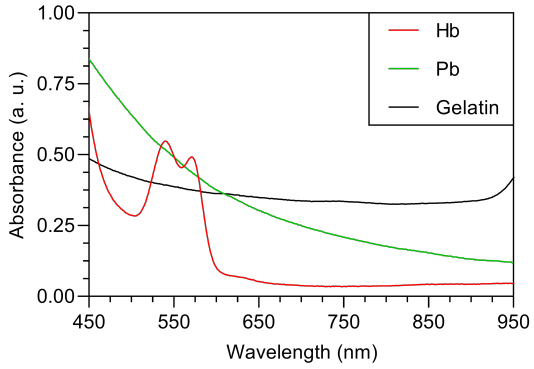


Figure 4.15: Absorbance spectra of hemoglobin (Hb), polystyrene beads (Pb) and gelatin.

as 750 nm) undergo significantly less scattering than those typically used in 1PEF, enabling deeper light penetration.

Gelatin, as anticipated is [191], exhibits relatively uniform attenuation across the spectrum, indicating that it does not introduce wavelength-selective effects but instead contributes primarily to a global reduction in transmitted intensity. A thickness of 1 cm was used for this first characterization. Since the final phantoms are approximately 20 times thinner, the attenuation is expected to decrease proportionally according to the Beer–Lambert law, resulting in substantially lower absorbance values in the final configuration.

4.4.5 Refractive Index of Gelatin

The refractive index of gelatin was also measured, as gelatin constitutes the base material of the solid phantoms and therefore largely determines their optical refractive index. Since the purpose of these phantoms is to mimic biological tissues, the refractive index of gelatin is expected to be comparable to that reported for biological tissues. To this end, a gelatin phantom was prepared and measured using a specifically developed experimental setup (Figure 4.9).

The refractive index was therefore measured at the three selected wavelengths, and the results are presented in Tables 4.3, 4.4, and 4.5. The mean refractive index values obtained were 1.42 ± 0.09 at 445 nm, 1.44 ± 0.11 at 515 nm, and 1.47 ± 0.09 at 638 nm.

Some variability between measurements is observed. This is expected, as the experimental setup

Table 4.3: Brewster angle measurements and refractive indices for gelatin at $\lambda = 445$ nm.

Laser Wavelength (nm)	Brewster Angle (rad)	n
445	0.92	1.31 ± 0.03
	0.91	
	0.93	
	1.00	1.54 ± 0.04
	1.00	
	0.98	
	0.96	1.40 ± 0.02
	0.95	
	0.94	

Table 4.4: Brewster angle measurements and refractive indices at $\lambda = 515$ nm.

Laser Wavelength (nm)	Brewster Angle (rad)	n
515	0.98	1.46 ± 0.03
	0.96	
	0.98	
	0.93	1.28 ± 0.04
	0.91	
	0.89	
	1.02	1.59 ± 0.04
	0.99	
	1.01	
	0.97	1.43 ± 0.02
	0.95	
	0.96	

is relatively simple and relies on visual detection of the minimum refraction angle, which introduces a significant measurement uncertainty. Nevertheless, despite the relatively large associated error, the results consistently indicate refractive index values in the range of approximately 1.4 to 1.5. Moreover, no clear wavelength dependence was observed, within experimental uncertainty, across these wavelengths. [145].

According to the literature, refractive index values for biological tissues typically lie in the range 1.36 – 1.40 for soft water-rich tissues, and 1.44 – 1.46 for lipid-rich tissues [145]. The refractive indices obtained for gelatin fall within or close to these ranges, being slightly higher in some cases. Given the experimental uncertainties, the measured values should be considered approximate estimates rather than precise determinations. Nevertheless, the results confirm that gelatin provides a reasonable refractive index match with biological tissues, supporting its suitability as a base material for solid tissue-mimicking phantoms.

Table 4.5: Brewster angle measurements and refractive indices for gelatin at $\lambda = 638$ nm.

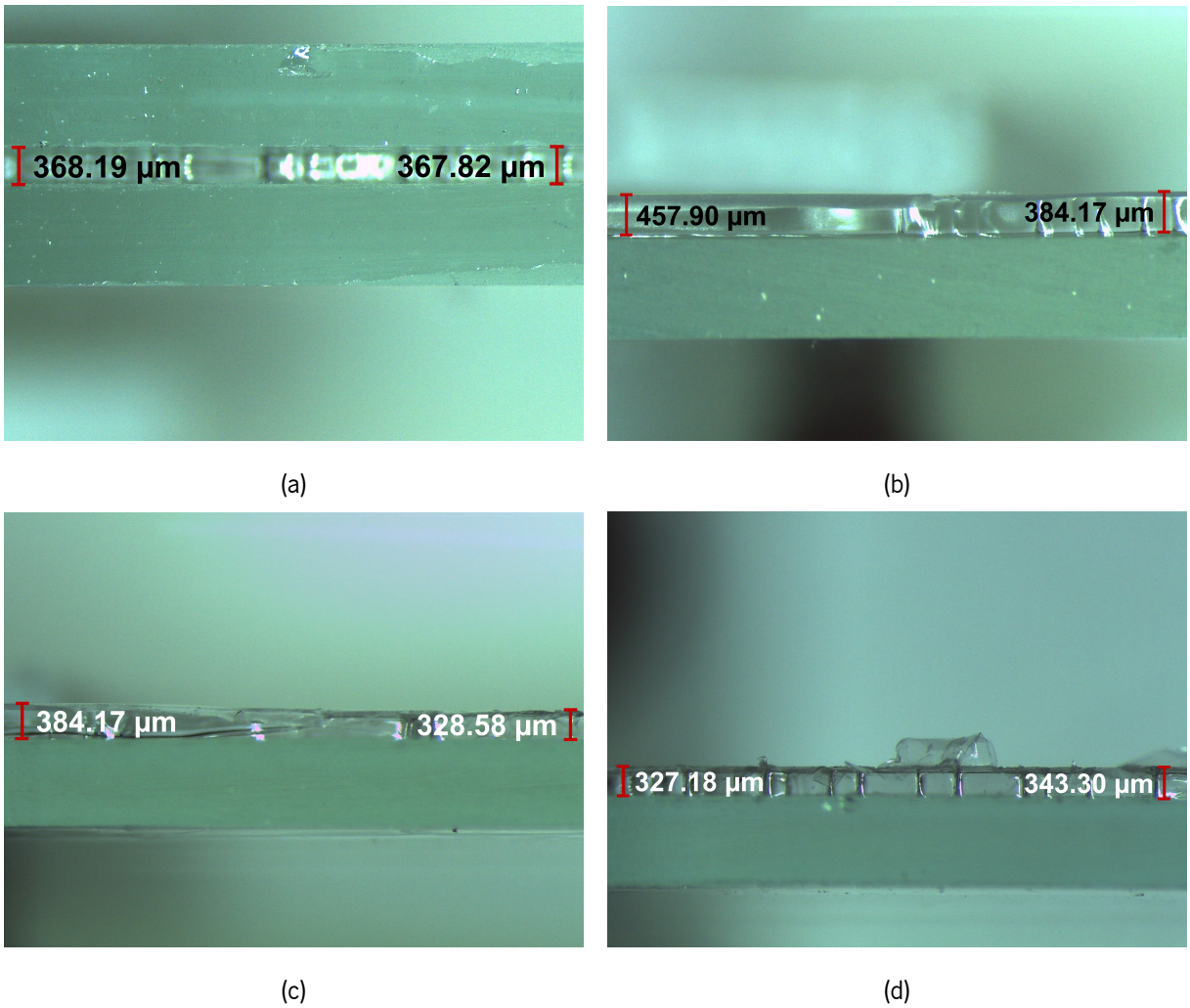
Laser Wavelength (nm)	Brewster Angle (rad)	n
638	0.93	1.30 ± 0.02
	0.91	
	0.92	
	1.00	1.54 ± 0.02
	0.99	
	0.99	
	1.40	1.52 ± 0.09
	1.63	
	1.54	
	1.46	1.50 ± 0.04
	1.51	
	1.54	

4.4.6 Gelatin Thickness

After completing all the characterization, it was necessary to verify whether the developed process produced a phantom with the desired thickness. The measured values are shown in Figure 4.16. The measurements presented correspond exclusively to the central region of the samples, as this is the area used for the 2PEF experiments. Figure 4.16(a) shows the phantom positioned between two glass slides, while in the remaining images, one of the glass slides had been removed before measurement. From these tests, it was concluded that removing one of the glass slides is not advisable, as the removal process can damage the phantom in certain regions, thereby compromising the thickness measurements.

The measured thickness values (ranging from $327.18\,\mu$m to $457.90\,\mu$m)are generally smaller than the nominal thickness defined by the spacer (approximately $500\,\mu$m). This behavior is expected, as the spacers are located at the lateral edges of the glass, where the total thickness approaches the spacer. In contrast, in the central region of the phantom, where the thickness measurements were performed and where the 2PEF measurements will be acquired, the effective thickness is reduced due to a slight curvature of the glass slides, which causes compression of the phantom in this region.

Overall, the obtained thickness values are close to the target thickness ($412\,\mu$m), although in some



(a) (b)

(c) (d)

Figure 4.16: Optical microscope images of gelatin phantoms acquired with a Leica M80 microscope, showing representative thickness measurements: (a) sample 1 measured between two glass slides; (b) sample 2, (c) sample 3, and (d) sample 4, each measured with one glass slide removed.

cases, smaller values are observed. The variability between samples is primarily attributed to the fabrication process, which is highly dependent on the pressure applied during the placement of the parafilm around the glass slices. Variations in the applied pressure can therefore introduce sample-to-sample thickness differences.

Despite this variability, both the minimum and maximum measured thicknesses fall within an acceptable range relative to the target value. Moreover, thickness variability is also a characteristic of real biological tissues, such as tumor growth, meaning that the observed variations may, in fact, enhance the realism of the phantom.

An additional source of uncertainty arises from the difficulty in precisely identifying the boundaries of the phantom when measuring its thickness, which can introduce further measurement error.

4.5 Outlook

In summary, this chapter addressed the development, fabrication, and comprehensive characterization of tissue-mimicking optical phantoms for validating the MPM setup.

A set of liquid and solid phantoms with increasing complexity was successfully developed. These phantoms incorporated endogenous fluorophores (NAD(P)H and FAD), an absorber (hemoglobin), a and scattering agent (polystyrene beads), at physiologically relevant concentrations representative of normal and tumoral colorectal tissues. The fabrication protocols allowed controlled and reproducible preparation of both simplified and fully tissue-mimicking configurations, enabling the independent evaluation of fluorescence, absorption, and scattering contributions.

A detailed optical characterization was performed, allowing us to conclude that the one-photon absorption and 1PEF measurements confirmed the expected spectral behavior of NAD(P)H and FAD, while also highlighting limitations, such as the instability of FAD in aqueous solutions. The 2PEF measurements demonstrated that excitation at $750\,\mathrm{nm}$ provides significantly higher efficiency for simultaneous excitation of both fluorophores compared to $800\,\mathrm{nm}$. Additionally, the quadratic dependence of fluorescence intensity on excitation power confirmed the nonlinear origin of the detected signal. A slight spectral shift between 1PEF and 2PEF emission was observed for NAD(P)H, consistent with literature reports.

The optical characterization of the remaining phantom components confirmed their expected roles: hemoglobin as the dominant absorber, polystyrene beads as the primary scattering source, and gelatin as a structurally stable matrix with minimal spectral selectivity. The measured refractive index of gelatin was found to lie within the typical range of biological tissues, supporting its suitability as a base material for solid phantoms, despite the relatively large experimental uncertainty associated with the measurement method.

Finally, the geometrical characterization demonstrated that the fabricated phantoms achieved thicknesses close to the target values derived from CAM tumor models. Some variability between samples was observed. This was attributed to fabrication constraints and measurement uncertainties and remains within acceptable limits. Importantly, such variability is also characteristic of the biological tissues, further supporting the realism of the developed phantoms.

Overall, the results demonstrate that the proposed phantom design and fabrication methodologies provide a reliable and flexible platform for the controlled validation of the 2PEF setup. These phantoms overcome the limitations of biological models, offering reproducibility, tunability, and well-defined optical properties, thereby constituting a robust foundation for subsequent experimental studies.

Part III

Optical Filters

Chapter 5

Fabry-Perot Optical Filters

This chapter addresses the design, fabrication, and validation of interference-based optical filters for the selective detection of NAD(P)H and FAD fluorescence signals under 2PEF excitation. Based on the spectroscopic analysis presented in the previous chapter, Fabry-Perot filters with Bragg reflectors are developed and optimized using both analytical calculations and numerical simulations. The fabricated filters are experimentally characterized and their performance is evaluated in terms of spectral selectivity and crosstalk. Finally, their applicability is assessed through fluorescence measurements using tissue-mimicking phantoms, aiming at future integration in an MPM setup.

5.1 Context

For the detection of 2PEF signals emitted by NAD(P)H and FAD, the implementation of selective optical filters was identified as a key requirement for future medical applications, particularly in endoscopic systems. These filters enable the selective visualization of the fluorescence signal from each fluorophore. As discussed in the introduction and confirmed by the spectroscopic characterization presented in the previous chapter, the emission spectra of NAD(P)H and FAD exhibit significant spectral overlap. Therefore, it is essential to employ filters capable of selectively transmitting the fluorescence of one fluorophore while suppressing the contribution of the other within the same spectral region.

Furthermore, as shown in Tables 4.1 and 4.2, there is considerable variability in the literature regarding the optimal detection wavelengths for these fluorophores. This variability highlights the need for additional analysis to determine the most appropriate spectral regions for selective detection. Based on the 1PEF and 2PEF spectra obtained in the previous chapter, an initial design choice was made to develop a narrow bandpass filter centered at $485\,\text{nm}$ for NAD(P)H detection and another centered at $530\,\text{nm}$ for FAD detection. These wavelengths were initially selected based on a compromise between fluorophore emission maxima, expected spectral overlap, and feasibility of narrowband filter fabrication.

It is important to emphasize that this selection represents an initial design decision. Further analysis is required to evaluate the overlap between the filter transmission bands and the fluorophore emission spectra, to confirm whether these filters provide optimal selectivity. This evaluation is addressed throughout the present chapter.

Although the current experimental MPM setup employs a spectrometer, allowing the acquisition of the

full emission spectrum, the goal of this work is the application of an MPM setup in an endoscopic system. In such systems, detection is typically performed using devices such as a photomultiplier tube (PMT), which require predefined spectral selection. Consequently, the use of optical filters becomes essential for isolating specific fluorescence signals. The use of a spectrometer in this work is therefore intended to facilitate the evaluation and validation of the filter performance under controlled conditions, where the full spectral information is available.

Regarding the optical filters, they are devices designed to selectively transmit, reflect, or absorb specific spectral components of incident light. Two major types of optical filters can be distinguished: absorptive filters and interference (dichroic) filters. Absorptive filters rely on the spectral absorption properties of the material, where specific wavelengths are attenuated due to electronic transitions within the medium. In contrast, interference filters consist of multilayer stacks of dielectric materials with alternating high and low refractive indices. Their spectral selectivity arises from multiple-beam interference between partial reflections at each interface [192].

Interference filters provide significantly narrower transmission or reflection bands compared to absorptive filters. The thickness of each layer is typically on the order of the wavelength of interest. When light is incident on such a multilayer structure, partial reflections and transmissions occur at each interface. The coherent superposition of these waves results in a well-defined spectral response governed by interference [192].

Therefore, in this work, interference filters were selected for development. The theoretical background underlying these filters is presented in the following section.

5.2 Theoretical Framework

The two configurations commonly used as the basis for interference-based optical filters are distributed Bragg reflectors and Fabry-Perot optical filters. A distributed Bragg reflector consists of alternating layers of high and low refractive indices. Constructive interference of reflected waves at each interface leads to high reflectivity around the selected wavelength. A Fabry-Perot optical filter is composed of two reflectors (usually Bragg reflectors) separated by a cavity (resonator). Depending on the cavity thickness, a specific wavelength is transmitted with a certain full width at half maximum (FWHM) through the filter. These filters can be defined in terms of finesse, which measures how spectrally narrow the peaks are at the operating range of an optical filter. In Figure 5.1 an example of an interference-based optical filter with this configuration is presented [192, 193].

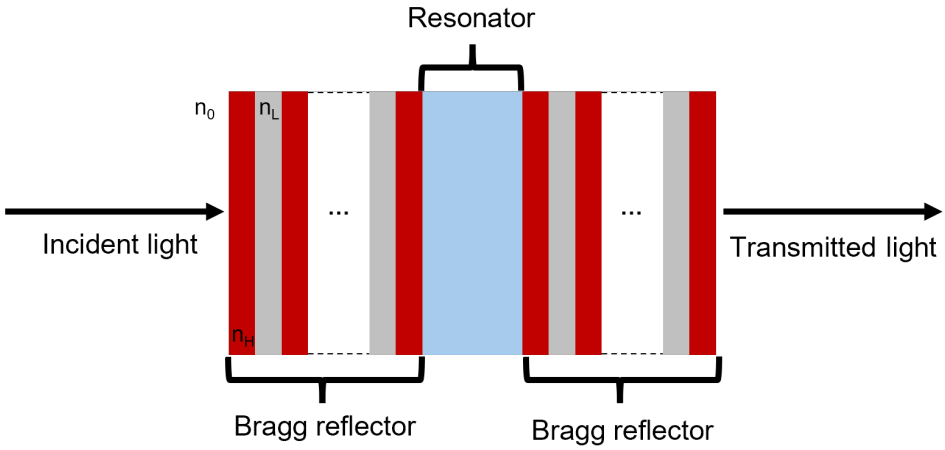


Figure 5.1: Interference-based optical filter with a Fabry–Perot structure, consisting of two Bragg mirrors acting as reflectors separated by an optical cavity (resonator).

Therefore, interference-based optical filters are composed of a multilayer of homogeneous dielectric thin-films, typically isotropic, non-conductive, and non-magnetic, where the complex interference pattern between the interfaces characterizes the spectral response of the structure. All this interference is based on the electromagnetic wave theory (physical optics) [192].

The propagation of light in such media is described by Maxwell's equations, from which it is possible to conclude that, for a homogeneous medium, the complex refractive index $(\tilde{n})$ is defined as [194]:

$$\tilde{n} = n + ik = \sqrt{\varepsilon_r}, \tag{5.1}$$

where n is the real part of the refractive index, k is the extinction coefficient, and ε_r is the relative permittivity.

In the development of interference filters, the refractive index contrast between adjacent layers plays a fundamental role in determining the overall filter performance. It can be defined as [192]:

$$\Delta = \frac{n_H^2 - n_L^2}{2n_H^2}, \tag{5.2}$$

where n_H and n_L are the refractive indices of the high- and low-index layers, respectively. A larger refractive index contrast increases the reflectance at each interface, leading to sharper spectral features and improved filter selectivity. Conversely, a lower index contrast requires more layers to achieve comparable reflectivity, increasing fabrication complexity. Therefore, the performance of interference filters is determined by the refractive index contrast and the number of layers. Although arbitrarily high peak reflectivity can be achieved by increasing the number of layers, the spectral bandwidth is fundamentally limited by

optical design constraints. Furthermore, material choice is restricted by intrinsic absorption bands. The n value is therefore an important parameter in an interference-based optical filter [192].

Interface between two dielectric media

At an interface between two dielectric materials with refractive indices n_1 and n_2, the electromagnetic boundary conditions, derived from Maxwell's equations, lead to the Fresnel equations. These equations describe the amplitudes of the reflected and transmitted fields at a dielectric boundary. One immediate consequence is that the frequency of the reflected and transmitted waves remains equal to that of the incident wave. Another important consideration is governed by Snell's law, which states that the reflected beam propagates at the same angle with respect to the interface normal as the incident beam. Snell's law governs the refraction of light and can be expressed as [2, 101, 193]:

$$n_1 \sin\theta_r = n_2 \sin\theta_t, \tag{5.3}$$

where θ_r is the angle of the reflected wave and θ_t the angle of the transmitted wave.

The fraction of light reflected or transmitted at an interface depends on the polarization of the electric field relative to the plane of incidence. For s-polarization, the electric field is perpendicular to the plane of incidence and parallel to the interface. For p-polarization (from parallel), the electric field lies in the plane of incidence and is therefore perpendicular to the interface. The reflection and transmission coefficients for both s- and p-polarized light can be expressed as follows [2, 101, 193]:

$$r_s = \frac{\cos\theta_i - \sqrt{\left(\frac{n_2}{n_1}\right)^2 - \sin^2\theta_i}}{\cos\theta_i + \sqrt{\left(\frac{n_2}{n_1}\right)^2 - \sin^2\theta_i}} \tag{5.4}$$

$$r_p = \frac{-\left(\frac{n_2}{n_1}\right)^2 \cos\theta_i + \sqrt{\left(\frac{n_2}{n_1}\right)^2 - \sin^2\theta_i}}{\left(\frac{n_2}{n_1}\right)^2 \cos\theta_i + \sqrt{\left(\frac{n_2}{n_1}\right)^2 - \sin^2\theta_i}} \tag{5.5}$$

With negligible absorption,

$$R + T = 1, \tag{5.6}$$

where T is the transmittance and R the reflectance, with $R = |r|^2$, and so $T = 1 - |r|^2$ [101, 193].

Interference between electromagnetic waves

Since interference-based optical filters rely on the superposition of electromagnetic waves, it is important to understand that when two waves of the same frequency overlap, they interfere. The resulting

intensity depends on the phase difference between the two waves. Consequently, the energy of the resultant electric field, expressed as irradiance $I[W/m^2]$, is given by [101]:

$$I = I_1 + I_2 + I_{12} = I_1 + I_2 + 2\sqrt{I_1 I_2}\cos(\delta), \tag{5.7}$$

where I_1 and I_2 are the irradiance of each wave, I_{12} reflects the interference of the two waves.

The interference depends on the phase difference between the two waves. For two waves of equal intensities, with δ being the phase difference between the two waves. If $\cos(\delta) = 1$, the fields constructively interfere and add up; if $\cos(\delta) = -1$, the fields interfere destructively.

In these filters, since there are multiple dielectric layers, the incident light undergoes a series of partial reflections and transmissions at each boundary. If the thickness of the layers is in the order of the wavelength, the cascading rays of reflected light at each boundary strongly interfere. This interference depends on the path-length difference, which in turn depends on the layer thickness, refractive index, and wavelength of the light. This strong spectral dependence on the dimension and optical properties of the structure is the basis of thin-film interference-based optical filters.

Considering a single layer over a substrate, where there are two interfaces and therefore two reflections, as schematized in Figure 5.2, the phase difference between the two reflected waves is proportional to the thickness of the layer (t_f) and to the cosine of the incident angle with respect to the normal of the surface. Considering this dielectric layer of refractive index n_f, the phase change during a single pass through the film is [193]:

$$\delta_t = \frac{2\pi}{\lambda_0} n_f t_f \cos\theta_t \tag{5.8}$$

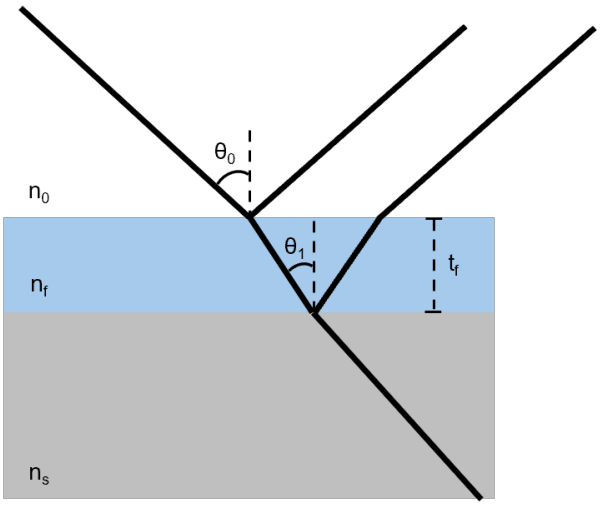


Figure 5.2: Representation of a thin-film on a substrate, showing partial reflection of the incident light at the air–film and film–substrate interfaces.

The total phase difference of the light after passing this film, being reflected at the interface with the substrate, and reappearing at the surface, is given by [193]:

$$\delta = 2\delta_t + \delta_r, \tag{5.9}$$

where δ_r accounts for phase shifts due to the reflection.

So, for normal incidence, the phase accumulated during propagation through the film is given by:

$$\delta_t = \frac{2\pi n_f t_f}{\lambda_0} \tag{5.10}$$

It is important to know that at normal incidence, the phase shift upon reflection depends on the refractive index contrast at the interface. A phase shift of $\delta_r = \pi$ occurs when light reflects from a medium of lower refractive index to a higher one, and no phase shift $(\delta_r = 0)$ occurs when reflecting from a higher to a lower refractive index [182].

If the film's thickness satisfies:

$$t_f = \frac{\lambda_0}{4n_f}, \tag{5.11}$$

then

$$\delta_t = \frac{\pi}{2}, \tag{5.12}$$

which corresponds to a quarter-wave optical thickness. Depending on the refractive index ordering, this condition can lead to destructive interference (anti-reflection coating) or constructive interference (high reflectivity).

For example, if the refractive index of the deposited film (n_f) is higher than the both surrounding medium $(n_0 < n_f > n_s)$, then the reflection at the air-film interface introduces a phase shift of $\delta_{r1} = \pi$. In contrast, the reflection at the film-substrate interface produces $\delta_{r2} = 0$. The total phase difference between the two reflected waves is therefore

$$\delta = \delta_{r2} + 2\delta_t - \delta_{r1} = 0 + 2\frac{\pi}{2} - \pi = 0 \tag{5.13}$$

Since the resulting phase difference is zero, constructive interference occurs. Under these conditions, the structure behaves as a mirror at wavelength λ_0, exhibiting high reflectance. This way, the quarter-wave optical thickness rule (Equation 5.11) is the basis for the development of a Bragg reflector.

Bragg reflector

As previously introduced and illustrated in Figure 5.1, a distributed Bragg reflector consists of alternating quarter-wave layers of high and low refractive indices. Constructive interference of the waves reflected at each interface results in high reflectivity around the Bragg wavelength.

This reflector is a structure composed of N alternating layers of high (n_H) and low (n_L) refractive index, each with a quarter-wave optical thickness. The structure consists of a sequence of interfaces with alternating refractive index contrast (e.g., $n_0 < n_1$, $n_1 > n_2$, ...). Therefore, each reflection contributes constructively at the design wavelength. As a result, the reflected waves add in phase, leading to a progressive increase in reflectance as the number of layer pairs increases [192].

Although the Bragg condition is strictly satisfied at a single wavelength, the mirror exhibits high reflectance over a finite spectral range around the Bragg wavelength. This high-reflectivity band arises from the coherent superposition of multiple reflections within the multilayer stack [194].

The reflection coefficient of the mirror can be obtained by [192, 193]:

$$r = \frac{n_o n_H^{2N} - n_S n_L^{2N}}{n_0 n_H^{2N} + n_S n_L^{2N}}, \tag{5.14}$$

with n_s the refraction index of the substrate and n_0 the refraction index of the air.

Fabry-Perot interferometer

As stated previously and illustrated in Figure 5.1, a Fabry-Perot filter consists of two parallel partially reflecting mirrors separated by a cavity of thickness d.

An incident wave propagating through the interferometer undergoes multiple partial reflections at each mirror. The interference between the multiple transmitted and reflected waves establishes a direct relationship between the cavity thickness and the wavelengths transmitted through the filter.

The electric field of the transmitted wave, assuming equal mirrors on each end of the Fabry-Perot cavity, can be written as [182]:

$$E_T = \frac{t^2 e^{-i\frac{\delta}{2}}}{1 - r^2 e^{-i\delta}} E_I, \tag{5.15}$$

where r and t are the amplitude reflection and transmission coefficients of the mirrors, respectively, and δ is the phase difference accumulated during one round trip inside the cavity. For normal incidence, this phase shift is given by:

$$\delta = \frac{4\pi n d}{\lambda} \tag{5.16}$$

The transmittance of the interferometer is obtained from the Airy formula [182]:

$$T = \frac{I_T}{I_I} = \left|\frac{E_T}{E_I}\right|^2 = \frac{T_{mirror}^2}{(1-R)^2}\left[1 + F\sin^2\left(\frac{\delta}{2}\right)\right]^{-1} \tag{5.17}$$

Considering that $R+T+A=1$ and that absorption losses (A) are negligible for dielectric mirrors, the expression simplifies to [101, 193]

$$T = \left[1 + F\sin^2\left(\frac{\delta}{2}\right)\right]^{-1} \tag{5.18}$$

F is the coefficient of finesse, defined as [182]:

$$F = \frac{4R}{(1-R)^2} \tag{5.19}$$

From Equation 5.18, maximum transmission ($T=1$) occurs when:

$$\delta = 2\pi q, \tag{5.20}$$

where q is an integer. Therefore, the transmitted wavelengths are given by:

$$\lambda_q = \frac{2nd}{q} \tag{5.21}$$

showing that the resonance wavelengths are determined by the cavity thickness d and the interference order q.

The two main parameters characterizing a Fabry-Perot interferometer are the FWHM and the free spectral range (FSR). The FSR corresponds to the phase separation between two consecutive transmission maxima and is given by $\delta_{\text{FSR}} = 2\pi$ [192].

The FWHM is obtained by imposing $T = 1/2$, which yields:

$$\delta_{\text{FWHM}} = 4\arcsin\left(\frac{1}{\sqrt{F}}\right) \tag{5.22}$$

The ratio between the FSR and the FWHM defines the finesse $\mathcal{F}$ [182]:

$$\mathcal{F} = \frac{\delta_{\text{FSR}}}{\delta_{\text{FWHM}}} = \frac{\pi}{2\arcsin\left(\frac{1}{\sqrt{F}}\right)} \tag{5.23}$$

So, an increase in mirror reflectivity reduces the resonance width and an increases the finesse, resulting in higher spectral resolution.

The spectral separation between adjacent transmission peaks in wavelength units (λ_{FSR}) is given by [182]:

$$\lambda_{\text{FSR}} = \lambda_q - \lambda_{q+1} = \frac{\lambda_q}{q+1} \tag{5.24}$$

The FWHM of the q-th order resonance in wavelength units is therefore [182]:

$$\text{FWHM} = \frac{\lambda_q}{q\mathcal{F}} \tag{5.25}$$

A dielectric single-cavity filter can, therefore, be regarded as a Fabry-Perot resonator in which the two mirrors are realized as Bragg reflectors. The design of such a filter requires accurate determination of the individual layer thicknesses so that the Bragg mirrors provide high reflectivity at the target wavelength. The cavity thickness satisfies the resonance condition, ensuring constructive interference at the desired transmission wavelength.

Thus, the key design relations for a Fabry-Perot filter incorporating Bragg reflectors are given by Equations 5.11 and 5.21. These equations define the phase condition for constructive interference and the resonance wavelengths of the cavity, while the Bragg mirrors are formed by a periodic stack of alternating high- and low-refractive index layers.

5.3 Experimental Methods

5.3.1 Optical Filters Design and Simulation

The developed optical filters (Figure 5.3) are based on a Fabry–Perot structure, which consists of an interferometer formed by two parallel, highly reflective mirrors separated by a resonant cavity.

For the filters developed in this work, the interference order was set to $q = 1$. Thin-films of silicon dioxide (SiO_2) and TiO_2 were selected as the low and high-refractive index materials, respectively. These materials were chosen due to their relatively wavelength-independent refractive indices within the spectral range of interest [195, 196] and the extensive expertise available in the MNFabs laboratory (at CMEMS-UMinho) regarding their deposition and use in the fabrication of optical filters.

Each optical filter (one for NAD(P)H fluorescence detection and another for FAD fluorescence detection) was designed with 11 layers, comprising five dielectric layers on each side of a single resonant cavity. The number of layers was selected based on previous work performed by Pimenta *et al.* [146], which demonstrated that this configuration provides an optimal balance between transmittance peak intensity and FWHM. The specific thickness values of the resonant cavity and dielectric layers were determined through calculations, numerical simulations, and optimization procedures, which are presented and discussed in the following section.

Considering the developed design, several optical filters were simulated using the OpenFilters software. Each filter consisted of a multilayer stack with varying layer thicknesses. The specific thickness values

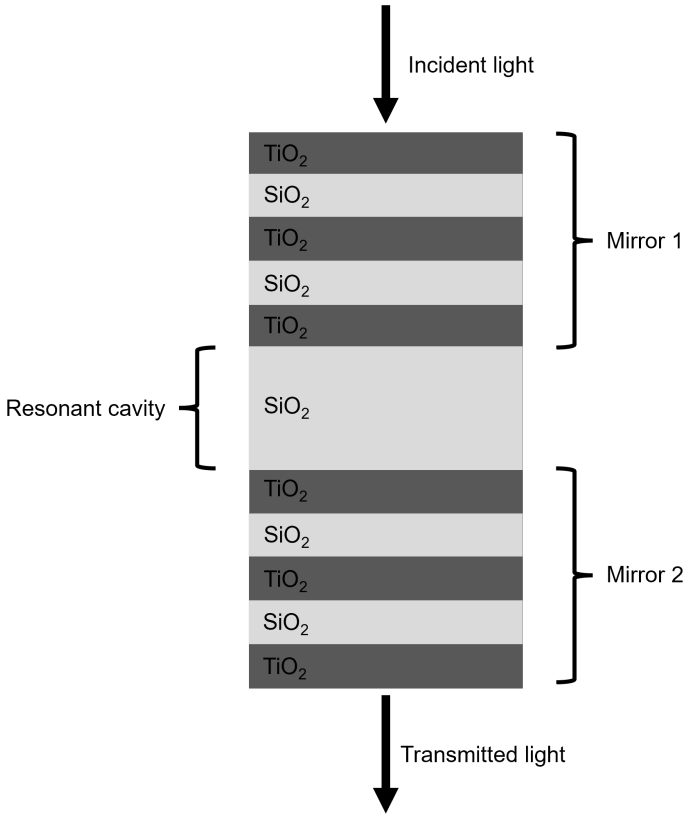


Figure 5.3: Developed optical filters, based on a Fabry–Perot structure.

adopted in each simulation are reported in the next section. For all simulations, the substrate was BK7 glass with a thickness of 1.1 mm. The spectral response was simulated over the wavelength range 300 - 1000 nm, using a wavelength step of 1 nm. The media in front of and behind the filter were assumed to be void.

All simulations were performed under normal incidence and assuming unpolarized illumination. The use of unpolarized light reflects the intended final experimental configuration, in which no polarizing element is placed before signal acquisition to simplify the optical setup. The rotating-analyzer ellipsometer (RAE) model available in OpenFilters was selected for these simulations.

The refractive index dispersion curves for both materials (SiO_2 and TiO_2) were experimentally obtained using a commercial ellipsometer (alpha-SE Ellipsometer, J.A. Woollam Co.). These measurements were performed on single thin-films deposited under the same conditions as those used for the final fabrication of the optical filters, ensuring consistency between simulation and experimental implementation.

In addition to spectral simulations, OpenFilters was employed to optimize the thickness of the resonant cavity layer. To simplify the fabrication process, the mirror layer thicknesses were modified so that both optical filters could be fabricated simultaneously using identical mirror structures. Therefore, the resonant

cavity thickness had to be re-optimized to maintain the transmission peak at the desired wavelength. This optimization was carried out by defining a target wavelength of either 485 nm or 530 nm, with a tolerance of 0.0001 and a target transmittance of unity under unpolarized illumination.

5.3.2 Optical Filters Fabrication

SiO_2 and TiO_2 thin-films were deposited by radio frequency (RF) sputtering, which is a physical vapor deposition technique. This process takes place within a vacuum chamber at low pressure, filled with an inert gas (usually argon (Ar)). A high-voltage alternating current (AC) power source is used to generate energetic waves along the chamber, leading to the ionization of Ar gas, creating Ar^+ ions. These high-energy ions then collide with the target (cathode), sputtering off its atoms that subsequently deposit onto the substrate (anode). RF sputtering is particularly advantageous for dielectric targets, as the alternating current prevents charge accumulation on the nonconductive target surface, ensuring the continuous ionization process [197, 198].

For all tests and studies performed with these materials, SiO_2 thin-films were deposited using a ceramic target (SiO_2, $99.995\,\%$ purity), while TiO_2 thin-films were deposited using a metallic titanium target (Ti, $99.7\,\%$ purity) through a reactive sputtering process in the presence of O_2. Deposition parameters, including applied power, working pressure, and gas flow rate (Ar and O_2), are specified individually for each deposition in the next section, as these conditions were adjusted according to the specific deposition and filter configuration.

The thin-films were deposited on a BK7 substrate (N-BK7, Präzisions Glas and Optik), known for its high purity of raw materials, high transmittance in visible and NIR wavelengths, and low dispersion. Before deposition, the substrate underwent a cleaning process to remove any impurities that could potentially impact the filter's performance. The cleaning procedure involved successive steps, starting with mechanical cleaning using isopropyl alcohol (IPA), followed by an ultrasound cleaning in acetone, and finally rinsing with IPA and distilled water. Subsequently, the substrate was dried using a nitrogen gun to ensure a pristine surface for thin-film deposition. This rigorous cleaning process was essential to ensure the integrity and optimal functioning of the optical filters.

It is important to note that, although the simulation and design processes were developed to enable simultaneous fabrication of the mirrors of both filters, the filters were fabricated separately. This decision was made because certain fabrication steps still require optimization. Nevertheless, the proposed design is compatible with simultaneous fabrication in future implementations.

5.3.3 Optical Filters Characterization

Ellipsometry (alpha-SE Ellipsometer, J.A. Woollam Co.) was employed to characterize single deposited dielectric thin-films (SiO_2 and TiO_2). Before the final optical filter fabrication, these materials were deposited on test substrates (glass or silicon) and characterized to determine their wavelength-dependent refractive indices and to assess possible variations with film thickness. The experimentally obtained refractive index dispersion curves were subsequently used as input parameters in the optical filter simulations.

The ellipsometer operates over a spectral range from 380 nm to 890 nm. Measurements were performed at three angles of incidence, namely $65°$, $70°$, and $75°$. The acquired ellipsometry data were analyzed using a Cauchy dispersion model to extract the refractive index of the thin-films. Each sample was measured three times, and the mean and corresponding standard deviations were calculated.

Accurate determination of the deposited film thickness was also necessary, as it is well known that the thickness indicated by the RF sputtering sensor during deposition may differ slightly from the experimental thickness achieved on the sample. To address this, three independent techniques were employed. First, ellipsometry was used not only to retrieve the optical constants but also to estimate the film thickness. Second, a stylus profilometer (Dektak 150, Veeco) was used to measure the step height of the deposited layers. Finally, samples were cleaved perpendicular to the film surface, and their cross-sectional thickness was analyzed using scanning electron microscopy (SEM) (NanoSEM - FEI Nova 200).

For the ellipsometry and profilometry measurements, thickness values were obtained at three slightly different locations on each sample, and the mean and standard deviation were calculated. For SEM analysis, the sample preparation and acquisition procedures were considerably more time-consuming, so two measurements were performed per sample.

After fabrication, the optical filters were characterized in terms of spectral transmittance and bandwidth using the transmission mode of the same ellipsometer. Transmittance was measured over the range 380-890 nm. The samples were carefully aligned with respect to both the light source and detector to ensure normal (perpendicular) incidence. Each filter was measured three times, and the corresponding mean transmittance spectra were obtained.

5.4 Results and Samples Analysis

5.4.1 Optical Filters Design Calculation

The initial step in the optical filters fabrication consisted of calculating the required thin-film thicknesses. Two optical filters must be implemented: one with a peak transmittance at 485 nm and another at 530 nm; thus, two distinct designs were required.

As previously referred, the filters are based on a Fabry–Perot configuration. Consequently, it is necessary to calculate the thicknesses of the materials forming the Bragg mirrors, and the thickness of the resonant cavity.

485 nm filter

For the filter centered at 485 nm, the Bragg mirrors consist of three TiO_2 layers interleaved with two SiO_2 layers. The thickness of each layer was determined according to the quarter-wave condition, given by Equation 5.11. Using a refractive index of $n_{SiO_2}(\lambda = 485\,\text{nm}) = 1.47$ [8], the thickness of the SiO_2 mirror layers is given by:

$$d_{SiO_2} = \frac{485\,\text{nm}}{4 \times 1.47} = 82.53\,\text{nm} \tag{5.26}$$

Similarly, using $n_{TiO_2}(\lambda = 485\,\text{nm}) = 2.50$ [9], the thickness of the TiO_2 mirror layers is given by:

$$d_{TiO_2} = \frac{485\,\text{nm}}{4 \times 2.50} = 48.46\,\text{nm} \tag{5.27}$$

After determining the thicknesses of the mirror layer, the thickness of the resonant cavity was calculated. The cavity, composed of SiO_2, was designed according to the half-wave condition described in Equation 5.21. Using the same refractive index value for SiO_2, the cavity thickness is:

$$d_{SiO_2} = \frac{485\,\text{nm}}{2 \times 1.47} = 165.07\,\text{nm} \tag{5.28}$$

Table 5.1 summarizes the complete multilayer structure and the corresponding thin-film thicknesses for the filter with a peak transmittance at 485 nm.

Table 5.1: Thicknesses of the SiO_2/TiO_2 thin-film multilayer for the optical filter with 485 nm transmittance peak.

Thin-film	Thickness (nm)
TiO_2	48.46
SiO_2	82.53
TiO_2	48.46
SiO_2	82.53
TiO_2	48.46
SiO_2 (resonant cavity)	165.07
TiO_2	48.46
SiO_2	82.53
TiO_2	48.46
SiO_2	82.53
TiO_2	48.46

530 nm filter

For the filter centered at 530 nm, the same design methodology was applied. The Bragg mirrors are again composed of alternating TiO_2 and SiO_2 layers, and thicknesses were calculated using Equation 5.11.

Using a refractive index of $n_{SiO_2}(\lambda = 530\,\text{nm}) = 1.47$ [8], the thickness of the SiO_2 mirror layers is:

$$d_{SiO_2} = \frac{530\,\text{nm}}{4 \times 1.47} = 90.33\,\text{nm}. \tag{5.29}$$

Using $n_{TiO_2}(\lambda = 530\,\text{nm}) = 2.46$ [9], the thickness of the TiO_2 mirror layers is:

$$d_{TiO_2} = \frac{530\,\text{nm}}{4 \times 2.46} = 53.81\,\text{nm}. \tag{5.30}$$

The thickness of the SiO_2 resonant cavity was calculated using the half-wave condition (Equation 5.21), yielding:

$$d_{SiO_2} = \frac{530\,\text{nm}}{2 \times 1.47} = 180.65\,\text{nm}. \tag{5.31}$$

Table 5.2 summarizes the complete multilayer structure and the corresponding thin-film thicknesses for the filter with a peak transmittance at 530 nm.

Table 5.2: Thicknesses of the SiO_2/TiO_2 thin-film multilayer for the optical filter with 530 nm transmittance peak.

Thin-film	**Thickness (nm)**
TiO_2	53.81
SiO_2	90.33
TiO_2	53.81
SiO_2	90.33
TiO_2	53.81
SiO_2 (resonant cavity)	180.65
TiO_2	53.81
SiO_2	90.33
TiO_2	53.81
SiO_2	90.33
TiO_2	53.81

5.4.2 Experimental Refractive Indices and Optical Filters Optimization

Since the refractive index of a thin-film can depend on deposition conditions and technique, and may also vary with film thickness, it is essential to experimentally determine the refractive indices of the thin-films TiO_2 and SiO_2 fabricated in the MNFabs laboratory for further optimization of the optical filters design.

Accordingly, a set of reference thin-films was deposited and subsequently characterized in terms of thickness and refractive index. Two SiO_2 thin-films of significantly different thicknesses (± 170 nm, and ± 80 nm), corresponding to two distinct thicknesses close to the required ones for design of the optical filters previously presented (mirrors and resonance cavities). One TiO_2 thin-film with a thickness comparable to that required for the mirrors of the filters (± 47 nm) was also deposited. This approach enables a more accurate determination of the refractive index values relevant to this work. Table 5.3 shows the deposition conditions for those three thin-films.

The thicknesses of the deposited thin- films were subsequently measured using three techniques: ellipsometry, profilometry, and SEM. The measured thickness values obtained with each technique are presented in Table 5.4.

Overall, the experimental values are close to the expected ones. From Table 5.4, it can be concluded that, in all cases, the profilometer measurements are slightly lower than those obtained using the other

Table 5.3: RF sputtering deposition conditions for SiO_2 thin-films (sample S1 (with ± 170 nm; sample S2 with ± 80 nm) and TiO_2 thin-film (sample T1 with ± 47 nm).

Sample	S1	S2	T1
Target	SiO_2	SiO_2	Ti
Power	150 W	150 W	200 W
Ar flux	15 sccm	15 sccm	10 sccm
O_2 flux	–	–	2 sccm
Working pressure	2×10^{-3} mbar	2×10^{-3} mbar	4×10^{-3} mbar
Deposition time	34 min	27 min	53 min

Table 5.4: Experimental thicknesses of SiO_2 thin-films (samples S1 and S2), and TiO_2 thin-film (sample T1), obtained using different characterization techniques.

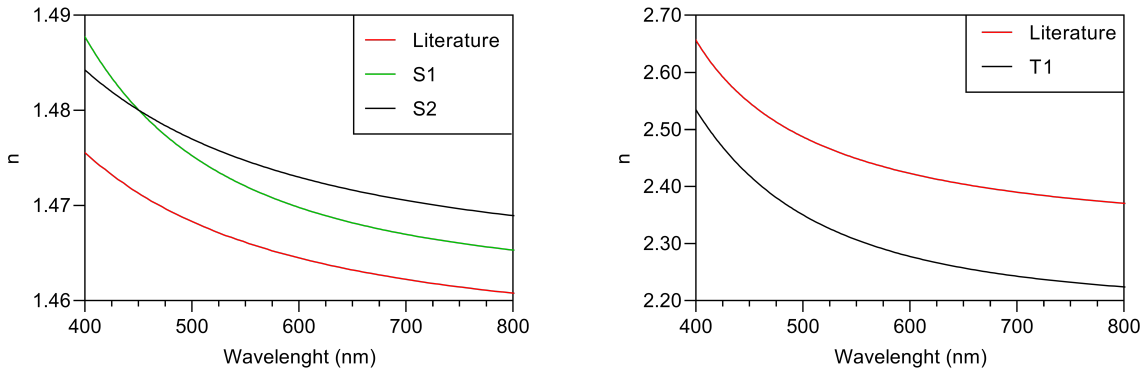
Sample	S1	S2	T1
Ellipsometer	$159.12\,\text{nm} \pm 2.75\,\text{nm}$	$80.43\,\text{nm} \pm 0.07\,\text{nm}$	$43.29\,\text{nm} \pm 0.01\,\text{nm}$
Profilometer	$112.00\,\text{nm} \pm 8.17\,\text{nm}$	$76.50\,\text{nm} \pm 1.23\,\text{nm}$	$40.28\,\text{nm} \pm 1.21\,\text{nm}$
SEM	$149.35\,\text{nm} \pm 0.75\,\text{nm}$	$80.15\,\text{nm} \pm 1.45\,\text{nm}$	$53.20\,\text{nm} \pm 2.20\,\text{nm}$

techniques. This may occur because the profilometer measurements are not performed at the center, but instead in the periphery of the sample. Considering ellipsometry measurements, the results are obtained from mathematical models of approximation, with some associated errors. Finally, the SEM technique can be considered the more reliable measurement, since the thin-film is cleaved and analyzed in cross-section.

The refractive indices of SiO_2 and TiO_2 thin-films were measured using ellipsometry (alpha-SE Ellipsometer, J.A. Woollam Co.). The measured curves are presented in Figure 5.4.

The refractive index dispersion of the deposited SiO_2 thin-films exhibits a similar trend to that reported in the literature [8], although slightly higher refractive index values are observed. Such deviations are commonly reported for sputtered thin-films, and can be attributed to differences in deposition conditions, film density, and internal stress, which influence the optical polarizability of the material.

Additionally, for wavelengths above approximately 450 nm, the thicker SiO_2 film (Sample S1) presents a slightly lower refractive index compared to the thinner film. This behavior can be associated with thickness-dependent growth effects in RF sputtering, including stress relaxation and microstructural evolution with increasing film thickness, which may lead to a reduced effective density and, consequently, a lower refrac-



(a) (b)

Figure 5.4: Refractive index as a function of wavelength for: (a) SiO_2 thin-films (samples S1 and S2, and literature sample [8]); and (b) TiO_2 thin-film (sample T1 and literature sample [9]).

tive index.

Similarly, the refractive index dispersion of the deposited TiO_2 thin-film shows good agreement with the general trend reported in the literature [9], although slightly lower refractive index values are obtained. As in the case of SiO_2, these differences are commonly observed in sputtered thin-films and can be attributed to the same variations that influence the optical response of the material.

The experimental refractive indices for the SiO_2 and TiO_2 thin-films were then used for the design optimization of the optical filters.

485 nm filter

For the Bragg mirrors of the $485\,\text{nm}$ filter, the quarter-wave condition given by Equation 5.11 was applied. Using the refractive index extracted from the experimental dispersion curve for SiO_2, $n_{SiO_2}(\lambda = 485\,\text{nm}) = 1.48$ (sample S2), the thickness of the SiO_2 mirror layers is given by:

$$d_{SiO_2} = \frac{485\,\text{nm}}{4 \times 1.48} = 82.05\,\text{nm} \tag{5.32}$$

Using the same equation and the experimentally determined refractive index for TiO_2, $n_{TiO_2}(\lambda = 485\,\text{nm}) = 2.3672$ (sample T1), the thickness of the TiO_2 mirror layers is:

$$d_{TiO_2} = \frac{485\,\text{nm}}{4 \times 2.37} = 51.22\,\text{nm} \tag{5.33}$$

The thickness of the resonant cavity, composed of SiO_2, was calculated using the half-wave condition given by Equation 5.21. Using the refractive index obtained from the dispersion curve, $n_{SiO_2}(\lambda = 485\,\text{nm}) =$

1.48 (sample S1), the cavity thickness is:

$$d_{SiO_2} = \frac{485\,\text{nm}}{2 \times 1.48} = 164.25\,\text{nm} \tag{5.34}$$

The thickness values for all the layers of this filter are summarized in Table 5.5.

Table 5.5: Thicknesses of the SiO_2/TiO_2 thin-films multilayer, for the 485 nm transmittance peak optical filter, with the experimental refractive index values.

Thin-film	**Thickness (nm)**
TiO_2	51.22
SiO_2	82.05
TiO_2	51.22
SiO_2	82.05
TiO_2	51.22
SiO_2 (resonant cavity)	164.25
TiO_2	51.22
SiO_2	82.05
TiO_2	51.22
SiO_2	82.05
TiO_2	51.22

530 nm filter

The same design procedure was applied to the filter with a target peak wavelength of 530 nm. For the Bragg mirrors, the quarter-wave condition (Equation 5.11) was used together with the experimentally determined refractive index values.

Using $n_{SiO_2}(\lambda = 530\,\text{nm}) = 1.48$ (sample S2), the thickness of the SiO_2 mirror layers is:

$$d_{SiO_2} = \frac{530\,\text{nm}}{4 \times 1.48} = 89.80\,\text{nm} \tag{5.35}$$

Using the refractive index of TiO_2 at this wavelength, $n_{TiO_2}(\lambda = 530\,\text{nm}) = 2.3211$ (sample T1), the corresponding mirror layer thickness is:

$$d_{TiO_2} = \frac{530\,\text{nm}}{4 \times 2.32} = 57.09\,\text{nm} \tag{5.36}$$

Finally, the thickness of the SiO_2 resonant cavity was calculated using the half-wave condition (Equation 5.21). With $n_{SiO_2}(\lambda = 530\,\text{nm}) = 1.47$ (sample S1), the cavity thickness is:

$$d_{SiO_2} = \frac{530\,\text{nm}}{2 \times 1.47} = 179.89\,\text{nm} \tag{5.37}$$

The thickness values for all the layers of this filter are summarized in Table 5.6.

Table 5.6: Thicknesses of the SiO_2/TiO_2 thin-films multilayer, for the 530 nm transmittance peak optical filter, with the experimental refractive index values.

Thin-film	**Thickness (nm)**
TiO_2	57.09
SiO_2	89.80
TiO_2	57.09
SiO_2	89.80
TiO_2	57.09
SiO_2 (resonant cavity)	179.89
TiO_2	57.09
SiO_2	89.80
TiO_2	57.09
SiO_2	89.80
TiO_2	57.09

5.4.3 Optical Filters Design Simplification

One effective strategy to reduce fabrication cost and processing time is to use identical Bragg mirror thicknesses for both filters, allowing the mirrors to be fabricated simultaneously in a single deposition run. This approach ensures identical deposition conditions for both devices, improves reproducibility, and reduces overall fabrication complexity and cost. To compensate for the fixed mirror design, the resonant cavity thickness is subsequently optimized for each filter. This strategy preserves the transmittance peak at the desired wavelength while maintaining a narrow FWHM.

Accordingly, the mirror layer thicknesses were fixed at 85 nm for SiO_2 and 55 nm for TiO_2. These values were selected because they are close to the theoretically calculated thicknesses for both filters.

Subsequently, the OpenFilters software was used to optimize the resonant cavity thickness for each

filter. The final thicknesses for each optical filter are summarized in Tables 5.7 and 5.8.

Table 5.7: Thicknesses of the SiO_2/TiO_2 thin-films multilayer, for the optical filter with 485 nm transmission peak, after design optimization and simplification.

Thin-film	**Thickness (nm)**
TiO_2	55.00
SiO_2	85.00
TiO_2	55.00
SiO_2	85.00
TiO_2	55.00
SiO_2 (resonant cavity)	149.78
TiO_2	55.00
SiO_2	85.00
TiO_2	55.00
SiO_2	85.00
TiO_2	55.00

Table 5.8: Thicknesses of the SiO_2/TiO_2 thin-films multilayer, for the 530 nm transmittance peak optical filter, after design optimization and simplification.

Thin-film	**Thickness (nm)**
TiO_2	55.00
SiO_2	85.00
TiO_2	55.00
SiO_2	85.00
TiO_2	55.00
SiO_2 (resonant cavity)	191.32
TiO_2	55.00
SiO_2	85.00
TiO_2	55.00
SiO_2	85.00
TiO_2	55.00

After defining the thin-film thicknesses, the transmittance of both filters was simulated using the Open-Filters software. The results are presented in Figure 5.5 and Table 5.9. Two simulation configurations were considered, one using the optimized design with identical Bragg mirrors and adjusted resonant cavities, and another using the thicknesses calculated in the previous section with individually designed mirrors.

From the simulated spectra, it can be observed that the transmittance of both filters increases rapidly for wavelengths above approximately 650 nm. For this reason, it is necessary to include a short-pass filter in the setup with a cut-off wavelength of around 650 nm, preventing residual light from the excitation laser in the detection sensor.

At wavelengths below 400 nm, both filters exhibit high transmittance. However, biological tissues do not typically emit significant fluorescence signals in this spectral region. The main optical signal expected

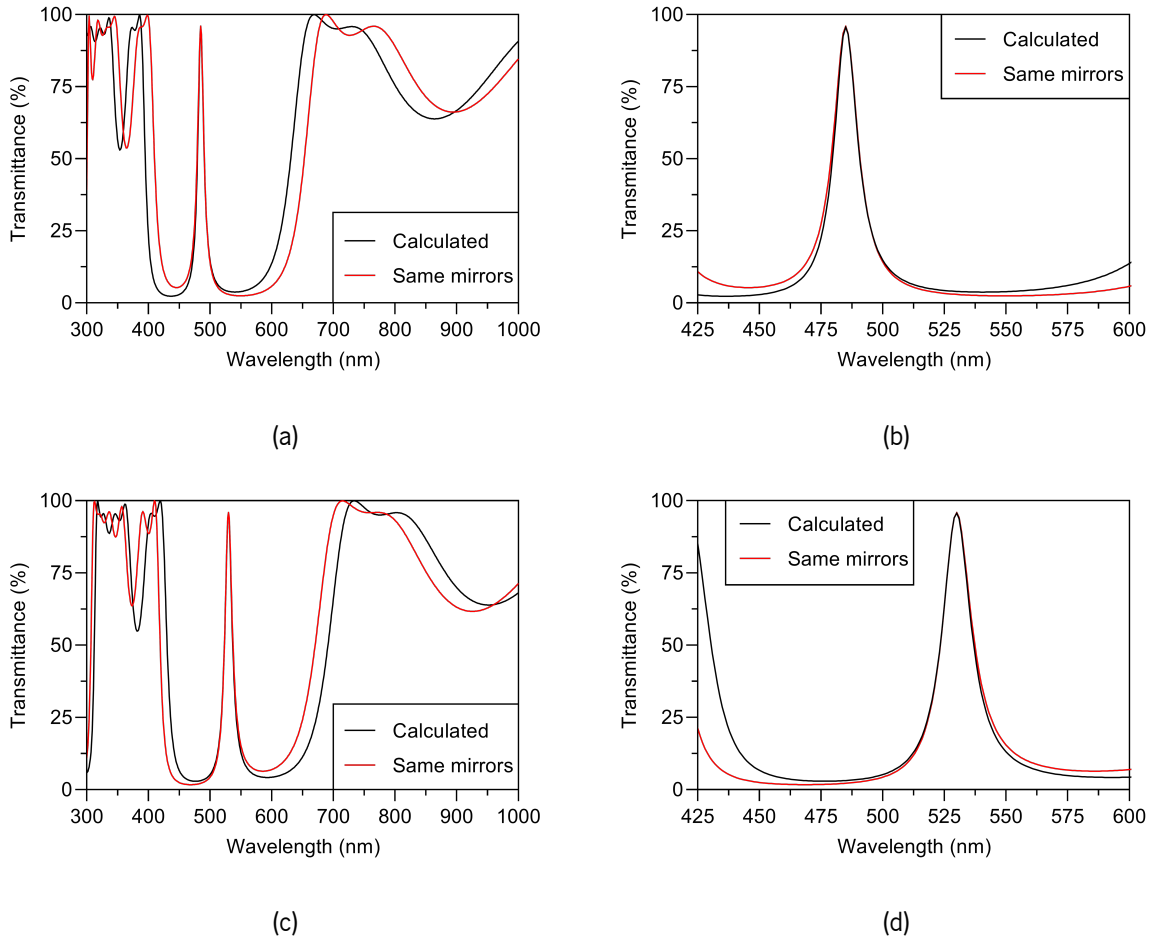


Figure 5.5: Simulated transmittance spectra of the Fabry–Perot filters: (a) broadband transmittance of the 485 nm filter; (b) transmittance of the 485 nm filter in the ROI; (c) broadband transmittance of the 530 nm filter; (d) transmittance of the 530 nm filter in the ROI. Black curves correspond to the individually calculated mirror design, while red curves represent the optimized designs using identical mirror thicknesses.

Table 5.9: FWHM values for the designed optical filters, considering the individually calculated mirror design and optimized design using identical mirror thicknesses.

Filter	FWHM (nm)
485 nm, calculated	11.34
485 nm, same mirrors	12.00
530 nm, calculated	13.78
530 nm, same mirrors	14.38

below 400 nm under 750 nm excitation is SHG, which occurs at 375 nm and is commonly associated with collagen fibers. Consequently, future tissue measurements should include a long-pass filter with a cut-off wavelength of around 400 nm to prevent SHG signals from contaminating fluorescence measurements. It should be noted that, for the phantom measurements performed in this work, such a filter is not required, because the phantoms do not contain collagen fibers.

For the 485 nm filter, both configurations exhibit very similar peak transmittance profiles, with only minor differences observed in the spectral tails. These differences are not expected to affect the filter performance. In terms of spectral bandwidth, the FWHM values are also very close. The slight increase in bandwidth indicates a marginal reduction in spectral selectivity. However, the difference is small and is not expected to compromise the filter's ability to discriminate between the fluorescence signals of interest.

The 530 nm filter also presents a similar peak transmittance in both configurations. However, differences are observed for wavelengths below approximately 450 nm. In the configuration using identical mirrors, the transmittance begins to increase at slightly shorter wavelengths, which could potentially reduce crosstalk from NAD(P)H fluorescence compared to the alternative configuration. Therefore, this configuration is more effective at selectively filtering the signals. As a result, this configuration provides improved spectral discrimination between fluorescence signals. Regarding the spectral bandwidth, although the identical mirror configuration presents a slightly broader bandwidth, this increase is relatively small and does not significantly compromise selectivity.

5.4.4 Second-order Resonant Cavity

The RF sputtering system used in this work presents limitations in the precise control of deposited layer thickness. While thickness variations in the Bragg mirror layers have only a moderate effect on the final filter performance, variations in the resonant cavity thickness have a much stronger influence on the position of

the transmittance peak. Consequently, although the 485 nm filter could be successfully fabricated despite these equipment limitations, several attempts to fabricate the 530 nm filter did not yield the desired spectral response. To address this issue, a second-order resonant cavity was adopted for the 530 nm filter. This approach is advantageous because higher-order Fabry–Perot resonances are less sensitive to variations in cavity thickness, resulting in more stable resonance wavelengths.

According to the Fabry–Perot resonance condition given by Equation 5.21, for a first-order cavity ($q = 1$), the resonance condition reduces to $\lambda = 2nd$, implying that small deviations in cavity thickness lead to relatively large shifts in the transmittance peak. In contrast, for a second-order cavity ($q = 2$), the relation becomes $\lambda = nd$, reducing the sensitivity of the resonance wavelength to thickness variations by a factor of two. Consequently, identical thickness deviations result in significantly smaller shifts of the peak transmittance wavelength, improving fabrication robustness.

Accordingly, a new resonant cavity thickness for the 530 nm filter was calculated using Equation 5.21, this time adopting a second-order resonance ($q = 2$). Using the refractive index extracted from the experimental dispersion curve shown in Figure 5.4(a), $n_{SiO_2}(\lambda = 530\,\text{nm}) = 1.47$ (sample S1), the corresponding SiO_2 cavity thickness is given by:

$$d_{SiO_2} = \frac{2 \times 530\,\text{nm}}{2 \times 1.47} = 359.79\,\text{nm} \tag{5.38}$$

After the analytical calculations, and to maintain identical Bragg mirrors for both filters, a numerical optimization was performed using the OpenFilters software. As a result, the final resonant cavity thickness for the 530 nm filter was set to 371.20 nm, accounting for the influence of the Bragg mirrors and ensuring optimal spectral performance. The final layers for the 530 nm filter are shown in Table 5.10.

Following the redefinition of the resonant cavity thickness, the updated filter design was simulated using OpenFilters software, and the results were compared with the initial configuration, as shown in Figure 5.6. The revised 530 nm filter (530 nm Filter v2) maintains a peak transmittance comparable to the initial design, while achieving a significant reduction in FWHM, from 14.38 nm to 10.50 nm, thereby improving spectral selectivity.

However, at wavelengths below approximately 450 nm, the revised filter (Filter v2) shows increased transmission compared to the first configuration (Filter v1), which could potentially increase the crosstalk from NAD(P)H fluorescence. Nevertheless, analysis of the fluorescence spectra (Figure 4.13) indicates that NAD(P)H emission in this wavelength range is far from its peak intensity, suggesting that its contribution is likely minimal. Therefore, the filter design employing identical Bragg mirrors is expected to be suitable for this application, although further experimental validation is required.

Table 5.10: Thicknesses of the SiO_2/TiO_2 thin-films multilayer, for the 530 nm transmittance peak optical filter with a second-order resonance cavity after design optimization, and simplification.

Thin-film	**Thickness (nm)**
TiO_2	55.00
SiO_2	85.00
TiO_2	55.00
SiO_2	85.00
TiO_2	55.00
SiO_2 (resonant cavity)	371.20
TiO_2	55.00
SiO_2	85.00
TiO_2	55.00
SiO_2	85.00
TiO_2	55.00

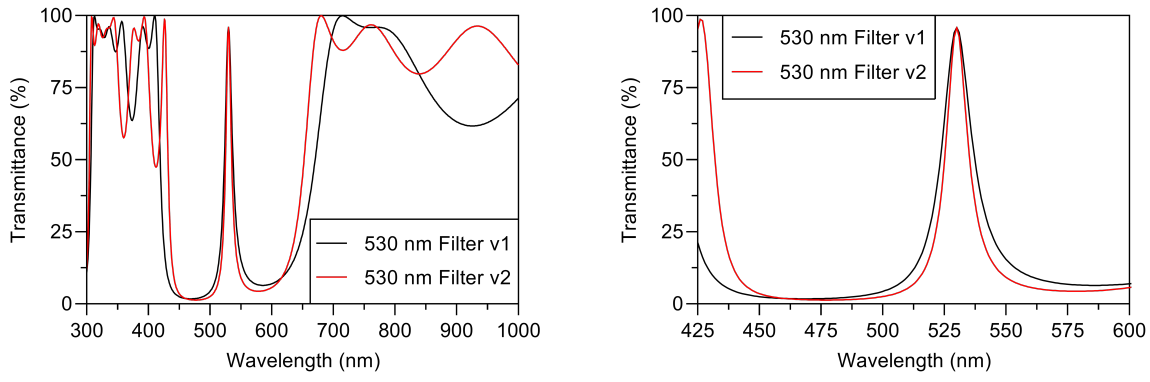
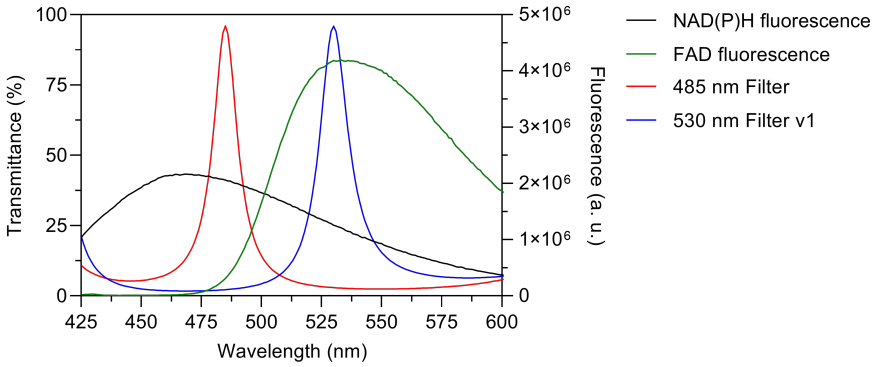


Figure 5.6: Comparison between the simulated transmittance spectra of the 530 nm filter versions: (a) broadband transmittance comparison between version 1 (first order cavity) and version 2 (second order cavity); (b) detailed view of the transmittance spectra in the ROI.

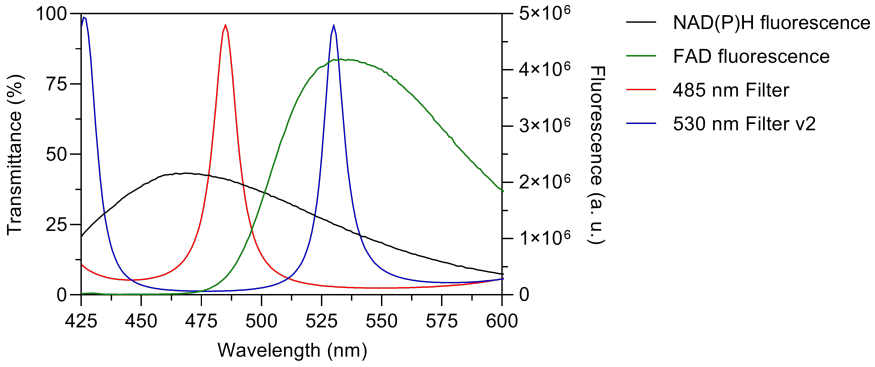
5.4.5 Expected Optical Filters Performance in Fluorescence Measurements

Some uncertainty remained regarding the practical applicability of the filters and whether the fluorescence crosstalk between channels was sufficiently low. Thus, additional analyses were performed. Accordingly, Figures 5.7 and 5.8 show the simulated transmittance curves of the filters overlaid with the 1PEF and 2PEF spectra of NAD(P)H and FAD.

The analysis of Figure 5.7(a) shows that the first-order 530 nm filter (v1) exhibits a peak transmittance wavelength close to the maximum emission of the FAD fluorophore. Although a contribution from NAD(P)H fluorescence is also present at the filter's peak transmittance wavelength, it is important to note that these wavelengths are far from the maximum emission peak of NAD(P)H. Moreover, the fluorescence intensity of NAD(P)H is nominally much lower than that of FAD in this spectral region. Consequently, this filter configuration is expected to be suitable for isolating the FAD signal. The 485 nm filter also presents a

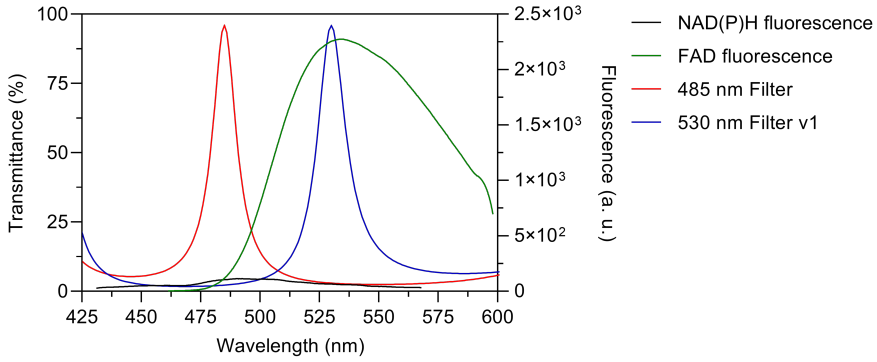


(a)

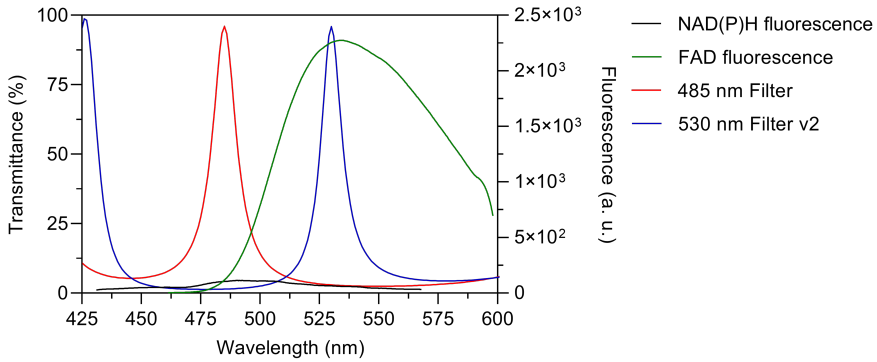


(b)

Figure 5.7: 1PEF spectra of NAD(P)H and FAD overlaid with the simulated transmittance spectra of the optical filters: (a) 485 nm filter and version 1 of the 530 nm filter; (b) 485 nm filter and version 2 of the 530 nm filter.



(a)



(b)

Figure 5.8: 2PEF spectra of NAD(P)H and FAD overlaid with the simulated transmittance spectra of the optical filters: (a) 485 nm filter and version 1 of the 530 nm filter; (b) 485 nm filter and version 2 of the 530 nm filter.

peak transmittance close to the 1PEF emission maximum of NAD(P)H. In this case, the contribution of FAD fluorescence within the passband of the filter is minimal, indicating effective spectral separation for NAD(P)H detection. It should be emphasized that, due to the partial overlap of the fluorescence spectra, it is not possible to eliminate spectral crosstalk. Instead, the objective is to reduce crosstalk to an acceptable level.

The analysis of Figure 5.7(b), which corresponds to the second-order 530 nm filter (v2), leads to the same conclusions with respect to the peak transmittance position. However, it is also observed that, for wavelengths below approximately 450 nm, this filter exhibits higher transmittance compared to version 1. In this wavelength region, a 1PEF contribution from NAD(P)H is still present. Nevertheless, when compared with the 1PEF of FAD, the contribution of NAD(P)H is significantly lower. Consequently, it is not expected that this residual contribution will compromise the intended fluorescence analysis. Even so, further experimental validation is required to assess the impact of this increased short-wavelength

transmittance.

Regarding the 2PEF analysis (Figure 5.8), it can be observed that the 485 nm filter response's peak transmittance does not completely overlap with the maximum of the 2PEF emission of NAD(P)H. Nevertheless, the selection of the filter passband was based on a compromise established through spectral analysis. At the peak of the 2PEF emission of NAD(P)H, the contribution of FAD fluorescence remains significant, as the 2PEF peak intensity of FAD is approximately 15 times higher than that of NAD(P)H. Consequently, even though the emission maxima of NAD(P)H and FAD are spectrally separated, the substantially higher 2PEF intensity of FAD results in a non-negligible contribution within the detection band. Thus, the selected filter wavelength represents a trade-off between maximizing NAD(P)H signal transmission and minimizing crosstalk from FAD fluorescence. At the peak transmittance wavelength, the 2PEF of FAD is reduced to 10 % of the maximum.

The analysis of version 1 of the 530 nm filter shows that the peak transmittance is closely aligned with the maximum of the 2PEF emission of FAD. Within the filter passband, the contribution from NAD(P)H fluorescence is residual. Version 2 of the 530 nm filter exhibits a similar behavior, with the main difference being a higher transmittance at wavelengths below approximately 450 nm, as discussed earlier. However, since the peak 2PEF intensity of NAD(P)H is approximately 15 times lower than that of FAD, this additional short-wavelength transmission is not expected to significantly affect the fluorescence measurements. Consequently, the use of this filter configuration is not expected to compromise the proposed analysis.

As a final step in the analysis, the transmittance curves of the filters were multiplied by the 1PEF spectra of both fluorophores (Figure 5.9), as well as by the 2PEF spectra (Figure 5.10). This procedure allows a direct visual assessment of the relative contribution of each fluorophore within the passband of each filter.

For the 485 nm filter, which was designed to selectively transmit NAD(P)H fluorescence, the analysis of Figure 5.9(a) shows that a substantial fraction of the 1PEF signal from NAD(P)H is transmitted through the filter. In contrast, only the residual 1PEF signal from FAD is transmitted. Although this residual contribution increases slightly at longer wavelengths, it remains comparatively small and is not expected to significantly affect the selective detection of NAD(P)H fluorescence.

For the first-order 530 nm Filter (v1), which was designed to selectively transmit FAD fluorescence, the analysis of Figure 5.9(b) shows strong transmission of the 1PEF signal from FAD, as intended. A contribution from NAD(P)H fluorescence is also observed, occurring both at the filter's peak transmittance wavelength and as a secondary feature around 415 nm. However, these NAD(P)H contributions are

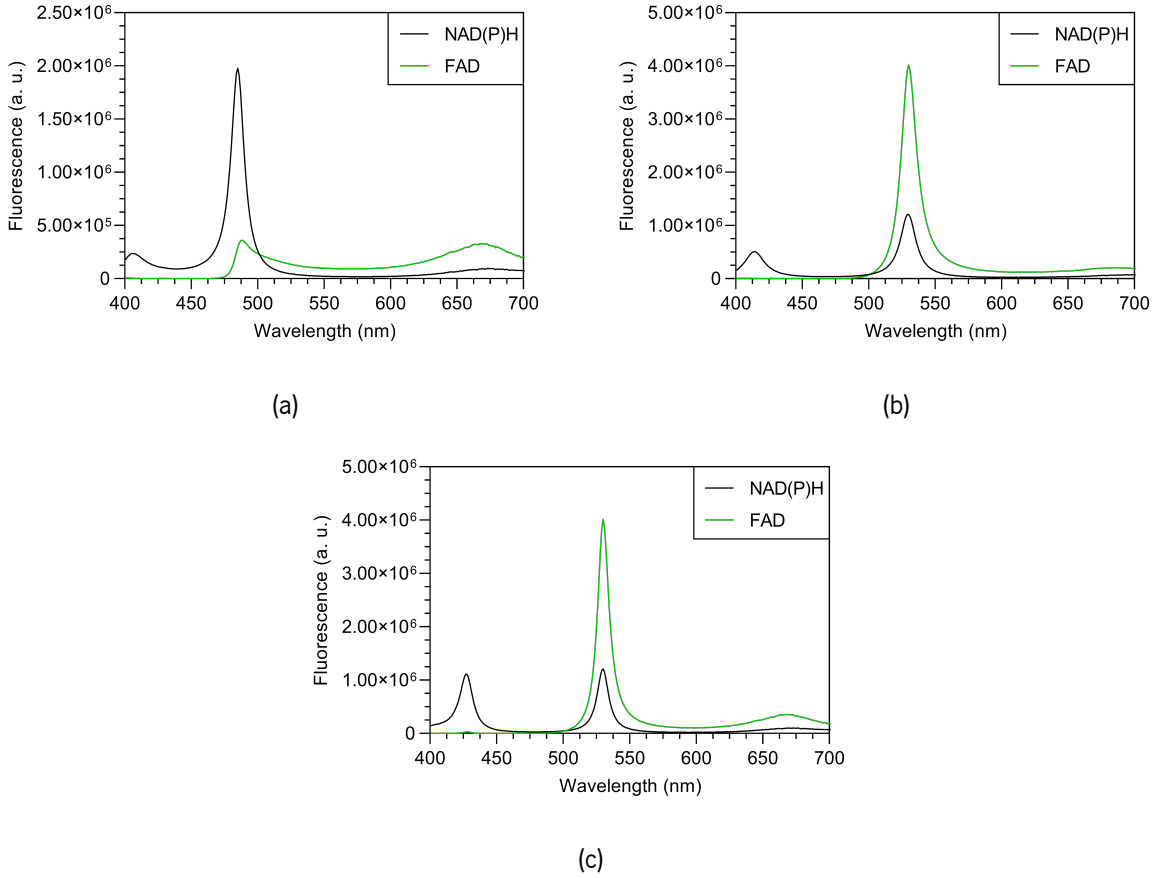


Figure 5.9: Product between the filter transmittance spectra and the 1PEF spectra of NAD(P)H and FAD, illustrating the effective spectral contribution of each fluorophore after filtering: (a) 485 nm filter; (b) first-order 530 nm filter, v1; (c) second-order 530 nm filter, v2.

relatively small when compared with the 1PEF signal from FAD. Consequently, they are not expected to compromise the selective detection of FAD fluorescence.

The analysis of Figure 5.9(c), corresponding to the second-order 530 nm filter (v2), leads similar conclusions. The main difference is a slightly higher transmission of NAD(P)H fluorescence around 415 nm. However, even in this case, the intensity of the transmitted NAD(P)H signal remains substantially lower than that of the FAD fluorescence. Consequently, the second-order filter (v2) is also expected to be suitable for selective FAD detection, although additional experimental validation would be beneficial.

The analysis of the 485 nm filter applied to the 2PEF spectra (Figure 5.10(a)) shows that the contribution from NAD(P)H remains significant, as observed in the 1PEF case. However, a major limitation becomes evident under 2PEF excitation. In this regime, a pronounced FAD contribution is observed, with a strong 2PEF peak intensity. Therefore, a substantial contribution from FAD fluorescence is transmitted through this filter, exceeding the contribution from NAD(P)H. This contribution is present not only at the filter's peak

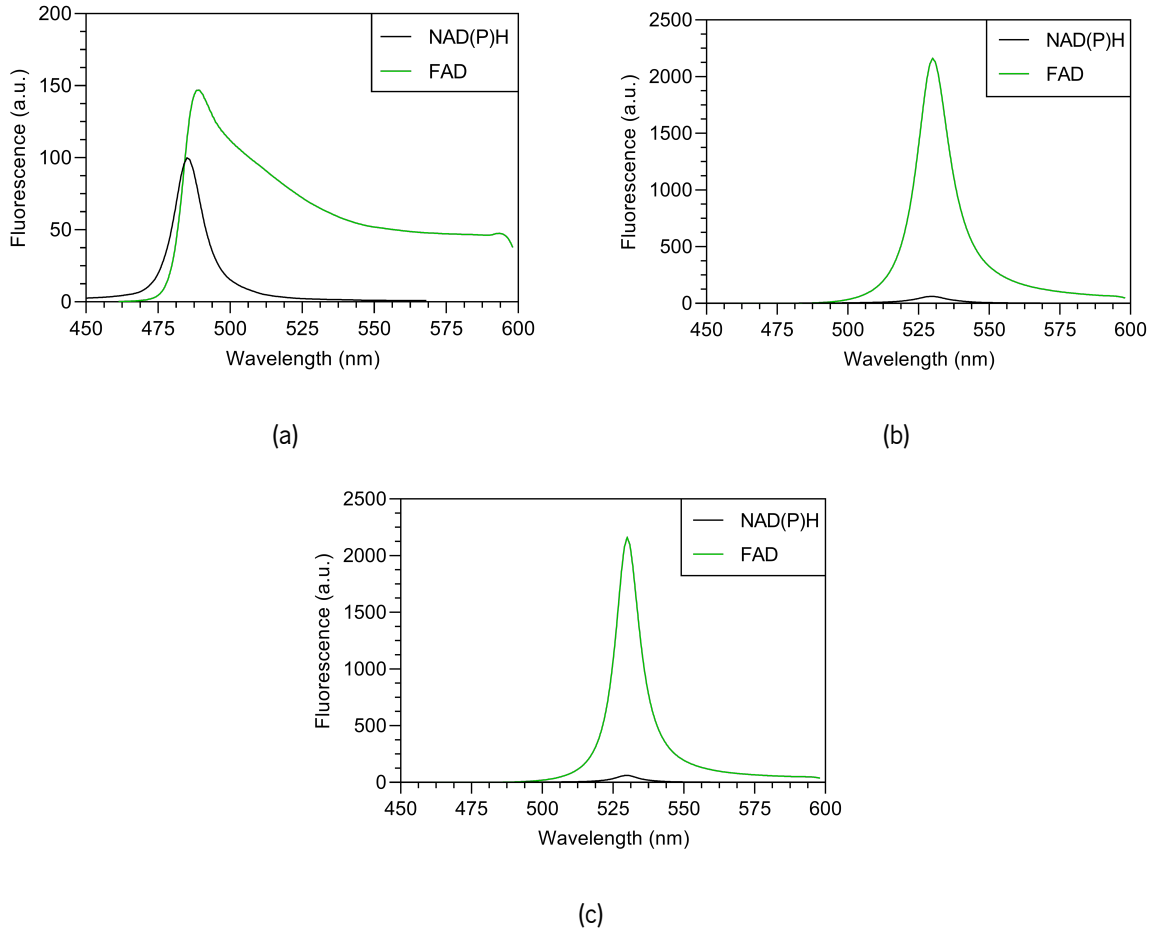


Figure 5.10: Product between the simulated filter transmittance spectra and the 2PEF spectra of NAD(P)H and FAD, illustrating the effective spectral contribution of each fluorophore after filtering: (a) 485 nm filter; (b) first-order 530 nm filter, v1; (c) second-order 530 nm filter, v2.

transmittance wavelength, but also at longer wavelengths. Thus, as discussed in previous sections, the inclusion of an additional short-pass filter to suppress part of this undesired signal is required.

An alternative approach to reduce FAD crosstalk would be to shift the filter passband towards shorter wavelengths. However, at shorter wavelengths, the NAD(P)H emission intensity decreases significantly, reducing the detected NAD(P)H signal and further complicating reliable detection. No single configuration provides an optimal solution, and the filter design necessarily represents a compromise between maximizing NAD(P)H signal transmission and minimizing FAD crosstalk. The practical suitability of the filter for 2PEF measurements must ultimately be assessed experimentally, as the optimal configuration depends on the balance between these competing contributions rather than on a single ideal design.

The analysis of the 530 nm filters (Figures 5.10(b) and 5.10(c)), designed to detect FAD fluorescence, shows a strong transmission of the FAD signal for both filter versions. In contrast, only a residual contribu-

tion from NAD(P)H fluorescence is observed. Consequently, this filter configuration is well-suited for the selective detection of FAD fluorescence in the present application.

5.4.6 Optical Filters Fabrication and Characterization

Following the complete analytical and numerical evaluation, both filters were fabricated using RF sputtering to deposit the required thin-film multilayer structures. The deposition conditions were carefully controlled to achieve the target layer thicknesses, thereby enabling the fabrication of filters with the desired spectral characteristics.

For the fabrication of the 485 nm filter, the deposition conditions are listed in Table 5.11, and for the 530 nm filter, the deposition conditions are listed in Table 5.12 .

After fabrication, the filters' transmittance was measured. The corresponding results are presented in

Table 5.11: RF sputtering deposition conditions for the fabrication of the 485 nm filter.

Layer	**Mirror**		**Resonant cavity**
	SiO_2	**TiO_2**	
Target	SiO_2	Ti	SiO_2
Power	150 W	200 W	150 W
Ar flux	15 sccm	10 sccm	15 sccm
O_2 flux	–	2 sccm	–
Working Pressure	2×10^{-3} mbar	4×10^{-3} mbar	2×10^{-3} mbar
Deposition time	17 min	45 min	39 min

Table 5.12: RF sputtering deposition conditions for thin-film for the fabrication of the 530 nm filter.

Layer	**Mirror**		**Resonant cavity**
	SiO_2	**TiO_2**	
Target	SiO_2	Ti	SiO_2
Power	150 W	200 W	150 W
Ar flux	15 sccm	10 sccm	15 sccm
O_2 flux	–	2 sccm	–
Working Pressure	2×10^{-3} mbar	4×10^{-3} mbar	2×10^{-3} mbar
Deposition time	17 min	45 min	90 min

Table 5.13: Experimental FWHM values for the fabricated filters.

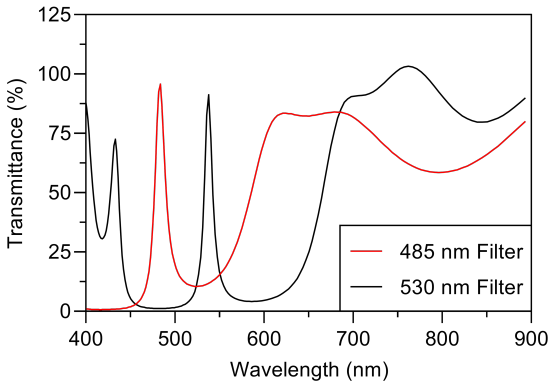
Filter	Experimental FWHM (nm)	Simulated FWHM (nm)
485 nm Filter	13.89	12.00
530 nm Filter	10.73	10.50

Table 5.13 and Figure 5.11(a). Figures 5.11(b) and 5.11(c) show a comparison between the experimentally measured transmittance curves of the fabricated filters and the corresponding simulated transmittance spectra.

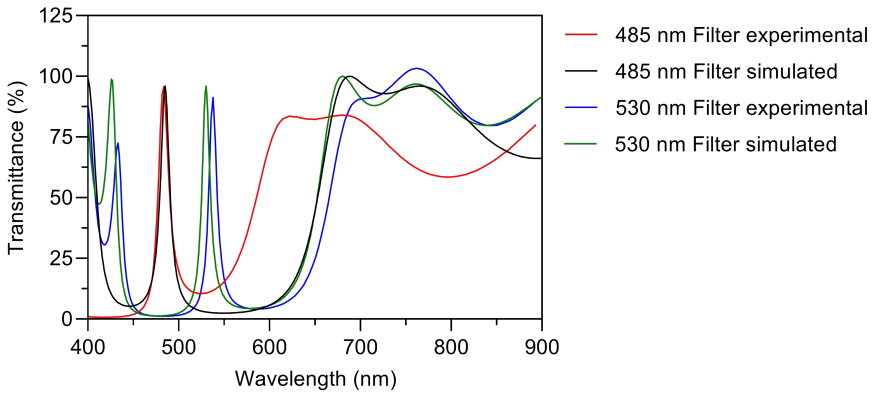
The analysis of the fabricated 485 nm filter shows that its bandpass region closely matches the simulated response, with only a slight shift of the peak transmittance towards shorter wavelengths. However, beyond the transmittance peak, the fabricated filter exhibits a more pronounced long-wavelength tail, resulting in increased transmittance at wavelengths above the peak. This behavior exacerbates the crosstalk from FAD fluorescence that was already identified in the simulated response. It further reinforces the need of the inclusion of an additional short-pass optical filter to suppress the unwanted FAD contribution, as previously discussed. The practical applicability of this filter must be evaluated experimentally to determine whether NAD(P)H fluorescence can be reliably detected with sufficiently low crosstalk from FAD. The fabricated filter presents a spectral bandwidth increase compared to the simulated filter. This reflects a broader transmission band, which contributes to the observed crosstalk increase and represents a slight reduction in spectral selectivity.

The fabricated 530 nm filter exhibits a transmittance spectrum that is in good agreement with the simulated response. Minor differences are observed, namely a slightly lower peak transmittance and a small shift of the peak position towards higher wavelengths. However, these deviations are not expected to significantly affect the suitability of the filter for the intended application, although further evaluation will be performed. At wavelengths below approximately 450 nm, the fabricated filter shows lower transmittance compared to the simulated design. This behavior is advantageous, as it reduces potential crosstalk from NAD(P)H fluorescence in this spectral region. In terms of spectral bandwidth, the fabricated filter presents a slightly higher FWHM value than the simulated filter. This small increase indicates a marginal broadening of the transmission band, but it is not expected to compromise the filter selectivity.

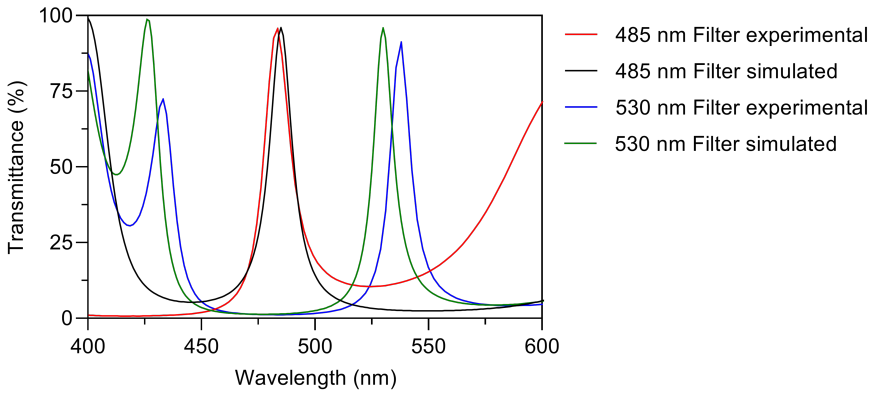
The observed differences between the simulated and experimental transmittance curves are mainly attributed to limitations in the precise control of individual layer thicknesses during fabrication, as well as to small variations in the optical properties of the deposited films. These variations are anticipated, as the deposition conditions cannot be precisely reproduced for all layers and deposition runs.



(a)



(b)



(c)

Figure 5.11: Transmittance spectra of the fabricated optical filters (485 nm and 530 nm): (a) experimental measured transmittance; (b) comparison between simulated and experimental transmittance over the full spectral range; (c) comparison between simulated and experimental transmittance in the ROI.

The same validation performed in the previous section was repeated, performing the product between the experimental transmittance spectra of the fabricated filters and the 2PEF spectra of the fluorophores.

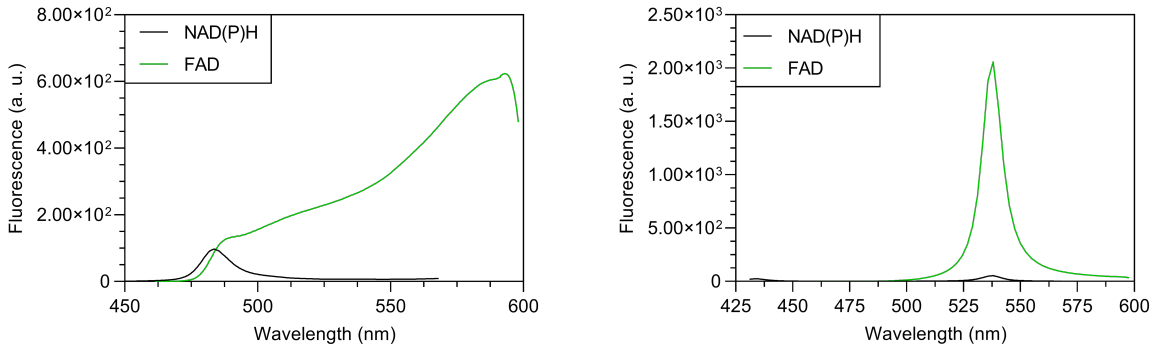
The resulting data are shown in Figure 5.12.

As expected, the results observed in Figure 5.12(a) confirm the effects previously identified in Figure 5.10(a). In particular, the contribution of FAD fluorescence within the 485 nm filter is significant and even more pronounced in the fabricated filter. This result further confirms the need to incorporate an additional short-pass filter to effectively suppress the unwanted contribution. Further experimental tests using tissue-mimicking phantoms will be required to determine whether this filter configuration is sufficiently selective to reliably distinguish CRC tissues.

The 530 nm filter (Figure 5.12(b)) exhibits strong transmission of the FAD fluorescence signal, while only negligible fluorescence from NAD(P)H is detected. This result confirms the effective performance of this filter for selective FAD detection.

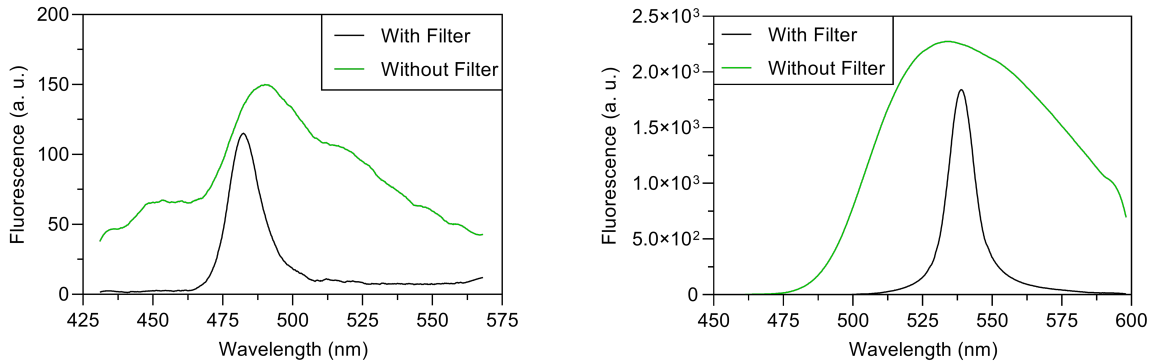
After completing the design and validation studies, the filters were integrated into the experimental setup and tested using two phantoms containing only NAD(P)H and FAD. The NAD(P)H phantom had a concentration of 93.98 µM, while the FAD phantom had a concentration of 56.26 µM. The phantoms were measured with the filters in place, using a mean laser power of 100 mW, and an acquisition time of 60 s. Figure 5.13 presents the resulting spectra for both filters, together with the corresponding measurements acquired without filters, allowing a direct comparison of the system response with and without spectral filtering.

From the acquired spectra, it can be observed that the filters operate as intended, selectively transmitting the fluorescence bands of each phantom. As expected, the peak fluorescence intensity measured with the filters in place is lower than that obtained without filtering, since the peak transmittance of the



(a) (b)

Figure 5.12: Fluorescence spectra resulting from the multiplication of the fabricated filter transmittance with the 2PEF spectra of NAD(P)H and FAD: (a) response with the 485 nm filter; (b) response with the 530 nm filter.

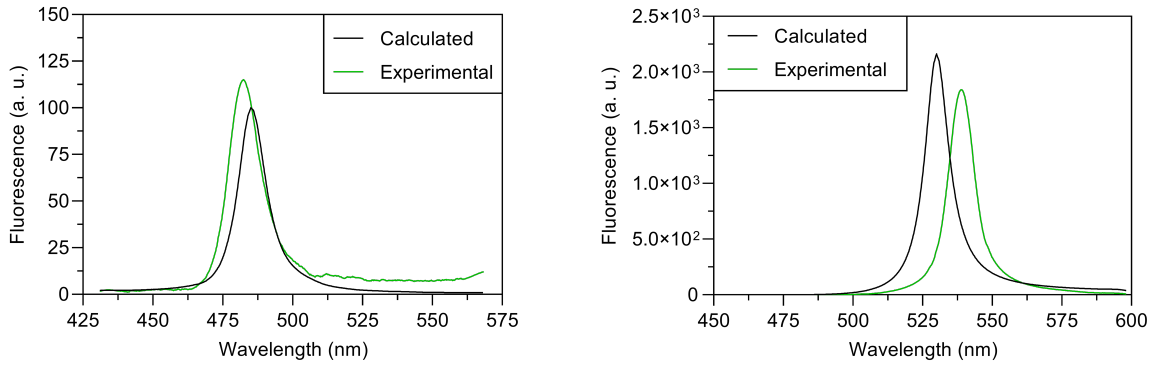


(a) (b)

Figure 5.13: Fluorescence spectra acquired with and without optical filtering, illustrating the effect of spectral selection for: (a) NAD(P)H phantom; and (b) FAD phantom.

filters is less than unity. Nevertheless, the signal reduction is moderate, and the detected fluorescence intensity remains sufficiently strong for analysis.

A comparison between the calculated 2PEF curves (shown previously in Figure 5.12) and the experimentally acquired spectra is presented in Figure 5.14. Some differences are observed in both peak intensity and peak position. These discrepancies are primarily attributed to variations in the thickness of the deposited filter layers across the filter area, which are inherent to the RF sputtering process. As a result, the central and peripheral regions of the filter may exhibit slightly different thicknesses, leading to variations in peak wavelength position, transmittance, and FWHM. Thus, small changes in optical alignment may cause the detection light to pass through different regions of the filter, further contributing to the observed



(a) (b)

Figure 5.14: Comparison between calculated and experimentally measured 2PEF spectra with optical filtering for: (a) NAD(P)H phantom; and (b) FAD phantom.

variations in the measured spectral response.

Finally, SEM images were acquired from a fabricated 485 nm filter, allowing visualization of the filter cross-section and the individual layers composing the structure (Figure 5.15).

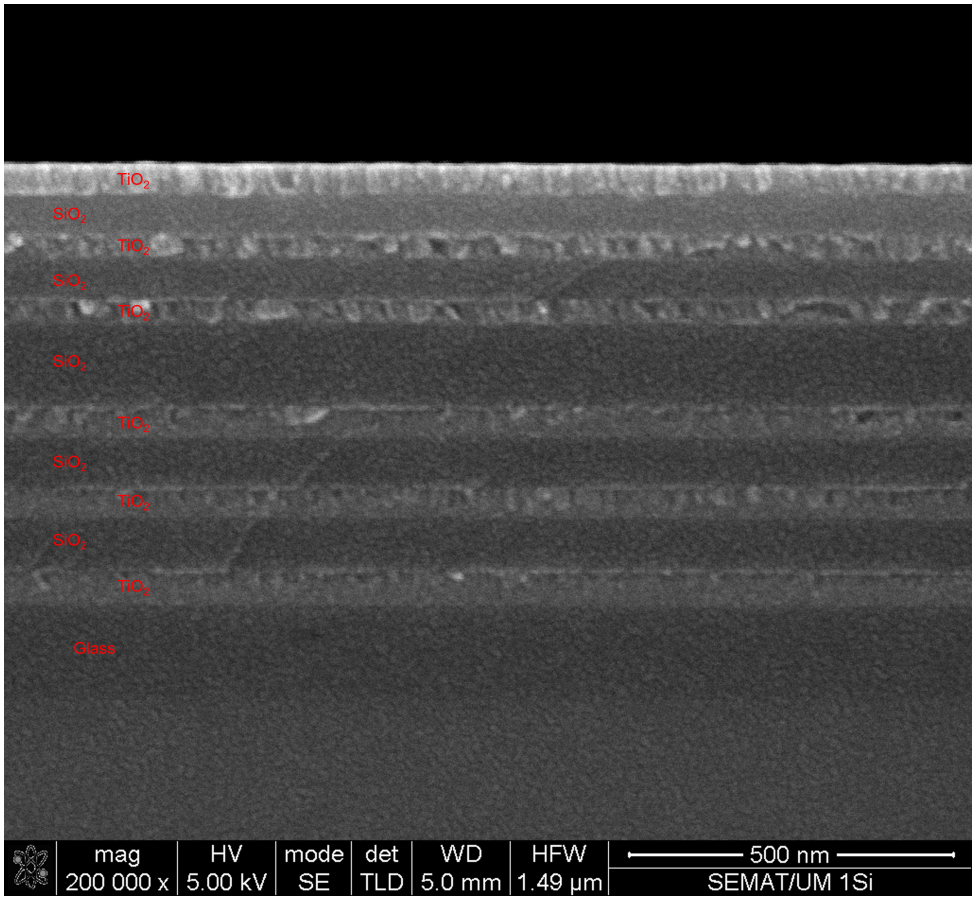


Figure 5.15: Cross-sectional SEM image of a fabricated 485 nm Fabry–Perot filter, showing the multilayer structure and layer interfaces.

5.5 Outlook

In summary, this chapter addressed the design, fabrication, and validation of interference-based optical filters for the selective detection of NAD(P)H and FAD fluorescence signals under 2PEF excitation. Fabry–Perot filters incorporating Bragg reflectors were selected as the most suitable configuration due to their ability to achieve narrowband spectral selectivity and high transmittance.

The initial design of the filters (centered at 485 nm for NAD(P)H and 530 nm for FAD) was derived from analytical calculations and subsequently refined through numerical simulations using the experimentally determined refractive indices of SiO_2 and TiO_2 thin-films. The incorporation of the experimental refractive indices improved design accuracy and ensured consistency between simulated and fabricated

structures. Additionally, a design simplification strategy based on identical Bragg mirrors was successfully implemented, reducing fabrication complexity while maintaining adequate spectral performance.

To address fabrication constraints associated with thin-film thickness control, a second-order resonant cavity was implemented for the 530 nm filter. This approach reduced the sensitivity of the spectral response to thickness variations, improving fabrication robustness while preserving the desired optical performance.

Detailed spectral analysis demonstrated that the proposed filters enable effective discrimination between the two fluorophores. However, the 485 nm filter shows a significant sensitivity to crosstalk under 2PEF conditions, primarily due to the higher fluorescence intensity of FAD when compared to NAD(P)H. This limitation highlights the inherent trade-off between NAD(P)H signal maximization and FAD crosstalk suppression. The 530 nm filter exhibited robust selectivity for FAD detection, with minimal contribution from NAD(P)H.

The fabricated optical filters exhibited a performance in good agreement with the simulated designs, with only minor deviations attributed to variations in deposition conditions and layer thickness control. Experimental validation using tissue-mimicking phantoms confirmed that the filters operate as intended, enabling selective transmission of the fluorescence signals while maintaining sufficient signal intensity for analysis. Nevertheless, the results also demonstrated that additional optical elements, such as short-pass filters, are required to suppress undesired spectral contributions, particularly for NAD(P)H detection under 2PEF excitation.

Overall, the results demonstrate that the proposed design and fabrication approach provides a viable solution for spectral filtering in 2PEF systems. The developed filters represent a significant step toward the implementation of compact and selective detection schemes, compatible with endoscopic applications.

Part IV

Tissue Models Analysis with Optical Coherence Tomography and Multiphoton Microscopy

Chapter 6

Optical Coherence Tomography of CAM Assays

This chapter explores the application of OCT in the structural characterization and classification of colorectal tissues obtained from CAM assays. The theoretical principles of low-coherence interferometry and depth-resolved signal formation are first introduced, followed by a description of the experimental setup and data processing methodology for attenuation coefficient extraction from the obtained OCT images. A feature-based analysis combined with a machine learning approach is then employed to assess the capability of OCT-derived parameters to discriminate non-malignant and malignant tissues. Finally, the obtained results are discussed.

6.1 Context

OCT is a tomographic technique that generates cross-sectional images of 3D objects. It is similar to other well-established tomographic techniques, but its operation involves a low-coherence light source in the NIR spectral range. Therefore, OCT is an optical imaging technique capable of producing high-resolution cross-sectional images through inhomogeneous samples, providing a 3D visualization of the internal biological microstructures.

In the last few decades, OCT has revolutionized the medical world [199], enabling optical biopsies of biological samples [79–82]. The introduction of optical fiber-based OCT systems has allowed the emergence of new OCT applications [83, 84], including cancer research [85]. Once OCT systems can be implemented entirely by optical fibers, their compactness makes OCT an ideal candidate for endoscopy, facilitating access to inner body regions, including the human colon.

Extensive research has demonstrated the great potential of OCT in oncology, particularly in tumor detection [86–90]. Consequently, gastroenterology is a relevant field for OCT due to the high incidence rates of gastrointestinal pathologies, including CRC. Several studies have been reported, concerning the performance of OCT imaging in gastroenterology [91–93], including the upper gastrointestinal tract [94, 95].

Therefore, OCT is a suitable imaging modality for this work, as it can assess the structural characteristics and morphology of biological tissue. Unlike fluorescence-based techniques (e.g., 2PEF), which provide biochemical information, OCT enables the acquisition of high-resolution, depth-resolved structural images in a non-invasive and non-destructive manner. This makes it particularly relevant for applications in early

cancer detection, where morphological alterations in tissue architecture play a critical role. In particular, malignant tissues are known to exhibit increased heterogeneity, altered cell density, and changes in optical scattering properties when compared to non-malignant tissues. These differences can be captured and quantified through OCT imaging.

In addition, the study of the OCT light attenuation as it propagates through biological tissues, due to scattering and absorbing characteristics of the medium, offers valuable insights into the morphology of different structures present within the tissue. The attenuation of NIR light in biological samples has proven to be a powerful tool for tissue characterization [200–203].

Furthermore, the use of the CAM model provides a controlled and reproducible environment for the evaluation of OCT methodologies. This model enables the growth of both non-malignant and malignant colorectal tissues, allowing a systematic comparison of their optical and structural characteristics. The combination of OCT imaging with the CAM assay thus constitutes a powerful platform for investigating tissue morphology and validating diagnostic approaches.

So, in this study, CAM assays were used as *in vivo* models mimicking human colorectal tissue, using appropriate cell lines. The potential of a classifier to distinguish non-malignant from malignant tissue samples was evaluated, using features extracted from OCT attenuation coefficient images.

6.2 Theoretical Framework

OCT is an imaging technique based on low-coherence optical interferometry. Optical interferometry relies on the interference of electromagnetic waves propagating through a medium. Interference occurs only when the waves exhibit a certain degree of correlation, known as coherence.

Coherence can be classified as temporal or spatial. Temporal coherence is the correlation of the phase of a wave at a given spatial point over different instants in time. It is directly related to the spectral bandwidth of the optical source. Spatial coherence, on the other hand, describes the phase correlation between different points across the transverse profile of the beam at a given instant [204].

In low-coherence interferometry, the parameter of primary interest is the temporal coherence of the source. The coherence properties determine the coherence length (l_c), which defines the axial resolution and the depth selectivity of OCT. Since temporal coherence is inversely related to the spectral bandwidth, broadband light sources provide short coherence lengths and therefore enable high-resolution depth-resolved imaging [204].

For broadband, low-coherence optical sources, when the emitted light is divided into two paths (as in

an interferometer), interference occurs only if the optical path difference between the two beams is shorter than the coherence length of the source. If the path difference exceeds this coherence length, the phase relationship between the waves becomes uncorrelated, and the interference fringes vanish [205, 206].

By analyzing the interference pattern produced by the interferometer, it is possible to extract detailed information about the optical properties and structure of the medium through which the light propagates. In low-coherence interferometry, this principle enables depth-resolved measurements with high axial resolution and precision [205, 206].

One of the most important interferometric configurations, used in OCT is the Michelson interferometer (Figure 6.1) [2, 207, 208]. In this configuration, light from a low-coherence source is incident on a beam splitter, which divides the beam into two separate paths (sample arm and reference arm). In the sample arm, the light propagates into the sample and is backscattered by structures located at different depths, depending on the optical properties of the medium. In the reference arm, the light travels toward a mirror positioned at a controllable distance. The reflected beams from both arms recombine at the beam splitter and interfere at the detector [2, 206].

A high interference signal indicates that the optical path length of the reference arm matches the optical path length of a specific reflecting structure within the sample. By mechanically adjusting the position of the reference mirror, different depths in the sample can be sequentially matched, allowing the acquisition of a depth-resolved reflectivity profile, known as an A-scan. This scanning procedure constitutes the fundamental operating principle of temporal domain optical coherence tomography (TD-OCT) systems

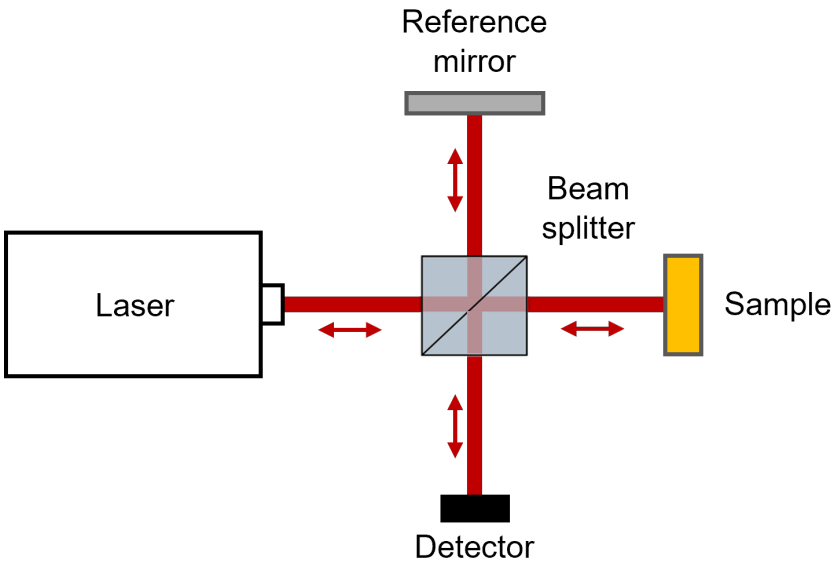


Figure 6.1: Schematic diagram of a Michelson interferometer, illustrating the principal optical components: a light source, beamsplitter, reference mirror, and detector.

[209].

There are two main operational configurations in OCT: TD-OCT and frequency domain optical coherence tomography (FD-OCT). The primary difference between these configurations lies in the reference arm. In TD-OCT, the reference mirror is mechanically scanned to vary the optical path length, enabling depth-resolved measurements. In contrast, in FD-OCT, the reference mirror remains fixed, and depth information is retrieved through spectral analysis of the interference signal [210–213].

FD-OCT can be further divided into two implementations, SD-OCT and swept-source optical coherence tomography (SS-OCT). In SD-OCT, a broadband light source is used, and the interference spectrum is measured with a spectrometer, while in SS-OCT, a tunable narrowband laser source sequentially sweeps across wavelengths, and the interference signal is detected with a photodetector as a function of time. In the present work, the system employed is an SD-OCT configuration [210–213].

The operation of SD-OCT is based on acquiring the interference signal in the frequency domain using a spectrometer. Since the reference mirror is fixed, no mechanical depth scanning is required, which significantly increases acquisition speed and improves sensitivity compared to time-domain systems. The depth information is encoded in the spectral modulation of the detected interference signal. This spectrum results from the interference between the light reflected by the reference mirror and the light backscattered from different depths within the sample. By applying a fast fourier transform (FFT) to the detected spectral signal, the frequency-domain data are converted into a depth-resolved reflectivity profile. This process allows reconstruction of the internal optical structure of the sample, producing cross-sectional images with high resolution [206, 207, 211–213].

OCT is capable of producing high-resolution cross-sectional images of non-homogeneous samples, such as biological tissues. By measuring the backscattered light as a function of depth, OCT provides detailed structural information in a non-invasive and non-destructive manner. The axial resolution of OCT depends primarily on the spectral bandwidth of the light source. Broadband sources yield shorter coherence lengths and, therefore, higher axial resolution. Typically, OCT systems achieve axial resolutions in the range of $1\,\mu$m to $5\,\mu$m, depending on the central wavelength and bandwidth of the source. However, OCT imaging depth is limited by optical scattering and absorption in biological tissues. For most biological tissues, the effective imaging depth is typically limited to approximately 1 mm to 2 mm [209].

The characteristics of the light source used in the Michelson interferometer have a strong influence on the resulting interference profile. For a broadband optical source, the electric field in the frequency domain can be expressed as [82]:

$$E(\omega, t) = s(\omega)e^{-i(\omega t)}, \tag{6.1}$$

where ω is the angular frequency, t is time, and $s(\omega)$ represents the spectral amplitude of the source. The electric field at the entrance of the interferometer is denoted by $E_{in}(\omega, t)$. The electric fields are denoted by $E_r(\omega, t, \Delta z)$ in the reference arm, $E_s(\omega, t)$ at the sample arm, and $E_{out}(\omega, t, \Delta z)$ in the exit arm. They can be calculated by [82]:

$$E_r(\omega, t, \Delta z) = (T_r T_s)^{1/2} E_{in}(\omega, t)e^{-i\varphi(\Delta z)} \tag{6.2}$$

$$E_s(\omega, t) = (T_r T_s)^{1/2} E_{in}(\omega, t)H(m) \tag{6.3}$$

$$E_{out}(\omega, t) = E_r(\omega, t, \Delta z) + E_s(\omega, t) \tag{6.4}$$

where T_r and T_s are the effective transmission coefficients associated with the beam splitter, and $\varphi(\Delta z)$ is the phase accumulated due to the optical path difference (Δz) between the two arms. In the sample arm, the electric field is modified by the sample response function $H(w)$, which accounts for the reflectivity and phase changes introduced by the sample. The phase term $\varphi(\Delta z)$ is given by [82]:

$$\varphi(\Delta z) = \frac{2\omega\Delta z}{c} \tag{6.5}$$

where c is the speed of light in vacuum. The factor of two appears because the light travels the distance Δz twice, once toward the reflector and once back to the detector.

Since the optical detectors used follow a quadratic response law, the detected intensity is proportional to the temporal average of the product of the electric field and its complex conjugate. Therefore, the detected intensity can be written as [80, 82, 214, 215]:

$$I(w, \Delta z) = \langle E_{out}E_{out}^* \rangle = \langle E_s E_s^* \rangle + \langle E_r E_r^* \rangle + 2\Re\left\{\langle E_s E_r^* \rangle\right\} \tag{6.6}$$

The first two terms correspond to the individual intensities of the sample and reference arms [82]:

$$\langle E_s E_s^* \rangle = |E_s|^2 = T_r T_s S(\omega)|H(\omega)|^2 \tag{6.7}$$

$$\langle E_r E_r^* \rangle = |E_r|^2 = T_r T_s S(\omega) \tag{6.8}$$

where $S(\omega) = \mathbb{s}(\omega)\mathbb{}^2$ represents the power spectral density of the source. The third term corresponds to the interference contribution [82]:

$$\langle E_s E_r^* \rangle = T_r T_s S(\omega)H(\omega)e^{i\varphi(\Delta z)}, \tag{6.9}$$

which contains the phase information associated with the optical path difference between the two arms. The function $H(\omega)$ describes the overall complex reflectivity of the sample along the axial direction and can be expressed as [82]:

$$H(\omega) = \int_{-\infty}^{+\infty} r(\omega, z) e^{i2n(\omega,z)\omega\frac{z}{c}} dz, \tag{6.10}$$

where $r(\omega, z)$ is the backscattering coefficient at depth z, $n(\omega, z)$ is the refractive index, which may depend on both frequency and depth, and the exponential term accounts for the phase accumulated during the round-trip propagation within the sample [82].

Due to the scattering and absorbing characteristics of the structures, OCT light is attenuated when it travels through biological tissue. The attenuation of the NIR light in the biological samples is governed by the Beer-Lambert law. From Equations 1.1, 4.8, and 4.9 is possible to obtain [101]:

$$I(z) = I_0 e^{-\mu z}, \tag{6.11}$$

where $I(z)$ is the light intensity at depth z, I_0 is the initial intensity, and μ is the attenuation coefficient, which represents the sum of absorption and scattering. This coefficient is then a measure of the attenuation magnitude. As attenuation is an optical property of the medium, determining the attenuation coefficient of the OCT images may provide valuable information about the composition of this medium [203]. The attenuation coefficient has been used for different diagnostic and classification purposes, including renal cancer diagnosis [216], bladder cancer tumor staging [217], cancer in axillary lymph node [218], oral cancer [219], and rectal cancer [220]. The OCT attenuation coefficient was also used in the past to evaluate cell lines [221]. However, this work is the first report about assessing the attenuation coefficient of OCT images obtained from CAM models. An automated depth-resolved attenuation coefficient was estimated using the method proposed by Smith [201].

According to Beer-Lambert's law, and using the adaptation from Faber *et al.* [222], who introduced a depth-dependent curve fitting model, the attenuation coefficient in biological samples (μ) is directly proportional to the intensity of the light back-scattered from the sample:

$$I(z) \propto h(z) e^{-2\mu z}, \tag{6.12}$$

where $h(z)$ is the confocal function [223]. The exponential part is multiplied by two, since the light travels twice the medium. In this relation, the $h\ (z)$ part accounts for optical system effects, and the $e^{-2\mu z}$ accounts for the tissue properties.

The $h(z)$ function describes how efficiently the system collects light as a function of the distance from

the focal plane, so it accounts for the reduction in detected signal as the sample position deviates from the focal plane, because the measured signal decreases not only because tissue attenuates light, but also because the beam is no longer in focus. The function at depth z is defined according to:

$$h(z) = \left(\left(\frac{z - z_0}{z_R} \right)^2 + 1 \right)^{-1}, \tag{6.13}$$

where z_0 is the depth of the focal plane, and z_R is the apparent Rayleigh range, which is related to the Rayleigh range (z_r) by:

$$z_R = \alpha_R n z_r, \tag{6.14}$$

with α_R being equal to 2 for diffuse reflectors, and n being the refractive index of the medium. The Rayleigh range z_r is the propagation distance from the beam waist to the point where the beam radius increases by a factor of $\sqrt{2}$. In OCT, the Rayleigh range defines the depth interval over which the probing beam remains well focused inside the sample. Beyond this range, beam divergence reduces the detected signal independently of tissue attenuation, requiring compensation during attenuation coefficient estimation. It is given by [101]:

$$z_r = \frac{\pi \omega_0^2}{\lambda} \tag{6.15}$$

For OCT attenuation coefficient estimation, a depth-resolved confocal (DRC) method first presented by Smith *et al.* [201] was used. This enables the estimation of the attenuation coefficient independently of the focal plane position. As in [201], we used an SD-OCT system, where the measured intensity of an A-scan corresponds to an integration of the interferometric information over a small depth range, according to:

$$I\,[m] = \int_{z_m}^{z_m+1} I(z) dz \tag{6.16}$$

The terms z_m and z_{m+1} represent the physical bounds of the sample in depth, $m \in [1, \cdots, M]$, where M denotes the M-pixel of the spectrometer. The function $I[m]$ is discrete, as is the case of sampling in an SD-OCT system. The model was extended to improve the estimation accuracy, so the measured signal $I_{meas}[m]$ also includes additive noise sources, $c[m] \in R$, a random variable that accounts for additive noise typical of most OCT systems. So, the measure signal is a sum of tissue back scattering, optical system effects, and noise.

$$I_{meas}[m] = I[m] + c[m] \tag{6.17}$$

To estimate the true attenuation coefficient, the effects of additive noise, confocal function, and sensitivity falloff must be removed. For that, a restoration filter $(H_{res}[m])$ was used [201]:

$$\hat{I}[m] = I_{meas}[m]H_{rest}[m] \tag{6.18}$$

where,

$$H_{rest}[m] = \frac{1}{f[m]h[m]} \frac{|I_{meas}[m]|^2}{|I_{meas}[m]|^2 + |c[m]|^2} \tag{6.19}$$

The expected average noise power $\left(\overline{|c[m]|^2}\right)$ is a hyperparameter of the algorithm [201]. The sensitivity fall-off function $(f[m])$ is a phenomenon that influences the depth-dependent intensity of the OCT signal, in Fourier-domain techniques [201]. This is determined from the OCT system parameters, specifically using the model created by Yun *et al.* [224] for spectral domain OCT systems. The confocal function [223] $(h[m])$ is experimentally determined using the location of the focal plane and the Rayleigh range of the scanning lens in the optical system. The attenuation coefficient $(\hat{\mu})$ according to Vermeer *et al.* [203], can be estimated using the estimated signal $\left(\hat{I}\right)$.

$$\hat{\mu}[m] \approx \frac{\hat{I}[m]}{2\Delta z \sum_{r=m}^{M} \hat{I}[r]} \tag{6.20}$$

where $\Delta z = z_{m+1} - z_m$. According to Equation 6.20, the attenuation coefficient at a certain depth (m) is proportional to the ratio between the intensity of light backscattered at depth m and the amount of light backscattered from all deeper positions. To improve the attenuation coefficient estimation, a denoising algorithm was also applied, based on the technique of intensity weighted horizontal total variation (iwhTV), developed by Smith *et al.* [201]. This is a smoothing filtering technique that preserves lateral structure in a sample and is preferable in samples with non-layered structures and with variations in signal-to-noise ratio as a function of depth.

6.3 Optical Coherence Tomography Setup

For the OCT measurements, a Telesto II-1325 LR SD-OCT system from Thorlabs was used. This commercial system is optimized for high-resolution imaging of biological tissues in both *in vivo* and *ex vivo* configurations. The system is based on a broadband superluminescent diode (SLD) source with a central wavelength of 1325 nm and a spectral bandwidth of 100 nm. Under these conditions, the Telesto II-1325 LR provides a theoretical axial resolution of approximately 12 µm in air and 9 µm in water, with a maximum imaging depth of 7 mm in air and 5.3 mm in water.

The imaging probe integrates a Michelson interferometer, a pair of galvanometric scanning mirrors, and a telecentric scanning objective (OCT-LK4 optical kit, Thorlabs). This configuration yields a lateral resolution of $20\,\mu m$ and incorporates an LSM04 lens with a Rayleigh range of $0.607\,mm$. Based on the spectrometer characteristics, the system provides a vertical pixel spacing of $6.91\,\mu m$ for a refractive index of n = 1.0. As is typical for SD-OCT systems, the axial and lateral resolutions are independent. The axial resolution is determined by the spectral bandwidth of the SLD source, while the lateral resolution is governed by the optical design of the scanning and focusing elements.

A key parameter in this study is the Rayleigh range, which was calculated using Equation 6.15. By considering the OCT source wavelength $(\lambda = 1325\,nm)$ and beam waist $(w_0 = 16\,\mu m)$, a value of $0.607\,mm$ was obtained.

6.4 Experimental Methods

6.4.1 Data Acquisition and Processing

The OCT evaluation started with the scanning of 30 CAM samples, 15 non-malignant colorectal tissue samples and 15 malignant colorectal tissue samples. OCT B-scan images of these samples were acquired using the OCT system previously described. Images were obtained by first selecting a central ROI of the tissue under analysis and then placing the sample in focus and determining the location of the focal plane. Each acquisition comprised a single B-scan with a depth of up to $2.61\,mm$ and a lateral imaging range up to $6\,mm$, depending on the tumor being examined. The images were acquired using the ThorImage OCT software from Thorlabs, and a refractive index of 1.34 was set for these samples as reported in previous work [2, 225].

After acquiring the OCT images, an image mask was created to isolate the tumor surface from the background. Equation 6.18 was then applied to the raw intensity values within the mask to account for the additive noise, the confocal function, and the effects of the sensitivity fall-off. Finally, the attenuation coefficient was calculated for each pixel using Equation 6.20. This resulted in an attenuation coefficient B-scan image, which was lastly denoised using the iwhTV filtering technique. These steps are schematically represented in Figure 6.2.

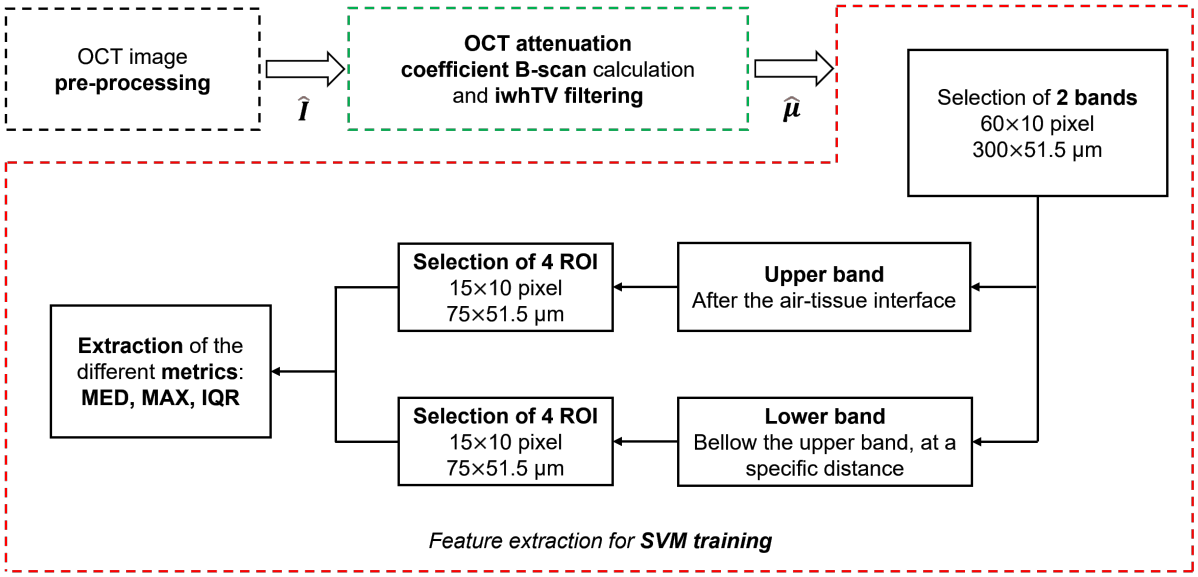


Figure 6.2: The workflow of the OCT image acquisition, processing, and extraction of features [10].

6.4.2 Data Analysis

A SVM classifier was implemented to distinguish non-malignant and malignant colon tumors. The SVM classifier is a classification method that defines a hyperplane that splits the data into two classes by maximizing the margin separation between the classes. The margin is defined as the distance between the closest data points from each class and the hyperplane. The computation of the optimal hyperplane is controlled by the hyperparameter C. The radial basis function was selected as the kernel of the SVM, whose hyperparameter is gamma. These two hyperparameters were chosen using cross–validation, as explained later.

The efficacy of the SVM classifier depends on the quality of the selected features, and the tumor growth process must be considered. As discussed in the introduction section of the thesis, the growth of malignant tumors is characterized by the appearance of highly vascularized regions and the presence of a higher-density core of cells in comparison to the surface, while non-malignant tumors show higher homogeneity in cell distribution. Although vascularization is not easily observed in OCT images, when limiting the analysis to B-scan imaging, the gradient of density variation from the surface to the interior of malignant tissues can be captured. Thus, the proposed approach is to capture this density variation by computing features in two distinct bands: one band is selected near the surface, just below the air-tissue interface, and the other band is selected within the interior of the tissue. The density of the tissue could be quantified, for example, by computing the mean value within each band.

However, during an examination, as the physician moves the probe along an area of interest, such as

a suspected tumoral region, there may be an influence from the interface zone between non-malignant tissue and malignant tissue, where both tissue types are captured within the same band. To address this, each band is further divided into smaller regions, and the features are computed separately within these regions along the band (Figure 6.3). Moreover, since the mean is susceptible to intensity dispersion caused by density gradients within each region, the median was evaluated instead. Considering the effect of vascularization, the interquartile range was also evaluated as another feature to characterize the tissue density. Finally, given that non-malignant tissue tends to be more homogeneous, while malignant tissue is denser in deeper layers, the maximum intensity was also included as a discriminatory feature between the two types of tissue. The distance between the two bands and the selection of features are evaluated in an ablation study presented in the next section.

To be effective, a machine learning method should generalize its predictive capacity to unseen data. This is accomplished by splitting the data into training, validation, and test datasets, with the validation dataset being used for hyperparameter tuning. When the number of samples is very large, it is possible to split them into these three types of datasets. However, due to the limited number of samples in this study,

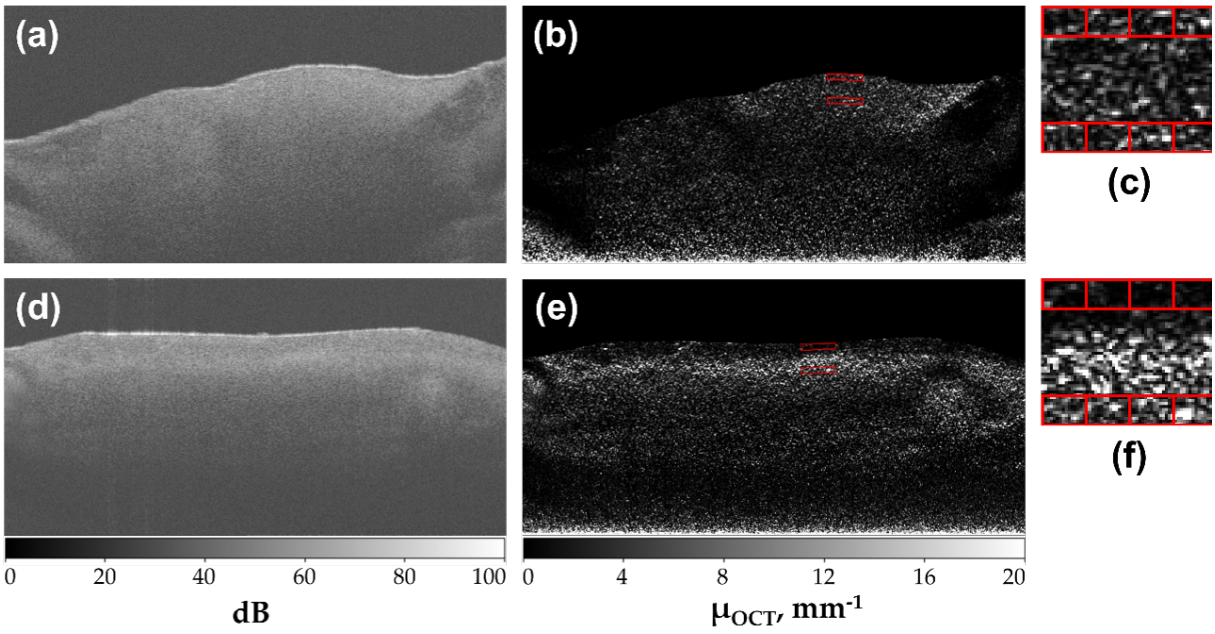


Figure 6.3: Raw B-scan OCT images in dB scale, obtained using the ThorImage OCT software: (a) a non-malignant CAM sample and (d) a malignant CAM sample; attenuation coefficient B-scan images fully processed with the algorithm previously detailed, with the selected two bands highlighted in red of: (b) a non-malignant CAM sample and (e) a malignant CAM sample; zoomed in section of the two highlighted bands of: (c) a nonmalignant CAM sample and (f) a malignant CAM sample, with a compensation for the air-tissue interface border irregularities and further division of each band into four ROI.

this kind of splitting is not feasible as it could lead to unreliable conclusions based on insufficient data.

Thus, a nested 5–fold stratified cross-validation method was implemented to train, tune, and test the proposed method. The nested cross-validation is a technique that ensures that samples from a small data set do not leak from training to tune or testing, which would skew the analysis of the performance and produce an overconfident classifier.

This is accomplished by using an inner cross–validation loop that trains and selects the best hyperparameters, and an outer loop that tests the best model in an independent fold. The implementation was based on the SciKit-Learn package [226]. The performance of each model was evaluated using four metrics: accuracy, recall, precision, and area under the receiver operating characteristic curve (ROC AUC). The performance metric for each model was then averaged over all folds of the outer cross-validation, resulting in an overall estimate of the SVM classifier's performance on the dataset.

6.5 Results and Samples Analysis

As discussed previously, the main objective of this work was to perform OCT analysis of CAM assays for evaluating whether structural information extracted from a limited spatial region of the OCT image was sufficient to distinguish between non-malignant and malignant samples. To address this objective, a systematic ablation study was conducted. First, the discriminative relevance of each extracted feature was evaluated individually, and then different feature combinations were analyzed. Subsequently, the influence of the spatial separation between depth bands on the classification performance was investigated. After this, the performance obtained using depth-resolved attenuation coefficient B-scans was compared with that obtained directly from raw OCT intensity B-scans, to assess the impact of the image transformation step on tissue discrimination.

Each depth band corresponded to a region of $300\,\mu$m in width and $51.5\,\mu$m in height, and was further divided into four sub-regions of equal size. An example of the acquired data are shown in Figure 6.3. Figures 6.3(a) and 6.3(d) present representative raw OCT B-scans of non-malignant and malignant CAM assays, respectively. Figures 6.3(b) and 6.3(e) show the corresponding depth-resolved attenuation coefficient B-scans. These transformed images enhance contrast related to internal tissue structure and optical properties. In the same figures, the two depth bands selected for analysis are highlighted. The first band is located immediately below the air–tissue interface, while the second band is positioned at a depth of $206\,\mu$m. These bands form the basis for subsequent feature extraction and classification.

Inspection of the attenuation coefficient images in Figures 6.3(b) and 6.3(e) reveals clear physiologi-

cal and morphological differences between non-malignant and malignant tissues. Non-malignant tumors tend to exhibit greater homogeneity along depth, whereas malignant tumors show pronounced structural heterogeneity, particularly in deeper regions. This behavior is consistent with the expected biological response of malignant tissue, where increased cell aggregation occurs in hypoxia regions due to limited O_2 and nutrient diffusion. These depth-dependent variations constitute critical cues for the discrimination of malignant lesions.

Based on these observations, it is reasonable to hypothesis that differences in cell density and distribution between non-malignant and malignant tissues can be captured by extracting features from the selected depth bands and used for classification with a SVM classifier. This hypothesis is supported by the boxplots shown in Figure 6.4. In this analysis, attenuation coefficient B-scans were used, and the distance between the two bands was fixed at $206\,\mu m$. This distance was selected by visually inspecting the images to ensure that, for the majority of malignant samples, the lower band encompassed regions associated with hypoxia and increased cell density. For this specific comparison, features were computed over the entire band. For non-malignant tissues, the distributions of the median (MED) and interquartile

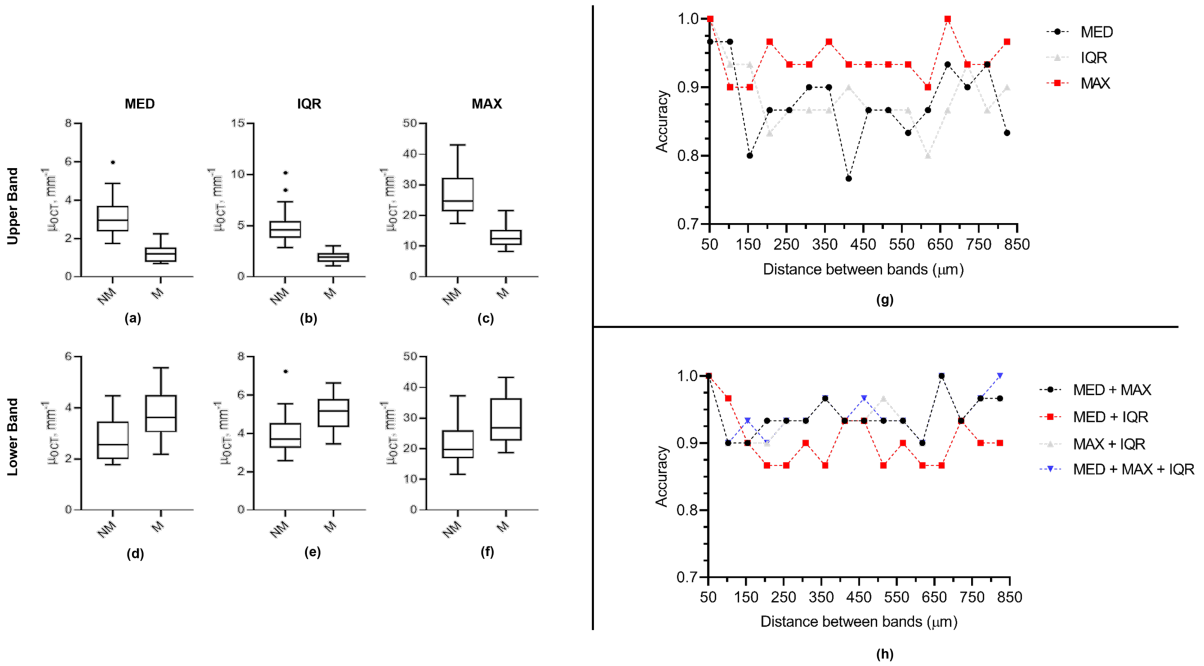


Figure 6.4: Boxplots showing the: (a) and (d) MED; (b) and (e) IQR; (c) and (f) MAX of the attenuation coefficient (μ_{OCT}) for non-malignant (NM) and malignant (M) tumors, in the upper and lower band. Analysis of the SVM classifier accuracy values in function of the distance between the two bands (μm) for: (g) isolated features MED, IQR and MAX; and (h) combined features MED + MAX, MED + IQR, MED + MAX + IQR [10].

range (IQR) features show only small differences between the upper and lower bands, indicating relatively uniform attenuation properties along depth. In contrast, malignant tissues exhibit marked differences between bands, with lower attenuation values in the upper band and higher values in the deeper band, consistent with the expected morphological organization. A similar trend is observed for the MAX feature, although, as a point-wise descriptor, it is less representative of overall tissue density.

The boxplots reveal a clear distinction between non-malignant and malignant tissues. In the upper band, non-malignant samples consistently exhibit higher feature values, whereas in the lower band the opposite trend is observed, with malignant samples presenting higher values. These results confirm the depth-dependent structural differences expected between the two types of tissues: non-malignant tissues remain relatively homogeneous, while malignant tissues display significant variations with depth.

The effect of the distance between the two bands on classifier performance was then systematically evaluated. This analysis was performed using each feature individually as well as different combinations of features. Unlike the previous analysis, features were computed for each of the four sub-regions within each band, resulting in a total of eight sub-regions per image. For each band separation, features were extracted from all sub-regions, and an SVM classifier was trained using a nested cross-validation procedure. The resulting classification accuracies are shown in Figures 6.4(g) and 6.4(h).

The results indicate that the highest classification accuracy is achieved when the two bands are adjacent, corresponding to a $51.5\,\mu$m distance between their centers. Based on this finding, additional performance metrics, namely recall, precision, and AUC, were computed for this optimal configuration. These metrics are summarized in Table 6.1. To assess the impact of the attenuation coefficient transformation, the same analysis was performed using raw OCT B-scans, with the bands positioned at the same optimal distance.

A marked performance difference is observed between the two image representations. The classifier trained on raw OCT images exhibits substantially lower and more variable performance compared to that trained on attenuation coefficient images. These results clearly favor the use of attenuation coefficient B-scans, as the structural differences visible in raw OCT intensity images alone are insufficient for reliable discrimination by the classifier.

The quantitative results in Table 6.1 further confirm the strong discriminative capability of the SVM classifier when attenuation coefficient images are used. An accuracy of 1.0 is achieved for all feature combinations, except for the MED feature alone, for which two malignant samples are misclassified, as reflected in the recall metric. In all cases, the AUC reaches 1.0, indicating robust classifier performance independent of the decision threshold. Although optimal results are obtained for the smallest band sep-

Table 6.1: Accuracy, recall, precision, and AUC of the SVM classifier for the different combination of features, at a distance between bands of 51.5 µm in the attenuation coefficient B-scans (AC) and in the raw OCT B-scans images (RAW).

Feature	Validation							
	Accuracy		Recall		Precision		AUC	
	AC	RAW	AC	RAW	AC	RAW	AC	RAW
MED	0.97	0.53	0.93	0.87	1.00	0.53	1.00	0.80
IQR	1.00	0.70	1.00	1.00	1.00	0.64	1.00	0.82
MAX	1.00	0.70	1.00	0.87	1.00	0.69	1.00	0.80
MED+MAX	1.00	0.70	1.00	0.87	1.00	0.69	1.00	0.80
MED+IQR	1.00	0.70	1.00	0.93	1.00	0.64	1.00	0.82
MAX+IQR	1.00	0.70	1.00	0.87	1.00	0.69	1.00	0.82
MED+MAX+IQR	1.00	0.70	1.00	0.87	1.00	0.69	1.00	0.82

aration, high accuracies (≥0.9) are also achieved for larger separations, particularly when using the MAX feature and feature combinations.

Overall, these results demonstrate that computing features from attenuation coefficient OCT B-scans enables accurate discrimination between non-malignant and malignant colon tumors, even when the analysis is restricted to a small spatial region of 300 µm in width and 103 µm in depth. This spatial scale is compatible with integration into microdevice-based diagnostic platforms, as previously reported in the literature [227–231].

6.6 Outlook

In summary, this chapter addresses the application of OCT imaging for the structural characterization and classification of colorectal tissues derived from the CAM model.

An SVM classifier was trained and evaluated using features computed from 8 ROI, distributed across two depth bands (4 ROI in each), and depth-resolved attenuation coefficient of B-scan OCT images of 15 non-malignant and 15 malignant colorectal tissues samples. The use of a nested cross-validation strategy ensured a robust and unbiased assessment of the classifier's performance. Using different combinations of features, such as MED + MAX, MED + IQR, MAX + IQR, and MED + MAX + IQR, the classifier achieved an accuracy of 1.0 in distinguishing between non-malignant and malignant tissue samples, demonstrating

the strong discriminative potential of the proposed methodology.

Thus, this work is the first to report about using an SVM classifier applied to attenuation coefficient images derived from OCT B-scans of tumors grown on CAM models. The results highlight the potential of the CAM assay as a reliable and reproducible platform for the study of CRC, enabling a controlled investigation of tissue optical properties and their relation to tumor morphology.

The analysis further demonstrated that the attenuation coefficient provides enhanced contrast compared to raw OCT intensity images, enabling accurate discrimination between tissue types based on structural differences. Importantly, it was shown that this discrimination can be achieved using a limited spatial region of approximately $300\,\mu m$ in width and $103\,\mu m$ in depth. This finding has significant implications for the design of future diagnostic systems, suggesting that large-area scanning may not be necessary, thereby enabling the development of more compact and efficient OCT-based devices.

Overall, this work represents a preliminary validation step toward integration of OCT imaging into clinical workflows for CRC detection. The combination of OCT with attenuation coefficient analysis and SVM classification demonstrates strong potential for real-time non-invasive identification of malignant tissues. In particular, the integration of miniaturized OCT systems into conventional colonoscopes could provide depth-resolved structural information that is currently unavailable, significantly improving diagnostic accuracy and potentially contributing to earlier detection and reduced mortality associated with CRC.

Chapter 7

Multiphoton Microscopy of Tissue Phantoms

This chapter introduces the fundamental concepts and theoretical framework underlying MPM for label-free biomedical imaging. The principles of nonlinear optical interactions are first outlined, with particular emphasis on SHG and 2PEF and their relevance in biological imaging. Building on this theoretical foundation, the design and characterization of a custom-built MPM setup are presented, followed by its application to tissue-mimicking phantoms and biological samples obtained from CAM assays. Finally, the system's capability to extract metabolic information via the optical redox ratio is assessed, demonstrating its potential for discriminating between normal and tumoral tissue and supporting future developments toward label-free optical biopsy.

7.1 Context

Historically, one of the first demonstrations of nonlinear optical phenomena in the optical regime was the SHG, reported by Franken *et al.* [232]. Although nonlinear microscopy concepts were proposed in 1978 [233] and demonstrated in the 1980s [234], the field remained relatively dormant until the development of ultrafast pulsed NIR lasers enabled practical implementations [235]. Despite significant advances [236, 237], nonlinear optical microscopy is still largely confined to specialized research environments and hindered from wider application in biomedicine, especially in histopathology, mostly due to limitations in contrast and stringent requirements for efficient signal generation [63].

Nonlinear optical processes can be broadly classified into parametric and non-parametric interactions. Parametric processes conserve photon energy and do not involve real electronic transitions. Instead, they proceed via virtual states with no net energy exchange with the medium. In contrast, non-parametric processes involve real electronic transitions and energy transfer between light and matter, as observed in absorption phenomena [238].

From a phenomenological perspective, the interaction between an intense optical field and a nonlinear material can be described as the collective response of induced dipoles within the medium. Each atom contributes an oscillating dipole moment, and the superposition of these dipoles gives rise to emitted radiation. Depending on the nonlinear process, this radiation may occur at the same frequency (degenerate processes) or at harmonic frequencies of the excitation field [238].

SHG is a second-order nonlinear optical process in which the emitted radiation has twice the frequency

of the incident light [105]. At the microscopic level, the nonlinear interaction induces dipole oscillations at double the excitation frequency. While the contribution from a single atom is negligible, the coherent summation of many dipoles can generate a detectable signal. Crucially, efficient signal generation requires phase matching, ensuring that the emitted waves remain in phase as they propagate through the material [109, 238].

Therefore, the detected signal results from the coherent superposition of fields emitted by molecular assemblies within the excitation volume, making it highly sensitive to molecular organization at the micrometer scale. Importantly, SHG occurs only in non-centrosymmetric structures, which explains its strong specificity for collagen fibers in biological tissues [63].

MPM is an advanced imaging technique that enables high-resolution, three-dimensional visualization of biological tissues. It typically combines two complementary modalities [28, 239–243]:

- multiphoton excitation fluorescence, such as 2PEF, which enables autofluorescence imaging of endogenous fluorophores (such as NAD(P)H and FAD);
- SHG, which provides structural information by detecting non-centrosymmetric components (such as collagen fibers).

Therefore, in SHG light interaction with non-centrosymmetric tissue structures such as collagen, two photons interact simultaneously and generate coherent radiation at exactly half of the excitation wavelength in the forward direction. There is no light absorption, thus, both photobleaching and photodamage associated with it are excluded in SHG. SHG only arises from media lacking a center of symmetry [1].

2PEF relies on the near-simultaneous absorption of two photons to excite a fluorophore. Because each photon carries approximately half the energy required for excitation, longer wavelengths (typically in the NIR range) are used. This results in deeper tissue penetration, reduced scattering, and lower phototoxicity compared to single-photon excitation [18, 28, 239–246]. Squirrell *et al.* [247] conducted a meticulous study, employing two-photon microscopy to monitor mitochondrial dynamics in hamster embryos over a 24 h period. Their findings highlight the superior safety of 2PEF compared to confocal microscopy (1PEF). The researchers successfully attained and sustained blastocyst and fetal development competence during 2PEF imaging, a result not replicated with confocal microscopy.

The nonlinear dependence of the excitation process confines fluorescence generation to the focal volume, inherently providing optical sectioning and reducing out-of-focus photobleaching, because the probability of two-photon absorption decreases with the distance (d) according to a d^{-4} relation. These characteristics represent major advantages over conventional confocal microscopy. Additionally, the use of NIR

wavelengths (between 700 nm and 1200 nm) places excitation within the biological optical window, further enhancing imaging depth and minimizing tissue damage, thanks to its low absorption and scattering coefficients in real biological tissues [1, 63].

Importantly, fluorescence emission spectra remain largely unchanged between 1PEF and 2PEF, as emission originates from the same excited electronic state [30]. However, excitation spectra differ significantly, with multiphoton excitation occurring at approximately twice the wavelength of single-photon excitation, often accompanied by broader spectral features [28, 30, 246].

An important difference between one-photon and two-photon excitation is the absorption coefficient, the light absorption capacity at a specific wavelength. This value is expressed as molar extinction coefficients ($M^{-1}\,cm^{-1}$) for one-photon excitation. Meanwhile, in two-photon excitation, the absorption coefficient is known as the cross-section, with its value expressed in GM ($cm^4\,s\,photon^{-1}$) units. The normal values for cross-section are between 1 and 300 GM. It is important to note that higher cross-section values increase the probability of fluorophore saturation [24, 30, 78, 246].

A key application of MPM is the investigation of cellular metabolism through the autofluorescence of NAD(P)H and FAD [18, 28, 239–243, 246]. As discussed in the introduction section of the thesis, these cofactors exhibit opposing behavior under different metabolic conditions, and their fluorescence intensity ratio, the redox ratio (NAD(P)H/FAD), serves as a robust indicator of cellular metabolic state. This metric enables differentiation between proliferative, quiescent, and apoptotic cells and has been widely applied in cancer research. Importantly, it enables the study of cancer heterogeneity, the in-situ identification of cancerous versus non-cancerous cells before observable morphological changes, and the assessment of chemotherapy responses [18, 21, 23, 25–27]. Several studies have demonstrated an increased redox ratio in human cancers, such as CRC [26], and breast and bladder [78].

MPM makes it possible to provide *in vivo* functional imaging. A unique advantage of 2PEF is the possibility of investigating three-dimensional distributions of chromophores excited with ultraviolet radiation in thick samples (such as NAD(P)H and FAD). This becomes possible because chromophores can be excited with laser radiation whose wavelength falls within the range where a tissue has a high transparency (low absorption). The excitation radiation reaches deeper layers and produces less damage in tissues. In this case, fluorescent emission lies in the visible range and comparatively easily emerges from a tissue and reaches a photodetector, which registers only the legitimate signal from the focal volume without any extraneous background [1].

Therefore, the concept of optical biopsy, which enables real-time *in vivo* tissue characterization, has gained significant interest in recent years [67–69]. Techniques such as MPM offer label-free imaging with

high spatial resolution and intrinsic molecular contrast, making them promising candidates for integration into clinical tools such as colonoscopy [75, 76].

Unlike conventional histopathology, nonlinear optical microscopy enables stain-free, real-time imaging based on endogenous contrast mechanisms. This avoids the limitations associated with exogenous markers, such as non-specific labeling, altered biological function, and heterogeneous distribution [63, 248].

Label-free nonlinear optical microscopy produces high-resolution images with rich functional and structural information based on intrinsic molecular contrast, overcoming many problems. It eliminates the need to site-specifically label or target receptors or cells and enables a broader array of volumetric signal generation from tissue structure and molecular composition [63].

Over the past decades, a variety of biological phenomena have been investigated using images based on the auto-fluorescence of endogenous molecules excited by two/three-photon processes [165, 249–252] or optical emission from specially structured molecules by second/third harmonic generation [109, 249, 253, 254]. While these studies demonstrate excellent possibilities for label-free imaging, each modality provides only a subset of intrinsically accessible information and promises to provide more comprehensive and informative images when augmented by complementary information from other modalities [63].

Simultaneous implementation of multiple nonlinear imaging modalities has been demonstrated over the last decade. One type of platform simultaneously collected the structural information (non-centrosymmetry) of SHG and the functional information of 2PEF for NAD(P)H, including its concentration and fluorescence lifetime) [23, 255–257] and three-photon fluorescence for serotonin excited at a short-wavelength band of $\leq 950\,\mathrm{nm}$ [249, 251]. The most problematic questions in these works were the efficient integration to simultaneously collect SHG, third-harmonic generation, and auto-fluorescence signals using a single (single-beam fixed-wavelength) excitation. The optimal spectral window for excitation and emission should also maximize the signal generation and detection efficiency for each multiphoton channel while ensuring orthogonality between them for spectral separation at detection [63].

The fundamental pursuit of most multiphoton microscopes is to get the most out of each pixel by pushing limits of the laser pulses in all possible domains, namely, space, time, and spectrum (and sometimes polarization). To combat the photon scarcity issue that is inherent to multiphoton imaging, careful design and implementation are needed to produce a well-focused pulse that is both short in the temporal domain and small in the spatial domain [63].

Compared to pulse conditions in the temporal and spatial domain, less attention has been paid to the optimization of spectral windows (both excitation and emission), on a single-wavelength pulsed laser or a tunable Ti-Sapphire laser with a limited spectral range [63].

The optimal excitation wavelength for SHG imaging was placed at around 900 nm for overall performance in signal strength, tissue penetration depth, and photodamage mitigation [258]. For 2PEF imaging, an excitation wavelength of 750 nm coupled with a blue detection band was optimized for imaging NAD(P)H, while an excitation wavelength of 900 nm coupled with an orange detection band was optimized for imaging FAD [165].

A major challenge with the development of a long-wavelength multiphoton platform is the significantly lower absorption cross sections of intrinsic fluorophores at longer excitation wavelengths [63]. Tu *et al*. [72] showed high-quality three-photon fluorescence imaging of NAD(P)H with 1140 ± 60 nm excitation, but this was with an undesirable cost of imaging speed (pixel dwelling time ranged from 200 µs to 1 ms).

Based on the insights gathered, particularly from the state of the art, a MPM system optimized for 2PEF measurements was developed. The optical setup is described in detail, followed by a comprehensive characterization of key parameters, such as focal spot size and spatial resolution, which is essential for controlled excitation and accurate scanning strategies.

Subsequently, the developed system was applied to the study of colorectal tissue-mimicking phantoms with increasing levels of complexity, ranging from simple fluorophore solutions to solid phantoms incorporating scattering and absorbing components. The acquired fluorescence signals were processed and analyzed using a robust workflow, with particular emphasis on the extraction of the redox ratio as a metabolic biomarker.

Finally, the capability of the proposed approach, including the selected excitation and emission wavelengths, to discriminate between normal and tumoral conditions was evaluated, with the aim of assessing its potential for future application in label-free optical biopsy and biomedical diagnostics. Special attention was given to the challenge of efficiently exciting and detecting signals from both fluorophores (NAD(P)H and FAD) using a single excitation wavelength (750 nm), a key step toward enabling simultaneous signal acquisition and reducing overall measurement time.

7.2 Theoretical Framework

The induced polarization in a material (P_{material}) can be expressed as shown in Equation 2.14, which is repeated here for convenience [105, 109]:

$$P_{\text{material}} = \varepsilon_0 \left(\sum \chi_{ij}^{(1)} E_j + \sum \chi_{ijk}^{(2)} E_j E_k + \sum \chi_{ijkl}^{(3)} E_j E_k E_l \right), \tag{7.1}$$

As previously discussed, the first term corresponds to linear optical phenomena, such as reflection, refraction, and one-photon absorption. The second term gives rise to second-order nonlinear processes, including SHG and frequency mixing, while the third term is responsible for third-order effects such as third-harmonic generation, 2PEF, and coherent Raman scattering [63, 105, 109].

In this chapter, particular emphasis is placed on SHG and 2PEF. These nonlinear processes require very high light intensities, typically in the range of $100\,\mathrm{MW\,cm^{-2}}$ to $\mathrm{TW\,cm^{-2}}$. Consequently, the most critical component of a MPM system is the light source, generally a femtosecond NIR laser. These lasers emit trains of ultrashort pulses with repetition rates ranging from the kilohertz to the hundreds of megahertz regime, depending on the laser architecture [1].

When such pulses are tightly focused into a small volume (on the order of a few micrometers), extremely high peak power densities can be achieved (up to $10^{13}\,\mathrm{W\,cm^{-2}}$). Under these conditions, nonlinear absorption processes occur, leading to the excitation of electronic states and, in some cases, the generation of free electrons within the focal volume. The allowable intensity strongly depends on the pulse duration: for continuous or long pulses (1 s), intensities should remain below $10\,\mathrm{W\,cm^{-2}}$, whereas for ultrashort pulses (10^{-9} s), intensities can reach up to $10^{9}\,\mathrm{W\,cm^{-2}}$ [1].

In typical two-photon microscopy applications, commonly reported laser parameters include excitation wavelengths in the range of 700 nm to 960 nm, pulse durations around 150 fs, repetition rates between 76 MHz and 80 MHz, and average powers generally below 10 mW at the sample. These specifications can be achieved using various laser technologies, including mode-locked dye lasers pumped by Nd:YAG sources, Ti:sapphire lasers pumped by Ar lasers, diode-pumped solid-state lasers, and fiber lasers [1]. In general, nonlinear optical effects are efficiently induced when the pulse duration is comparable to or shorter than the relaxation time of biological molecules, typically $\tau \leq 10^{-13}$ s [1].

The occurrence and efficiency of nonlinear optical processes are strongly dependent on the symmetry properties of the material. In centrosymmetric media, second-order nonlinear effects are forbidden, and only third-order processes can occur. In contrast, non-centrosymmetric materials allow both second- and third-order nonlinear interactions [238]. This dependence on material structure plays a crucial role in determining which nonlinear processes dominate under specific experimental conditions.

A schematic comparison between SHG and 2PEF is presented in Figure 7.1, highlighting the different excitation mechanisms and emission pathways involved in each process. SHG (Figure 7.1(a)) is a coherent process involving a virtual state, where two photons are instantaneously combined to generate a single photon at twice the frequency. In 2PEF (Figure 7.1(b)), two photons are absorbed to populate a real excited state, followed by radiative relaxation.

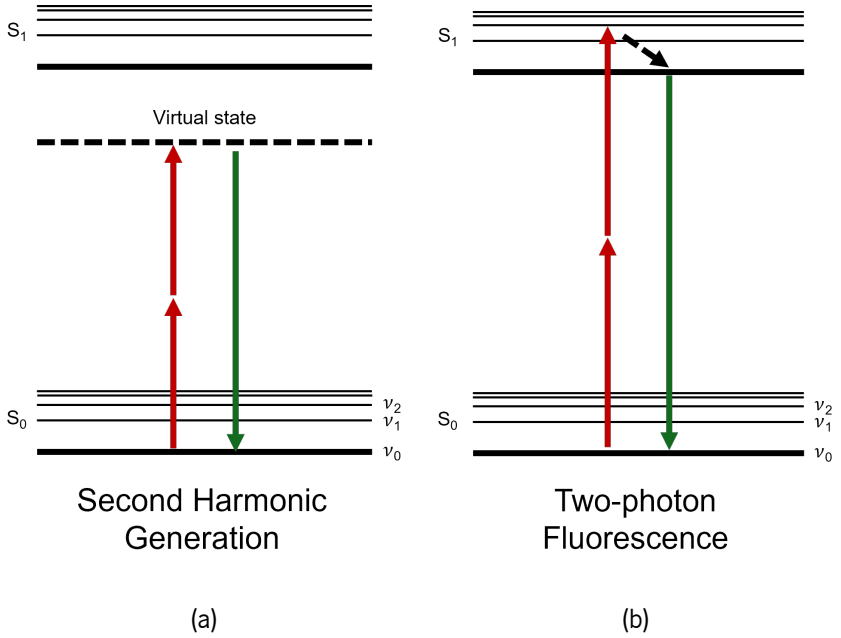


Figure 7.1: Energy-level diagrams comparing: (a) SHG; and (b) 2PEF.

7.2.1 Second Harmonic Generation

One of the most important second-order nonlinear optical processes is SHG, in which two photons of the same frequency $(\omega_1 = \omega_2 = \omega)$ interact within a nonlinear medium to generate a new photon at twice the frequency $(\overline{h}\omega_3 = \overline{h}\omega + \overline{h}\omega)$. This process can be described by [100]:

$$\vec{P}^{(2)} = \varepsilon_0 \chi^{(2)} \left(\omega_3; \omega, \omega\right) \vec{E}_\omega^2 \tag{7.2}$$

$$I_{\omega_3} \propto \left|\vec{P}_{\omega_3}\right|^2 \propto \left|\chi^{(2)} \left(\omega_3; \omega, \omega\right)\right|^2 I_\omega^2 \tag{7.3}$$

These expressions highlight the quadratic dependence of the SHG intensity on the incident field intensity.

Considering an incident electric field defined as [105]:

$$\tilde{E}(t) = Ee^{-i\omega t} + c.c., \tag{7.4}$$

the second-order polarization can also be expressed as [105]:

$$\tilde{P}^{(2)}(t) = \epsilon_0 P^{(2)}(0) + P^{(2)}(2\omega)e^{-j2\omega t} + c.c. = \frac{1}{4}\epsilon_0 \chi^{(2)} \left|E(\omega)\right|^2 + \frac{1}{4}\epsilon_0 \chi^{(2)} E^2(\omega)e^{-j2\omega t} + c.c. \tag{7.5}$$

It is important to note that $\vec{P}$ denotes the real vector polarization, while $\tilde{P}(t)$ represents its complex time-dependent form used for harmonic analysis.

Equation 7.5 contains two main contributions: a static term associated with optical rectification and a time-dependent term oscillating at 2ω, corresponding to the SHG. As expected, the latter exhibits a quadratic dependence on the incident field amplitude.

Harmonic generation is a parametric process involving only virtual states (Figure 7.1(a)), which means that no real population transfer occurs between energy levels. As a result, the process is effectively instantaneous when compared to fluorescence, where finite excited-state lifetimes are involved.

The efficiency of SHG is strongly influenced by phase-matching conditions. From the coupled-wave formalism, the generated intensity can be expressed as:

$$I \propto \left[\frac{\sin\left(\frac{\Delta k L}{2}\right)}{\frac{\Delta k L}{2}} \right]^2, \tag{7.6}$$

where $\Delta k = 2k_\omega - k_{2\omega}$ represents the phase mismatch between the interacting waves. The maximum conversion efficiency is achieved when $\Delta k = 0$, corresponding to perfect phase matching.

Phase matching is intrinsically linked to the coherent nature of SHG. Unlike fluorescence, which is an incoherent process involving spontaneous emission from excited states, SHG arises from the coherent superposition of the nonlinear polarization induced across the excitation volume. As a result, the generated second-harmonic waves preserve a fixed phase relationship with the incident field, and their constructive or destructive interference depends critically on the relative phase between different emitting regions. This coherence is directly responsible for the strong dependence of SHG efficiency on phase-matching conditions and leads to highly directional emission, typically in the forward propagation direction. In heterogeneous or highly scattering media, such as biological tissues, partial phase mismatch and structural disorder can give rise to backward-emitted SHG signals, which still retain information about the underlying organization of the nonlinear scatterers.

In biological tissues, perfect phase matching is rarely achieved due to structural disorder and dispersion. Instead, quasi-phase-matching conditions arise, leading to a distribution of forward- and backward-emitted SHG signals. These directional components provide valuable information about the organization of fibrous structures, such as collagen, and have been used to assess tissue morphology and pathology [258].

Therefore, the efficiency and occurrence of SHG are strongly dependent on the symmetry properties of the medium. Second-order nonlinear processes are forbidden in centrosymmetric materials [253].

Under spatial inversion:

$$\vec{P} \to -\vec{P}, \quad \vec{E} \to -\vec{E}, \tag{7.7}$$

for a second-order process:

$$-\tilde{P}^{(2)}(t) = \epsilon_0 \chi^{(2)} \left(-\tilde{E}(t)\right)^2 = \epsilon_0 \chi^{(2)} \tilde{E}(t)^2 \tag{7.8}$$

For these conditions to be simultaneously satisfied, it follows that $\chi^{(2)} = 0$, demonstrating that second-order nonlinear effects vanish in centrosymmetric media [238].

Consequently, SHG can only occur in non-centrosymmetric materials. This imposes strict constraints on the types of biological structures that can generate SHG signals. In practice, this makes SHG highly selective for ordered, non-centrosymmetric assemblies, such as collagen fibers.

Collagen molecules exhibit a triple-helical structure formed by three α-chains, lacking inversion symmetry. These molecules assemble into fibrils with diameters ranging from approximately 20 nm to 250 nm, which further organize into fibers with diameters spanning from 500 nm to several micrometers [259]. This hierarchical organization satisfies the structural requirements for efficient SHG generation, enabling visualization of collagen architecture in biological tissues.

Overall, the strong dependence of SHG on molecular symmetry, organization, and phase matching makes it a powerful tool for probing structural properties in biological systems. Its sensitivity to non-centrosymmetric structures and interfacial properties enables applications ranging from collagen imaging in tissues to the investigation of surface charge, molecular orientation, and symmetry.

7.2.2 Two-photon Excitation Fluorescence

In materials where second-order nonlinear processes are weak or forbidden (e.g., centrosymmetric media), third-order nonlinearities become dominant. The third-order susceptibility, $\chi^{(3)}$, gives rise to several nonlinear optical effects, including third-harmonic generation, the optical Kerr effect, four-wave mixing, SRS, stimulated Brillouin scattering, and 2PEF.

The third-order nonlinear polarization can be expressed as:

$$\vec{P}_{\omega_4} = \varepsilon_0 \chi^{(3)} \left(\omega_4; \omega_1, \omega_2, \omega_3\right) \vec{E}_{\omega_1} \vec{E}_{\omega_2} \vec{E}_{\omega_3} \tag{7.9}$$

In transparent media, third-order nonlinear interactions primarily generate new frequency components. In contrast, in absorbing media, processes such as Raman scattering, Brillouin scattering, and multiphoton absorption become dominant.

In 2PEF, two low-energy photons are absorbed nearly simultaneously, resulting in an electronic transition to a higher-energy excited state in a fluorescent molecule (Figure 7.1(b)) [236, 260, 261]. Unlike parametric nonlinear processes, multiphoton fluorescence involves real electronic states and population

transfer, followed by spontaneous emission. Consequently, 2PEF is an incoherent process, in contrast to coherent processes such as SHG. The probability of excitation depends on the likelihood of two photons interacting with the molecule within an extremely short time window (on the order of 10^{-16} s).

The first demonstration of two-photon microscopy was reported in 1990 [29]. Since then, MPM has become a key technique for *in vivo* and deep-tissue imaging, enabling applications such as monitoring calcium dynamics in the brain, lymphocyte trafficking, angiogenesis, and cancer metastasis [236, 237, 262].

In two-photon excitation, two NIR photons are absorbed simultaneously to generate fluorescence typically in the visible range (Figure 7.1(b)).

The intensity of the 2PEF signal can be expressed as [1]:

$$I_{2f}(t) = k\left(\frac{4}{\pi}\right)^2 \sigma_2 \eta \left(\frac{P_0}{\tau_p f_p}\right)^2 \left[\frac{(NA)^2}{hc\lambda_{exc}}\right]^2 \tag{7.10}$$

where P_0 is the average incident power, τ_p is the pulse duration, f_p is the pulse repetition rate, $\sigma_2 = \sigma_2(\lambda_{exc})$ is the two-photon absorption cross section, $\eta = \eta(\lambda_{em})$ is the fluorescence quantum yield, NA is the numerical aperture of the objective, k accounts for the collection efficiency, h is Planck's constant, c is the speed of light, and λ_{exc} is the excitation wavelength. Note that $I_{2f}(t)$ denotes the instantaneous two-photon fluorescence rate generated during the pulse itself, rather than the rate averaged over the full pulse period. Therefore, the efficiency of an n-photon process scales with the n-th power of the excitation intensity, following a P^n dependence. For 2PEF, the signal scales as P^2/τ_p, indicating that higher peak power and shorter pulse durations (τ_p) enhance fluorescence generation [1].

The time-averaged fluorescence photon flux can be written as [105, 236, 237]:

$$\left\langle F^{(n)}(t)\right\rangle = \frac{1}{n}\frac{g_p^{(n)}}{\left(f_{rep}\tau_{pulse}\right)^{n-1}}\eta_{quantum}\eta_{collect}C_{conc}\sigma_{abs}\frac{(NA)^{2n-4}}{8\pi^{3-n}\lambda^{2n-3}} \times \left(\frac{\langle P(t)\rangle\lambda}{hc}\right)^n, \tag{7.11}$$

where n is the number of photons involved in the process, $g_p^{(n)}$ is the temporal coherence of the excitation source, τ_{pulse} is the laser pulse duration, $\eta_{quantum}$ is the fluorescence quantum efficiency, $\eta_{collect}$ is the system collection efficiency, C_{conc} is the concentration of the fluorescent molecules, σ_{abs} is the n-photon absorption cross section of the fluorophore, and λ is the excitation wavelength in vacuum. From this expression, it is evident that the fluorescence signal strongly depends on the quantum efficiency and the multiphoton absorption cross section of the fluorophore under fixed excitation conditions.

The multiphoton absorption cross-section can be estimated using perturbation theory [263]. The probability of multiphoton excitation is determined by the molecular cross-sectional area (typically on the order

of 10^{-16} cm^2) and the photon coincidence time, associated with the lifetime of virtual intermediate states (approximately 10^{-16} s) [262]. Based on these considerations, the two-photon absorption cross-section is estimated to be on the order of 100 GM, which is consistent with experimental observations [262]. The relatively low cross-section of higher-order nonlinear processes explains why 2PEF remains the most widely used multiphoton modality.

The fluorescence quantum efficiency can vary significantly depending on the molecular environment. For example, bound NAD(P)H exhibits a quantum yield up to ten times higher than that of its free form [264], highlighting the strong influence of molecular properties on signal generation.

Optimization of excitation parameters is therefore essential to maximize signal generation. From the expressions above, it follows that the fluorescence signal can be enhanced by reducing the repetition rate, shortening the pulse duration, increasing the numerical aperture, and selecting shorter excitation wavelengths, while maintaining the same average power.

Finally, 2PEF and SHG differ significantly in their spectral and temporal characteristics. In 2PEF, the emission spectrum is determined by the electronic structure of the fluorophore, and the fluorescence lifetime is typically in the order of nanoseconds. In contrast, SHG is an instantaneous coherent process, where the emitted signal is temporally synchronized with the excitation pulse and its spectral bandwidth, scales as $\frac{1}{\sqrt{2}}$ of the excitation pulse bandwidth. Additionally, SHG depends on the square of the molecular density and does not involve absorption, although it can be resonance-enhanced when the harmonic frequency overlaps with an electronic transition [1].

7.3 Multiphoton Microscopy Setup

7.3.1 Setup Description

To acquire 2PEF and SHG signals, an experimental setup was developed and is illustrated in Figure 7.2. The setup can be divided into four main parts: the excitation arm, which generates the light and directs it onto the sample; the imaging arm, an auxiliary arm that works as a microscope to assist in sample visualization; and two additional arms for detection (transillumination and reflection), used for transparent and opaque samples, respectively.

The excitation source of the setup was a mode-locked Ti:sapphire laser (Mira 900-f, Coherent Inc.) oscillator pumped by a frequency-doubled CW Neodymium-laser (Verdi, Coherent Inc.), which generates femtosecond pulses from 700 nm to 1000 nm.

In normal operating conditions, the source produces 10 nJ pulses with a duration of approximately 85 fs

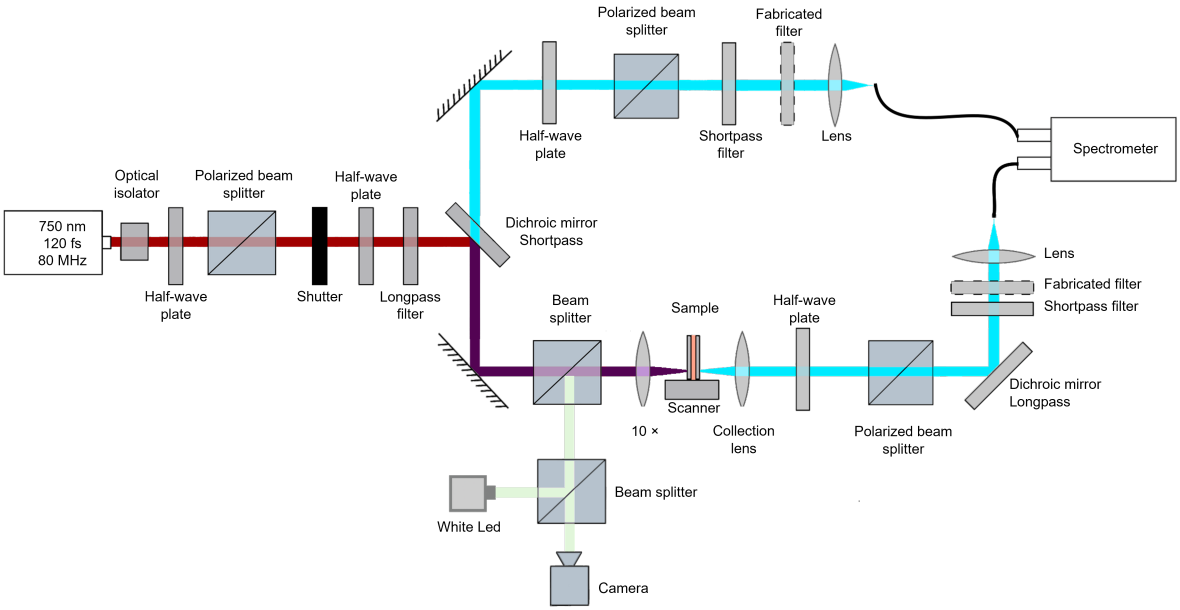


Figure 7.2: MPM experimental setup for 2PEF measurements, including excitation beam conditioning, polarization control, auxiliary imaging arm (white-light source and camera), and detection system with spectral filtering and spectrometer acquisition (both transmission and reflection paths).

and a bandwidth of 11 nm at a constant repetition rate of 76 MHz. The short pulses are generated by a process called Kerr lens mode-locking [265], to force the different cavity modes to oscillate in phase with each other. This causes the modes to interfere constructively to form a single and intense short pulse at a repetition rate equal to the round-trip time of the oscillator laser cavity. The greater the number of modes oscillating together at a fixed phase, the shorter the pulse duration [266]. To synchronize the phase of the circulating laser modes, some sort of modulation is introduced into the cavity. In this case, the passive mode-locking technique is used, more specifically, a Kerr lens mode-locking in which intense light alters the local refractive index. When a sufficiently intense light beam passes through the gain medium, the third-order susceptibility provokes a temporary increase in the medium's refractive index proportional to the incident light's intensity. Since the beam has a higher intensity on axis, this provokes a positive lens that focuses the beam downstream. By placing a narrow aperture at the point where the Kerr lens focuses the beam to its smallest diameter, intense pulses will experience lower losses and be favored over the lower intensity continuous wave oscillation. To initiate this process, an initial perturbation is required. This perturbation will provoke a random increase in the light circulating in the cavity, initiating the Kerr lens self-focusing mechanism.

Immediately after the laser output, an optical isolator (IQ-5-NIR-Mpa, Thorlabs) was introduced to pro-

tect the laser cavity from back reflections that could arise from optical elements downstream, such as half-wave plates and polarizing beam splitters.

Control of the incident laser power was achieved using a zero-order half-wave plate (464-4215, Eksma) followed by a calcite Glan–Taylor polarizer (Glan-laser $\lambda/2$ PSG 800 nm, Eksma). This combination allowed continuous and precise adjustment of the excitation power delivered to the sample.

A software-controlled shutter was positioned after this unit. This shutter enables the laser beam to be blocked, allowing background noise measurements to be acquired between successive acquisitions.

A second half-wave plate (464-4215, Eksma), mounted on a motorized rotation stage and controlled via software, was placed after the power control optics and the shutter. This element enabled control of the polarization orientation of the incident beam, allowing variation of the effective incident polarization at the sample. This capability was particularly relevant for experiments involving polarization-dependent nonlinear processes, such as SHG.

To suppress spurious nonlinear signals generated within upstream optical components, such as half-wave plates or polarizing elements, a long-pass filter (FELH0600, Thorlabs) was inserted before the beam-steering optics. This filter removes any unwanted short-wavelength radiation originating from phenomena such as SHG within the optical train.

Beam delivery to the sample was achieved using a short-pass dichroic mirror (ff720 SDi01 25x36, Semrock), which reflected the excitation beam toward the sample while transmitting the backward-propagating fluorescence and second harmonic signals generated at the sample.

A $50/50$ beam splitter (BS013, Thorlabs) was optionally inserted into the excitation path. This beam splitter was only used when the auxiliary imaging arm of the setup was active and was removed during fluorescence and second-harmonic measurements. The imaging arm, comprising a white-light source (MCWHL5, Thorlabs) and a camera (D1024G13C (DCU224C), Thorlabs), functioned as an optical microscope and was used to visualize the sample surface and assist in selecting the ROI for laser excitation.

The excitation beam was then focused onto the sample using a $\times 10$ objective (CFI Plan Fluor, Nikon). Samples were positioned at the focal plane using a xyz piezo-controlled translation stage (P-616.3c NanoCube, PI), providing sub-micrometer positioning precision.

In the detection arm along the transillumination direction, the emitted signal was collected using a best-form lens with a focal length of 40 mm (LBF254-040-A, Thorlabs) to collimate the fluorescence and nonlinear signals.

The collimated beam then passed through a half-wave plate (WPH05M-405, Thorlabs) and a calcite Glan–Taylor polarizer (GI10-A, Thorlabs). The half-wave plate, also software-controlled, allowed analysis of

the polarization state of the detected signal, which is particularly relevant for studies involving SHG. The polarizer ensured that only horizontally polarized light reached the detector, corresponding to the optimal sensitivity axis of the detection system.

Spectral filtering at the transillumination arm was achieved using a long-pass dichroic mirror (DMLP650, Thorlabs), which efficiently suppressed residual excitation light while reflecting approximately $99\,\%$ of the emitted fluorescence.

The signal subsequently passed through a short-pass filter (FESH0600, Thorlabs) followed by one of the fabricated band-pass filters. Finally, the filtered light was focused by an aspheric lens (C220TME-A f=11 nm, Thorlabs) into a fiber bundle coupled to an imaging spectrometer (Shamrock 300i, Andor Technology), equipped with a cooled CCD array (Newton DU920 UVB, Andor Technology).

When measurements were performed in reflection rather than transillumination mode, the overall configuration remained unchanged. In this case, the emitted signal was collected and collimated by the same objective used to focus the excitation beam, eliminating the need for the external collection lens.

It is important to notice that despite the theoretical Fourier limit of the pulse duration being approximately $85\,$fs, the actual pulse duration at the sample was estimated to be stretched to around $120\,$fs. This elongation in pulse duration can be attributed to the combined effect of the calcite polarizer and the microscope objective in the experimental setup.

In Figure 7.3, a Rhodamine B solution placed in the developed setup and the resulting 2PEF signal can be observed. The image shows that fluorescence (yellow emission) is generated only at the focal point,

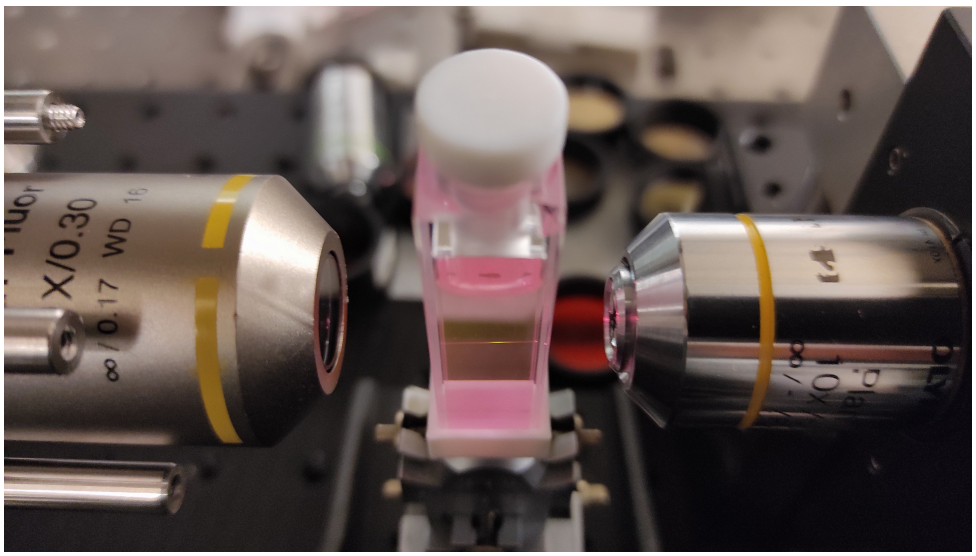


Figure 7.3: Experimental multiphoton microscopy setup showing a cuvette containing a Rhodamine B solution positioned at the focal region between the excitation and collection objectives.

rather than along the entire beam path, as expected for nonlinear phenomena.

7.3.2 Setup Characterization

Focal point diameter

One important characterization of the experimental setup is the size of the focal spot, as it determines the area of the sample illuminated at any given time. This information is essential for defining the appropriate step size during the scanning of solid samples.

To estimate the focal spot size, it was first necessary to measure the beam diameter at the entrance of the objective (Position 2), since no equipment was available to directly measure the beam at the focal plane after the objective. For this purpose, a knife-edge experiment was performed at the entrance of the objective to determine the beam diameter at this position. Among the various beam profiling techniques, the knife-edge method is widely used due to its simplicity and high accuracy. This method does not require a camera or spatial resolving detector. Instead, it relies on measuring the integrated power of a Gaussian beam as it is progressively occluded by a sharp edge.

The laser beam exhibits a transverse intensity distribution that follows a Gaussian profile. At the focal plane, assuming propagation along the z-axis, the intensity distribution can be expressed as [194]:

$$I(x, y) = I_0 \cdot e^{-\frac{2(x^2+y^2)}{w^2}}, \tag{7.12}$$

where I_0 is the peak intensity at the beam center, and w is the beam radius defined at the $1/e^2$ intensity level (i.e., the radial distance at which the intensity drops to approximately 13.5% of its maximum value). At the focus, this parameter corresponds to the beam waist [194].

In the knife-edge technique, a sharp opaque blade is translated across the beam along one transverse direction (denoted as x), while a photodetector placed behind the blade measures the transmitted power. As the blade position D progressively blocks the beam, the detected power $P(D)$ decreases from its maximum value (P_∞) to zero [267, 268].

The transmitted power can be expressed as [268]:

$$P(D) = P_\infty \int_D^{+\infty} I(x)dx, \tag{7.13}$$

which, for a Gaussian beam profile, leads to [268]:

$$P(D) = P_\infty \cdot \frac{1}{2} \cdot \text{erfc}\left(\sqrt{2} \cdot \frac{D - D_0}{w}\right), \tag{7.14}$$

where D_0 represents the beam center position, and erfc is the complementary error function, defined as:

$$\text{erfc}(a) = \frac{2}{\sqrt{\pi}} \int_a^{+\infty} e^{-t^2} dt \tag{7.15}$$

The resulting curve is a monotonically decreasing S-shaped function, approaching P_∞ when the blade is fully retracted and tending to zero when the beam is completely blocked. Experimentally, the transmitted power is recorded as a function of the blade position to obtain this characteristic curve (Figure 7.4) [268].

During the setup alignment, it was observed that the laser beam was not perfectly collimated and exhibited slight convergence along its propagation path. To account for this effect and improve the estimation of the beam waist after the objective, a second knife-edge measurement was performed at a position 105 cm before the objective (Position 1). This allows the beam propagation characteristics to be considered in subsequent calculations.

Two independent knife-edge measurements were therefore performed, one at each position. The corresponding experimental curves are shown in Figure 7.4.

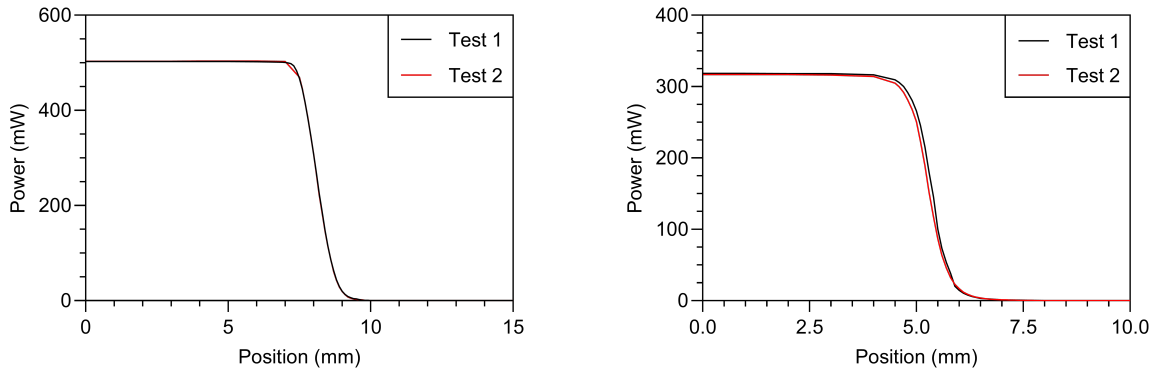
In this work, the experimental data were then fitted using a nonlinear least-squares algorithm (Levenberg–Marquardt method) implemented in Python using the SciPy library. The fitting procedure provides two key parameters: the beam center position (D_0) and the beam radius (w).

From the fitted curves, the mean beam radius was determined to be 0.954 mm at Position 1 and 0.758 mm at Position 2.

Since the laser beam exhibits a slight convergence along its propagation path, it can be schematically represented as shown in Figure 7.5.

In this representation, z_1 corresponds to Position 1 of the knife edge measurement, z_2 to Position 2 (the entrance of the objective), to the location of the beam waist (focal point) of the laser in the absence of the objective. In this work z_3 is defined as 0.

From the knife-edge measurements, the beam diameters were determined to be $2w_1 = 1.908$ mm



(a) (b)

Figure 7.4: Knife-edge measurements of the laser beam (750 nm) at two positions along the optical path: (a) Position 1, located 105 cm before the objective; (b) Position 2, at the entrance of the objective.

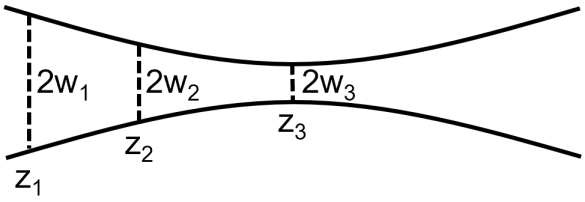


Figure 7.5: Schematic representation of the Gaussian beam propagation along the optical axis, illustrating the variation of the beam diameter from $2w_1$ at position z_1 to $2w_2$ at z_2, and approaching the beam waist $2w_3$ at z_3.

(Position 1) and $2w_2 = 1.516$ mm (Position 2). The axial separation between these positions is $\Delta z = z_2 - z_1 = 1050$ mm.

Assuming Gaussian beam propagation, the beam radius at a given position (z) can be given by [269]:

$$w(z)^2 = w_0 \left(1 + \left(\frac{(z - z_0)\lambda}{w_0^2 n \lambda}\right)\right), \tag{7.16}$$

where w_0 is the radius at the focal point $(w_0 = w_3)$, z_0 is the position of the focal point $(z_0 = z_3 = 0)$, n is the refractive index of the medium where the light is traveling (in this work is air, so $n = 1$), and λ is the light wavelength (750 nm). So, it is possible to obtain the following system of equations:

$$\begin{cases} w_1^2 = w_3^2 \left(1 + \frac{|z_1|^2}{z_R^2}\right) \\ w_2^2 = w_3^2 \left(1 + \frac{|z_2|^2}{z_R^2}\right) \\ z_R = \frac{\pi w_3^2}{\lambda} \\ z_2 - z_1 = 1050\,\text{mm} \end{cases}, \tag{7.17}$$

where z_R is Rayleigh range.

The system of equations can be solved, yielding:

$$\begin{cases} z_1 = -1900.86\,\text{mm} \\ z_2 = -850.86\,\text{mm} \\ w_3 = 0.70\,\text{mm} \\ z_R = 2053.24\,\text{mm} \end{cases} \tag{7.18}$$

These results indicate that both measurement positions are located before the beam waist, confirming the converging nature of the beam in this region.

After introducing the objective into the laser path, the propagation of the beam can be described as illustrated in Figure 7.6. The objective, represented by the element M, modifies the convergence of the

incident Gaussian beam, effectively transforming its propagation characteristics.

At position z_2, corresponding to the entrance of the objective, the beam has a diameter $2w_2$ and a radius of curvature R_2, reflecting the fact that the beam is converging. Upon passing through the objective, the beam is refracted and emerges at position z_4 with a new diameter $2w_4$ and a modified radius of curvature R_4. This change in curvature indicates that the objective has altered the wavefront of the beam, leading to a stronger convergence toward a new focal point. The objective thus acts as a focusing element, reducing the beam diameter and shifting the position of the beam waist closer to the sample. As a result, the beam achieves a smaller focal spot size.

This representation highlights the transformation of the beam parameters, namely the wavefront curvature, before and after the objective, providing a basis for estimating the focal spot size at the sample plane.

According to Menzel *et al.* [269], the wavefront curvature at a given position (z), can be given by:

$$R(z) = z - z_0 + \frac{1}{z - z_0}\left(\frac{w_0^2 n\pi}{\lambda}\right)^2 \tag{7.19}$$

So, the radius of curvature of the beam at Position 2 can be written as:

$$R_2 = z_2 + \frac{1}{z_2}\left(\frac{w_3^2 \cdot \pi}{\lambda}\right)^2 \tag{7.20}$$

By substituting $z_2 = -850.86\,\text{mm}$, and $w_3 = 0.70\,\text{mm}$, the radius of curvature at this position is $R_2 = -5805.61\,\text{mm}$.

The effect of the objective on the Gaussian beam can be described using the ABCD matrix formalism.

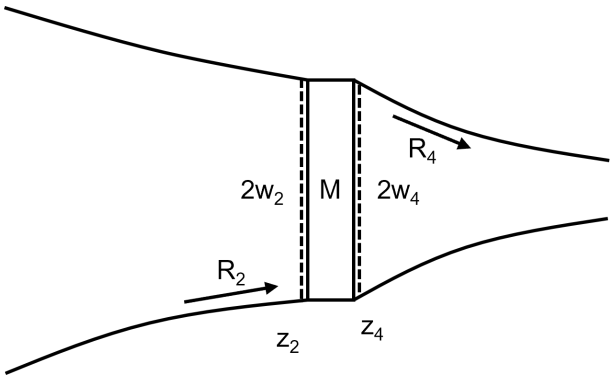


Figure 7.6: Schematic representation of the Gaussian beam propagation through the objective lens M, illustrating the modification of the beam diameter and wavefront curvature from $2w_2$ and R_2, at the entrance (z_2), to $2w_4$ and R_4, after the objective (z_4).

For a thin lens (objective) with focal length f, the transfer matrix is given by [269]:

$$M = \begin{pmatrix} 1 & 0 \\ \frac{-1}{f} & 1 \end{pmatrix} \tag{7.21}$$

In this work, $f = 20\,\text{mm}$ (×10 objective CFI Plan Fluor, Nikon).

Using the standard Gaussian beam transformation through an optical system, the beam radius w_4 and radius of curvature R_4 after the objective can be expressed as [269]:

$$\begin{cases} w_4^2 = \frac{2abR_2w_2^2+a^2R_2^2w_2^4+b^2\left(w_2^4+\frac{R_2^2\lambda^2}{\pi^2}\right)}{R_2^2w_2^2w(ad-bc)} \\ R_4 = \frac{2abR_2w_2^4+a^2R_2^2w_2^4+b^2\left(w_2^4+\frac{R_2^2\lambda^2}{\pi^2}\right)}{aR_2(d+cR_2)w_2^4+b\left(cR_2w_2^4+d\left(w_2^4+\frac{R_2^2\lambda^2}{\pi^2}\right)\right)} \end{cases} \tag{7.22}$$

being the a,b,c,d, the values of the ABCD matrix of the objective, so it is possible to obtain:

$$\begin{cases} w_4^2 = \frac{R_2^2w_2^4}{R_2^2w_2^2} \\ R_4 = \frac{R_2}{1-\frac{R_2}{f}} \end{cases} \tag{7.23}$$

Substituting the known values yields $w4$ =0.758 mm and R_4 =-19.93 mm. This result indicates a strong modification of the wavefront curvature induced by the objective, leading to a rapid convergence of the beam toward its focal point.

After the objective, the beam propagates a distance L in free space until the focal point, as illustrated in Figure 7.7. The corresponding ABCD matrix for free-space propagation is [269]:

$$\begin{pmatrix} 1 & L \\ 0 & 1 \end{pmatrix} \tag{7.24}$$

The beam waist is reached when the radius of curvature becomes infinite $(R5 = \infty)$, so $\frac{1}{R_5} = 0$.

Using the Gaussian beam propagation relations, the beam radius w_5 waist can be obtained by solving the following system [269]:

$$\begin{cases} w_5^2 = \frac{R_4^2w_4^4+2LR_4w_4^4+L^2\left(k^2R_4^2+w_4^4\right)}{R_4^2w_4^2} \\ \frac{1}{R_5} = \frac{R_4w_4^4+L\left(k^2R_4^2+w_4^4\right)}{R_4^2w_4^4+2LR_4w_4^4+L^2\left(k^2R_4^2+w_4^4\right)} \\ k = \frac{\lambda}{\pi} \end{cases} \tag{7.25}$$

Thus, it is possible to obtain $w_5 = 6.28\,\mu\text{m}$ and $L = 19.93\,\text{mm}$.

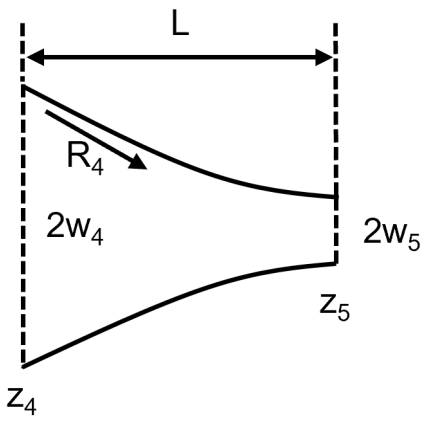


Figure 7.7: Schematic representation of the Gaussian beam propagation after the objective lens, showing the evolution of the beam radius from $2w_4$ at position z_4 to the minimum beam waist $2w_5$ at position z_5. The parameter R_4 represents the radius of curvature of the wavefront immediately after the objective, while L denotes the propagation distance required to reach the focal point where the beam waist is formed.

Therefore, the beam reaches its minimum size at approximately 19.93 mm after the objective, with a waist radius of 6.28 µm. This corresponds to a beam diameter at the focal point of:

$$2w_5 = 12.56\,\mu\text{m} \tag{7.26}$$

The result provides an estimate of the illuminated area at the sample, which is a critical parameter for defining the step size in scanning experiments.

Lateral and axial resolution

Another important characterization of the setup is its lateral and axial resolution. In the case of 2PEF, not all the illuminated volume contributes equally to fluorescence, due to the quadratic dependence of the signal on the incident intensity. As a result, the effective excitation volume is smaller than the diffraction-limited focal spot.

Zipfel *et al.* [236] defined the following expressions for the lateral and axial resolution of a multiphoton system:

$$\omega_{xy} = \begin{cases} \frac{0.320\lambda}{\sqrt{2}\cdot \mathrm{NA}}, & \mathrm{NA} \leq 0.7 \\ \frac{0.325\lambda}{\sqrt{2}\cdot \mathrm{NA}^{0.91}}, & \mathrm{NA} > 0.7 \end{cases} \tag{7.27}$$

$$\omega_z = \frac{0.532\lambda}{\sqrt{2}} \left[\frac{1}{n - \sqrt{n^2 - \mathrm{NA}^2}} \right] \tag{7.28}$$

Considering the objective numerical aperture NA $= 0.25$, the lateral resolution is given by:

$$\omega_{xy} = 0.679\,\mu\text{m} \tag{7.29}$$

For the axial resolution, assuming a refractive index $n = 1.34$, representative of biological tissue [2, 225], the following value is obtained:

$$\omega_z = 11.99\,\mu\text{m} \tag{7.30}$$

The significant difference between lateral and axial resolutions is expected in low-NA systems. While the lateral resolution scales inversely with NA, the axial resolution depends more strongly on NA^2, resulting in an elongated focal volume along the propagation direction.

Equations 7.27 and 7.28 give the diffraction-limited lateral and axial resolution corresponding to full utilization of the objective's numerical aperture. As shown before, the excitation beam did not fill the entire back aperture of the objective (12 mm), consequently, the values reported here represent the best-case resolution achievable with this objective, rather than the resolution actually realized in the present setup.

It is important to note that during scanning, the sample was translated by a distance equal to the focal spot diameter, even though not all the illuminated area generates fluorescence. In this case, since no biological samples were analyzed and no significant variations were expected between adjacent regions of the phantom, this approach was adopted to minimize photodamage and reduce thermal effects induced by the laser. Consequently, re-irradiation of the same area was intentionally avoided. In future studies, particularly when detecting more subtle spatial variations becomes necessary, the step size should be reduced to match the lateral resolution.

7.4 Experimental Methods

7.4.1 Data Acquisition and Processing

The 2PEF measurements were performed using the non-miniaturized experimental setup described in a previous section (Figure 7.2), operating in transmission mode.

For liquid phantoms, the samples were placed in a cuvette, mounted on the piezo-controlled translation stage. Measurements were acquired at a single location within each sample. However, the exact position varied slightly between acquisitions, as identical positioning could not be guaranteed across different measurement times. Before data acquisition, the cuvette position was adjusted to maximize the fluorescence intensity.

For solid phantoms, the samples were mounted in a custom 3D-printed holder attached to the piezo-controlled translation stage. For each solid phantom, a 2D scan was performed, and fluorescence signals were acquired at multiple spatial positions corresponding to adjacent pixels. The translation step between pixels was defined according to the focal spot size ($12.56\,\mu$m), ensuring that each measurement corresponded to a distinct excitation volume.

The excitation power, exposure time, and, for solid phantoms, the number of imaged pixels were adjusted between tests to ensure adequate signal levels, while keeping both the excitation power and acquisition time as low as possible, to minimize phototoxicity and photobleaching. The scanned area (number of pixels) for solid phantoms depended on the available measurement time during each experimental session. The specific values used for these parameters are reported individually for each test.

Each measurement was repeated three times, and the resulting signals were averaged to reduce random noise. For every measurement, a background signal was also acquired under identical experimental conditions, except that the excitation laser was blocked using a shutter. The background signal was likewise obtained by averaging of three measurements.

Occasional spurious spikes, attributed to cosmic radiation events, were observed in the acquired signals. These spikes were removed using a modified Z-score–based outlier detection algorithm originally proposed by Whitaker and Hayes [270]. The modified Z-score is computed as:

$$Z_t = \frac{0.6745\,(\nabla Y_t - \mathrm{M})}{\mathrm{MAD}} \tag{7.31}$$

Here, ∇Y_t is the detrended differenced series from the input values (Y_t), M is the median of ∇Y_t, and MAD is the median absolute deviation, calculated as $|\nabla Y_t - \mathrm{M}|$, which represents a robust measure of spread. The constant is a normalization parameter for MAD, allowing it to be comparable to the standard deviation in standard Gaussian distributions. The resulting Z_t is analogous to a score representing how sharp a spike in point τ is compared to the local variation. Using this score, a threshold (τ) is then defined and optimized for the data: if $Z_t \geq \tau$, the point is flagged as a cosmic spike to be processed; if $Z_t < \tau$, the point is kept as is. The flagger data series (ρ_t) is given as:

$$\rho_t = \begin{cases} 1, |Z_t| < \tau \\ 0, |Z_t| \geq \tau \end{cases} \tag{7.32}$$

The clean signal $\tilde{Y}_t$ is then obtained by replacing all flagged cosmic spikes $(\text{where } \rho = 0, \text{ otherwise } \tilde{Y}_t = Y_t)$ with the weighted mean of their neighbors, as given by:

$$\tilde{Y}_t = \frac{1}{W_t} \sum_{k=t-m}^{t+m} \rho_k Y_k \tag{7.33}$$

Here, the multiplication by ρ_k ensures that no neighbors (and the detected point) that are cosmic spikes are used when calculating the new value. m is the number of neighbors used for calculating the new value, and W_t is the number of unflagged neighbors as given by:

$$W_t = \sum_{k=t-m}^{t+m} \rho_k \tag{7.34}$$

The τ and m values were analyzed and optimized for each set of data, in order to remove most of the spikes, but do not change the fluorescence peak.

Using the described spike removal process, the spikes presented in the background signal were removed. The processed background was then subtracted from the average measurement signal, after which any spike in the corrected signal was removed using the same procedure. Finally, a Savitzky–Golay filter was applied to the resulting signal to suppress high-frequency noise.

The Savitzky–Golay filter operates by fitting a low-order polynomial to successive subsets of the data using a least-squares approach and replacing each data point with the value of the fitted polynomial at the center of the window. This method effectively reduces noise while preserving spectral features, such as fluorescence peak shape and width, which is essential for accurate spectral analysis. The filtered signal is given by:

$$\tilde{Y}_t = \sum_{k=t-m}^{t+m} c_k Y_k, \tag{7.35}$$

where $2m + 1$ is the window length, and c_k are convolution coefficients determined by the polynomial order and window size. For each dataset, both parameters were carefully optimized to balance noise suppression and spectral fidelity.

A schematic representation of the complete 2PEF signal acquisition and processing workflow for a single spatial pixel is shown in Figure 7.8. The processed signals obtained through this procedure were subsequently used for further analysis.

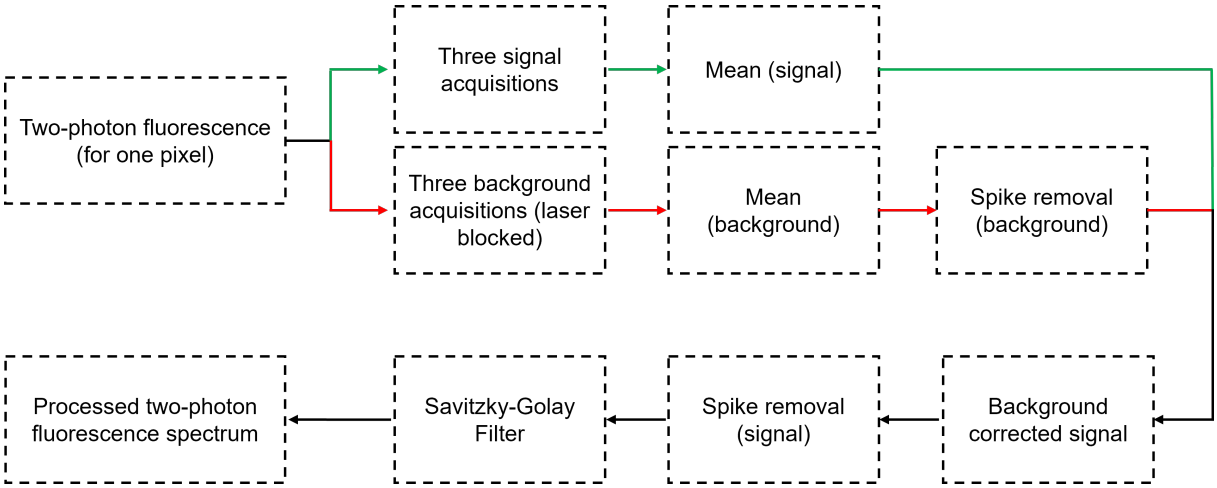


Figure 7.8: The workflow of 2PEF signal acquisition and processing for a single spatial pixel.

7.4.2 Data Analysis

Visual inspection and comparison of the spectra revealed that the absolute fluorescence intensity is sensitive to experimental factors, such as optical alignment, which are difficult to reproduce exactly between measurements. Consequently, a more robust metric was needed to analyze the data and enable automated discrimination between normal and tumoral samples using the fabricated optical filters.

As discussed before, a well-established approach is the evaluation of the redox ratio derived from the fluorescence signals. The redox ratio is a widely used metabolic marker in tissue diagnostics and is defined as the ratio between the fluorescence contributions of NAD(P)H and FAD, as given in [26]:

$$\text{Redox ratio} = \frac{\text{NAD(P)H Fluorescence intensity}}{\text{FAD Fluorescence intensity}} \tag{7.36}$$

To compute the redox ratio, the fluorescence intensity of each spectrum was integrated over the full emission wavelength range. This approach provides a comprehensive and robust estimate of the total fluorescence contribution of each endogenous fluorophore. Importantly, this method is not limited to spectrometer-based systems. It can also be applied to detection schemes employing broadband detectors, such as PMT, thereby extending its applicability across different optical detection platforms.

Numerical integration of the fluorescence spectra was performed using the Simpson's rule, and implemented in the SciPy library. Simpson's rule is a widely used numerical method for estimating definite integrals from discretely sampled data. It approximates the integrand locally by quadratic polynomials fitted over successive pairs of intervals (three adjacent sampling points), providing high accuracy for smooth functions such as fluorescence and absorption spectra. The method requires evenly spaced sampling points and is exact for polynomial functions up to third order. When the number of sampling intervals was

odd, Simpson's rule was applied to the largest even subset of the data, and the remaining interval was integrated using the trapezoidal rule, following the standard SciPy implementation. The Simpson integration is expressed as:

$$\int_0^m f(x)\,dx \approx \frac{h}{3}\left[y_0 + 4\sum_{\substack{i=1\\ i\ \text{odd}}}^{m-1} y_i + 2\sum_{\substack{j=2\\ j\ \text{even}}}^{m-2} y_j + y_m\right], \tag{7.37}$$

where m is an even number of intervals and $h = \frac{b-a}{m}$ is the wavelength sampling interval.

After the calculation of the redox ratio, statistical analyses were performed to determine whether the observed differences between normal and tumoral samples were statistically significant. Initially, the normality of each dataset was evaluated using the Shapiro–Wilk test. In all cases, the results indicated that the redox ratio distributions did not follow a normal distribution. Consequently, a non-parametric statistical approach was adopted, and the two groups were compared using the two-tailed Mann–Whitney U test. Statistical significance was assessed at a significance level of $\alpha = 0.05$. The Shapiro-Wilk test was conducted using SciPy, and the Mann-Whitney U test was performed using GraphPad Prism.

7.4.3 Preliminary SHG Measurements with Biological Tissues

Preliminary tests were conducted using membranes extracted from CAM assays. The primary objective of these experiments was to verify whether detectable signals could be generated from this type of sample, thereby establishing a foundation for future validation studies.

These initial measurements were intentionally simple and were performed at a stage when the experimental setup had not yet been fully optimized or validated using phantom samples. As such, only a limited number of signals were acquired, serving primarily as a proof-of-concept. The experimental setup (Figure 7.2) was used in transmission mode.

The samples were mounted between two microscope slides, with parafilm applied around the edges to prevent separation during the measurements. This configuration was necessary due to the requirement of positioning the sample vertically within the current setup.

The tests were conducted without the use of fabricated optical filters. Signals were acquired from both normal and tumoral tissue samples at a mean incident power of 32 mW. No background signal was recorded in this case. Therefore, no post-processing or background subtraction was performed. The sole purpose of this test was to confirm the feasibility of signal generation in the sample, and consequently, no further signal processing was applied. As the excitation and emission wavelengths had not yet been fully defined, this initial experiment focused on the detection of SHG signals. The excitation wavelength was set

to 800 nm, as the use of 750 nm had not yet been established.

7.5 Results and Samples Analysis

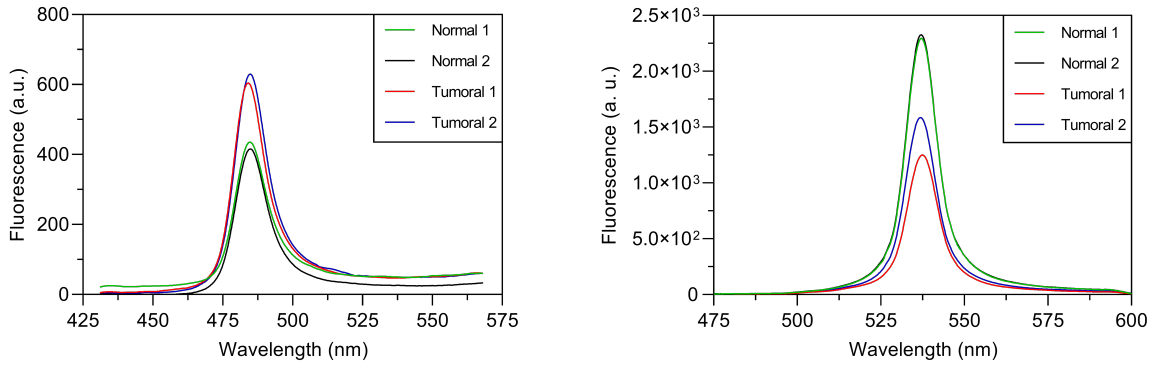
7.5.1 Liquid Phantoms with a Fluorophore (NAD(P)H or FAD)

The 2PEF response of the fluorophore was experimentally evaluated using the fabricated optical filters. For this first study, four different liquid phantoms were prepared. Two phantoms contained only NAD(P)H, with concentrations chosen to mimic those typically associated with normal and tumoral tissues, respectively. The remaining two phantoms contained only FAD, also prepared at concentrations representative of normal and tumoral tissue conditions.

Each phantom was measured using the developed two-photon optical setup under two experimental configurations corresponding to the fabricated filters. For each configuration, the measurements were performed at three different incident laser powers, 50 mW, 100 mW, and 150 mW, using an excitation wavelength of 750 nm. The fluorescence spectra were acquired with an integration time of 60 s, for each measurement.

Figure 7.9 presents the fluorescence spectra acquired at an incident laser power of 100 mW, where each curve corresponds to the average of three independent measurements. A clear distinction between normal and tumoral phantoms is observed for both fluorophores. In the case of NAD(P)H, the tumoral phantom exhibits higher fluorescence intensity, as expected due to its increased NAD(P)H concentration relative to the normal phantom.

Similarly, the FAD phantoms show a clear separation between normal and tumoral conditions. As anticipated, the normal phantom presents higher fluorescence intensity, consistent with its higher FAD concentration compared to the tumoral phantom. Minor variations between repeated measurements of the tumoral phantom are observed and can be attributed to small differences in optical alignments in the multiphoton setup.



(a) (b)

Figure 7.9: 2PEF spectra acquired from liquid phantoms mimicking normal and tumoral tissue conditions: (a) NAD(P)H phantoms; (b) FAD phantoms. Each curve represents the average of three measurements acquired with an excitation wavelength of 750 nm and an incident laser power of 100 mW.

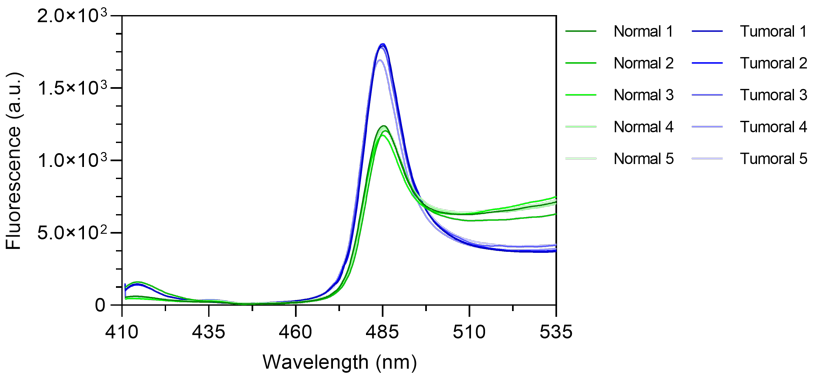
7.5.2 Liquid Phantoms with Both Fluorophores (NAD(P)H and FAD)

Given the spectral crosstalk between NAD(P)H and FAD and considering that both fluorophores are simultaneously present in real biological tissues, it is essential to evaluate whether the differences observed in previous experiments remain detectable when both fluorophores coexist in the same sample.

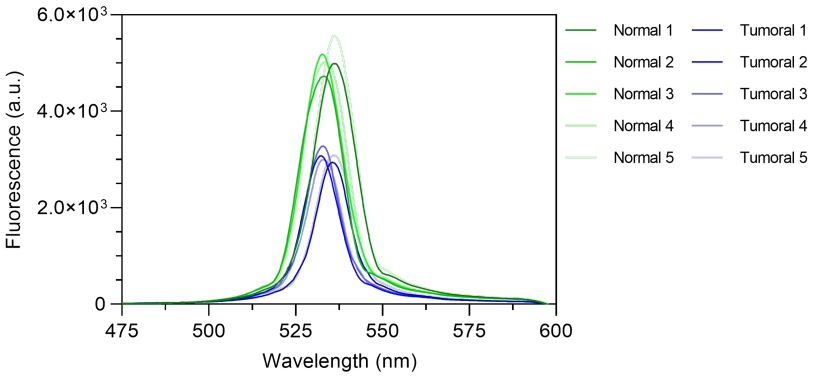
To address this, two liquid phantoms containing both NAD(P)H and FAD were prepared, with concentrations representative of normal and tumoral tissue conditions. Each phantom was measured on two different days: once on the day of fabrication and again on the following day. On the first day, measurements were performed using an average incident laser power of 150 mW, with an integration time of 30 s. Each phantom was measured five times under these conditions. On the second day, measurements were acquired using a higher incident laser power of 325 mW, with the same integration time, and two measurements were performed per phantom. The increase in excitation power on the second day was required due to a reduction in the detected fluorescence signal, which may be associated with factors such as minor variations in optical alignment, photobleaching, or partial degradation of the samples over time. Consequently, comparisons between measurements acquired on different days should be considered qualitative rather than strictly quantitative.

The resulting fluorescence spectra are shown in Figure 7.10. Figures 7.10(a) and 7.10(b) correspond to measurements acquired on the first day, while Figures 7.10(c) and 7.10(d) correspond to those acquired on the second day. Each curve represents the average of three repeated acquisitions.

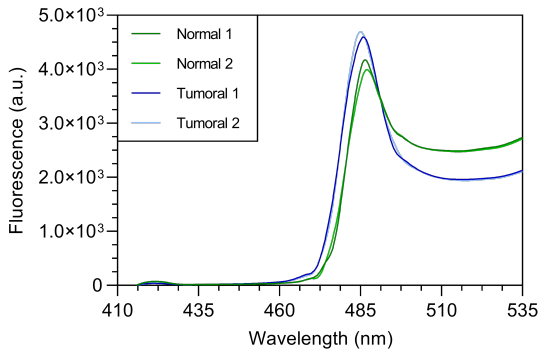
It can be observed that, even when both fluorophores are present simultaneously, differences between



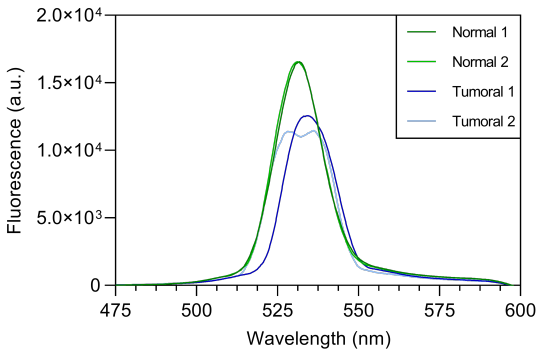
(a)



(b)



(c)



(d)

Figure 7.10: 2PEF spectra acquired from mixed NAD(P)H/FAD phantoms under normal and tumoral conditions: (a) NAD(P)H channel, day 1; (b) FAD channel, day 1; (c) NAD(P)H channel, day 2; (d) FAD channel, day 2.

the normal and tumoral phantoms remain consistently observable at the selected detection wavelengths. In Figure 7.10(a), the tumoral phantom exhibits higher fluorescence intensity than the normal phantom. This behavior is consistent with the higher NAD(P)H concentration in the tumoral phantom, which con-

tributes more strongly to the signal around 485 nm. The presence of a red-shifted tail in the spectrum is attributed to a combination of residual crosstalk from FAD fluorescence and out-of-band transmission of the fabricated 485 nm optical filter. Conversely, Figure 7.10(b) shows that the normal phantom exhibits higher fluorescence intensity at 530 nm. This observation is consistent with the higher FAD concentration in the normal phantom, as FAD fluorescence dominates in this spectral region. The same qualitative trends are also observed in the measurements acquired on the second day, as shown in Figures. 7.10(c) and 7.10(d). However, the differences are less pronounced than on the first day of measurements.

A shift in the peak emission wavelength is observed in the graphics of Figures 7.10(b), 7.10(c) and 7.10(d). This shift can be associated with slight variations in phantom positioning and optical alignments during different measurements. Since the optical system is custom-built and manually aligned, minor differences in cuvette placement can modify the optical path. In addition, the optical filters were fabricated on a relatively large substrate to facilitate integration into the setup, which may introduce small thickness non-uniformities across the filter area. As a result, light passing through different regions of the filter may experience slightly different peak transmittance wavelengths, leading to spectral shifts. Furthermore, the red-shifted tail observed in Figure 7.10(c) is more pronounced than the red-shifted tail observed in Figure 7.10(a). This behavior is consistent with the known lower stability of NAD(P)H in solution compared to FAD. Over time, NAD(P)H is more susceptible to fluorescence degradation, whereas FAD remains comparatively stable [30]. Consequently, the relative contribution of FAD fluorescence may increase in measurements performed at later times. Nevertheless, contributions from alignment variations and excitation power differences cannot be fully excluded.

These observations indicate that, to minimize degradation-related effects and ensure reliable measurements, fluorescence acquisitions should ideally be performed within 24 h of phantom fabrication. Beyond this time-frame, degradation of the samples, particularly of NAD(P)H, may begin to influence the measured spectral response.

Overall, these results demonstrate that, despite spectral overlap and residual crosstalk, the fabricated optical filters and selected detection wavelengths preserve sufficient contrast to discriminate between normal and tumoral metabolic conditions in mixed-fluorophore phantoms.

As discussed in the introduction section, a critical step toward enabling automated discrimination between normal and tumoral tissues using the fabricated optical filters is the evaluation of the redox ratio derived from the fluorescence measurements.

Therefore, to further validate the presented observations, the redox ratio was explicitly calculated for these experiments, and the corresponding results are presented in Figure 7.11. As shown in the figure, a

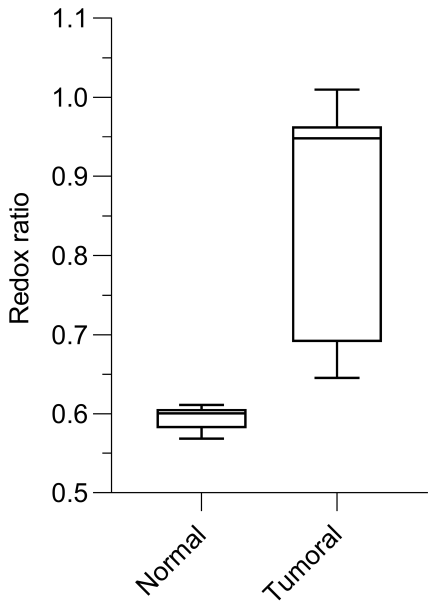


Figure 7.11: Redox ratio calculated from 2PEF measurements of mixed NAD(P)H/FAD phantoms under normal and tumoral conditions.

clear difference is observed between the redox ratios of the normal and tumoral phantoms. As expected, the tumoral phantom exhibits a higher redox ratio, reflecting its increased NAD(P)H concentration and reduced FAD concentration relative to the normal phantom. This behavior is consistent with previously reported findings in studies of cancer metabolism [26].

Quantitatively, the redox ratio of the tumoral group (median=0.9479, n=8) was significantly higher than that of the normal group (median=0.6006, n=7). Statistical analysis was performed using a Mann–Whitney U test, which confirmed a statistically significant difference between the two groups (U=0.0, exact two-tailed P=0.0003). This non-parametric test was selected because normality could not be assumed for both datasets: a Shapiro–Wilk test yielded a P-value of 0.194 for the normal group and 0.019 for the tumoral group, indicating that at least one distribution deviates from normality.

Despite the presence of spectral overlap and a red-shifted tail in the 485 nm filter measurements arising from residual FAD emission, the calculated redox ratios remain robust. The fabricated filters effectively reduce crosstalk to a level that allows reliable quantification of the redox ratio. These results confirm that the optical system, even in its current prototype configuration, can support meaningful metabolic measurements and discriminate between normal and tumoral conditions based on intrinsic fluorescence signals.

Nevertheless, to further minimize the influence of the red-shifted tail on the 485 nm channel, future

experiments involving more complex phantoms or biological tissues will incorporate an additional short-pass filter with a cut-off wavelength around $510\,\mathrm{nm}$. This modification is expected to further suppress residual FAD contributions and improve the specificity of NAD(P)H detection.

To further strengthen the robustness of the conclusions, additional experiments were conducted on three different days, during which six new mixed-fluorophore phantoms were fabricated: three representing normal tissue conditions and the other three representing tumoral conditions. The same measurement protocol was applied to all phantoms. Fluorescence measurements were performed using a mean incident laser power of $150\,\mathrm{mW}$, with a signal integration time of $30\,\mathrm{s}$. For each acquisition, the redox ratio was calculated from the measured fluorescence signals, and the resulting distributions are shown in Figure 7.12.

The analysis confirms consistent separation between the two groups. The redox ratio of the tumoral group (median=0.7442, n=19) was significantly higher than that of the normal group (median=0.5707, n=14). A Mann–Whitney U test was used to assess statistical significance, yielding a significant result (U=43.50, exact two-tailed P=0.0007). This non-parametric test was selected because normality could not be assumed for both datasets: the Shapiro–Wilk test resulted in a P-value of 0.000 for the normal group and 0.1960 for the tumoral group, indicating that at least one of the distributions deviates from normality.

Taken together, all the results presented demonstrate that the proposed optical filtering strategy, com-

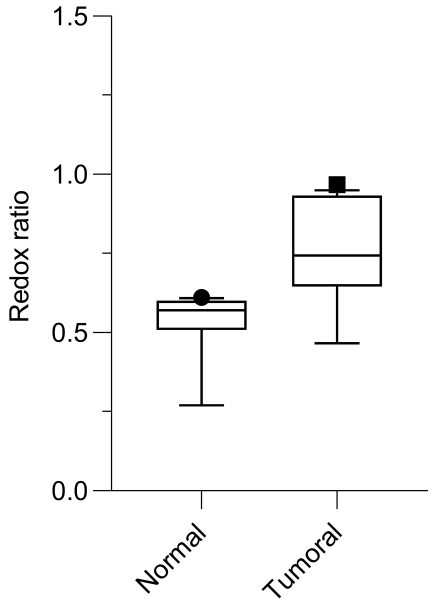


Figure 7.12: Distribution of redox ratio values obtained from 2PEF measurements of mixed NAD(P)H/FAD phantoms fabricated on three different days, comparing normal and tumoral conditions.

bined with two-photon excitation at 750 nm, enables robust discrimination between normal and tumoral metabolic conditions based on intrinsic fluorescence signals. Despite the presence of spectral overlapping and residual crosstalk between NAD(P)H and FAD, the redox ratio remains a stable and statistically significant metric across multiple measurement days and independent phantom preparations.

The consistency of the redox ratio separation observed both in initial experiments and in extended validation studies highlights the robustness of this approach against variations in sample preparation, alignment, and acquisition conditions. These findings support the feasibility of applying the developed optical system and filtering scheme to more complex biological samples and, ultimately, to tissue measurements, where metabolic contrast may serve as a reliable indicator for CRC detection.

7.5.3 Liquid Phantoms with Hemoglobin, Polystyrene Beads, and Fluorophores (NAD(P)H and FAD)

To further increase the complexity and physiological relevance of the phantoms, additional components were incorporated, namely polystyrene beads as scattering elements and hemoglobin as an absorbing element. Thus, these phantoms reproduce several key optical characteristics of biological tissues, including increased scattering and wavelength-dependent absorption.

For these experiments, four phantoms were prepared: two representing normal tissue conditions and two representing tumoral conditions. Two of the phantoms (one normal and one tumoral) were measured on the day of fabrication (test 1) using a mean incident laser power of 100 mW and an integration time of 30 s. The corresponding fluorescence spectra are shown in Figures 7.13(a) and 7.13(b). For each phantom, five measurements were performed, and each curve represents the average of three consecutive acquisitions. The remaining two phantoms (one normal and one tumoral) were measured between 24 h and 36 h after fabrication (test 2) under a mean laser power of 200 mW and 30 s of integration time. The resulting spectra are presented in Figures 7.13(c) and 7.13(d). As before, five measurements were acquired per phantom, with each curve representing the mean of three consecutive runs.

In all measurements, the recorded fluorescence signals are significantly lower than those obtained from phantoms containing only the fluorophores, as expected. The presence of scattering and absorbing components reduces both the excitation and collection efficiency of the fluorescence signal, thereby lowering the detected intensity.

As observed in previous experiments, measurements performed after 24 h exhibit a pronounced reduction in the NAD(P)H fluorescence signal. It is important to note that, although the absolute fluorescence intensity in the NAD(P)H channel may appear higher on the second day, this does not necessarily indicate

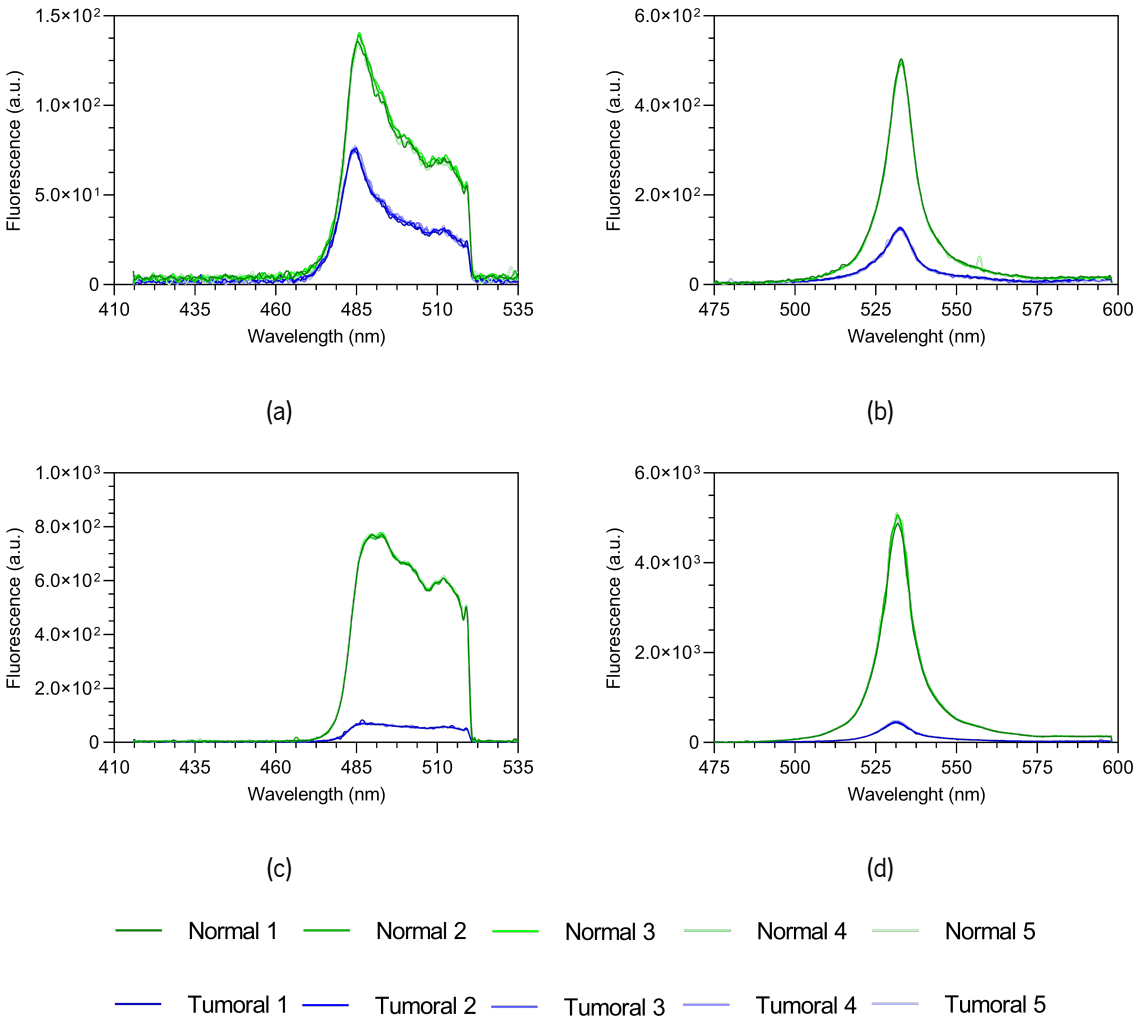


Figure 7.13: 2PEF spectra acquired from phantoms containing NAD(P)H, FAD, polystyrene beads and hemoglobin: (a) 485 nm filter channel, test 1; (b) 530 nm filter channel, test 1; (c) 485 nm filter channel, test 2; (d) 530 nm filter channel, test 2. Normal and tumoral phantoms are shown for comparison. Each curve represents the average of three consecutive acquisitions.

an increase in NAD(P)H fluorescence, as absolute intensity values depend strongly on excitation power and alignment conditions. Therefore, the relative ratio between the NAD(P)H and FAD fluorescence peaks is the relevant parameter for analysis. In this case, a significant reduction in the relative contribution of NAD(P)H is observed. Consequently, this reduction enhances the relative contribution of FAD crosstalk in the 485 nm detection channel. To mitigate this effect, an additional short-pass filter with a cut-off wavelength of 520 nm was introduced in the 485 nm detection path for these measurements. It is important to note that, although a cut-off wavelength of 510 nm was identified in the previous analysis, the filter

used in this work has a cut-off wavelength of 520 nm. This choice was made because it was the closest option available. Based on the spectral curves, this 10 nm shift is not expected to significantly affect the conclusions.

Analysis of the spectra shows that, across all measurements, the normal phantoms exhibit higher overall fluorescence intensity than the tumoral phantoms, including in the NAD(P)H channel, where the opposite trend would be expected based on fluorophore concentration alone.

This behavior can be explained by the higher concentration of hemoglobin and polystyrene beads in the tumoral phantoms, which leads to increased absorption and scattering. Consequently, the fluorescence emitted by all fluorophores is more strongly attenuated in the tumoral phantoms, regardless of their intrinsic concentration. These results demonstrate that, in complex and tissue-mimicking phantoms, absolute fluorescence intensity alone is not a reliable metric for distinguishing between normal and tumoral conditions. Instead, a ratio-based metric that compensates for global attenuation effects, namely the redox ratio, is required.

To further evaluate the robustness of the redox ratio under these more complex conditions, two additional phantoms (one normal and one tumoral) were fabricated and measured. Fluorescence spectra were acquired with an integration time of 30 s using different mean incident laser powers (100 mW, 150 mW, 200 mW, and 300 mW). The excitation powers were selected to ensure detectable signals within a reasonable acquisition time. In these measurements, precise alignments optimization to maximize absolute signal intensity was not prioritized. Instead, the objective was to assess whether the redox ratio remains stable under varying alignment and excitation conditions, provided that the same alignment is used for both detection channels.

The redox ratios calculated from all these experiments, together with those from the previous mixed-phantom studies, are presented in Figure 7.14. The tumoral group exhibits a significantly higher redox ratio (median=0.8338, n=69) than the normal group (median=0.3020, n=75). A Mann–Whitney U test confirmed the statistical significance of this difference (U = 4890, exact two-tailed P < 0.0001). This non-parametric test was selected because neither group followed a normal distribution, as indicated by the Shapiro–Wilk test (P = 0.0000 for the normal group and P = 0.0010 for the tumoral group).

In summary, it was demonstrated that the redox ratio derived from 2PEF measurements remains a robust and reliable metric even in complex, tissue-mimicking phantoms that include scattering and absorbing components such as polystyrene beads and hemoglobin. While absolute fluorescence intensities are strongly affected by absorption, scattering, alignment, and sample aging, the redox ratio consistently preserves metabolic contrast between normal and tumoral conditions.

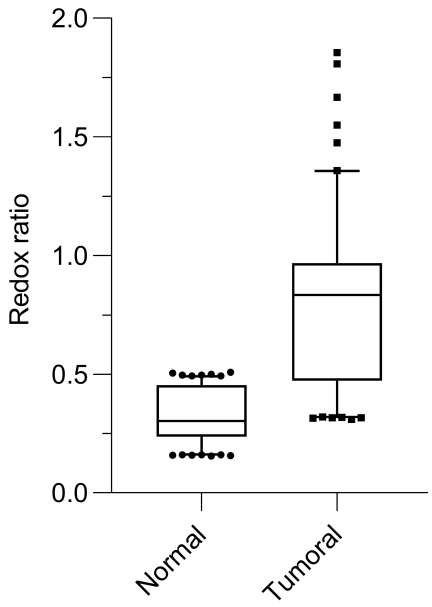


Figure 7.14: Redox ratio calculated from 2PEF measurements of phantoms containing NAD(P)H, FAD, polystyrene beads and hemoglobin. Results are shown in normal and tumoral conditions.

The statistically significant separation observed across multiple phantom preparations, acquisition days, and excitation powers highlights the resilience of this ratio-based approach against experimental variability. These findings strongly support the suitability of the proposed optical filtering strategy and detection wavelengths for application in realistic biological environments, reinforcing the potential of this methodology for future studies on biological tissues and for the development of miniaturized diagnostic systems for CRC detection.

7.5.4 Solid Phantoms with Both Fluorophores (NAD(P)H and FAD)

After completing the study with liquid phantoms, the investigation was extended to solid phantoms. These studies are essential for understanding how solid samples can be analyzed, since, unlike liquid phantoms, it is not possible to probe a single point. In solid phantoms, spatial heterogeneity is expected, making area-based measurements necessary.

In total, 14 solid gelatin phantoms containing NAD(P)H and FAD were fabricated: 7 with concentrations representative of normal tissues and 7 representing tumoral tissues. All phantoms were imaged using two-dimensional scans. Two phantoms were scanned over an area of 8 pixels $\times$ 4 pixels, while the remaining phantoms were scanned over an area of 8 pixels $\times$ 8 pixels. The maximum scan area was limited by the maximum travel range of the scanning system. Therefore, 8 pixels $\times$ 8 pixels corresponds

to the largest area that can be imaged with the available equipment. The reduced scan area used for the two phantoms was due to limited experimental time on that day. Each pixel corresponds to an area of $12.56\,\mu m \times 12.56\,\mu m$, defined by the laser voxel size at the focal plane.

Measurements were performed using different mean laser powers, depending on the sample. For normal phantoms, a mean power of 150 mW was used in six cases, while 200 mW was used in one case. The signal integration time was 10 s for four phantoms, 15 s for one phantom, and 30 s for the remaining phantom. These parameters were selected to obtain adequate signal quality within a reasonable acquisition time, while minimizing laser power to reduce photobleaching and photodamage. The same acquisition strategy, with the same parameters, was adopted for the tumoral phantoms. This consistency ensures comparability between normal and tumoral measurements. All reported curves correspond to the mean of three repeated acquisitions.

Given the large number of spectra acquired for each phantom, a representative analysis was performed to facilitate visual interpretation of the results. One normal and one tumoral phantom, measured on the same day using a mean laser power of 150 mW and an integration time of 10 s, and scanned over an area of 8 pixels $\times$ 8 pixels, were selected. For the final 64 signals, the mean and the median were calculated, and the resulting curves are shown in Figure 7.15. The mean was used to provide a general visual overview of the fluorescence behavior across the sample. However, as discussed in the OCT study, the mean is sensitive to outliers, which may significantly influence the results. For this reason, the median was also computed as a more robust estimator.

The results show higher fluorescence intensity in the normal phantom when using the 530 nm filter, as expected due to the higher concentration of FAD. Conversely, a higher peak fluorescence is observed in the tumoral phantom when using the 485 nm filter, consistent with the increased concentration of NAD(P)H in these phantoms. In addition, a red-shifted tail is observed in the spectra, as previously discussed. The impact of this effect on the results can only be fully assessed through redox ratio calculations, which are addressed in the following analysis.

The redox ratio was computed on a pixel-by-pixel basis for each phantom. The corresponding spatial distributions for the normal and tumoral phantoms are presented in Figures 7.16 and 7.17, respectively.

The redox ratio maps clearly show that, in general, normal phantoms present lower redox ratio values than tumoral phantoms, as expected from their respective NAD(P)H and FAD concentrations. This overall trend is consistent throughout the different acquisition days and tests, supporting the robustness of the method.

Nevertheless, some local outliers can be observed in several images. These deviations may arise from

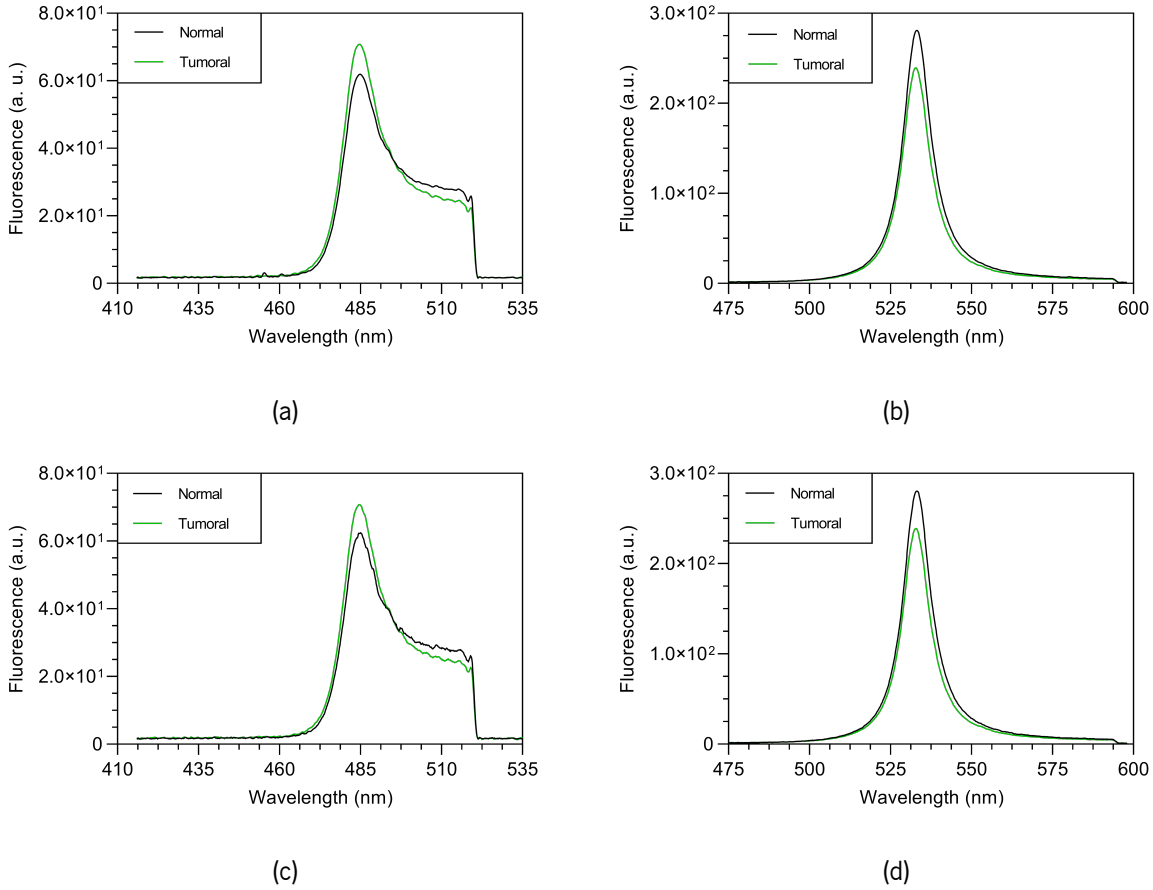


Figure 7.15: Mean and median fluorescence emission spectra obtained from 2D scans of representative solid gelatin phantoms containing NAD(P)H and FAD: (a) mean and (c) median spectra acquired using the 485 nm filter, highlighting the NAD(P)H emission region; (b) mean and (d) median spectra acquired using the 530 nm filter, corresponding to the FAD emission region.

spatial heterogeneity within the gelatin matrix, such as locally higher concentrations of one fluorophore due to imperfect mixing. Additional contributing factors may include minor contamination during fabrication or slight misalignment in the optical system during acquisition. Given these potential sources of variability, it is important to focus on the global behavior of each phantom rather than isolated extreme values. Importantly, despite these local fluctuations, the expected difference between normal and tumoral phantoms is consistently verified.

For future automatic discrimination between normal and tumoral samples, similarly to the approach used in the OCT study, a supervised classifier such as an SVM could be implemented. In this case, statistical descriptors of the redox ratio distribution within each scan could be used as input features. The mean and median are natural candidates, as they summarize the global metabolic behavior of the phantom. However, given the presence of outliers, the maximum value is likely not an appropriate feature,

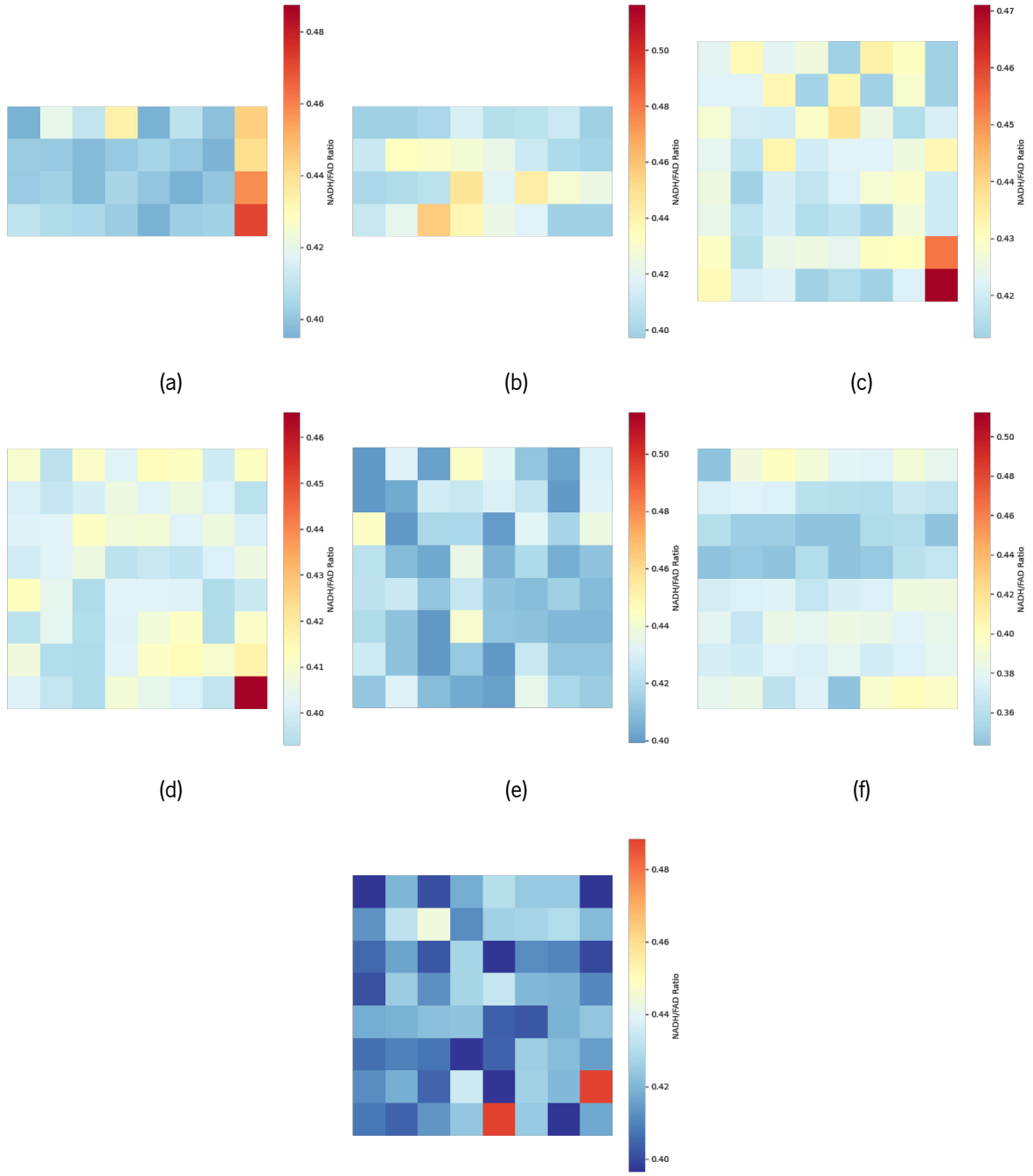


Figure 7.16: Spatial distribution maps of the redox ratio for the normal gelatin phantoms containing NAD(P)H and FAD. Each subfigure ((a) to (g)) corresponds to a different acquisitions. The color scale represents the redox ratio value calculated on a pixel-by-pixel basis for the scanned area.

since it is highly sensitive to isolated artifacts and may not represent meaningful biological information. The IQR provides a robust measure of dispersion that is insensitive to extreme values, quantifying the variability of the central 50% of the data. In this context, the IQR could capture differences in spatial heterogeneity

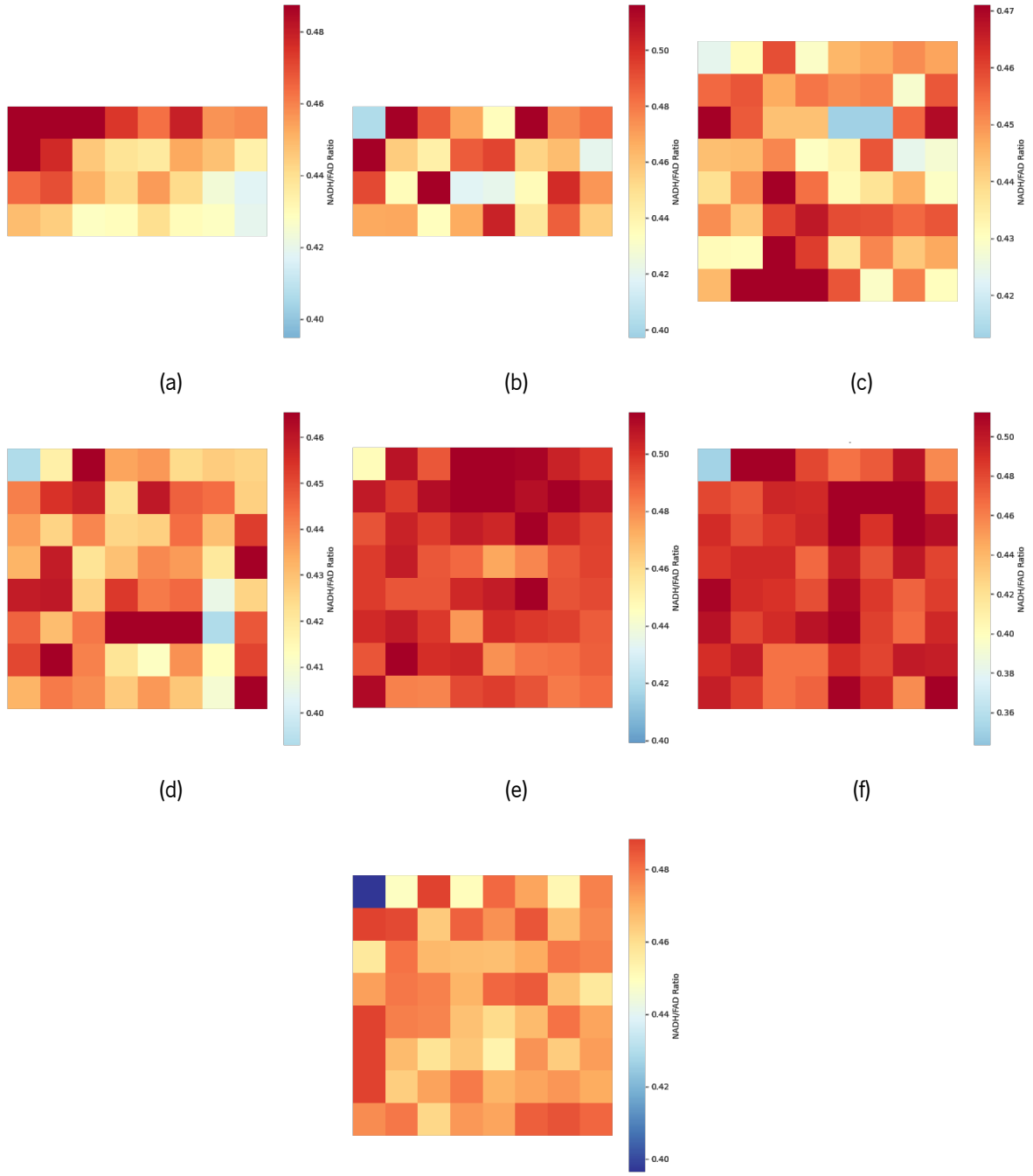


Figure 7.17: Spatial distribution maps of the redox ratio for the tumoral gelatin phantoms containing NAD(P)H and FAD. Each subfigure ((a) to (g)) corresponds to a different acquisitions. The color scale represents the redox ratio value calculated on a pixel-by-pixel basis for the scanned area.

between normal and tumoral phantoms. For example, if tumoral phantoms exhibit greater metabolic variability, this could be reflected in a larger IQR. Therefore, combining central tendency metrics (mean or median) with a robust dispersion metric such as the IQR could improve classification performance and

provide a more comprehensive description of the redox ratio distribution.

To further analyze the differences between normal and tumoral phantoms before implementing the SVM classifier, a boxplot including all redox ratio values acquired from both groups was constructed (Figure 7.18). The boxplot visually demonstrates a clear separation between the two datasets. To statistically validate this observed difference, inferential analysis was performed.

The tumoral group presented a higher redox ratio (median = 0.4739, n = 447) compared to the normal group (median = 0.4084, n = 382). A Mann–Whitney U test confirmed that this difference is statistically significant ($U = 7614$, exact two-tailed $p < 0.0001$). The Mann–Whitney test was selected because normality could not be assumed: the Shapiro–Wilk test yielded $p = 0.000$ for the normal group and $p = 0.001$ for the tumoral group, indicating that both distributions significantly deviate from normality.

From visual inspection of the boxplot, the IQRs of the two groups appear relatively similar, suggesting comparable dispersion within the central 50% of the data. Therefore, in this specific dataset, the primary difference between groups is driven by a shift in central tendency rather than variability. Although the IQR may not provide strong discriminative power in this simplified phantom model, it should not be disregarded for future studies. These phantoms represent controlled and relatively homogeneous systems when compared to real biological tissues, where greater metabolic heterogeneity is expected. In

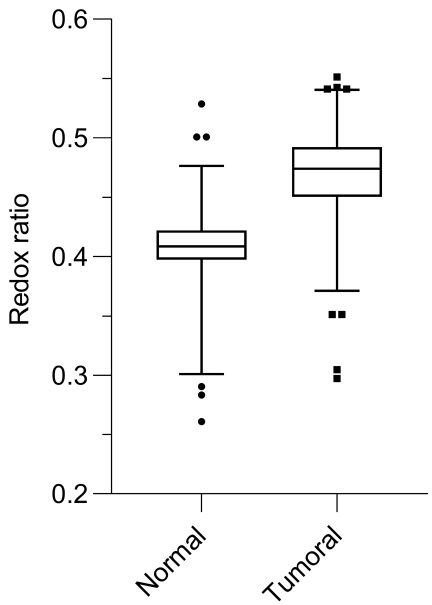


Figure 7.18: Boxplot representation of the redox ratio values obtained from all scanned normal and tumoral phantoms. The central line represents the median, the box corresponds to the interquartile range (IQR), the whiskers indicate the data spread, and the points represent outliers.

such cases, dispersion-related metrics, such as the IQR, may become more informative and contribute meaningfully to the classification performance.

7.5.5 Solid Phantom with Hemoglobin, Polystyrene Beads, and Fluorophores (NAD(P)H and FAD)

To conclude the phantom studies, a final set of solid phantoms incorporating both fluorophores (NAD(P)H and FAD), polystyrene beads (scattering component), and hemoglobin (absorbing component) was developed to better approximate the optical complexity of biological tissues.

In total, 12 solid gelatin phantoms were fabricated: 6 with concentrations representative of normal tissue and 6 representing tumoral tissue. All phantoms were imaged using two-dimensional scans. Two phantoms were scanned over an area of 4 pixels $\times$ 4 pixels, while the remaining phantoms were scanned over an area of 8 pixels $\times$ 8 pixels. The reduced scan area for two phantoms was due to limited experimental time on the respective acquisition day.

For the normal phantoms, measurements were performed using a mean laser power of 150 mW. The signal integration time was 5 s for three phantoms, 10 s for one phantom, and 15 s for the remaining two phantoms. These acquisition parameters were selected to ensure adequate signal quality within a reasonable measurement time, while minimizing laser power to reduce photobleaching and photodamage. The same acquisition strategy, with the same parameters, was adopted for the tumoral phantoms. This consistency ensures comparability between normal and tumoral measurements. All reported curves correspond to the mean of three repeated acquisitions.

Given the large number of spectra obtained for each phantom, a representative analysis was performed to facilitate visual interpretation. One normal and one tumoral phantom, measured on the same day using a mean laser power of 150 mW and an integration time of 15 s, and scanned over an area of 8 pixels $\times$ 8 pixels, were selected for detailed analysis. For the resulting 64-pixel signals, both the mean and the median spectra were calculated, and the corresponding curves are presented in Figure 7.19.

The results show higher fluorescence intensity in the normal phantom for both emission filters. This occurs despite the higher concentration of NAD(P)H in the tumoral phantoms, which is not reflected in an increased signal in the 485 nm filter. This behavior was expected, as previously observed in the liquid phantoms containing scattering and absorbing components. In the tumoral models, the higher concentrations of hemoglobin and scattering particles lead to increased absorption and scattering losses, reducing the detected fluorescence intensity.

However, when compared with the liquid phantoms incorporating the same components, the fluo-

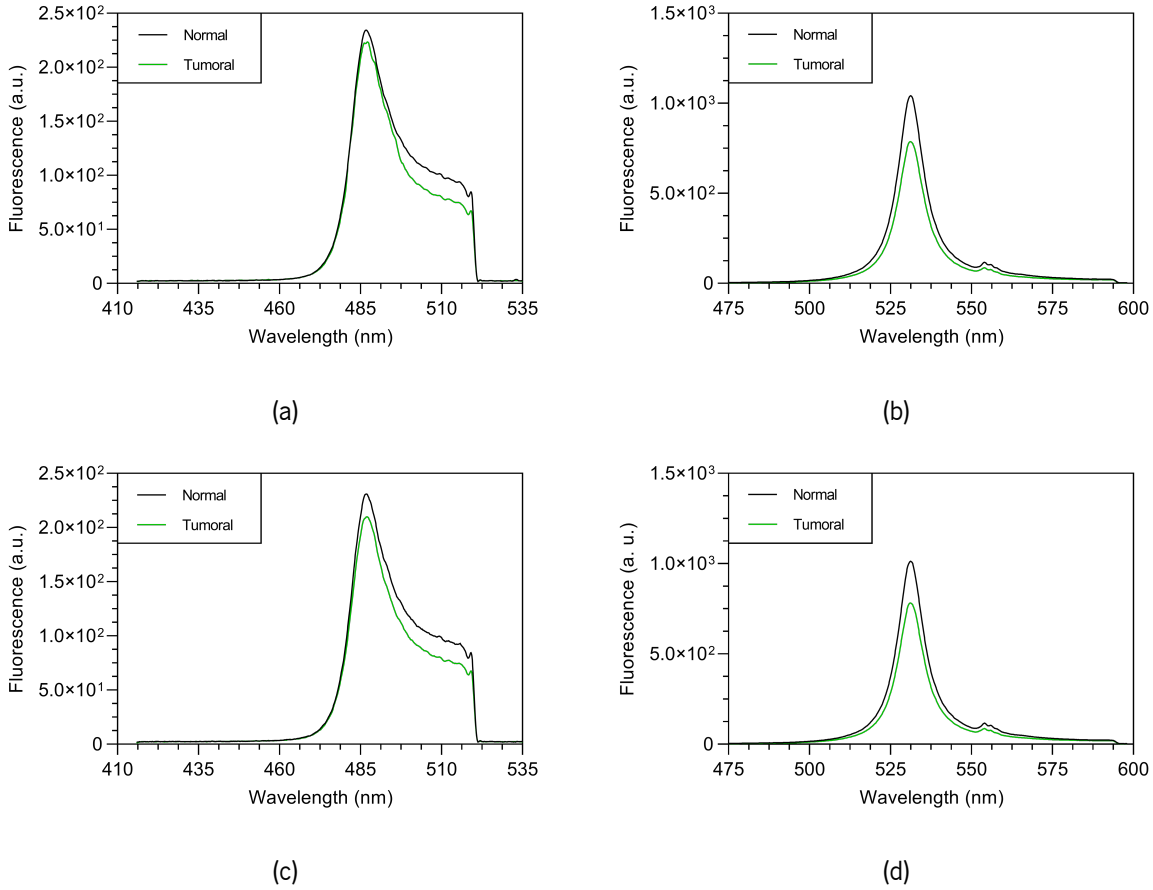


Figure 7.19: Mean and median fluorescence emission spectra obtained from 2D scans of representative solid gelatin phantoms containing NAD(P)H, FAD, hemoglobin, and polystyrene beads: (a) mean spectrum using the 485 nm filter; (b) mean spectrum using the 530 nm filter; (c) median spectrum using the 485 nm filter; (d) median spectrum using the 530 nm filter.

rescence signals obtained from the solid phantoms are stronger. This difference is likely related to the reduced thickness of the solid phantoms (approximately 400 µm) compared to the liquid samples, where the excitation and emission light must propagate through the full cuvette thickness of 10 mm. The shorter optical path length in the solid phantoms reduces cumulative absorption and scattering effects, resulting in higher detected signals. Therefore, the influence of the absorbing and scattering components is more pronounced in the liquid configuration due to the substantially longer propagation distance.

The overall impact of these effects on metabolic interpretation can only be properly assessed through redox ratio calculations, which account for the relative contributions of NAD(P)H and FAD. Accordingly, the redox ratio was computed on a pixel-by-pixel basis for each phantom. The corresponding spatial distributions for the normal and tumoral phantoms are presented in Figures 7.20 and 7.21, respectively.

The redox ratio maps clearly demonstrate that, in general, normal phantoms exhibit lower redox ratio

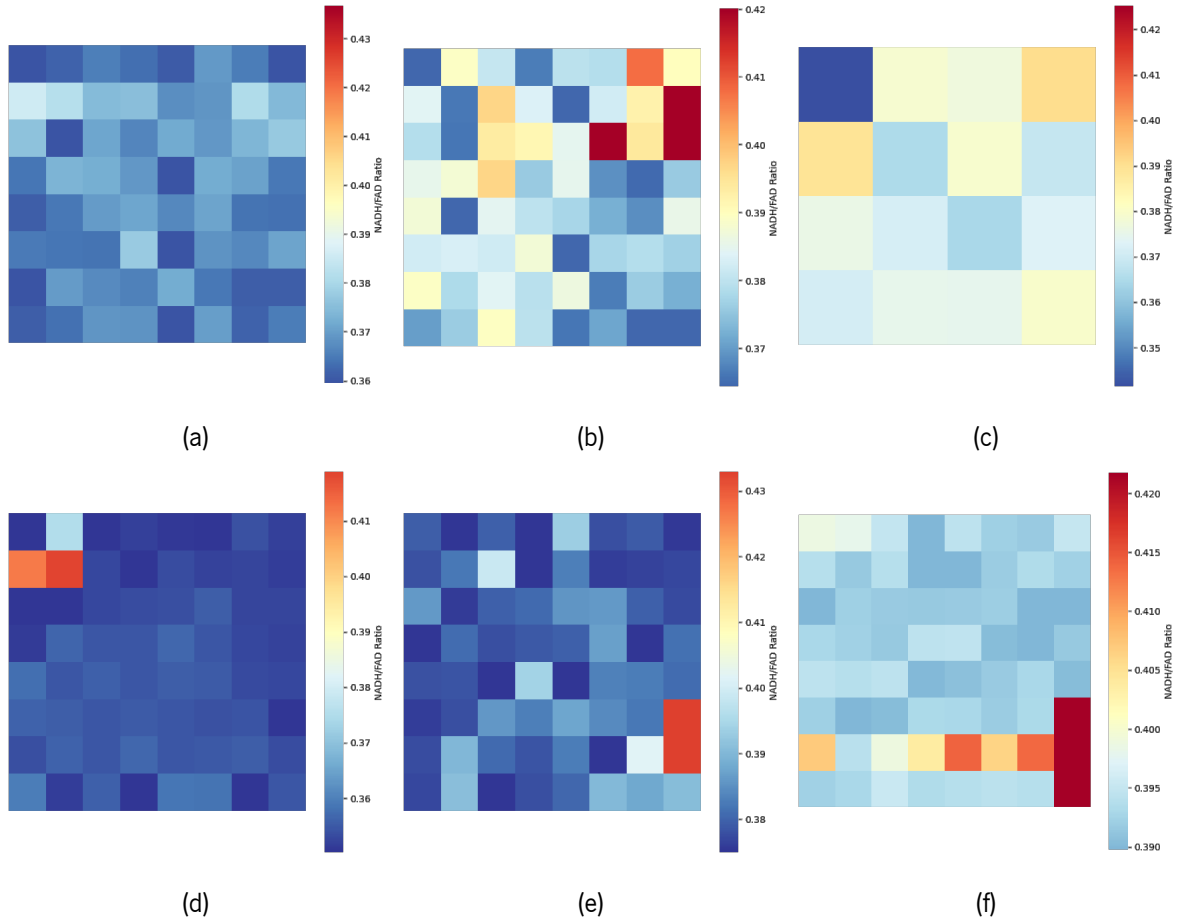


Figure 7.20: Spatial distribution maps of the redox ratio for normal solid phantoms containing NAD(P)H, FAD, hemoglobin, and polystyrene beads. Each subfigure ((a) to (f)) corresponds to a different acquisitions. The color scale represents the redox ratio calculated on a pixel-by-pixel basis.

values than tumoral phantoms, consistent with their respective NAD(P)H and FAD concentrations. This trend is observed across different acquisition days and experimental conditions, supporting the robustness and reproducibility of the methodology.

Nevertheless, local outliers are visible in several maps. These deviations arise from spatial heterogeneity within the gelatin matrix, such as locally increased concentrations of a fluorophore or hemoglobin due to imperfect mixing. The random spatial distribution of polystyrene beads also contributes to local variations in scattering properties, influencing the detected fluorescence signal. Additional factors, including minor contamination during fabrication or slight optical misalignment during acquisition, may further contribute to these isolated extreme values. Given these potential sources of variability, interpretation should prioritize the global behavior of each phantom rather than isolated pixels. Importantly, despite these local fluctuations, the expected systematic difference between normal and tumoral phantoms remains consistently

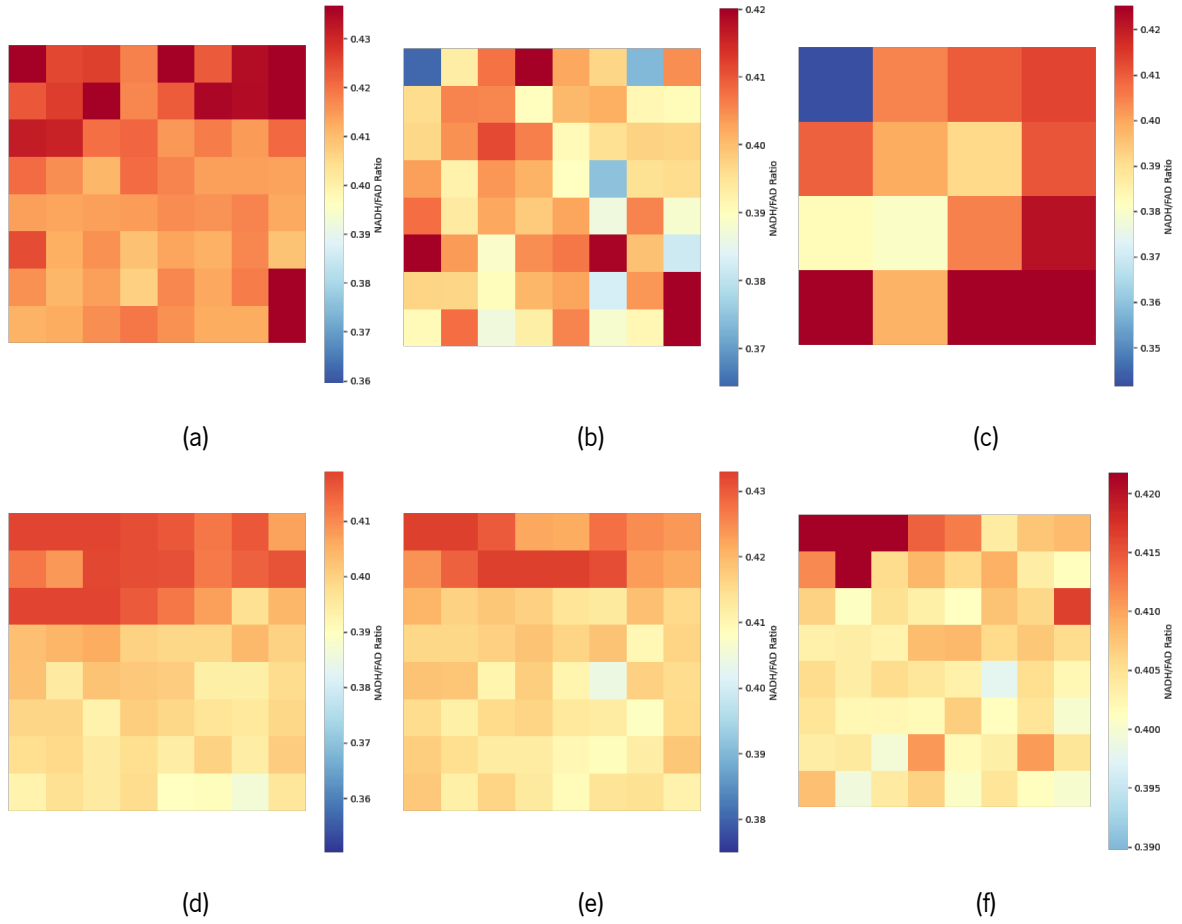


Figure 7.21: Spatial distribution maps of the redox ratio for tumoral solid phantoms containing NAD(P)H, FAD, hemoglobin, and polystyrene beads. Each subfigure ((a) to (f)) corresponds to a different acquisitions. The color scale represents the redox ratio calculated on a pixel-by-pixel basis.

observable.

As previously discussed, future automatic discrimination between normal and tumoral samples could be performed using a supervised classifier, such as SVM, following a similar strategy to that adopted in the OCT study.

To quantitatively assess the separation between groups before classifier implementation, a boxplot incorporating all redox ratio values from both normal and tumoral phantoms was generated (Figure 7.22). The boxplot visually indicates a clear shift between the two datasets. To statistically validate this observed separation, inferential statistical analysis was subsequently performed.

The tumoral group presented a higher redox ratio (median = 0.4087, n = 335) compared to the normal group (median = 0.3769, n = 335). A Mann–Whitney U test confirmed that this difference is statistically significant ($U = 6981$, exact two-tailed $p < 0.0001$). The Mann–Whitney test was selected because the

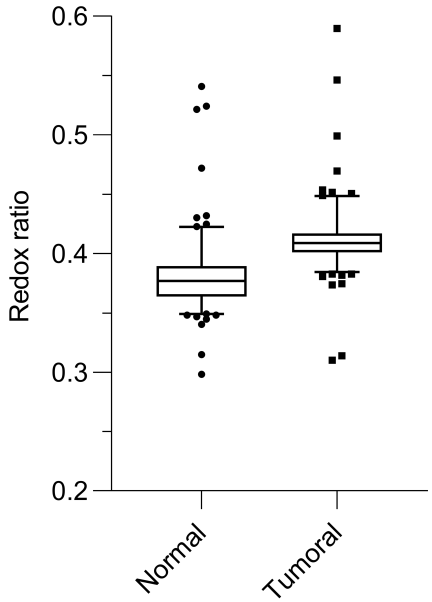


Figure 7.22: Boxplot representation of the redox ratio values obtained from all solid phantoms containing NAD(P)H, FAD, hemoglobin, and polystyrene beads.

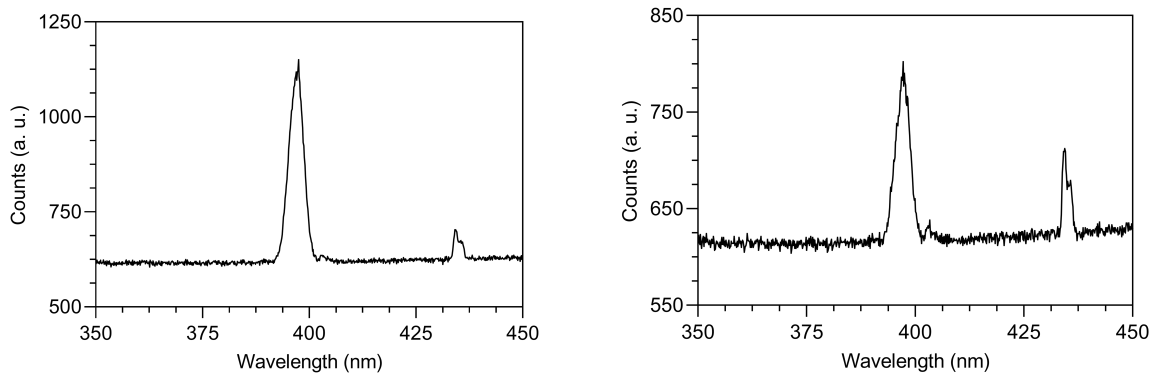
assumption of normality was not satisfied. The Shapiro–Wilk test yielded $p = 0.000$ for both the normal and tumoral groups, indicating that neither distribution follows a normal distribution. Therefore, a non-parametric test was considered the most appropriate approach for comparing the two groups.

Overall, these results demonstrate that the redox ratio provides a statistically significant distinction between normal and tumoral phantoms, even in the presence of scattering and absorption components that increase optical complexity. The observed shift in central tendency, confirmed by non-parametric statistical analysis, supports the robustness of the redox ratio as a metabolic indicator in this model. These findings reinforce the potential of this parameter to serve as a reliable feature for subsequent automatic classification using machine learning approaches.

7.5.6 Preliminary SHG Measurements with Biological Tissues

The signals obtained from the biological samples (generated by CAM assays) are presented in Figure 7.23.

The detected SHG signals demonstrate the feasibility of generating nonlinear optical responses from biological samples using the proposed setup. However, it is important to consider that, according to the CAM assay preparation protocol, Matrigel is used as part of the sample matrix. Since Matrigel contains collagen, a strong non-centrosymmetric structure, the measured SHG signal may originate not only from the implanted human tissue but also from this component. Therefore, for a more accurate assessment of



(a) (b)

Figure 7.23: Measured SHG signals from: (a) normal CAM sample; (b) tumoral CAM sample.

tissue-specific SHG signals, future studies should consider alternative preparation protocols that exclude Matrigel. This represents an important step for further development of this methodology.

Additional tests were performed at different stages of the setup development, focusing on the detection of 2PEF signals from biological samples. In these experiments, no significant fluorescence signal was observed, and therefore, the corresponding data are not presented. This outcome highlights the challenges of detecting weak nonlinear signals in complex biological samples and indicates that improvements in signal acquisition are required. For instance, the use of more sensitive detection systems, such as PMT, could significantly enhance signal collection efficiency.

Overall, these preliminary results confirm that nonlinear signals can be generated from biological samples. Nevertheless, further optimization of the detection system is essential to enable reliable and quantitative measurements in such complex environments.

7.6 Outlook

In summary, this chapter addressed the development and validation of a MPM setup optimized for 2PEF measurements, with the main goal of label-free metabolic characterization of colorectal tissue-mimicking phantoms.

The proposed optical filtering strategy (fabricated optical filters centered at 485 nm and 530 nm), combined with excitation at 750 nm, enabled the selective detection of fluorescence signals associated with NAD(P)H and FAD. Across progressively more complex phantom models, ranging from simple fluorophore solutions to highly scattering and absorbing solid phantoms, the system demonstrated consistent capability to extract meaningful metabolic information. Despite variations in absolute fluorescence intensity caused

by alignment, scattering, absorption, and sample degradation, the redox ratio proved to be a robust and reliable metric for discriminating between normal and tumoral samples.

Statistical analysis confirmed that the redox ratio provides a significant separation between the two groups across multiple experimental conditions, acquisition days, and phantom compositions. These results highlight the resilience of the proposed methodology against experimental variability and its suitability for application in more complex and realistic biological environments.

Importantly, this work demonstrates that discrimination between metabolic states can be achieved using a single excitation wavelength, representing a key step toward simplifying MPM setups and enabling faster acquisitions. This finding is particularly relevant for the development of compact and cost-effective devices, where minimizing system complexity is essential.

The results obtained open the possibility of implementing automated classification approaches. In this context, the redox ratio, combined with statistical descriptors, could serve as input features for machine learning algorithms, such as SVM, enabling an automated tissue classification.

As an initial step toward biological validation, preliminary experiments were conducted using CAM assay membranes. These tests confirmed the capability of the MPM setup to measure nonlinear signals from biological samples, particularly SHG. However, it was observed that the detected signals may be influenced by the presence of Matrigel, a component of the CAM sample preparation protocol that contains collagen, which can contribute significantly to the SHG response. This highlights the need for improved sample preparation strategies to isolate tissue-specific signals.

In contrast, the detection of 2PEF signals in these complex biological samples proved to be more challenging, with no significant fluorescence signal observed under the tested conditions. This limitation emphasizes the need for further optimization of the detection system, particularly through the implementation of more sensitive detectors, such as PMT, and improved signal collection efficiency. These results underline both the potential and current limitations of the optical setup when transitioning from controlled phantom environments to real biological tissues.

Overall, this work represents a significant step toward the development of label-free optical biopsy techniques based on MPM. The integration of such systems into clinical tools, such as endoscopic platforms, could enable real-time, *in vivo* assessment of tissue metabolic state, improving early detection and diagnosis of CRC. Future work will focus on optimizing the spectral filtering, improving signal collection efficiency, and validating the methodology in biological tissues.

Part V

Systems Miniaturization

Chapter 8

Colonoscope Integration

This chapter addresses the key challenges and future directions associated with the translation of optical imaging techniques into clinically compatible systems for CRC diagnosis. Building upon the results presented throughout this thesis, the focus is placed on the miniaturization of OCT and MPM technologies, aiming to enable their integration into conventional colonoscopy platforms. The chapter discusses current technological limitations, reviews existing miniaturized approaches, and proposes conceptual system designs to overcome these constraints. Additionally, preliminary experimental developments are presented, highlighting essential steps toward compact and efficient implementations.

8.1 Context

As discussed previously, conventional cancer diagnosis relies on the preparation, staining, visualization, and interpretation of histological tissue samples, which remains the gold-standard diagnosis technique. Although these methods have been extensively developed and are widely used in pathology, they are inherently time- and labor-intensive. The histochemical processing of tissue, including fixation, embedding, sectioning, and staining, can require from 10 h up to several days [63].

Secondly, these processes may introduce artifacts, such as distortion or loss of biological structures, potentially leading to ambiguity or inaccuracies in the interpretation of histological images [63].

Due to the significant time, hard labor, and destructive nature of conventional histopathology, the biophotonics and microscopy communities have increasingly focused on the development of stain-free and slide-free diagnostic techniques. A long-standing goal in biomedical engineering is the realization of real-time, *in vivo*, label-free, three-dimensional molecular imaging with optical resolution.

In parallel, the clinical need for improved CRC diagnosis highlights the importance of reducing the time between tissue inspection and diagnosis. Ideally, this could reduce the need for physical biopsies in selected cases by enabling real-time optical assessment during colonoscopy. However, integrating advanced optical imaging techniques into endoscopic platforms presents significant technical challenges. For example, the instrumentation channel of a typical colonoscope, such as the Pentax FC-38FW2, has a diameter of 3.8 mm, imposing strict constraints on the size of any integrated optical system.

Among the candidate techniques for endoscopic optical biopsy, OCT and MPM stand out as particularly promising.

OCT systems can be implemented using optical fibers, making them highly suitable for miniaturization and integration into endoscopic devices. Their compactness enables access to internal organs, including colon, allowing structural imaging with micrometer-scale resolution.

On the other hand, MPM provides complementary functional information, enabling real-time imaging of cellular morphology and 3D tissue structure based on endogenous contrast mechanisms. It has been successfully applied in various fields, including neuroscience, developmental biology, immunology, cancer biology, and endocrinology [28, 240, 271, 272]. However, current MPM systems remain bulky and are not readily compatible with miniaturized implementations [240, 271, 272]. The MPM systems face relevant challenges related to the limited contrast from individual modalities, relatively low signal efficiency, and the reliance on complex and bulky laser systems. These factors hinder their widespread adoption in clinical environments.

The ultimate goal of this work is to contribute the integration of MPM and OCT into conventional colonoscopy systems, allowing simultaneous structural and functional imaging for enhanced cancer diagnostics. Achieving this objective requires significant advances in the miniaturization and optimization of optical components, as well as improvements in signal generation and detection efficiency.

Future work should focus on developing efficient light-delivery systems (e.g., fiber-based solutions) and miniaturized scanning mechanisms compatible with the limited dimensions of endoscopic channels. Additionally, improving detection sensitivity and filtering, for instance, using high-sensitivity detectors, such as PMT, and specific bandpass filters, will be essential to ensure higher signal levels in biological tissues, making it possible to detect CRC.

Overall, while the integration of MPM and OCT into clinical endoscopic platforms has not yet been achieved, the results presented in this thesis demonstrate important progress toward this objective. Continued developments in system miniaturization will be the key to achieving real-time, *in vivo*, label-free optical biopsy for CRC diagnosis.

8.2 Optical Coherence Tomography Miniaturization

Figure 8.1 illustrates the conceptual integration of OCT into a conventional colonoscope using an optical fiber, as well as the miniaturized design of an OCT catheter for optical biopsy. The proposed approach consists of maintaining the laser source and spectrometer outside the colonoscope, while delivering light to the sample through an optical fiber inserted into the instrument channel of conventional colonoscopes.

At the distal end of the fiber, a microfabricated optical assembly is implemented, comprising a beam

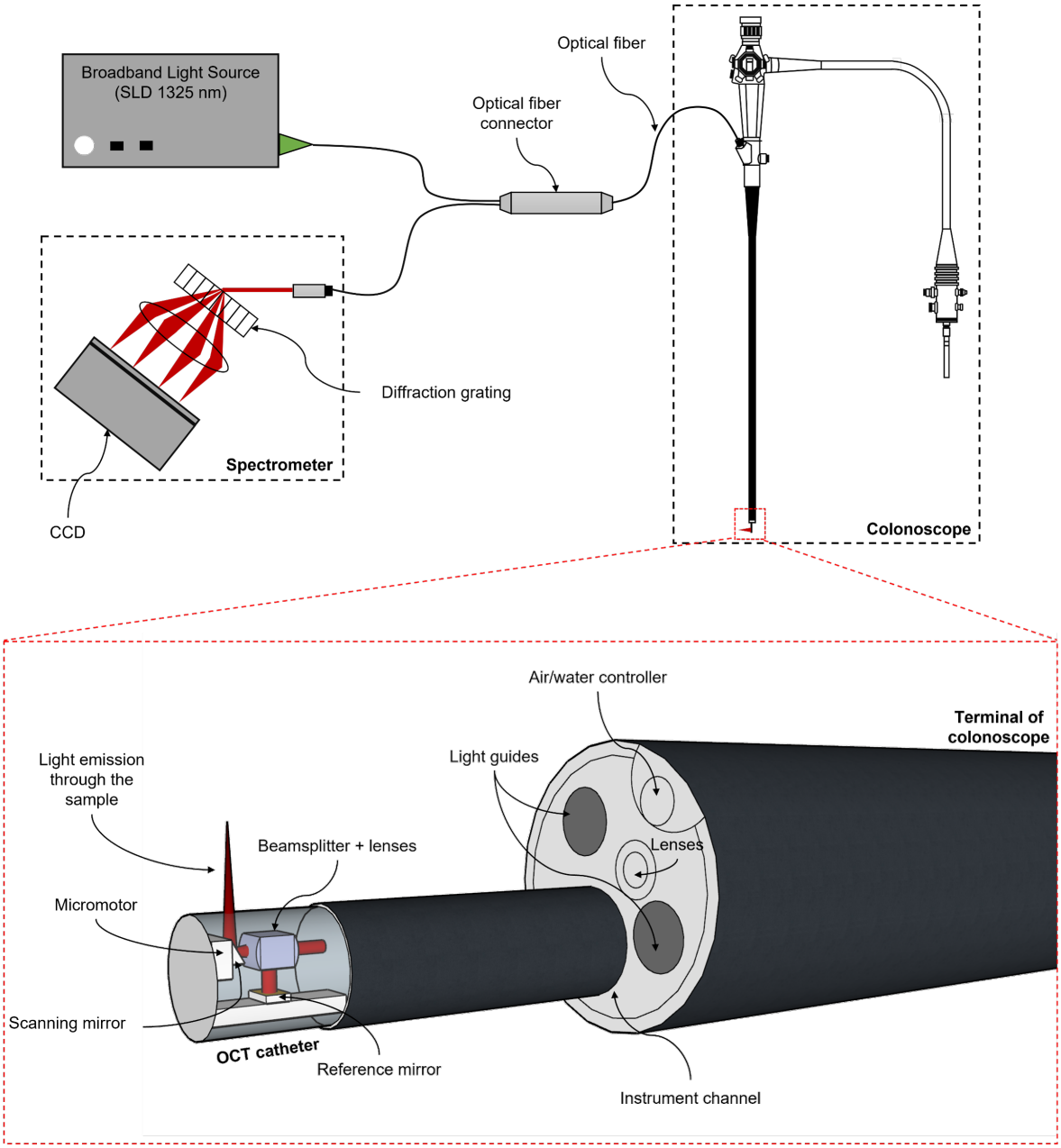


Figure 8.1: Illustration of the OCT integration in a conventional colonoscope for optical biopsy of the colorectal tissues. The OCT catheter is connected to the OCT system through an optical fiber [10].

splitter, focusing optics, a reference mirror, and a scanning element. The latter consists of a mirror coupled to a micromotor, enabling lateral beam-scanning across the sample. This configuration allows the acquisition of depth-resolved structural information.

It is important to note that the primary aim of this thesis was to evaluate the feasibility of detecting CRC using OCT imaging. The miniaturization process of the OCT technique was not the central focus of this work and was not investigated in depth. However, in the context of miniaturization, the key question will be wether the image quality obtained after imposing such constraints remains sufficient for reliable tumor

detection.

Nevertheless, previous work carried out within the MNFabs laboratory has addressed some of the challenges associated with system miniaturization, focusing on the development of key optical components, such as Michelson interferometers, beam splitters, and metallic mirrors, using techniques including dicing and thin-film deposition.

In this context, significant efforts have been devoted to the miniaturization of OCT systems using MOEMS-based approaches. Microfabrication strategies have been developed to enable compact, robust, and scalable OCT architectures. These contributions have advanced the feasibility of portable and endoscopic OCT devices for biomedical imaging applications. Representative works include studies on microfabrication techniques for OCT system miniaturization [81, 229, 273].

Additionally, a European patent application [274] was developed, addressing the conception, system design, and integration of a miniaturized OCT microsystem for colorectal applications. This patent describes a novel approach for screening, monitoring, and analyzing the colorectal tract using OCT technology. The proposed system is specifically designed to be compatible with conventional colonoscopy, enabling insertion through the instrument channel of a standard colonoscope by leveraging micro-opto-electro-mechanical systems (MOEMS) technologies. This innovation introduces a new diagnostic capability for endoscopic procedures, enabling high-resolution optical imaging and contributing to ongoing efforts in early CRC detection.

8.3 Multiphoton Microscopy Miniaturization

The integration of MPM technology into a conventional colonoscope can be achieved through: (1) the combination of multiple imaging modalities within a single platform, namely conventional high-definition white-light imaging and MPM, enabling improved sensitivity and specificity for malignant tissue identification; (2) the adaptation of photonic technologies for optical biopsy through the development of compact and miniaturized systems; and (3) the design of flexible probes capable of accessing lesions in hollow organs via the instrument channel of standard colonoscopes.

However, integrating MPM into a commercial colonoscope to enable automated optical biopsy presents several challenges, primarily related to the size constraints of conventional optical systems. Consequently, substantial efforts must be directed toward the miniaturization of the MPM setup.

A key aspect of this process involves the design, simulation, and fabrication of highly selective optical filters, specifically tailored to transmit the emission wavelengths of the target fluorophores. This work

has already been developed and presented along this thesis, resulting in two relevant scientific publications [13, 14]. These filters constitute a critical component of the proposed system. Their high spectral selectivity enables efficient multi-channel fluorescence detection, which is essential for metabolic analysis of colorectal tissues, as demonstrated through the redox ratio evaluation of normal and tumoral phantoms.

The main limitation to achieve the integration of MPM into a colonoscope, as discussed in the context of OCT miniaturization, is the diameter of the colonoscope instrumentation channel (typically 3.8 mm), which constitutes a fundamental design constraint for the proposed system.

8.3.1 Current Miniaturized Systems

In the last decade, several projects have emerged related to the development of miniaturized probes with MPM technology. In 2011, Rivera *et al.* [275] developed a compact and flexible endoscope (3 mm outer diameter), including a miniaturized resonant/non-resonant cantilever fiber raster scanner. In 2015, Ducourthial *et al.* [276] developed a miniaturized fiber scanning system with a piezoelectric tube embedded inside a 2.2 mm outer diameter probe. A bidimensional micro-electro-mechanical systems (MEMS) mirror was developed in 2015 by Duan *et al.* [277] to perform beam scanning in an endomicroscope, with a 3.4 mm distal diameter. In 2017, Liang *et al.* [278] developed an extremely compact, fiber-optic endomicroscopy platform in a flexible probe with 2.1 mm outer diameter, also containing a piezoelectric tubular scanner. Similarly, in 2018, Akhoundi *et al.* [279] developed a compact MPM endoscope based on a piezoelectric scanning tube with an outer diameter of 5 mm. The high diameter makes it impossible to place the probe in the colonoscope instrumentation channel. All the setups described previously use optical fiber between the MPM setup and the miniaturized scanning system, with appropriate optics for focusing light onto the tissues. Very recently (2019), Dilipkumar *et al.* [280] developed a compact multiphoton endomicroscope for *in vivo* imaging in small animals (such as mice) using a side-viewing needle objective. However, this approach presents a poor axial resolution (30-60 µm).

All previously presented studies primarily focus on the miniaturization of the scanning system (i.e., the probe), while largely neglecting the miniaturization and optimization of other critical optical components, such as lenses and spectral filtering elements.

In addition, most reported systems have been validated only in *ex vivo* samples or small-animal models, with limited translation to realistic clinical scenarios. Importantly, these works are mainly oriented toward imaging performance rather than diagnostic capability, and do not address the development of fully automated systems for CRC detection. As a result, the ability to reliably distinguish between normal and tumoral tissues, and, more importantly, to optimize this discrimination, remains largely unexplored in

the context of miniaturized multiphoton systems.

Additionally, most systems rely primarily on structural imaging, without exploiting intrinsic metabolic contrast mechanisms, such as autofluorescence-based biomarkers (e.g., NAD(P)H and FAD), which are essential for functional tissue characterization.

Moreover, these systems typically operate under fixed excitation conditions, without exploring optimized wavelength strategies for simultaneous or selective excitation of multiple endogenous fluorophores.

Overall, a significant gap remains between technological miniaturization and clinical applicability, particularly in terms of robustness, real-time analysis, and integration into existing medical workflows.

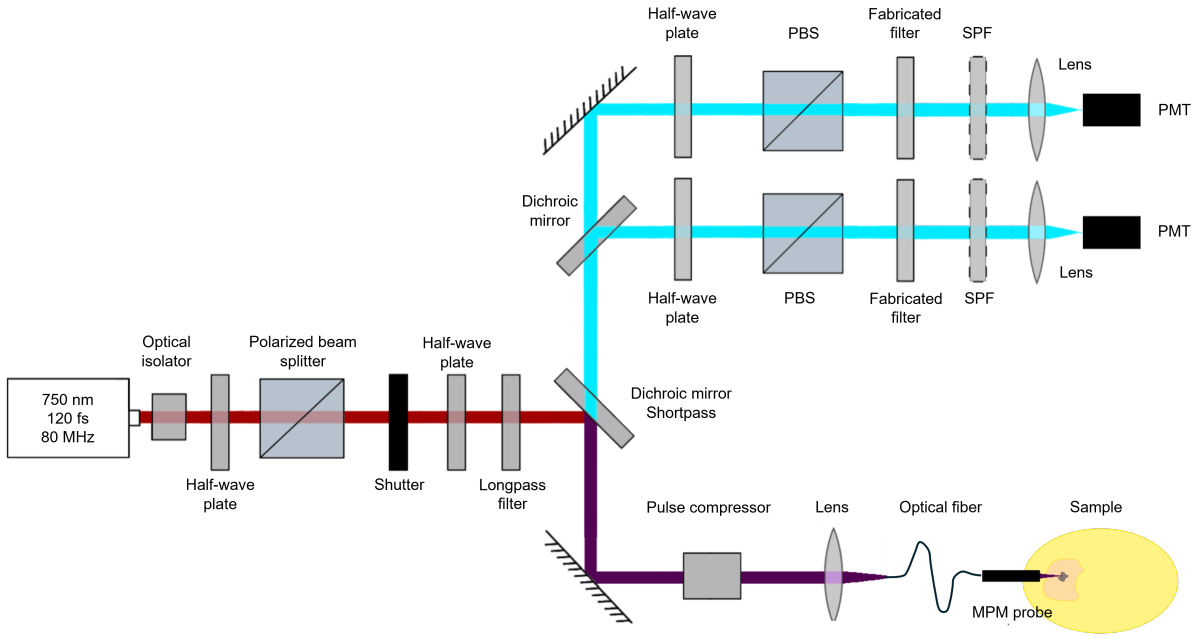
More recently, Zong *et al.* [281] developed a highly advanced miniaturized two-photon microscope, representing a significant step forward in multiphoton system miniaturization. This device achieves a total weight below $3\,\mathrm{g}$, enabling imaging in freely moving animals without significantly affecting their natural behavior [281]. The system integrates several key innovations, including a hollow-core photonic crystal fiber for femtosecond pulse delivery, a fast MEMS scanner for beam scanning, and a micro-tunable lens for rapid axial focusing. These features allow high-resolution, multiplane imaging with a field of view up to approximately $500\,\mu\mathrm{m}$ and imaging speeds up to $40\,\mathrm{Hz}$. Additionally, the system enables three-dimensional imaging and large-scale data acquisition, with the capability to monitor more than 1,000 neurons simultaneously and, through field stitching, up to 10,000 neurons in a single experiment [281].

Despite these significant advances, the current system design remains primarily suited for neuroscience applications rather than clinical endoscopic integration, and is therefore not compatible with conventional colonoscopy. Nevertheless, this work represents a major milestone in the development of compact multiphoton systems, highlighting both the progress achieved and the remaining challenges toward full miniaturization and clinical translation.

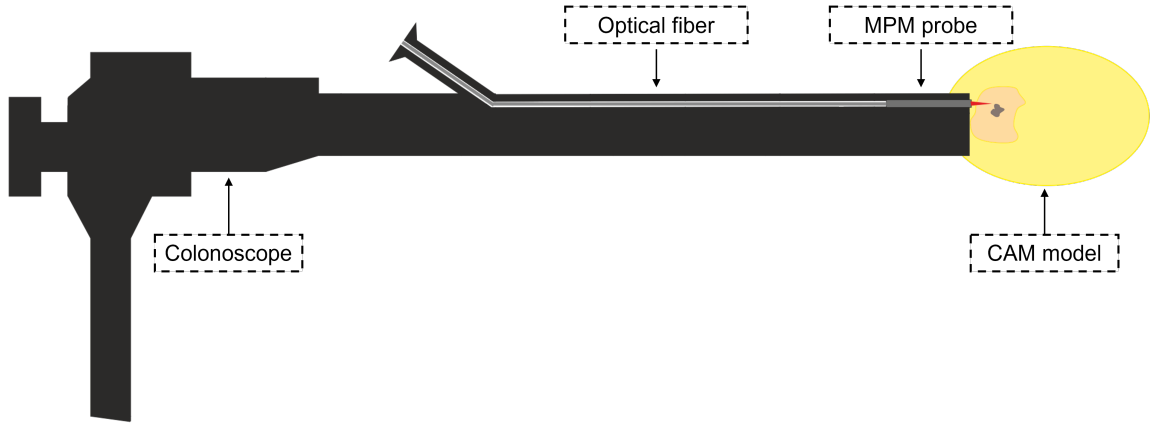
8.3.2 Proposed System

An initial conceptual design for a miniaturized multiphoton system is presented in Figure 8.2. The proposed setup maintains the laser source and detection system outside the colonoscope. The detection stage is expected to be enhanced by the optical filtering strategies developed in this work. The excitation light is delivered through an optical fiber, which connects to a miniaturized multiphoton probe positioned at the distal end of the colonoscope.

This probe is envisioned to incorporate a piezoelectric scanning tube (e.g., commercially available devices from PI (Physik Instrumente) [282]) to enable two-dimensional beam scanning, combined with gradient refractive index (GRIN) lenses for efficient focusing onto the sample. Additionally, the integration



(a)



(b)

Figure 8.2: (a) Schematic representation of the proposed miniaturized MPM system for endoscopic integration. Abbreviations: PMT - photomultiplier tube; PBS - polarizing beam splitter; SPF - short-pass filter; (b) conceptual illustration of the multiphoton probe integration within a conventional colonoscope. The excitation light is guided through an optical fiber along the instrument channel, reaching the distal end where the miniaturized probe interacts with the biological sample (represented by a CAM model).

of micro-tunable lenses, like those reported by Zong *et al.* [281], would provide dynamic axial focusing, enabling depth-resolved imaging and, consequently, three-dimensional scanning capability.

It is important to note that, although commercially available piezoelectric scanning tubes and GRIN lenses exist, a detailed design and simulation of the probe are required to assess whether custom com-

ponents with specific characteristics are necessary to ensure proper integration within the endoscope and optimal system performance. This may involve the use of microfabrication techniques to meet the stringent size and optical constraints. The MNFAbs laboratory has prior experience in the development of optical components using innovative fabrication approaches [227, 228], which provides a strong foundation for addressing these challenges.

An essential component of the system is a pulse compressor setup placed before coupling the laser into the optical fiber. Since multiphoton excitation critically depends on high peak intensities, temporal pulse broadening due to dispersion in the fiber must be compensated. Therefore, pre-compensation of the pulse is required to ensure that, after propagation through the fiber, the pulse duration remains sufficiently short to efficiently generate 2PEF signals.

It is important to note that a key improvement in signal acquisition involves replacing the spectrometer with a PMT, which offers higher sensitivity and detection efficiency. This modification is particularly relevant to compensate for the expected signal losses associated with light transmission through long optical fibers and operation within confined geometries.

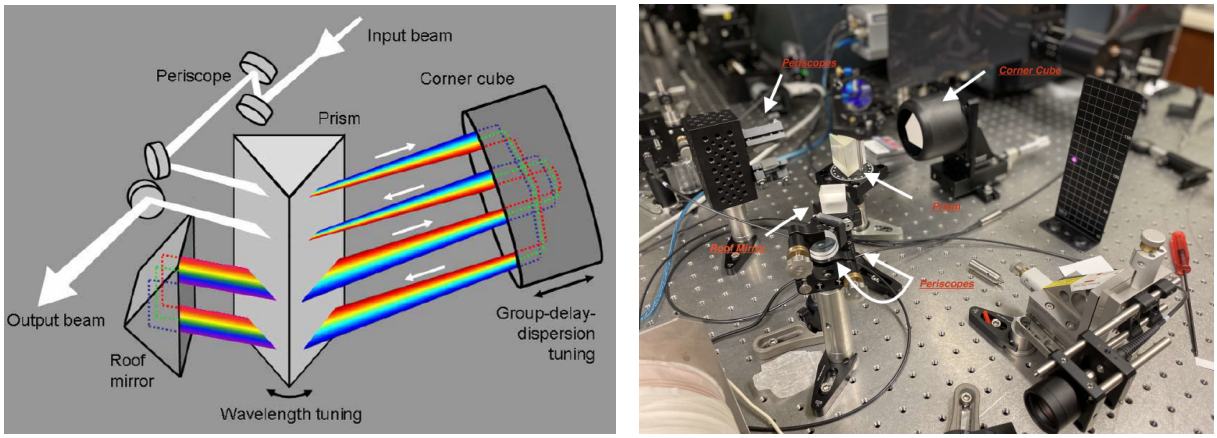
It should be noted that the design presented in Figure 8.2 serves as a preliminary conceptual framework intended to guide future developments, rather than a fully implemented system within the scope of this thesis.

8.3.3 Preliminary Experimental Results

An initial step towards MPM miniaturization was achieved by developing a pulse compressor, a critical component of the system. As previously discussed, pulse compression is essential because optical pulses broaden temporally during propagation through the fiber due to dispersion, which significantly reduces the peak intensity and, consequently, the efficiency of 2PEF signal generation.

The developed pulse compressor was based on the approach proposed by Akturk *et al.* in 2006 [11]. A schematic representation of the concept, and the implemented setup is shown in Figure 8.3.

To validate the compressor's performance, a set of experiments was conducted to assess its ability to compress the laser pulses temporally. In these experiments, the separation between the prism and the corner cube varied over a total range of 15 cm, in steps of 1 cm, using a translation rail. The FWHM of the output pulse was measured using an autocorrelator (APE Mini). The results are presented in Figure 8.4. The observed dependence of the pulse duration on the prism–corner cube separation confirms the correct operation of the pulse compressor.



(a) (b)

Figure 8.3: (a) Schematic representation of the prism-based pulse compressor, adapted from Akturk *et al.* [11]; (b) Experimental implementation of the pulse compressor setup, showing the optical components mounted on a translation stage.

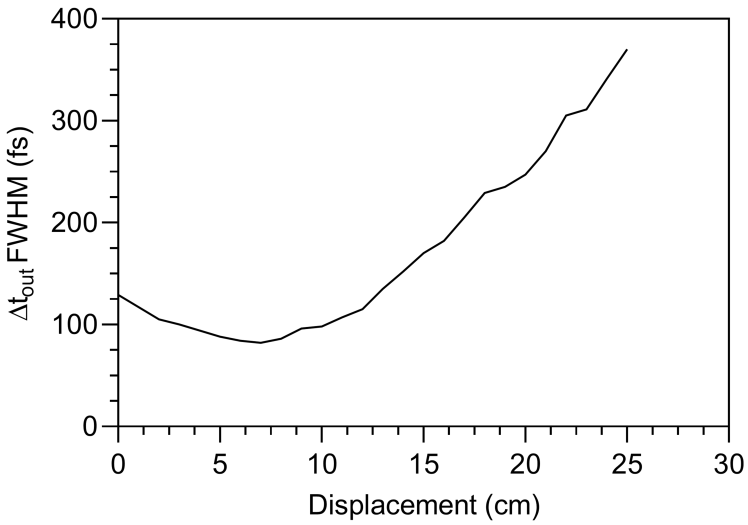


Figure 8.4: FWHM of the output pulse as a function of the distance between the prism and the corner cube.

8.4 Outlook

This chapter presented the conceptual framework and initial experimental steps toward the miniaturization of OCT and MPM systems for integration into conventional colonoscopy platforms. The results obtained provide important insights into the feasibility and key challenges associated with this ultimate objective.

In the case of OCT, the analysis demonstrated that meaningful structural information can still be ob-

tained under miniaturization constraints, supporting the potential of this technique for endoscopic optical biopsy. Furthermore, previous work within the research group has already addressed critical aspects of OCT miniaturization through microfabrication of optical components and system integration strategies, providing a solid foundation for future developments.

For MPM, the developed work contributes to bridging the gap between laboratory-scale systems and clinically compatible implementations. In particular, the development of highly selective optical filters and the validation of metabolic contrast through the redox ratio represent significant steps toward functional optical biopsy. Additionally, the successful implementation and validation of a pulse compressor highlight the importance of dispersion management in fiber-based multiphoton systems, which is a key requirement for future miniaturized configurations.

Despite these advances, several challenges remain. One of the main limitations is the efficient delivery and collection of optical signals within the strict dimensional constraints imposed by endoscopic systems. Future work should therefore focus on optimizing fiber-based light delivery, improving signal collection efficiency, and integrating high-sensitivity detection schemes, such as PMT.

Moreover, the design and fabrication of the miniaturized multiphoton probe will require detailed optical and mechanical simulations to ensure optimal performance within the limited available space. This includes the development of customized MOEMS, such as GRIN lenses, scanning mechanisms, and adaptive focusing elements. The integration of pulse pre-compensation strategies will also be essential to preserve ultrashort pulse durations at the sample.

Ultimately, the successful integration of OCT and MPM into a single miniaturized platform could enable simultaneous structural and functional imaging during colonoscopy, significantly enhancing the capability for real-time, *in vivo*, label-free optical biopsy. Although this goal has not yet been fully achieved, the work presented in this thesis establishes a strong technological and methodological foundation for its accomplishment.

Part VI

Final Remarks

Chapter 9

Conclusions

This thesis addressed the development and application of advanced optical imaging techniques for CRC diagnosis, with a particular focus on OCT and MPM. By combining experimental models, technological developments, and data analysis methodologies, this work contributes to the advancement of optical biopsy approaches aimed at real-time, *in vivo* tissue characterization.

A central contribution of this work was the development and validation of tissue models, including CAM assays and tissue-mimicking phantoms, which provided controlled and reproducible environments for the systematic evaluation of optical imaging techniques. These models enabled the investigation of both structural and functional tissue properties, effectively bridging the gap between simplified experimental conditions and complex biological systems.

From a structural imaging perspective, OCT demonstrated a strong capability to discriminate between non-malignant and malignant colorectal tissues. The extraction of quantitative features, particularly the attenuation coefficient, proved to be a robust approach for tissue characterization. The integration of machine learning further enhanced this capability, with the implemented SVM classifier achieving an accuracy of 1.0 in distinguishing non-malignant and malignant tissues under the studied conditions, using a nested cross-validation framework, supporting the robustness of the classification approach. This classification was based on features extracted from depth-resolved attenuation coefficient maps using multiple statistical descriptors (MED, MAX, and IQR combinations). Importantly, accurate discrimination was achieved using small tissue regions of approximately 300 µm (lateral) × 103 µm (depth), highlighting the potential for simplified and miniaturized OCT implementations in endoscopic applications. These results support the feasibility of real-time identification of suspicious tissues during colonoscopy with reduced scanning requirements.

Complementarily, MPM enabled the investigation of functional and metabolic tissue properties through the detection of endogenous fluorophores such as NAD(P)H and FAD. The development and implementation of highly selective Fabry–Perot optical filters allowed efficient spectral separation of these fluorophores, significantly reducing cross-talk and improving signal specificity. One of the fabricated filters achieved a peak transmittance of approximately 95 % at 483–485 nm with a FWHM of about 13.89 nm, enabling selective detection of NAD(P)H fluorescence. The other filter achieved a peak transmittance of approximately 91 % at 535–538 nm with a FWHM of about 10.73 nm, enabling selective detection of FAD fluorescence.

Experimental validation using tissue-mimicking phantoms demonstrated that the MPM system is capable of reliably detecting fluorescence signals associated with each fluorophore under excitation at 750 nm. Importantly, the analysis of the redox ratio revealed a reproducible distinction between normal and tumoral phantom conditions, demonstrating sensitivity to metabolic differences associated with pathological states. This supports the potential of MPM for metabolic-based tissue discrimination. These results demonstrate that biochemical differences associated with cancer can be detected using label-free techniques, representing a key step toward functional optical biopsy.

Beyond individual components, this thesis also explored the miniaturization of OCT and MPM systems for integration into conventional colonoscopes, presenting initial design concepts and identifying key technical challenges, including optical signal delivery, detection efficiency, and system integration constraints.

Despite these promising results, it is important to note that part of the validation was performed using simplified phantom models, and that further studies in complex biological tissues and clinical settings are required to fully assess the robustness and translational potential of the proposed approaches, as detailed in the following chapter.

Overall, this work suggests that the combination of OCT and MPM provides complementary structural and functional information, enabling a more comprehensive characterization of colorectal tissues. While OCT enables accurate morphological assessment and quantitative tissue classification, MPM adds metabolic insight through redox-based contrast, significantly enhancing diagnostic capability.

In summary, the main contribution of this thesis lies in the demonstration that the combination of structural (OCT) and functional (MPM) optical techniques enables accurate and complementary discrimination of colorectal tissues, under conditions compatible with future endoscopic implementation.

Ultimately, this thesis contributes to the long-term goal of enabling real-time, label-free optical biopsy during endoscopic procedures, with the potential to significantly improve early detection, diagnostic accuracy, and clinical outcomes in CRC.

Chapter 10

Future work

The results obtained in this thesis open several directions for future research, aiming to further improve the developed methodologies and advance their translation toward clinical applications. The main proposed directions are summarized as follows:

- **Validation in biological samples:** evaluation of the developed MPM setup using CAM assays and *ex vivo* colorectal tissues, enabling validation under biologically relevant conditions.
- **Advanced data analysis and classification:** application of machine learning methods, such as SVM, to MPM data, including the use of redox ratio and other extracted features for automated tissue classification.
- **Improvement of CAM model preparation:** development of CAM assays without Matrigel to minimize external contributions, such as collagen-induced SHG, and improve the reliability of tissue-specific signal interpretation.
- **Investigation of nonlinear optical signals:** systematic study of SHG signals in biological samples to better understand their origin and contribution to tissue characterization, as well as their potential integration with the fluorescence-based metrics.
- **Optimization of detection efficiency:** replacement of the current detection system with PMT to improve sensitivity and signal-to-noise ratio. Additional optimization of collection optics may also be considered.
- **Pulse delivery and dispersion management:** implementation of a pulse compressor in the MPM setup to compensate for temporal pulse broadening. Further investigation of pulse propagation in optical fibers, including dispersion effects, and exploration of alternative solutions such as photonic crystal fibers.
- **Development of a miniaturized MPM probe:** design and implementation of a compact multiphoton probe compatible with the dimensional constraints of conventional colonoscopes.
- **Integration of advanced contrast mechanisms:** evaluation of the incorporation of FLIM into the MPM system to enhance metabolic contrast and improve diagnostic performance.

Bibliography

[1] V. V. Tuchin, "Tissue Optics and Photonics: Light-Tissue Interaction II," *Journal of Biomedical Photonics and Engineering*, vol. 2, no. 3, p. 030201, 2016. [Online]. Available: http://jbpe.ssau.ru/index.php/JBPE/article/view/3042

[2] V. V. Tuchin, "Tissue Optics and Photonics: Light-Tissue Interaction," *Journal of Biomedical Photonics & Engineering*, vol. 2, no. 3, pp. 98–134, jun 2015. [Online]. Available: http://jbpe.ssau.ru/index.php/JBPE/article/view/2469

[3] "New cancer cases worldwide by type 2022| statista." [Online]. Available: https://www.statista.com/statistics/288559/new-cancer-cases-worldwide-by-type/

[4] "Colon rectum cancer deaths number u.s. 1999-2023| statista." [Online]. Available: https://www.statista.com/statistics/533965/colon-and-rectum-cancer-deaths-in-us/

[5] "New cancer cases rate worldwide by type 2022| statista." [Online]. Available: https://www.statista.com/statistics/1030500/new-cancer-cases-rate-worldwide-by-type/

[6] "Cancer death rates by type worldwide 2022| statista." [Online]. Available: https://www.statista.com/statistics/1031260/cancer-death-rate-worldwide-by-type/

[7] "Cancer deaths forecast worldwide 2022| statista." [Online]. Available: https://www.statista.com/statistics/1031323/cancer-deaths-forecast-worldwide/

[8] L. V. Rodríguez-de Marcos, J. I. Larruquert, J. A. Méndez, and J. A. Aznárez, "Self-consistent optical constants of SiO2 and Ta2O5 films," *Optical Materials Express*, vol. 6, no. 11, p. 3622, nov 2016. [Online]. Available: https://opg.optica.org/abstract.cfm?URI=ome-6-11-3622

[9] A. Jolivet, C. Labbé, C. Frilay, O. Debieu, P. Marie, B. Horcholle, F. Lemarié, X. Portier, C. Grygiel, S. Duprey, W. Jadwisienczak, D. Ingram, M. Upadhyay, A. David, A. Fouchet, U. Lüders, and J. Cardin, "Structural, optical, and electrical properties of TiO2 thin films deposited by ALD: Impact of the substrate, the deposited thickness and the deposition temperature," *Applied Surface Science*, vol. 608, p. 155214, jan 2023. [Online]. Available: https://linkinghub.elsevier.com/retrieve/pii/S0169433222027428

[10] H. M. Pereira, R. B. Freitas, M. J. Maciel, S. Pimenta, M. Costa, F. Baltazar, C. A. Silva, and J. H. Correia, "The chick chorioallantoic membrane assay as an in vivo model for colon tumor analysis

with optical coherence tomography," *Expert Systems with Applications*, vol. 255, p. 124611, dec 2024. [Online]. Available: https://linkinghub.elsevier.com/retrieve/pii/S0957417424014787

[11] S. Akturk, X. Gu, M. Kimmel, and R. Trebino, "Extremely simple single-prism ultrashort-pulse compressor," *Optics Express*, vol. 14, no. 21, p. 10101, 2006. [Online]. Available: https://opg.optica.org/oe/abstract.cfm?uri=oe-14-21-10101

[12] R. B. Freitas and H. M. Pereira, "Human colorectal tissue oct dataset: Neoplastic and non-neoplastic samples from chorioallantoic membrane (cam) assays," 2024. [Online]. Available: https://zenodo.org/records/10782863

[13] R. B. Freitas, M. J. L. F. Rodrigues, S. Pimenta, M. Belsley, J. H. Correia, and M. J. Maciel, "Highly-selective optical filter for NADH fluorescence detection in multiphoton microscopy," *Biomedical Optics Express*, vol. 15, no. 5, p. 3317, may 2024. [Online]. Available: https://opg.optica.org/boe/abstract.cfm?doi=10.1364/BOE.506777

[14] R. B. Freitas, M. J. L. F. Rodrigues, N. F. Cunha, S. Pimenta, M. Belsley, J. H. Correia, and M. J. Maciel, "NAD(P)H–FAD fluorescence detection using multiphoton microscopy improved with highly selective optical filters," *Optical and Quantum Electronics*, vol. 57, no. 7, p. 389, jun 2025. [Online]. Available: https://link.springer.com/10.1007/s11082-025-08309-7

[15] R. M. F. Baptista, C. S. B. Gomes, B. Silva, J. Oliveira, B. Almeida, C. Castro, P. V. Rodrigues, A. Machado, R. B. Freitas, M. J. L. F. Rodrigues, E. de Matos Gomes, and M. Belsley, "A Polymorph of Dipeptide Halide Glycyl-L-Alanine Hydroiodide Monohydrate: Crystal Structure, Optical Second Harmonic Generation, Piezoelectricity and Pyroelectricity," *Materials*, vol. 16, no. 10, p. 3690, may 2023. [Online]. Available: https://www.mdpi.com/1996-1944/16/10/3690

[16] V. V. Tuchin, "Tissue Optics and Photonics: Biological Tissue Structures," *Journal of Biomedical Photonics and Engineering*, vol. 1, no. March, pp. 98–134, jun 2015. [Online]. Available: http://jbpe.ssau.ru/index.php/JBPE/article/view/2469

[17] J. M. Berg, J. L. Tymoczko, and S. Lubert, *Biochemistry*, 5th ed. New York: W. H. Freeman Publishing, 2002.

[18] M. Gooz and E. N. Maldonado, "Fluorescence microscopy imaging of mitochondrial metabolism in cancer cells," *Frontiers in Oncology*, vol. 13, no. June, pp. 1–18, jun 2023. [Online]. Available: https://www.frontiersin.org/articles/10.3389/fonc.2023.1152553/full

[19] X. Bao, B. Hou, Z. Guo, L. Song, H. Chen, Q. Zheng, Y. Zhao, D. Gao, C. Fan, X. Xiong, C. Sun, and J. Zhao, "Absolute dynamic and relative static: the relationship of glycolysis and OXPHOS in cancer development," *Cell Death Discovery*, no. September 2025, mar 2026. [Online]. Available: https://www.nature.com/articles/s41420-026-02992-5

[20] Y. Tong, W.-Q. Gao, and Y. Liu, "Metabolic heterogeneity in cancer: An overview and therapeutic implications," *Biochimica et Biophysica Acta (BBA) - Reviews on Cancer*, vol. 1874, no. 2, p. 188421, dec 2020. [Online]. Available: https://doi.org/10.1016/j.bbcan.2020.188421

[21] R. Cao, H. K. Wallrabe, and A. Periasamy, "Multiphoton FLIM imaging of NAD(P)H and FAD with one excitation wavelength," *Journal of Biomedical Optics*, vol. 25, no. 01, p. 1, jan 2020. [Online]. Available: https://www.spiedigitallibrary.org/journals/journal-of-biomedical-optics/volume-25/issue-01/014510/Multiphoton-FLIM-imaging-of-NADPH-and-FAD-with-one-excitation/10.1117/1.JBO.25.1.014510.full

[22] A. Podder, N. Thirumalaivasan, Y. K. Chao, P. Kukutla, S.-P. Wu, and S. Bhuniya, "Two-photon active fluorescent indicator for detecting NADH dynamics in live cells and tumor tissue," *Sensors and Actuators B: Chemical*, vol. 324, no. July, p. 128637, dec 2020. [Online]. Available: https://linkinghub.elsevier.com/retrieve/pii/S0925400520309837

[23] C. Stringari, R. A. Edwards, K. T. Pate, M. L. Waterman, P. J. Donovan, and E. Gratton, "Metabolic trajectory of cellular differentiation in small intestine by Phasor Fluorescence Lifetime Microscopy of NADH," *Scientific Reports*, vol. 2, no. 1, p. 568, aug 2012.

[24] R. K. Benninger and D. W. Piston, "Two□Photon Excitation Microscopy for the Study of Living Cells and Tissues," *Current Protocols in Cell Biology*, vol. 59, no. 1, 2013. [Online]. Available: https://onlinelibrary.wiley.com/doi/10.1002/0471143030.cb0411s20

[25] R. Cicchi, A. Sturiale, G. Nesi, D. Kapsokalyvas, G. Alemanno, F. Tonelli, and F. S. Pavone, "Multi-photon morpho-functional imaging of healthy colon mucosa, adenomatous polyp and adenocarcinoma," *Biomedical Optics Express*, vol. 4, no. 7, p. 1204, jul 2013.

[26] S. M. Hong, S. W. Hwang, T. Wang, C. W. Park, Y. Ryu, J. Jung, J. H. Shin, S. Kim, J. L. Lee, C. W. Kim, G. Yoon, K. H. Kim, S. Myung, and K. Y. Choi, "Increased nicotinamide adenine dinucleotide pool promotes colon cancer progression by suppressing reactive oxygen species level," *Cancer Science*, vol. 110, no. 2, pp. 629–638, feb 2019. [Online]. Available: https://onlinelibrary.wiley.com/doi/10.1111/cas.13886

[27] S. Zhuo, J. Yan, G. Chen, J. Chen, Y. Liu, J. Lu, X. Zhu, X. Jiang, and S. Xie, "Label-free monitoring of colonic cancer progression using multiphoton microscopy," *Biomedical Optics Express*, vol. 2, no. 3, p. 615, mar 2011. [Online]. Available: https://opg.optica.org/boe/abstract.cfm?uri=boe-2-3-615

[28] R. K. P. Benninger, M. Hao, and D. W. Piston, "Multi-photon excitation imaging of dynamic processes in living cells and tissues," in *Reviews of Physiology Biochemistry and Pharmacology*. Berlin, Heidelberg: Springer Berlin Heidelberg, 2008, vol. 160, pp. 71–92. [Online]. Available: http://link.springer.com/10.1007/112_2008_801

[29] W. Denk, J. H. Strickler, and W. W. Webb, "Two-Photon Laser Scanning Fluorescence Microscopy," *Science*, vol. 248, no. 4951, pp. 73–76, apr 1990. [Online]. Available: https://www.science.org/doi/10.1126/science.2321027

[30] J. R. Lakowicz, *Principles of Fluorescence Spectroscopy*, 3rd ed., J. R. Lakowicz, Ed. Boston, MA: Springer US, 2006. [Online]. Available: http://link.springer.com/10.1007/978-0-387-46312-4

[31] S. Villette, S. Pigaglio-Deshayes, C. Vever-Bizet, P. Validire, and G. Bourg-Heckly, "Ultraviolet-induced autofluorescence characterization of normal and tumoral esophageal epithelium cells with quantitation of NAD(P)H," *Photochemical and Photobiological Sciences*, vol. 5, no. 5, pp. 483–492, may 2006. [Online]. Available: https://link.springer.com/10.1039/b514801d

[32] Y. Wu and J. Y. Qu, "Two-photon autofluorescence spectroscopy and second-harmonic generation of epithelial tissue," *Optics Letters*, vol. 30, no. 22, p. 3045, nov 2005. [Online]. Available: https://opg.optica.org/abstract.cfm?URI=ol-30-22-3045

[33] P. P. Provenzano, K. W. Eliceiri, J. M. Campbell, D. R. Inman, J. G. White, and P. J. Keely, "Collagen reorganization at the tumor-stromal interface facilitates local invasion," *BMC Medicine*, vol. 4, no. 1, p. 38, dec 2006. [Online]. Available: http://bmcmedicine.biomedcentral.com/articles/10.1186/1741-7015-4-38

[34] M. Fernandes, D. Rosel, and J. Brábek, "Translation in solid cancer: are size‐based response criteria an anachronism?" *Clinical and Translational Oncology*, vol. 17, no. 1, pp. 1–10, jan 2015. [Online]. Available: http://link.springer.com/10.1007/s12094-014-1207-5

[35] H. Kobayashi, R. Watanabe, and P. L. Choyke, "Improving Conventional Enhanced Permeability and Retention (EPR) Effects; What Is the Appropriate Target?" *Theranostics*, vol. 4, no. 1, pp. 81–89, 2014. [Online]. Available: http://www.thno.org/v04p0081.htm

[36] J. Piñeiro Fernández, K. A. Luddy, C. Harmon, and C. O'Farrelly, "Hepatic Tumor Microenvironments and Effects on NK Cell Phenotype and Function," *International Journal of Molecular Sciences*, vol. 20, no. 17, p. 4131, aug 2019. [Online]. Available: https://www.mdpi.com/1422-0067/20/17/4131

[37] W. health organization, "Cancer." [Online]. Available: https://www.who.int/news-room/fact-sheets/detail/cancer

[38] Y. Xi and P. Xu, "Global colorectal cancer burden in 2020 and projections to 2040," *Translational Oncology*, vol. 14, no. 10, p. 101174, oct 2021.

[39] I. Puig and T. Kaltenbach, "Optical Diagnosis for Colorectal Polyps: A Useful Technique Now or in the Future?" *Gut and Liver*, vol. 12, no. 4, pp. 385–392, jul 2018. [Online]. Available: http://www.gutnliver.org/journal/view.html?doi=10.5009/gnl17137

[40] G. Pellino, G. Gallo, P. Pallante, R. Capasso, A. De Stefano, I. Maretto, U. Malapelle, S. Qiu, S. Nikolaou, A. Barina, G. Clerico, A. Reginelli, A. Giuliani, G. Sciaudone, C. Kontovounisios, L. Brunese, M. Trompetto, and F. Selvaggi, "Noninvasive Biomarkers of Colorectal Cancer: Role in Diagnosis and Personalised Treatment Perspectives," *Gastroenterology Research and Practice*, vol. 2018, pp. 1–21, jun 2018. [Online]. Available: https://www.hindawi.com/journals/grp/2018/2397863/

[41] H. Brenner, C. Stock, and M. Hoffmeister, "Effect of screening sigmoidoscopy and screening colonoscopy on colorectal cancer incidence and mortality: systematic review and meta-analysis of randomised controlled trials and observational studies," *BMJ*, vol. 348, no. apr09 1, pp. g2467–g2467, apr 2014. [Online]. Available: http://dx.doi.org/doi:10.1136/bmj.g2467

[42] A. C. Society, "Colorectal Cancer Survival Rates | Colorectal Cancer Prognosis." [Online]. Available: https://www.cancer.org/cancer/types/colon-rectal-cancer/detection-diagnosis-staging/survival-rates.html

[43] C. of the European Union, "Proposal for a Council Recommendation (CR) on Strengthening prevention through early detection: A new approach on cancer screening replacing CR 2003/878/EC - Public Health," 2003. [Online]. Available: https://health.ec.europa.eu/publications/proposal-council-recommendation-cr-strengthening-prevention-through-early-detection-new-approach_en

[44] M. Vieth, P. Quirke, R. Lambert, L. von Karsa, and M. Risio, "European guidelines for quality assurance in colorectal cancer screening and diagnosis," *Endoscopy*, vol. 44, no. S 03, pp. SE131–SE139, sep 2012. [Online]. Available: http://www.thieme-connect.de/DOI/DOI?10.1055/s-0032-1309798

[45] K. W. Davidson, M. J. Barry, C. M. Mangione, M. Cabana, A. B. Caughey, E. M. Davis, K. E. Donahue, C. A. Doubeni, A. H. Krist, M. Kubik, L. Li, G. Ogedegbe, D. K. Owens, L. Pbert, M. Silverstein, J. Stevermer, C.-W. Tseng, and J. B. Wong, "Screening for Colorectal Cancer: US Preventive Services Task Force Recommendation Statement," *JAMA*, vol. 325, no. 19, p. 1965, may 2021. [Online]. Available: https://jamanetwork.com/journals/jama/fullarticle/2779985

[46] A. M. Wolf, E. T. Fontham, T. R. Church, C. R. Flowers, C. E. Guerra, S. J. LaMonte, R. Etzioni, M. T. McKenna, K. C. Oeffinger, Y. T. Shih, L. C. Walter, K. S. Andrews, O. W. Brawley, D. Brooks, S. A. Fedewa, D. Manassaram□Baptiste, R. L. Siegel, R. C. Wender, and R. A. Smith, "Colorectal cancer screening for average□risk adults: 2018 guideline update from the American Cancer Society," *CA: A Cancer Journal for Clinicians*, vol. 68, no. 4, pp. 250–281, jul 2018. [Online]. Available: https://acsjournals.onlinelibrary.wiley.com/doi/10.3322/caac.21457

[47] A. C. Society, "Guideline for Colorectal Cancer Screening." [Online]. Available: https://www.cancer.org/cancer/types/colon-rectal-cancer/detection-diagnosis-staging/acs-recommendations.html

[48] Council of the European Union, "Council Recommendation on Strengthening Prevention through Early Detection: A New EU Approach on Cancer Screening Replacing Council Recommendation 2003/878/EC. Off. J." *Official Journal of the European Union*, no. 2, pp. 1–10, 2022. [Online]. Available: https://eur-lex.europa.eu/legal-content/EN/TXT/PDF/?uri=CELEX:32022H1213(01)

[49] J. E. Allison, L. C. Sakoda, T. R. Levin, J. P. Tucker, I. S. Tekawa, T. Cuff, M. P. Pauly, L. Shlager, A. M. Palitz, W. K. Zhao, J. S. Schwartz, D. F. Ransohoff, and J. V. Selby, "Screening for colorectal neoplasms with new fecal occult blood tests: Update on performance characteristics," *Journal of the National Cancer Institute*, vol. 99, no. 19, pp. 1462–1470, 2007.

[50] J. K. Lee, E. G. Liles, S. Bent, T. R. Levin, and D. A. Corley, "Accuracy of Fecal Immunochemical Tests for Colorectal Cancer," *Annals of Internal Medicine*, vol. 160, no. 3, pp. 171–181, feb 2014. [Online]. Available: https://www.acpjournals.org/doi/10.7326/M13-1484

[51] T. F. Imperiale, D. F. Ransohoff, S. H. Itzkowitz, T. R. Levin, P. Lavin, G. P. Lidgard, D. A. Ahlquist, and B. M. Berger, "Multitarget Stool DNA Testing for Colorectal-Cancer Screening," *New*

England Journal of Medicine, vol. 370, no. 14, pp. 1287–1297, apr 2014. [Online]. Available: http://www.nejm.org/doi/10.1056/NEJMoa1311194

[52] P. J. Pickhardt, J. R. Choi, I. Hwang, J. A. Butler, M. L. Puckett, H. A. Hildebrandt, R. K. Wong, P. A. Nugent, P. A. Mysliwiec, and W. R. Schindler, "Computed Tomographic Virtual Colonoscopy to Screen for Colorectal Neoplasia in Asymptomatic Adults," *New England Journal of Medicine*, vol. 349, no. 23, pp. 2191–2200, dec 2003. [Online]. Available: http://www.nejm.org/doi/abs/10.1056/NEJMoa031618

[53] D. Shahsavari, M. Waqar, and V. Thoguluva Chandrasekar, "Image enhanced colonoscopy: updates and prospects—a review," *Translational Gastroenterology and Hepatology*, vol. 8, no. 1, pp. 26–26, jul 2023. [Online]. Available: https://tgh.amegroups.com/article/view/8117/html

[54] S.-A. McLachlan, A. Clements, and J. Austoker, "Patients' experiences and reported barriers to colonoscopy in the screening context—A systematic review of the literature," *Patient Education and Counseling*, vol. 86, no. 2, pp. 137–146, feb 2012. [Online]. Available: http://dx.doi.org/10.1016/j.pec.2011.04.010

[55] Y. R. Paudel, S. Mah, A. Aboyeji, and K. Adhikari, "Barriers and facilitators to colonoscopy participation for colorectal cancer screening: a rapid review," *Journal of Public Health*, no. 0123456789, mar 2025. [Online]. Available: https://doi.org/10.1007/s10389-025-02446-9

[56] G. G. Ginsberg, "Risks of Colonoscopy and Polypectomy," *Techniques in Gastrointestinal Endoscopy*, vol. 10, no. 1, pp. 7–13, jan 2008. [Online]. Available: https://linkinghub.elsevier.com/retrieve/pii/S1096288307000484

[57] W. Waddingham, U. Kamran, B. Kumar, N. J. Trudgill, Z. P. Tsiamoulos, and M. Banks, "Complications of colonoscopy: common and rare—recognition, assessment and management," *BMJ Open Gastroenterology*, vol. 10, no. 1, p. e001193, dec 2023. [Online]. Available: https://bmjopengastro.bmj.com/lookup/doi/10.1136/bmjgast-2023-001193

[58] S. Jain, J. Maque, A. Galoosian, A. Osuna-Garcia, and F. P. May, "Optimal Strategies for Colorectal Cancer Screening," *Current Treatment Options in Oncology*, vol. 23, no. 4, pp. 474–493, apr 2022. [Online]. Available: https://link.springer.com/10.1007/s11864-022-00962-4

[59] C. Spada, C. Hassan, M. Munoz-Navas, H. Neuhaus, J. Deviere, P. Fockens, E. Coron, G. Gay, E. Toth, M. E. Riccioni, C. Carretero, J. P. Charton, A. Van Gossum, C. A. Wientjes,

S. Sacher-Huvelin, M. Delvaux, A. Nemeth, L. Petruzziello, C. P. de Frias, R. Mayershofer, L. Aminejab, E. Dekker, J.-P. Galmiche, M. Frederic, G. W. Johansson, P. Cesaro, and G. Costamagna, "Second-generation colon capsule endoscopy compared with colonoscopy," *Gastrointestinal Endoscopy*, vol. 74, no. 3, pp. 581–589.e1, sep 2011. [Online]. Available: http://dx.doi.org/10.1016/j.gie.2011.03.1125

[60] C. N. Klabunde, D. Lanier, E. S. Breslau, J. G. Zapka, R. H. Fletcher, D. F. Ransohoff, and S. J. Winawer, "Improving Colorectal Cancer Screening in Primary Care Practice: Innovative Strategies and Future Directions," *Journal of General Internal Medicine*, vol. 22, no. 8, pp. 1195–1205, jul 2007. [Online]. Available: http://link.springer.com/10.1007/s11606-007-0231-3

[61] A. A. Plekhanov, M. A. Sirotkina, E. V. Gubarkova, E. B. Kiseleva, A. A. Sovetsky, M. M. Karabut, V. E. Zagainov, S. S. Kuznetsov, A. V. Maslennikova, E. V. Zagaynova, V. Y. Zaitsev, and N. D. Gladkova, "Towards targeted colorectal cancer biopsy based on tissue morphology assessment by compression optical coherence elastography," *Frontiers in Oncology*, vol. 13, no. March, pp. 1–15, mar 2023.

[62] R. Djinbachian, A.-J. Dubé, and D. von Renteln, "Optical Diagnosis of Colorectal Polyps: Recent Developments," *Current Treatment Options in Gastroenterology*, vol. 17, no. 1, pp. 99–114, mar 2019. [Online]. Available: http://link.springer.com/10.1007/s11938-019-00220-x

[63] S. You, "Multiphoton microscopy for stain-free slide-free histopathology," Ph.D. dissertation, University of Illinois, 2019.

[64] M. Gurcan, L. Boucheron, A. Can, A. Madabhushi, N. Rajpoot, and B. Yener, "Histopathological Image Analysis: A Review," *IEEE Reviews in Biomedical Engineering*, vol. 2, pp. 147–171, 2009. [Online]. Available: http://ieeexplore.ieee.org/document/5299287/

[65] A. L. Polglase, W. J. McLaren, S. A. Skinner, R. Kiesslich, M. F. Neurath, and P. M. Delaney, "A fluorescence confocal endomicroscope for in vivo microscopy of the upper- and the lower-GI tract," *Gastrointestinal Endoscopy*, vol. 62, no. 5, pp. 686–695, nov 2005. [Online]. Available: https://linkinghub.elsevier.com/retrieve/pii/S0016510705021024

[66] M. Kekelidze, "Colorectal cancer: Current imaging methods and future perspectives for the diagnosis, staging and therapeutic response evaluation," *World Journal of Gastroenterology*, vol. 19, no. 46, p. 8502, 2013. [Online]. Available: http://www.wjgnet.com/1007-9327/full/v19/i46/8502.htm

[67] S. E. Mason, L. Poynter, Z. Takats, A. Darzi, and J. M. Kinross, "Optical Technologies for Endoscopic Real-Time Histologic Assessment of Colorectal Polyps: A Meta-Analysis," *American Journal of Gastroenterology*, vol. 114, no. 8, pp. 1219–1230, aug 2019. [Online]. Available: https://journals.lww.com/00000434-201908000-00012

[68] B. Glover, J. Teare, and N. Patel, "A Review of New and Emerging Techniques For Optical Diagnosis of Colonic Polyps," *Journal of Clinical Gastroenterology*, vol. 53, no. 7, pp. 495–506, aug 2019. [Online]. Available: https://journals.lww.com/00004836-201908000-00011

[69] J. E. East and C. J. Rees, "Making optical biopsy a clinical reality in colonoscopy," *The Lancet Gastroenterology and Hepatology*, vol. 3, no. 1, pp. 10–12, jan 2018. [Online]. Available: https://linkinghub.elsevier.com/retrieve/pii/S2468125317303667

[70] C. W. Freudiger, W. Min, B. G. Saar, S. Lu, G. R. Holtom, C. He, J. C. Tsai, J. X. Kang, and X. S. Xie, "Label-Free Biomedical Imaging with High Sensitivity by Stimulated Raman Scattering Microscopy," *Science*, vol. 322, no. 5909, pp. 1857–1861, dec 2008. [Online]. Available: http://ieeexplore.ieee.org/xpls/abs_all.jsp?arnumber=6151800

[71] L. V. Wang and S. Hu, "Photoacoustic Tomography: In Vivo Imaging from Organelles to Organs," *Science*, vol. 335, no. 6075, pp. 1458–1462, mar 2012. [Online]. Available: https://www.science.org/doi/10.1126/science.1216210

[72] H. Tu, Y. Liu, D. Turchinovich, M. Marjanovic, J. K. Lyngsø, J. Lægsgaard, E. J. Chaney, Y. Zhao, S. You, W. L. Wilson, B. Xu, M. Dantus, and S. A. Boppart, "Stain-free histopathology by programmable supercontinuum pulses," *Nature Photonics*, vol. 10, no. 8, pp. 534–540, aug 2016. [Online]. Available: http://dx.doi.org/10.1038/nphoton.2016.94

[73] Y. Lecun, Y. Bengio, and G. Hinton, "Deep learning," *Nature*, vol. 521, no. 7553, pp. 436–444, 2015.

[74] T. Jaiswal and S. Dash, "Deep learning in medical image analysis," in *Mining Biomedical Text, Images and Visual Features for Information Retrieval*. Elsevier, 2025, pp. 287–295. [Online]. Available: https://linkinghub.elsevier.com/retrieve/pii/B9780443154522000145

[75] D. R. Miller, J. W. Jarrett, A. M. Hassan, and A. K. Dunn, "Deep tissue imaging with multiphoton fluorescence microscopy," *Current Opinion in Biomedical Engineering*, vol. 4, pp. 32–39, dec 2017. [Online]. Available: https://linkinghub.elsevier.com/retrieve/pii/S2468451117300466

[76] R. Niesner, V. Andresen, J. Neumann, H. Spiecker, and M. Gunzer, "The Power of Single and Multibeam Two-Photon Microscopy for High-Resolution and High-Speed Deep Tissue and Intravital Imaging," *Biophysical Journal*, vol. 93, no. 7, pp. 2519–2529, oct 2007. [Online]. Available: https://linkinghub.elsevier.com/retrieve/pii/S0006349507715060

[77] K. Awasthi, D. Moriya, T. Nakabayashi, L. Li, and N. Ohta, "Sensitive detection of intracellular environment of normal and cancer cells by autofluorescence lifetime imaging," *Journal of Photochemistry and Photobiology B: Biology*, vol. 165, pp. 256–265, dec 2016. [Online]. Available: https://linkinghub.elsevier.com/retrieve/pii/S1011134416304699

[78] M. Lukina, M. Shirmanova, T. Sergeeva, and E. Zagaynova, "Metabolic Imaging in the Study of Oncological Processes (Review)," *Sovremennye tehnologii v medicine*, vol. 8, no. 4, pp. 113–126, dec 2016. [Online]. Available: http://www.stm-journal.ru/en/numbers/2016/4/1288

[79] E. L. Bird-Lieberman and R. C. Fitzgerald, "Early diagnosis of oesophageal cancer," *British Journal of Cancer*, vol. 101, no. 1, pp. 1–6, jul 2009. [Online]. Available: https://www.nature.com/articles/6605126

[80] A. F. Fercher, "Optical coherence tomography – development, principles, applications," *Zeitschrift für Medizinische Physik*, vol. 20, no. 4, pp. 251–276, nov 2010. [Online]. Available: https://linkinghub.elsevier.com/retrieve/pii/S0939388909001524

[81] M. J. Maciel, C. C. Rosa, R. F. Wolffenbuttel, and J. H. Correia, "Optical coherence tomography within a single microsystem," *Journal of Physics D: Applied Physics*, vol. 51, no. 36, sep 2018. [Online]. Available: https://iopscience.iop.org/article/10.1088/1361-6463/aad4b4

[82] P. H. Tomlins and R. K. Wang, "Theory, developments and applications of optical coherence tomography," *Journal of Physics D: Applied Physics*, vol. 38, no. 15, pp. 2519–2535, aug 2005. [Online]. Available: https://iopscience.iop.org/article/10.1088/0022-3727/38/15/002

[83] B. H. Lee, E. J. Min, and Y. H. Kim, "Fiber-based optical coherence tomography for biomedical imaging, sensing, and precision measurements," *Optical Fiber Technology*, vol. 19, no. 6, pp. 729–740, dec 2013. [Online]. Available: http://dx.doi.org/10.1016/j.yofte.2013.07.011

[84] S. Zheng, Y. Bai, Z. Xu, P. Liu, and G. Ni, "Optical Coherence Tomography for Three-Dimensional Imaging in the Biomedical Field: A Review," *Frontiers in Physics*, vol. 9, no. September, pp. 1–13,

sep 2021. [Online]. Available: https://www.frontiersin.org/articles/10.3389/fphy.2021.744346/full

[85] C. Zhou, D. W. Cohen, Y. Wang, H.-C. Lee, A. E. Mondelblatt, T.-H. Tsai, A. D. Aguirre, J. G. Fujimoto, and J. L. Connolly, "Integrated Optical Coherence Tomography and Microscopy for Ex Vivo Multiscale Evaluation of Human Breast Tissues," *Cancer Research*, vol. 70, no. 24, pp. 10 071–10 079, dec 2010. [Online]. Available: https://aacrjournals.org/cancerres/article/70/24/10071/561174/Integrated-Optical-Coherence-Tomography-and

[86] V. Panzarella, F. Buttacavoli, A. Gambino, G. Capocasale, O. Di Fede, R. Mauceri, V. Rodolico, and G. Campisi, "Site-Coded Oral Squamous Cell Carcinoma Evaluation by Optical Coherence Tomography (OCT): A Descriptive Pilot Study," *Cancers*, vol. 14, no. 23, p. 5916, nov 2022. [Online]. Available: https://www.mdpi.com/2072-6694/14/23/5916

[87] F. H. Silver, A. Mesica, M. Gonzalez-Mercedes, and T. Deshmukh, "Identification of Cancerous Skin Lesions Using Vibrational Optical Coherence Tomography (VOCT): Use of VOCT in Conjunction with Machine Learning to Diagnose Skin Cancer Remotely Using Telemedicine," *Cancers*, vol. 15, no. 1, p. 156, dec 2022. [Online]. Available: https://www.mdpi.com/2072-6694/15/1/156

[88] B. J. Vakoc, D. Fukumura, R. K. Jain, and B. E. Bouma, "Cancer imaging by optical coherence tomography: preclinical progress and clinical potential," *Nature Reviews Cancer*, vol. 12, no. 5, pp. 363–368, may 2012. [Online]. Available: http://dx.doi.org/10.1038/nrc3235

[89] L. van Manen, J. Dijkstra, C. Boccara, E. Benoit, A. L. Vahrmeijer, M. J. Gora, and J. S. D. Mieog, "The clinical usefulness of optical coherence tomography during cancer interventions," *Journal of Cancer Research and Clinical Oncology*, vol. 144, no. 10, pp. 1967–1990, oct 2018. [Online]. Available: http://dx.doi.org/10.1007/s00432-018-2690-9

[90] L. Yang, Y. Chen, S. Ling, J. Wang, G. Wang, B. Zhang, H. Zhao, Q. Zhao, and J. Mao, "Research progress on the application of optical coherence tomography in the field of oncology," *Frontiers in Oncology*, vol. 12, no. July, pp. 1–13, jul 2022. [Online]. Available: https://www.frontiersin.org/articles/10.3389/fonc.2022.953934/full

[91] D. C. Adler, C. Zhou, T.-H. Tsai, J. Schmitt, Q. Huang, H. Mashimo, and J. G. Fujimoto, "Three-dimensional endomicroscopy of the human colon using optical coherence tomography," *Optics Express*, vol. 17, no. 2, p. 784, 2009.

[92] P. R. Pfau, M. V. Sivak, A. Chak, M. Kinnard, R. C. Wong, G. A. Isenberg, J. A. Izatt, A. Rollins, and V. Westphal, "Criteria for the diagnosis of dysplasia by endoscopic optical coherence tomography," *Gastrointestinal Endoscopy*, vol. 58, no. 2, pp. 196–202, aug 2003. [Online]. Available: https://linkinghub.elsevier.com/retrieve/pii/S0016510703801116

[93] B. Shen, G. Zuccaro, T. L. Gramlich, N. Gladkova, P. Trolli, M. Kareta, C. P. Delaney, J. T. Connor, B. A. Lashner, C. L. Bevins, F. Feldchtein, F. H. Remzi, M. L. Bambrick, and V. W. Fazio, "In vivo colonoscopic optical coherence tomography for transmural inflammation in inflammatory bowel disease," *Clinical Gastroenterology and Hepatology*, vol. 2, no. 12, pp. 1080–1087, dec 2004. [Online]. Available: https://linkinghub.elsevier.com/retrieve/pii/S1542356504006214

[94] B. E. Bouma, G. J. Tearney, C. C. Compton, and N. S. Nishioka, "High-resolution imaging of the human esophagus and stomach in vivo using optical coherence tomography," *Gastrointestinal Endoscopy*, vol. 51, no. 4, pp. 467–474, apr 2000. [Online]. Available: https://linkinghub.elsevier.com/retrieve/pii/S0016510700704494

[95] Y. Chen, A. Aguirre, P. Hsiung, S. Desai, P. Herz, M. Pedrosa, Q. Huang, M. Figueiredo, S.-W. Huang, A. Koski, J. Schmitt, J. Fujimoto, and H. Mashimo, "Ultrahigh resolution optical coherence tomography of Barrett's esophagus: preliminary descriptive clinical study correlating images with histology," *Endoscopy*, vol. 39, no. 07, pp. 599–605, jul 2007. [Online]. Available: http://eprints.ncrm.ac.uk/2879/1/NCRM_workingpaper_0412.pdf

[96] L. D. Landau and E. M. Lifshitz, *Electrodynamics of continuous media*. Pergamon Press, 1960. [Online]. Available: https://link.aps.org/doi/10.1103/PhysRevB.47.9080

[97] W. Hayes and R. Loudon, *Scattering of Light by Crystals*. New York: John Wiley and Sons, Inc., 1978.

[98] P. Y. Yu and M. Cardona, *Fundamentals of Semiconductors*, ser. Graduate Texts in Physics. Berlin, Heidelberg: Springer Berlin Heidelberg, jun 2010, vol. 59, no. 6. [Online]. Available: http://www.ncbi.nlm.nih.gov/pubmed/7189984

[99] C. F. Klingshirn, *Semiconductor optics*, 3rd ed. Berlin: Springer, 1995. [Online]. Available: https://linkinghub.elsevier.com/retrieve/pii/B9780323908009000470

[100] C. R. d. F. Bernardo, "Linear and non-Linear Optical Properties Owing to Interactions of Elementary Excitations in Nanostructures," Ph.D. dissertation, University of Minho, 2020.

[101] M. Born and E. Wolf, *Principles of Optics*, 7th ed. Cambridge University Press, oct 1999. [Online]. Available: https://www.cambridge.org/core/product/identifier/9781139644181/type/book

[102] C. V. Raman, "A new radiation [Reproduced from Indian J. Phys., 1928, 2, 387–398]," *Current Science*, vol. 74, no. 4, pp. 382–386, 1998. [Online]. Available: https://about.jstor.org/terms

[103] D. A. Long, *Raman spectroscopy*. New York: McGraw-Hill, 1997. [Online]. Available: https://archive.org/details/ramanspectroscop0000long

[104] G. P. Agrawal, *Nonlinear fiber optics*, 5th ed., P. F. Liao, P. F. Kelley, and I. Kaminow, Eds. Amsterdam: Academic Press, 2013.

[105] R. W. Boyd, *Nonlinear optics*, 3rd ed. Orlando: Academic Press, 2008.

[106] P. N. Butcher and D. Cotter, *The Elements of Nonlinear Optics*. Cambridge: Cambridge University Press, 1990.

[107] R. W. Munn and C. N. Ironside, *Principles and Applications of Nonlinear Optical Materials*, R. W. Munn and C. N. Ironside, Eds. Dordrecht: Springer Netherlands, 1993. [Online]. Available: http://link.springer.com/10.1007/978-94-011-2158-3

[108] J. D. Jackson, *Classical Electrodynamics*. New York: John Wiley and Sons, Inc., 1962.

[109] B. Weigelin, G.-J. Bakker, and P. Friedl, "Third harmonic generation microscopy of cells and tissue organization," *Journal of Cell Science*, vol. 129, no. 2, pp. 245–255, jan 2016. [Online]. Available: https://journals.biologists.com/jcs/article/doi/10.1242/jcs.152272/259228/Third-harmonic-generation-microscopy-of-cells-and

[110] A. M. Cimpean, D. Ribatti, and M. Raica, "The chick embryo chorioallantoic membrane as a model to study tumor metastasis," *Angiogenesis*, vol. 11, no. 4, pp. 311–319, dec 2008. [Online]. Available: http://link.springer.com/10.1007/s10456-008-9117-1

[111] K. Harper, A. Yatsyna, M. Charbonneau, K. Brochu-Gaudreau, A. Perreault, C. Jeldres, P. P. McDonald, and C. M. Dubois, "The Chicken Chorioallantoic Membrane Tumor Assay as a Relevant In Vivo Model to Study the Impact of Hypoxia on Tumor Progression and Metastasis," *Cancers*, vol. 13, no. 5, p. 1093, mar 2021. [Online]. Available: https://www.mdpi.com/2072-6694/13/5/1093

[112] L. Chen, S. Wang, Y. Feng, J. Zhang, Y. Du, J. Zhang, C. V. Ongeval, Y. Ni, and Y. Li, "Utilisation of Chick Embryo Chorioallantoic Membrane as a Model Platform for Imaging-Navigated Biomedical Research," *Cells*, vol. 10, no. 2, p. 463, feb 2021. [Online]. Available: https://www.mdpi.com/2073-4409/10/2/463

[113] D. Fischer, G. Fluegen, P. Garcia, N. Ghaffari-Tabrizi-Wizsy, L. Gribaldo, R. Y.-J. Huang, V. Rasche, D. Ribatti, X. Rousset, M. T. Pinto, J. Viallet, Y. Wang, and R. Schneider-Stock, "The CAM Model—Q&A with Experts," *Cancers*, vol. 15, no. 1, p. 191, dec 2022. [Online]. Available: https://www.mdpi.com/2072-6694/15/1/191

[114] A. K. Mapanao, P. P. Che, P. Sarogni, P. Sminia, E. Giovannetti, and V. Voliani, "Tumor grafted – chick chorioallantoic membrane as an alternative model for biological cancer research and conventional/nanomaterial-based theranostics evaluation," *Expert Opinion on Drug Metabolism & Toxicology*, vol. 17, no. 8, pp. 947–968, aug 2021. [Online]. Available: https://doi.org/10.1080/17425255.2021.1879047

[115] P. Nowak-Sliwinska, T. Segura, and M. L. Iruela-Arispe, "The chicken chorioallantoic membrane model in biology, medicine and bioengineering," *Angiogenesis*, vol. 17, no. 4, pp. 779–804, oct 2014. [Online]. Available: https://link.springer.com/10.1007/s10456-014-9440-7

[116] P. Pawlikowska, T. Tayoun, M. Oulhen, V. Faugeroux, V. Rouffiac, A. Aberlenc, A. L. Pommier, A. Honore, V. Marty, O. Bawa, L. Lacroix, J. Y. Scoazec, A. Chauchereau, C. Laplace-Builhe, and F. Farace, "Exploitation of the chick embryo chorioallantoic membrane (CAM) as a platform for anti-metastatic drug testing," *Scientific Reports*, vol. 10, no. 1, p. 16876, oct 2020. [Online]. Available: https://doi.org/10.1038/s41598-020-73632-w

[117] D. Ribatti, "The chick embryo chorioallantoic membrane as a model for tumor biology," *Experimental Cell Research*, vol. 328, no. 2, pp. 314–324, nov 2014. [Online]. Available: http://dx.doi.org/10.1016/j.yexcr.2014.06.010

[118] B. T. Vu, S. A. Shahin, J. Croissant, Y. Fatieiev, K. Matsumoto, T. Le-Hoang Doan, T. Yik, S. Simargi, A. Conteras, L. Ratliff, C. M. Jimenez, L. Raehm, N. Khashab, J.-O. Durand, C. Glackin, and F. Tamanoi, "Chick chorioallantoic membrane assay as an in vivo model to study the effect of nanoparticle-based anticancer drugs in ovarian cancer," *Scientific Reports*, vol. 8, no. 1, p. 8524, jun 2018. [Online]. Available: http://dx.doi.org/10.1038/s41598-018-25573-8

[119] P. Sarogni, A. K. Mapanao, S. Marchetti, C. Kusmic, and V. Voliani, "A Standard Protocol for the Production and Bioevaluation of Ethical In Vivo Models of HPV-Negative Head and Neck Squamous Cell Carcinoma," *ACS Pharmacology & Translational Science*, vol. 4, no. 3, pp. 1227–1234, jun 2021. [Online]. Available: https://pubs.acs.org/doi/10.1021/acsptsci.1c00083

[120] C. Mesas, M. A. Chico, K. Doello, P. Lara, J. Moreno, C. Melguizo, G. Perazzoli, and J. Prados, "Experimental Tumor Induction and Evaluation of Its Treatment in the Chicken Embryo Chorioallantoic Membrane Model: A Systematic Review," *International Journal of Molecular Sciences*, vol. 25, no. 2, p. 837, jan 2024. [Online]. Available: https://www.mdpi.com/1422-0067/25/2/837

[121] M. Cecilia Subauste, T. A. Kupriyanova, E. M. Conn, V. C. Ardi, J. P. Quigley, and E. I. Deryugina, "Evaluation of metastatic and angiogenic potentials of human colon carcinoma cells in chick embryo model systems," *Clinical & Experimental Metastasis*, vol. 26, no. 8, pp. 1033–1047, dec 2009. [Online]. Available: http://link.springer.com/10.1007/s10585-009-9293-4

[122] A. Weiss, J. R. van Beijnum, D. Bonvin, P. Jichlinski, P. J. Dyson, A. W. Griffioen, and P. Nowak□Sliwinska, "Low□dose angiostatic tyrosine kinase inhibitors improve photodynamic therapy for cancer: lack of vascular normalization," *Journal of Cellular and Molecular Medicine*, vol. 18, no. 3, pp. 480–491, mar 2014. [Online]. Available: https://onlinelibrary.wiley.com/doi/10.1111/jcmm.12199

[123] Y. Adar, M. Stark, E. E. Bram, P. Nowak-Sliwinska, H. van den Bergh, G. Szewczyk, T. Sarna, A. Skladanowski, A. W. Griffioen, and Y. G. Assaraf, "Imidazoacridinone-dependent lysosomal photodestruction: a pharmacological Trojan horse approach to eradicate multidrug-resistant cancers," *Cell Death & Disease*, vol. 3, no. 4, pp. e293–e293, apr 2012. [Online]. Available: https://www.nature.com/articles/cddis201230

[124] G. M. Sys, L. Lapeire, N. Stevens, H. Favoreel, R. Forsyth, M. Bracke, and O. De Wever, "The In ovo CAM-assay as a Xenograft Model for Sarcoma," *Journal of Visualized Experiments*, no. 77, p. e50522, jul 2013. [Online]. Available: https://app.jove.com/t/50522

[125] M. Balke, A. Neumann, C. Kersting, K. Agelopoulos, C. Gebert, G. Gosheger, H. Buerger, and M. Hagedorn, "Morphologic characterization of osteosarcoma growth on the chick chorioallantoic membrane," *BMC Research Notes*, vol. 3, 2010.

[126] P. Fergelot, J.-C. Bernhard, F. Soulet, W. W. Kilarski, C. Léon, N. Courtois, C. Deminière, J. M. J. Herbert, P. Antczak, F. Falciani, N. Rioux-Leclercq, J.-J. Patard, J.-M. Ferrière, A. Ravaud, M. Hagedorn, and A. Bikfalvi, "The experimental renal cell carcinoma model in the chick embryo," *Angiogenesis*, vol. 16, no. 1, pp. 181–194, jan 2013. [Online]. Available: http://link.springer.com/10.1007/s10456-012-9311-z

[127] D. Ribatti, G. De Falco, B. Nico, R. Ria, E. Crivellato, and A. Vacca, "In vivo time□course of the angiogenic response induced by multiple myeloma plasma cells in the chick embryo chorioallantoic membrane," *Journal of Anatomy*, vol. 203, no. 3, pp. 323–328, sep 2003. [Online]. Available: https://onlinelibrary.wiley.com/doi/10.1046/j.1469-7580.2003.00220.x

[128] S. Gronau, B. Thess, H. Riechelmann, Y. Fischer, A. Schmitt, and M. Schmitt, "An autologous system for culturing head and neck squamous cell carcinomas for the assessment of cellular therapies on the chorioallantois membrane," *European Archives of Oto-Rhino-Laryngology*, vol. 263, no. 4, pp. 308–312, apr 2006. [Online]. Available: http://link.springer.com/10.1007/s00405-005-1008-0

[129] D. Ribatti, B. Nico, A. M. Cimpean, M. Raica, E. Crivellato, S. Ruggieri, and A. Vacca, "B16-F10 melanoma cells contribute to the new formation of blood vessels in the chick embryo chorioallantoic membrane through vasculogenic mimicry," *Clinical and Experimental Medicine*, vol. 13, no. 2, pp. 143–147, may 2013. [Online]. Available: http://link.springer.com/10.1007/s10238-012-0183-8

[130] D. H. Ausprunk, D. R. Knighton, and J. Folkman, "Vascularization of normal and neoplastic tissues grafted to the chick chorioallantois. Role of host and preexisting graft blood vessels," *American Journal of Pathology*, vol. 79, no. 3, pp. 597–618, 1975.

[131] M. Ismail, U. Torsten, C. Dressler, J. Diederichs, S. Hüske, H. Weitzel, and H.-P. Berlien, "Photodynamic Therapy of Malignant Ovarian Tumours Cultivated on CAM," *Lasers in Medical Science*, vol. 14, no. 2, pp. 91–96, jun 1999. [Online]. Available: http://link.springer.com/10.1007/s101030050028

[132] V. Isachenko, P. Mallmann, A. M. Petrunkina, G. Rahimi, F. Nawroth, K. Hancke, R. Felberbaum, F. Genze, I. Damjanoski, and E. Isachenko, "Comparison of In Vitro- and Chorioallantoic Membrane (CAM)-Culture Systems for Cryopreserved Medulla-Contained Human Ovarian Tissue," *PLoS ONE*, vol. 7, no. 3, p. e32549, mar 2012. [Online]. Available: https://dx.plos.org/10.1371/journal.pone.0032549

[133] M. Klagsbrun, D. Knighton, and J. Folkman, "Tumor angiogenesis activity in cells grown in tissue culture," *Cancer research*, vol. 36, no. 1, pp. 110–4, jan 1976. [Online]. Available: http://www.ncbi.nlm.nih.gov/pubmed/1247990

[134] S. M. McCabe, H. Gardiner, C. Mullen, G. Q. Wallace, N. C. Shand, A. B. Mullen, L. Horan, D. Graham, K. Faulds, and M. Boyd, "Live chicken egg embryos as an alternative in vivo tumour model for deep surface enhanced Raman spectroscopy," *The Analyst*, vol. 149, no. 13, pp. 3513–3517, 2024. [Online]. Available: https://xlink.rsc.org/?DOI=D4AN00617H

[135] E. Lucarelli, L. Sangiorgi, S. Benassi, D. Donati, G. A. Gobbi, P. Picci, A. Vacca, and D. Ribatti, "Angiogenesis in lipoma: An experimental study in the chick embryo chorioallantoic membrane," *International Journal of Molecular Medicine*, vol. 4, no. 6, pp. 593–596, dec 1999. [Online]. Available: http://www.spandidos-publications.com/10.3892/ijmm.4.6.593

[136] P. C. Brooks, A. M. Montgomery, M. Rosenfeld, R. A. Reisfeld, T. Hu, G. Klier, and D. A. Cheresh, "Integrin v3 antagonists promote tumor regression by inducing apoptosis of angiogenic blood vessels," *Cell*, vol. 79, pp. 1157–1164, 12 1994. [Online]. Available: https://www.cell.com/action/showFullText?pii=0092867494900078

[137] M. Pudliszewski and L. Pardanaud, "Vasculogenesis and angiogenesis in the mouse embryo studied using quail/mouse chimeras," *The International Journal of Developmental Biology*, vol. 49, no. 2-3, pp. 355–361, 2005. [Online]. Available: https://ijdb.ehu.eus/article/041956mp

[138] F. Tamanoi, "Recent excitements in the study of the CAM assay," in *Enzymes*, 1st ed. Elsevier Inc., 2019, vol. 46, pp. 1–9. [Online]. Available: http://dx.doi.org/10.1016/bs.enz.2019.10.002

[139] P. Kunze, L. Kreiss, V. Novosadová, A. V. Roehe, S. Steinmann, J. Prochazka, C. I. Geppert, A. Hartmann, S. Schürmann, O. Friedrich, and R. Schneider-Stock, "Multiphoton Microscopy Reveals DAPK1-Dependent Extracellular Matrix Remodeling in a Chorioallantoic Membrane (CAM) Model," *Cancers*, vol. 14, no. 10, p. 2364, may 2022. [Online]. Available: https://www.mdpi.com/2072-6694/14/10/2364

[140] T. Tsimpaki, N. E. Bechrakis, B. Seitz, M. M. Kraemer, H. Liu, S. Dalbah, E. Sokolenko, U. Berchner-Pfannschmidt, and M. Fiorentzis, "Chick Chorioallantoic Membrane as a Patient-Derived Xenograft Model for Uveal Melanoma: Imaging Modalities for Growth and Vascular Evaluation," *Cancers*, vol. 15, no. 5, p. 1436, feb 2023. [Online]. Available: https://www.mdpi.com/2072-6694/15/5/1436

[141] R. D. Roshan Dsouza, H. S. Hrebesh Subhash, K. N. Kai Neuhaus, P. M. M. Paul M. McNamara, J. H. Josh Hogan, C. W. Carol Wilson, and M. J. L. Martin J. Leahy, "Feasibility study of phase-sensitive imaging based on multiple reference optical coherence tomography," *Chinese Optics Letters*, vol. 15, no. 9, p. 090007, 2017.

[142] R. Amorim, C. Pinheiro, V. Miranda-Gonçalves, H. Pereira, M. P. Moyer, A. Preto, and F. Baltazar, "Monocarboxylate transport inhibition potentiates the cytotoxic effect of 5-fluorouracil in colorectal cancer cells," *Cancer Letters*, vol. 365, no. 1, pp. 68–78, aug 2015. [Online]. Available: http://dx.doi.org/10.1016/j.canlet.2015.05.015

[143] Cancer Research UK, "Benign and malignant tumours and how cancers grow." [Online]. Available: https://www.cancerresearchuk.org/about-cancer/what-is-cancer/how-cancer-start-grow-spread/how-cancers-grow

[144] S. J. Jang, J. M. Gardner, and J. Y. Ro, "Diagnostic approach and prognostic factors of cancers," *Advances in Anatomic Pathology*, vol. 18, no. 2, pp. 165–172, 2011.

[145] V. V. Tuchin, *Tissue optics: Light scattering methods and instruments for medical diagnosis*, 3rd ed. Washington: SPIE, feb 2015.

[146] S. Pimenta, "Optical Microsystem for Spectroscopy Signals Extraction Applied to Gastrointestinal Dysplasia Detection," Ph.D. dissertation, University do Minho, 2016.

[147] C. Freymüller, S. Kalinina, A. Rück, R. Sroka, and A. Rühm, "Quenched coumarin derivatives as fluorescence lifetime phantoms for NADH and FAD," *Journal of Biophotonics*, vol. 14, no. 7, pp. 1–13, jul 2021. [Online]. Available: https://onlinelibrary.wiley.com/doi/10.1002/jbio.202100024

[148] B. Yu, J. Y. Lo, T. F. Kuech, G. M. Palmer, J. E. Bender, and N. Ramanujam, "Cost-effective diffuse reflectance spectroscopy device for quantifying tissue absorption and scattering in vivo," *Journal of Biomedical Optics*, vol. 13, no. 6, p. 060505, 2008. [Online]. Available: http://biomedicaloptics.spiedigitallibrary.org/article.aspx?doi=10.1117/1.3041500

[149] C. C. Yu, J. Mirkovic, C. Lau, G. O'Donoghue, S. A. McGee, A. Elackattu, G. A. Grillone, Z. Wang, E. A. Stier, R. R. Dasari, K. Badizadegan, and M. S. Feld, "Quantitative Spectroscopic Imaging for Non-Invasice Early Cancer Diagnosis," in *Biomedical Optics*, vol. 16, no. 20. Washington, D.C.: OSA, 2008, p. BWD3. [Online]. Available: https://opg.optica.org/abstract.cfm?URI=BIOMED-2008-BWD3

[150] J. Y. Lo, B. Yu, H. L. Fu, J. E. Bender, G. M. Palmer, T. F. Kuech, and N. Ramanujam, "A strategy for quantitative spectral imaging of tissue absorption and scattering using light emitting diodes and photodiodes," *Optics Express*, vol. 17, no. 3, pp. 1372–1384, feb 2009. [Online]. Available: https://opg.optica.org/oe/abstract.cfm?uri=oe-17-3-1372

[151] N. D. Kirkpatrick, J. B. Hoying, S. K. Botting, J. A. Weiss, and U. Utzinger, "In vitro model for endogenous optical signatures of collagen," *Journal of Biomedical Optics*, vol. 11, no. 5, p. 054021, 2006. [Online]. Available: http://biomedicaloptics.spiedigitallibrary.org/article.aspx?doi=10.1117/1.2360516

[152] K. Sokolov, J. Galvan, A. Myakov, A. Lacy, R. Lotan, and R. Richards-Kortum, "Realistic three-dimensional epithelial tissue phantoms for biomedical optics," *Journal of Biomedical Optics*, vol. 7, no. 1, p. 148, 2002. [Online]. Available: http://biomedicaloptics.spiedigitallibrary.org/article.aspx?doi=10.1117/1.1427052

[153] K. B. Nivetha and N. Sujatha, "Development of thin skin mimicking bilayer solid tissue phantoms for optical spectroscopic studies," *Biomedical Optics Express*, vol. 8, no. 7, p. 3198, jul 2017. [Online]. Available: https://opg.optica.org/abstract.cfm?URI=boe-8-7-3198

[154] A. I. Chen, M. L. Balter, M. I. Chen, D. Gross, S. K. Alam, T. J. Maguire, and M. L. Yarmush, "Multilayered tissue mimicking skin and vessel phantoms with tunable mechanical, optical, and acoustic properties," *Medical Physics*, vol. 43, no. 6, pp. 3117–3131, jun 2016. [Online]. Available: http://dx.doi.org/10.1118/1.4951729

[155] M. Balu, T. Baldacchini, J. Carter, T. B. Krasieva, R. Zadoyan, and B. J. Tromberg, "Effect of excitation wavelength on penetration depth in nonlinear optical microscopy of turbid media," *Journal of Biomedical Optics*, vol. 14, no. 1, p. 010508, 2009. [Online]. Available: http://biomedicaloptics.spiedigitallibrary.org/article.aspx?doi=10.1117/1.3081544

[156] F. E. Robles, S. Chowdhury, and A. Wax, "Assessing hemoglobin concentration using spectroscopic optical coherence tomography for feasibility of tissue diagnostics," *Biomedical Optics Express*, vol. 1, no. 1, pp. 310–317, aug 2010. [Online]. Available: https://opg.optica.org/boe/abstract.cfm?uri=boe-1-1-310

[157] B. Leh, R. Siebert, H. Hamzeh, L. Menard, M.-A. Duval, Y. Charon, and D. Abi Haidar, "Optical phantoms with variable properties and geometries for diffuse and fluorescence optical

spectroscopy," *Journal of Biomedical Optics*, vol. 17, no. 10, p. 108001, oct 2012. [Online]. Available: http://biomedicaloptics.spiedigitallibrary.org/article.aspx?doi=10.1117/1.JBO.17.10.108001

[158] P. Lai, X. Xu, and L. V. Wang, "Dependence of optical scattering from Intralipid in gelatin-gel based tissue-mimicking phantoms on mixing temperature and time," *Journal of Biomedical Optics*, vol. 19, no. 3, p. 035002, 2014.

[159] K. A. Heslop, P. Burger, C. Kappler, A. K. Solanki, M. Gooz, Y. K. Peterson, C. Mills, T. Benton, S. A. Duncan, P. M. Woster, and E. N. Maldonado, "Small molecules targeting the NADH-binding pocket of VDAC modulate mitochondrial metabolism in hepatocarcinoma cells," *Biomedicine and Pharmacotherapy*, vol. 150, no. March, p. 112928, 2022. [Online]. Available: http://dx.doi.org/10.1016/j.biopha.2022.112928

[160] S. Wu, Y. Huang, Q. Tang, Z. Li, H. Horng, J. Li, Z. Wu, Y. Chen, and H. Li, "Quantitative evaluation of redox ratio and collagen characteristics during breast cancer chemotherapy using two-photon intrinsic imaging," *Biomedical Optics Express*, vol. 9, no. 3, p. 1375, mar 2018. [Online]. Available: https://opg.optica.org/abstract.cfm?URI=boe-9-3-1375

[161] J. Jiang, M. Feng, A. Jacob, L. Z. Li, and H. N. Xu, "Optical Redox Imaging Differentiates Triple-Negative Breast Cancer Subtypes," in *Advances in Experimental Medicine and Biology*, 2021, vol. 1269, pp. 253–258. [Online]. Available: https://link.springer.com/10.1007/978-3-030-48238-1_40

[162] R. Patalay, C. Talbot, Y. Alexandrov, I. Munro, M. A. A. Neil, K. König, P. M. W. French, A. Chu, G. W. Stamp, and C. Dunsby, "Quantification of cellular autofluorescence of human skin using multiphoton tomography and fluorescence lifetime imaging in two spectral detection channels," *Biomedical Optics Express*, vol. 2, no. 12, p. 3295, dec 2011. [Online]. Available: https://opg.optica.org/boe/abstract.cfm?uri=boe-2-12-3295

[163] M. Monici, "Cell and tissue autofluorescence research and diagnostic applications," *Biotechnology Annual Review*, vol. 11, pp. 227–256, 1 2005. [Online]. Available: https://www.sciencedirect.com/science/chapter/bookseries/abs/pii/S1387265605110072

[164] T. S. Blacker, Z. F. Mann, J. E. Gale, M. Ziegler, A. J. Bain, G. Szabadkai, and M. R. Duchen, "Separating NADH and NADPH fluorescence in live cells and tissues using

FLIM," *Nature Communications*, vol. 5, no. 1, p. 3936, may 2014. [Online]. Available: https://www.nature.com/articles/ncomms4936

[165] S. Huang, A. A. Heikal, and W. W. Webb, "Two-Photon Fluorescence Spectroscopy and Microscopy of NAD(P)H and Flavoprotein," *Biophysical Journal*, vol. 82, no. 5, pp. 2811–2825, may 2002. [Online]. Available: http://dx.doi.org/10.1016/S0006-3495(02)75621-X

[166] F. Bartolomé and A. Y. Abramov, "Measurement of mitochondrial nadh and fad autofluorescence in live cells," *Methods in Molecular Biology*, vol. 1264, pp. 263–270, 2015. [Online]. Available: https://link.springer.com/protocol/10.1007/978-1-4939-2257-4_23

[167] M. C. Skala, K. M. Riching, A. Gendron-Fitzpatrick, J. Eickhoff, K. W. Eliceiri, J. G. White, and N. Ramanujam, "In vivo multiphoton microscopy of NADH and FAD redox states, fluorescence lifetimes, and cellular morphology in precancerous epithelia," *Proceedings of the National Academy of Sciences*, vol. 104, no. 49, pp. 19 494–19 499, dec 2007. [Online]. Available: https://pnas.org/doi/full/10.1073/pnas.0708425104

[168] T. M. Heaster, A. J. Walsh, Y. Zhao, S. W. Hiebert, and M. C. Skala, "Autofluorescence imaging identifies tumor cell-cycle status on a single-cell level," *Journal of Biophotonics*, vol. 11, p. e201600276, 1 2018. [Online]. Available: https://onlinelibrary.wiley.com/doi/abs/10.1002/jbio.201600276

[169] M. V. Shirmanova, A. I. Gavrina, T. F. Kovaleva, V. V. Dudenkova, E. E. Zelenova, V. I. Shcheslavskiy, A. M. Mozherov, L. B. Snopova, K. A. Lukyanov, and E. V. Zagaynova, "Insight into redox regulation of apoptosis in cancer cells with multiparametric live-cell microscopy," *Scientific Reports*, vol. 12, no. 1, pp. 1–12, 2022. [Online]. Available: https://doi.org/10.1038/s41598-022-08509-1

[170] A. A. Gillette, C. P. Babiarz, A. R. Vandommelen, C. A. Pasch, L. Clipson, K. A. Matkowskyj, D. A. Deming, and M. C. Skala, "Autofluorescence imaging of treatment response in neuroendocrine tumor organoids," *Cancers*, vol. 13, no. 8, 2021.

[171] A. Podsednik, J. Jiang, A. Jacob, L. Z. Li, and H. N. Xu, "Optical Redox Imaging of Treatment Responses to Nampt Inhibition and Combination Therapy in Triple-Negative Breast Cancer Cells," *International Journal of Molecular Sciences*, vol. 22, no. 11, p. 5563, may 2021. [Online]. Available: https://www.mdpi.com/1422-0067/22/11/5563

[172] M. Yang, A. Mahanty, C. Jin, A. N. N. Wong, and J. S. Yoo, "Label-free metabolic imaging for sensitive and robust monitoring of anti-CD47 immunotherapy response in triple-negative breast cancer," *Journal for ImmunoTherapy of Cancer*, vol. 10, no. 9, p. e005199, sep 2022. [Online]. Available: https://jitc.bmj.com/lookup/doi/10.1136/jitc-2022-005199

[173] D. Pouli, H.-T. Thieu, E. M. Genega, L. Baecher-Lind, M. House, B. Bond, D. M. Roncari, M. L. Evans, F. Rius-Diaz, K. Munger, and I. Georgakoudi, "Label-free, High-Resolution Optical Metabolic Imaging of Human Cervical Precancers Reveals Potential for Intraepithelial Neoplasia Diagnosis," *Cell Reports Medicine*, vol. 1, no. 2, p. 100017, may 2020. [Online]. Available: https://doi.org/10.1016/j.xcrm.2020.100017

[174] D. Chen, D. W. Nauen, H.-C. Park, D. Li, W. Yuan, A. Li, H. Guan, C. Kut, K. L. Chaichana, C. Bettegowda, A. Quiñones-Hinojosa, and X. Li, "Label-free imaging of human brain tissue at subcellular resolution for potential rapid intra-operative assessment of glioma surgery," *Theranostics*, vol. 11, no. 15, pp. 7222–7234, 2021. [Online]. Available: https://www.thno.org/v11p7222.htm

[175] B. Gaitan, C. Inglut, U. Kanniyappan, H. N. Xu, E. F. Conant, L. Frankle, L. Z. Li, Y. Chen, and H.-C. Huang, "Development of an Endoscopic Auto-Fluorescent Sensing Device to Aid in the Detection of Breast Cancer and Inform Photodynamic Therapy," *Metabolites*, vol. 12, no. 11, p. 1097, nov 2022. [Online]. Available: https://www.mdpi.com/2218-1989/12/11/1097

[176] E. A. Zherebtsov, E. V. Potapova, A. V. Mamoshin, V. V. Shupletsov, K. Y. Kandurova, V. V. Dremin, A. Y. Abramov, and A. V. Dunaev, "Fluorescence lifetime needle optical biopsy discriminates hepatocellular carcinoma," *Biomedical Optics Express*, vol. 13, no. 2, p. 633, feb 2022. [Online]. Available: https://opg.optica.org/abstract.cfm?URI=boe-13-2-633

[177] D. C. Harris, *Quantitative Chemical Analysis*, 7th ed. New York: W. H. Freeman and Company, 2007. [Online]. Available: https://linkinghub.elsevier.com/retrieve/pii/B9780444408266500091

[178] T. L. Brown, H. E. LeMay, B. E. Bursten, C. J. Murphy, and P. M. Woodward, *Chemistry: The Central Science*, 12th ed. Upper Saddle River, NJ: Pearson Prentice Hall, 2012.

[179] Sigma-Aldrich Co, "Product Information (Nicotinamide adenine dinucleotide, reduced disodium salt hydrate)," 2012. [Online]. Available: https://www.sigmaaldrich.com/deepweb/assets/sigmaaldrich/product/documents/379/651/n6005pis.pdf

[180] Sigma-Aldrich Co, "Product Specification (Flavin adenine dinucleotide disodium salt hydrate)." [Online]. Available: https://www.sigmaaldrich.com/specification-sheets/260/115/F6625-BULK_ _____SIGMA____.pdf

[181] A. D. Skoog, F. J. Holler, and S. R. Crounch, *Principles of Instrumental Analysis*, 7th ed. Cengage Learning, 2016.

[182] E. Hecht, *Optics*, 5th ed. Pearson Education Limited, 2017.

[183] C. Kim, A. Garcia-Uribe, S.-R. Kothapalli, and L. V. Wang, "Optical phantoms for ultrasound-modulated optical tomography," *Design and Performance Validation of Phantoms Used in Conjunction with Optical Measurements of Tissue*, vol. 6870, p. 68700M, 2008.

[184] R. L. Lundblad and F. M. Macdonald, Eds., *Handbook of biochemistry and molecular biology*, 5th ed. CRC Press, 2018, vol. 32, no. 3.

[185] A. A. Heikal, "Intracellular Coenzymes as Natural Biomarkers for Metabolic Activities and Mitochondrial Anomalies," *Biomarkers in Medicine*, vol. 4, no. 2, pp. 241–263, apr 2010. [Online]. Available: https://www.tandfonline.com/doi/full/10.2217/bmm.10.1

[186] W. Zheng, Y. Wu, D. Li, and J. Y. Qu, "Autofluorescence of epithelial tissue: single-photon versus two-photon excitation," *Journal of Biomedical Optics*, vol. 13, no. 5, p. 054010, 2008.

[187] C. Xu and W. W. Webb, "Multiphoton Excitation of Molecular Fluorophores and Nonlinear Laser Microscopy," in *Topics in Fluorescence Spectroscopy*. Boston, MA: Springer US, 2002, vol. 5, pp. 471–540. [Online]. Available: http://link.springer.com/10.1007/0-306-47070-5_11

[188] F. Bestvater, E. Spiess, G. Stobrawa, M. Hacker, T. Feurer, T. Porwol, U. Berchner□Pfannschmidt, C. Wotzlaw, and H. Acker, "Two□photon fluorescence absorption and emission spectra of dyes relevant for cell imaging," *Journal of Microscopy*, vol. 208, no. 2, pp. 108–115, nov 2002. [Online]. Available: http://doi.wiley.com/10.1046/j.1365-2818.2002.01074.x

[189] S. Prahl, "Optical Absorption of Hemoglobin." [Online]. Available: https://omlc.org/spectra/hemoglobin/

[190] C. F. Bohren and D. R. Huffman, *Absorption and scattering of light by small particles*. John Wiley and Sons, Inc., 1983.

[191] B. W. Pogue and M. S. Patterson, "Review of tissue simulating phantoms for optical spectroscopy, imaging and dosimetry," *Journal of Biomedical Optics*, vol. 11, no. 4, p. 041102, 2006. [Online]. Available: http://biomedicaloptics.spiedigitallibrary.org/article.aspx?doi=10.1117/1.2335429

[192] A. Ghaderi, "Airgap-based MEMS optical filters for the ultraviolet-visible spectrum," Ph.D. dissertation, TU Delft, 2016.

[193] H. A. MacLeod, *Thin-Film Optical Filters*. CRC Press, mar 2010. [Online]. Available: https://link.springer.com/10.1007/978-3-642-19409-2_6

[194] B. E. A. SALEH and M. C. TEICH, *FUNDAMENTALS OF PHOTONICS*, 3rd ed. John Wiley and Sons, Inc., 2019.

[195] E. D. Palik, *Handbook of Optical Constants of Solids*. Academic Press, 1998.

[196] H. A. Macleod, *Thin-Film Optical Filters*, 5th ed. CRC Press, 2018.

[197] D. Yang, *Thin Films - Deposition Methods and Applications*, D. Yang, Ed. IntechOpen, mar 2023.

[198] K. Y. Cheong and L. C. Chen, *Sustainable Materials for Next Generation Energy Devices*. Elsevier, 2021.

[199] D. Huang, E. a. Swanson, C. P. Lin, J. S. Schuman, W. G. Stinson, W. Chang, M. R. Hee, T. Flotte, K. Gregory, C. a. Puliafito, and J. G. Fujimoto, "Optical Coherence Tomography," *Science*, vol. 254, no. 5035, pp. 1178–1181, nov 1991. [Online]. Available: https://www.science.org/doi/10.1126/science.1957169

[200] M. J. Maciel, H. M. Pereira, S. Pimenta, A. Miranda, E. J. Nunes-Pereira, and J. H. Correia, "Differentiation between normal and tumor mammary glands with depth-resolved attenuation coefficient from optical coherence tomography," *Biomedical Physics & Engineering Express*, vol. 8, no. 1, p. 015007, jan 2022. [Online]. Available: https://iopscience.iop.org/article/10.1088/2057-1976/ac37ca

[201] G. T. Smith, N. Dwork, D. O'Connor, U. Sikora, K. L. Lurie, J. M. Pauly, and A. K. Ellerbee, "Automated, Depth-Resolved Estimation of the Attenuation Coefficient From Optical Coherence Tomography Data," *IEEE Transactions on Medical Imaging*, vol. 34, no. 12, pp. 2592–2602, dec 2015. [Online]. Available: http://ieeexplore.ieee.org/document/7134771/

[202] D. Tes, A. Aber, M. Zafar, L. Horton, A. Fotouhi, Q. Xu, A. Moiin, A. D. Thompson, T. C. Moraes Pinto Blumetti, S. Daveluy, W. Chen, and M. Nasiriavanaki, "Granular Cell Tumor Imaging Using Optical Coherence Tomography," *Biomedical Engineering and Computational Biology*, vol. 9, jan 2018. [Online]. Available: https://journals.sagepub.com/doi/10.1177/1179597218790250

[203] K. A. Vermeer, J. Mo, J. J. A. Weda, H. G. Lemij, and J. F. de Boer, "Depth-resolved model-based reconstruction of attenuation coefficients in optical coherence tomography," *Biomedical Optics Express*, vol. 5, no. 1, p. 322, jan 2014. [Online]. Available: https://opg.optica.org/boe/abstract.cfm?uri=boe-5-1-322

[204] A. B. L. Ribeiro, "White-Light Interferometry: Applications to Fibre Optic Sensors for AC and DC Measurands," Ph.D. dissertation, University of Kent, 1992.

[205] B. E. Bouma and G. J. Tearney, *Handbook of optical coherence tomography*. Informa Healthcare, 2002.

[206] P. Serranho, A. M. Morgado, and R. Bernardes, *Optical Coherence Tomography: A Concept Review*. Springer, Berlin, Heidelberg, 2012, pp. 139–156. [Online]. Available: https://link.springer.com/10.1007/978-3-642-27410-7_7

[207] A. G. PODOLEANU, "Optical coherence tomography," *Journal of Microscopy*, vol. 247, no. 3, pp. 209–219, sep 2012. [Online]. Available: https://onlinelibrary.wiley.com/doi/10.1111/j.1365-2818.2012.03619.x

[208] M. Wojtkowski, "High-speed optical coherence tomography: basics and applications," *Applied Optics*, vol. 49, no. 16, p. D30, jun 2010. [Online]. Available: https://opg.optica.org/abstract.cfm?URI=ao-49-16-D30

[209] M. J. Maciel, "Sistema miniaturizado de Tomografia de Coerência Ótica - MiniOCT," Ph.D. dissertation, University of Minho, 2018.

[210] M. E. van Velthoven, D. J. Faber, F. D. Verbraak, T. G. van Leeuwen, and M. D. de Smet, "Recent developments in optical coherence tomography for imaging the retina," *Progress in Retinal and Eye Research*, vol. 26, no. 1, pp. 57–77, jan 2007. [Online]. Available: https://linkinghub.elsevier.com/retrieve/pii/S1350946206000541

[211] M. L. Gabriele, G. Wollstein, H. Ishikawa, J. Xu, J. Kim, L. Kagemann, L. S. Folio, and J. S. Schuman, "Three dimensional optical coherence tomography imaging: Advantages and

advances," *Progress in Retinal and Eye Research*, vol. 29, no. 6, pp. 556–579, nov 2010. [Online]. Available: http://dx.doi.org/10.1016/j.preteyeres.2010.05.005

[212] R. Hamdan, R. G. Gonzalez, S. Ghostine, and C. Caussin, "Optical coherence tomography: From physical principles to clinical applications," *Archives of Cardiovascular Diseases*, vol. 105, no. 10, pp. 529–534, oct 2012. [Online]. Available: http://dx.doi.org/10.1016/j.acvd.2012.02.012

[213] W. Drexler and J. G. Fujimoto, Eds., *Optical Coherence Tomography*. Cham: Springer International Publishing, 2015. [Online]. Available: https://link.springer.com/10.1007/978-3-319-06419-2

[214] A. F. Fercher, W. Drexler, C. K. Hitzenberger, and T. Lasser, "Optical coherence tomography - principles and applications," *Reports on Progress in Physics*, vol. 66, no. 2, pp. 239–303, feb 2003. [Online]. Available: https://linkinghub.elsevier.com/retrieve/pii/B9780121335700X50008

[215] J. Schmitt, "Optical coherence tomography (OCT): a review," *IEEE Journal of Selected Topics in Quantum Electronics*, vol. 5, no. 4, pp. 1205–1215, 1999. [Online]. Available: https://linkinghub.elsevier.com/retrieve/pii/B9780128174401000073

[216] K. Barwari, D. M. de Bruin, D. J. Faber, T. G. van Leeuwen, J. J. de la Rosette, and M. P. Laguna, "Differentiation between normal renal tissue and renal tumours using functional optical coherence tomography: a phase I in vivo human study," *BJU International*, vol. 110, no. 8b, pp. 1–6, oct 2012. [Online]. Available: https://bjui-journals.onlinelibrary.wiley.com/doi/10.1111/j.1464-410X.2012.11220.x

[217] E. C. C. Cauberg, D. M. de Bruin, D. J. Faber, T. M. de Reijke, M. Visser, J. J. M. C. H. de la Rosette, and T. G. van Leeuwen, "Quantitative measurement of attenuation coefficients of bladder biopsies using optical coherence tomography for grading urothelial carcinoma of the bladder," *Journal of Biomedical Optics*, vol. 15, no. 6, p. 066013, 2010. [Online]. Available: http://biomedicaloptics.spiedigitallibrary.org/article.aspx?doi=10.1117/1.3512206

[218] R. A. McLaughlin, L. Scolaro, P. Robbins, C. Saunders, S. L. Jacques, and D. D. Sampson, "Parametric imaging of cancer with optical coherence tomography," *Journal of Biomedical Optics*, vol. 15, no. 4, p. 046029, 2010. [Online]. Available: http://biomedicaloptics.spiedigitallibrary.org/article.aspx?doi=10.1117/1.3479931

[219] P. H. Tomlins, O. Adegun, E. Hagi-Pavli, K. Piper, D. Bader, and F. Fortune, "Scattering attenuation microscopy of oral epithelial dysplasia," *Journal of Biomedical Optics*, vol. 15, no. 6, p.

066003, 2010. [Online]. Available: http://biomedicaloptics.spiedigitallibrary.org/article.aspx?doi=10.1117/1.3505019

[220] Q. Q. Zhang, X. J. Wu, T. Tang, S. W. Zhu, Q. Yao, B. Z. Gao, and X. C. Yuan, "Quantitative analysis of rectal cancer by spectral domain optical coherence tomography," *Physics in Medicine and Biology*, vol. 57, no. 16, pp. 5235–5244, aug 2012. [Online]. Available: https://iopscience.iop.org/article/10.1088/0031-9155/57/16/5235

[221] J. Li, Z. Tu, Z. Shen, Y. Xia, Y. He, S. Liu, and C. Chen, "Quantitative measurement of optical attenuation coefficients of cell lines CNE1, CNE2, and NP69 using optical coherence tomography," *Lasers in Medical Science*, vol. 28, no. 2, pp. 621–625, feb 2013. [Online]. Available: http://link.springer.com/10.1007/s10103-012-1124-1

[222] D. J. Faber, F. J. van der Meer, M. C. G. Aalders, and T. G. van Leeuwen, "Quantitative measurement of attenuation coefficients of weakly scattering media using optical coherence tomography," *Optics Express*, vol. 12, no. 19, p. 4353, 2004. [Online]. Available: https://opg.optica.org/oe/abstract.cfm?uri=oe-12-19-4353

[223] T. van Leeuwen, D. Faber, and M. Aalders, "Measurement of the axial point spread function in scattering media using single-mode fiber-based optical coherence tomography," *IEEE Journal of Selected Topics in Quantum Electronics*, vol. 9, no. 2, pp. 227–233, mar 2003. [Online]. Available: http://ieeexplore.ieee.org/document/1238986/

[224] S. Yun, G. Tearney, B. Bouma, B. Park, and J. de Boer, "High-speed spectral-domain optical coherence tomography at 13 μm wavelength," *Optics Express*, vol. 11, no. 26, p. 3598, dec 2003. [Online]. Available: https://opg.optica.org/oe/abstract.cfm?uri=oe-11-26-3598

[225] R. Khan, B. Gul, S. Khan, H. Nisar, and I. Ahmad, "Refractive index of biological tissues: Review, measurement techniques, and applications," *Photodiagnosis and Photodynamic Therapy*, vol. 33, no. January, p. 102192, mar 2021. [Online]. Available: https://linkinghub.elsevier.com/retrieve/pii/S1572100021000181

[226] S. Learn, "Nested versus non-nested cross-validation." [Online]. Available: https://scikit-learn.org/stable/auto_examples/model_selection/plot_nested_cross_validation_iris.html

[227] M. Maciel, R. P. Rocha, J. P. Carmo, and J. H. Correia, "Measurement and statistical analysis toward reproducibility validation of AZ4562 cylindrical microlenses obtained by

reflow," *Measurement*, vol. 49, no. 1, pp. 60–67, mar 2014. [Online]. Available: http://dx.doi.org/10.1016/j.measurement.2013.11.056

[228] J. Freitas, S. Pimenta, J. Ribeiro, T. Dong, Z. Yang, and J. Correia, "Simulation, fabrication and morphological characterization of a PDMS microlens for light collimation on optrodes," *Optik*, vol. 227, feb 2021. [Online]. Available: https://doi.org/10.1016/j.ijleo.2020.166098

[229] M. Maciel, C. Costa, M. Silva, A. Peixoto, R. Wolffenbuttel, and J. Correia, "A wafer-level miniaturized Michelson interferometer on glass substrate for optical coherence tomography applications," *Sensors and Actuators A: Physical*, vol. 242, pp. 210–216, may 2016. [Online]. Available: http://dx.doi.org/10.1016/j.sna.2016.03.007

[230] M. Maciel, N. Gomes, S. Pimenta, J. Ribeiro, and J. Correia, "TiO2/airgap-based polarizing beam splitter: design, simulation, and fabrication based on MEMS technologies," *Optics and Lasers in Engineering*, vol. 133, no. March, p. 106110, oct 2020. [Online]. Available: https://doi.org/10.1016/j.optlaseng.2020.106110

[231] R. P. Rocha, M. J. Maciel, J. M. Gomes, J. P. Carmo, and J. H. Correia, "Fabricating Microlenses on Photodiodes to Increase the Light-Current Conversion Efficiency," *IEEE Sensors Journal*, vol. 14, no. 5, pp. 1343–1344, may 2014. [Online]. Available: http://ieeexplore.ieee.org/document/6739089/

[232] P. A. Franken, A. E. Hill, C. W. Peters, and G. Weinreich, "Generation of Optical Harmonics," *Physical Review Letters*, vol. 7, no. 4, pp. 118–119, aug 1961. [Online]. Available: https://link.aps.org/doi/10.1103/PhysRevLett.7.118

[233] C. J. R. Sheppard and R. Kompfner, "Resonant scanning optical microscope," *Applied Optics*, vol. 17, no. 18, p. 2879, sep 1978. [Online]. Available: https://opg.optica.org/abstract.cfm?URI=ao-17-18-2879

[234] I. Freund and M. Deutsch, "Second-harmonic microscopy of biological tissue," *Optics Letters*, vol. 11, no. 2, p. 94, feb 1986. [Online]. Available: https://opg.optica.org/abstract.cfm?URI=ol-11-2-94

[235] W. Sibbett, A. A. Lagatsky, and C. T. A. Brown, "The development and application of femtosecond laser systems," *Optics Express*, vol. 20, no. 7, p. 6989, 2012.

[236] W. R. Zipfel, R. M. Williams, and W. W. Webb, "Nonlinear magic: multiphoton microscopy in the biosciences," *Nature Biotechnology*, vol. 21, no. 11, pp. 1369–1377, nov 2003. [Online]. Available: https://www.nature.com/articles/nbt899

[237] E. E. Hoover and J. A. Squier, "Advances in multiphoton microscopy technology," *Nature Photonics*, vol. 7, no. 2, pp. 93–101, feb 2013. [Online]. Available: https://opg.optica.org/abstract.cfm?URI=FiO-2012-FM4D.4

[238] M. J. d. L. F. Rodrigues, "Nonlinear optical effects in 2D materials," Ph.D. dissertation, University of Minho, 2022.

[239] I. Georgakoudi and K. P. Quinn, "Label-Free Optical Metabolic Imaging in Cells and Tissues," *Annual Review of Biomedical Engineering*, vol. 25, no. 1, pp. 413–443, jun 2023. [Online]. Available: https://www.annualreviews.org/doi/10.1146/annurev-bioeng-071516-044730

[240] F. Helmchen and W. Denk, "Deep tissue two-photon microscopy," *Nature Methods*, vol. 2, no. 12, pp. 932–940, dec 2005. [Online]. Available: http://www.nature.com/articles/nmeth818

[241] C. Lefort, "A review of biomedical multiphoton microscopy and its laser sources," *Journal of Physics D: Applied Physics*, vol. 50, no. 42, p. 423001, oct 2017. [Online]. Available: https://iopscience.iop.org/article/10.1088/1361-6463/aa8050

[242] M. Sidani, J. Wyckoff, C. Xue, J. E. Segall, and J. Condeelis, "Probing the Microenvironment of Mammary Tumors Using Multiphoton Microscopy," *Journal of Mammary Gland Biology and Neoplasia*, vol. 11, no. 2, pp. 151–163, nov 2006. [Online]. Available: http://link.springer.com/10.1007/s10911-006-9021-5

[243] P.-J. Treacy, A. Khosla, N. Kyprianou, U. G. Falagario, N. Tsavaras, P. Wiklund, A. K. Tewari, and M. Durand, "Value of multiphoton microscopy in uro-oncology: a narrative review," *Translational Andrology and Urology*, vol. 12, no. 3, pp. 508–518, mar 2023. [Online]. Available: https://tau.amegroups.com/article/view/110061/html

[244] H. J. Cho, H. J. Chun, E. S. Kim, and B. R. Cho, "Multiphoton microscopy: An introduction to gastroenterologists," *World Journal of Gastroenterology*, vol. 17, no. 40, p. 4456, 2011. [Online]. Available: http://www.wjgnet.com/1007-9327/full/v17/i40/4456.htm

[245] J. Xu, D. Kang, Y. Zeng, S. Zhuo, X. Zhu, L. Jiang, J. Chen, and J. Lin, "Multiphoton microscopy for label-free identification of intramural metastasis in human esophageal squamous cell carcinoma," *Biomedical Optics Express*, vol. 8, no. 7, p. 3360, 2017.

[246] M. Rubart, "Two-Photon Microscopy of Cells and Tissue," *Circulation Research*, vol. 95, no. 12, pp. 1154–1166, dec 2004. [Online]. Available: https://www.ahajournals.org/doi/10.1161/01.RES.0000150593.30324.42

[247] J. M. Squirrell, D. L. Wokosin, J. G. White, and B. D. Bavister, "Long-term two-photon fluorescence imaging of mammalian embryos without compromising viability," *Nature Biotechnology*, vol. 17, no. 8, pp. 763–767, aug 1999. [Online]. Available: https://www.nature.com/articles/nbt0899_763

[248] T. Kitamura, J. W. Pollard, and M. Vendrell, "Optical Windows for Imaging the Metastatic Tumour Microenvironment in vivo," *Trends in Biotechnology*, vol. 35, no. 1, pp. 5–8, 2017. [Online]. Available: http://dx.doi.org/10.1016/j.tibtech.2016.05.001

[249] W. R. Zipfel, R. M. Williams, R. Christie, A. Y. Nikitin, B. T. Hyman, and W. W. Webb, "Live tissue intrinsic emission microscopy using multiphoton-excited native fluorescence and second harmonic generation," *Proceedings of the National Academy of Sciences*, vol. 100, no. 12, pp. 7075–7080, jun 2003. [Online]. Available: https://pnas.org/doi/full/10.1073/pnas.0832308100

[250] K. A. Kasischke, H. D. Vishwasrao, P. J. Fisher, W. R. Zipfel, and W. W. Webb, "Neural Activity Triggers Neuronal Oxidative Metabolism Followed by Astrocytic Glycolysis," *Science*, vol. 305, no. 5680, pp. 99–103, jul 2004. [Online]. Available: https://www.science.org/doi/10.1126/science.1096485

[251] A. Zoumi, A. Yeh, and B. J. Tromberg, "Imaging cells and extracellular matrix in vivo by using second-harmonic generation and two-photon excited fluorescence," *Proceedings of the National Academy of Sciences*, vol. 99, no. 17, pp. 11 014–11 019, aug 2002. [Online]. Available: https://pnas.org/doi/full/10.1073/pnas.172368799

[252] S. Maiti, J. B. Shear, R. M. Williams, W. R. Zipfel, and W. W. Webb, "Measuring Serotonin Distribution in Live Cells with Three-Photon Excitation," *Science*, vol. 275, no. 5299, pp. 530–532, jan 1997. [Online]. Available: https://www.science.org/doi/10.1126/science.275.5299.530

[253] P. J. Campagnola and L. M. Loew, "Second-harmonic imaging microscopy for visualizing biomolecular arrays in cells, tissues and organisms," *Nature Biotechnology*, vol. 21, no. 11, pp. 1356–1360, nov 2003. [Online]. Available: https://www.nature.com/articles/nbt894

[254] D. Débarre, W. Supatto, A. M. Pena, A. Fabre, T. Tordjmann, L. Combettes, M. C. Schanne-Klein, and E. Beaurepaire, "Imaging lipid bodies in cells and tissues using third-harmonic generation microscopy," *Nature Methods*, vol. 3, no. 1, pp. 47–53, 2006.

[255] C. Stringari, K. T. Pate, R. A. Edwards, M. L. Waterman, and E. Gratton, "Metabolic Imaging of Colon Cancer Tumors In Vivo by Phasor Fluorescence Lifetime Microscopy of NADH," *Biophysical Journal*, vol. 104, no. 2, pp. 342a–343a, jan 2013. [Online]. Available: https://linkinghub.elsevier.com/retrieve/pii/S0006349512031487

[256] A. A. Mossakowski, J. Pohlan, D. Bremer, R. Lindquist, J. M. Millward, M. Bock, K. Pollok, R. Mothes, L. Viohl, M. Radbruch, J. Gerhard, J. Bellmann-Strobl, J. Behrens, C. Infante-Duarte, A. Mähler, M. Boschmann, J. L. Rinnenthal, M. Füchtemeier, J. Herz, F. C. Pache, M. Bardua, J. Priller, A. E. Hauser, F. Paul, R. Niesner, and H. Radbruch, "Tracking CNS and systemic sources of oxidative stress during the course of chronic neuroinflammation," *Acta Neuropathologica*, vol. 130, no. 6, pp. 799–814, dec 2015. [Online]. Available: http://link.springer.com/10.1007/s00401-015-1497-x

[257] H. Radbruch, D. Bremer, R. Guenther, Z. Cseresnyes, R. Lindquist, A. E. Hauser, and R. Niesner, "Ongoing Oxidative Stress Causes Subclinical Neuronal Dysfunction in the Recovery Phase of EAE," *Frontiers in Immunology*, vol. 7, mar 2016. [Online]. Available: http://journal.frontiersin.org/Article/10.3389/fimmu.2016.00092/abstract

[258] X. Chen, O. Nadiarynkh, S. Plotnikov, and P. J. Campagnola, "Second harmonic generation microscopy for quantitative analysis of collagen fibrillar structure," *Nature Protocols*, vol. 7, no. 4, pp. 654–669, apr 2012. [Online]. Available: https://www.nature.com/articles/nprot.2012.009

[259] P. Stoller, P. M. Celliers, K. M. Reiser, and A. M. Rubenchik, "Quantitative second-harmonic generation microscopy in collagen," *Appl. Opt.*, vol. 42, no. 25, pp. 5209–5219, Sep 2003. [Online]. Available: https://opg.optica.org/ao/abstract.cfm?URI=ao-42-25-5209

[260] K. Svoboda and R. Yasuda, "Principles of two-photon excitation microscopy and its applications to neuroscience," *Neuron*, vol. 50, pp. 823–839, 6 2006. [Online]. Available: https://linkinghub.elsevier.com/retrieve/pii/S0896627306004119

[261] L.-C. Cheng, N. G. Horton, K. Wang, S.-J. Chen, and C. Xu, "Measurements of multiphoton action cross sections for multiphoton microscopy," *Biomed. Opt. Express*, vol. 5, no. 10, pp. 3427–3433, Oct 2014. [Online]. Available: https://opg.optica.org/boe/abstract.cfm?URI=boe-5-10-3427

[262] C. Xu, W. Zipfel, J. B. Shear, R. M. Williams, and W. W. Webb, "Multiphoton fluorescence excitation: new spectral windows for biological nonlinear microscopy." *Proceedings of the National Academy of Sciences*, vol. 93, no. 20, pp. 10 763–10 768, 1996. [Online]. Available: https://www.pnas.org/doi/abs/10.1073/pnas.93.20.10763

[263] F. H. M. Faisal and A. Dalgarno, "Theory of multiphoton processes," 1987. [Online]. Available: https://api.semanticscholar.org/CorpusID:121609153

[264] K. P. Quinn, G. V. Sridharan, R. S. Hayden, D. L. Kaplan, K. Lee, and I. Georgakoudi, "Quantitative metabolic imaging using endogenous fluorescence to detect stem cell differentiation," *Scientific Reports*, vol. 3, no. 1, p. 3432, dec 2013. [Online]. Available: https://www.nature.com/articles/srep03432

[265] T. Brabec, C. Spielmann, P. F. Curley, and F. Krausz, "Kerr lens mode locking," *Optics Letters, Vol. 17, Issue 18, pp. 1292-1294*, vol. 17, pp. 1292–1294, 9 1992. [Online]. Available: https://opg.optica.org/viewmedia.cfm?uri=ol-17-18-1292&seq=0&html=true

[266] W. Koechner, *Mode Locking*. Berlin, Heidelberg: Springer Berlin Heidelberg, 1992, pp. 482–507. [Online]. Available: https://doi.org/10.1007/978-3-662-14513-5_9

[267] J. A. Arnaud, W. M. Hubbard, G. D. Mandeville, B. de la Clavière, E. A. Franke, and J. M. Franke, "Technique for fast measurement of gaussian laser beam parameters," *Appl. Opt.*, vol. 10, no. 12, pp. 2775–2776, Dec 1971. [Online]. Available: https://opg.optica.org/ao/abstract.cfm?URI=ao-10-12-2775

[268] M. A. de Araújo, R. Silva, E. de Lima, D. P. Pereira, and P. C. de Oliveira, "Measurement of Gaussian laser beam radius using the knife-edge technique: improvement on data analysis," *Applied Optics*, vol. 48, no. 2, p. 393, jan 2009. [Online]. Available: https://opg.optica.org/abstract.cfm?URI=ao-48-2-393

[269] R. Menzel, *Photonics*, ser. Physics and astronomy). Berlin: Springer, cop. 2001.

[270] D. A. Whitaker and K. Hayes, "A simple algorithm for despiking Raman spectra," *Chemometrics and Intelligent Laboratory Systems*, vol. 179, no. March, pp. 82–84, aug 2018. [Online]. Available: https://doi.org/10.1016/j.chemolab.2018.06.009

[271] K. He, L. Zhao, Y. Chen, X. Huang, Y. Ding, H. Hua, L. Liu, X. Wang, M. Wang, Y. Zhang, and Z. Fan, "Label□free multiphoton microscopic imaging as a novel real□time approach for discriminating colorectal lesions: A preliminary study," *Journal of Gastroenterology and Hepatology*, vol. 34, no. 12, pp. 2144–2151, dec 2019. [Online]. Available: https://onlinelibrary.wiley.com/doi/abs/10.1111/jgh.14772

[272] C. J. R. Sheppard, "Multiphoton microscopy: a personal historical review, with some future predictions," *Journal of Biomedical Optics*, vol. 25, no. 01, jan 2020. [Online]. Available: https://www.spiedigitallibrary.org/journals/journal-of-biomedical-optics/volume-25/issue-01/014511/Multiphoton-microscopy--a-personal-historical-review-with-some-future/10.1117/1.JBO.25.1.014511.full

[273] M. J. Maciel, C. G. Costa, M. F. Silva, S. B. Gonçalves, A. C. Peixoto, A. Fernando Ribeiro, R. F. Wolffenbuttel, and J. H. Correia, "A 45° saw-dicing process applied to a glass substrate for wafer-level optical splitter fabrication for optical coherence tomography," *Journal of Micromechanics and Microengineering*, vol. 26, no. 8, p. 084001, aug 2016. [Online]. Available: https://iopscience.iop.org/article/10.1088/0960-1317/26/8/084001

[274] J. H. G. Correia and M. d. J. C. Maciel, "EP 4039169A2: System for screening, diagnosis, or monitoring a colorectal tissue and method thereof," 2022.

[275] D. R. Rivera, C. M. Brown, D. G. Ouzounov, I. Pavlova, D. Kobat, W. W. Webb, and C. Xu, "Compact and flexible raster scanning multiphoton endoscope capable of imaging unstained tissue," *Proceedings of the National Academy of Sciences*, vol. 108, no. 43, oct 2011. [Online]. Available: http://www.pnas.org/cgi/doi/10.1073/pnas.1114746108

[276] G. Ducourthial, P. Leclerc, T. Mansuryan, M. Fabert, J. Brevier, R. Habert, F. Braud, R. Batrin, C. Vever-Bizet, G. Bourg-Heckly, L. Thiberville, A. Druilhe, A. Kudlinski, and F. Louradour, "Development of a real-time flexible multiphoton microendoscope for label-free imaging in a live animal," *Scientific Reports*, vol. 5, no. 1, dec 2015. [Online]. Available: http://dx.doi.org/10.1038/srep18303

[277] X. Duan, H. Li, Z. Qiu, B. P. Joshi, A. Pant, A. Smith, K. Kurabayashi, K. R. Oldham, and T. D. Wang, "MEMS-based multiphoton endomicroscope for repetitive imaging of mouse colon," *Biomedical Optics Express*, vol. 6, no. 8, aug 2015. [Online]. Available: https://www.osapublishing.org/abstract.cfm?URI=boe-6-8-3074

[278] W. Liang, G. Hall, B. Messerschmidt, M.-J. Li, and X. Li, "Nonlinear optical endomicroscopy for label-free functional histology in vivo," *Light: Science & Applications*, vol. 6, no. 11, nov 2017. [Online]. Available: http://dx.doi.org/10.1038/lsa.2017.82

[279] F. Akhoundi, Y. Qin, N. Peyghambarian, J. K. Barton, and K. Kieu, "Compact fiber-based multi-photon endoscope working at 1700 nm," *Biomedical Optics Express*, vol. 9, no. 5, may 2018. [Online]. Available: https://www.osapublishing.org/abstract.cfm?URI=boe-9-5-2326

[280] A. Dilipkumar, A. Al□Shemmary, L. Kreiß, K. Cvecek, B. Carlé, F. Knieling, J. Gonzales Menezes, O. Thoma, M. Schmidt, M. F. Neurath, M. Waldner, O. Friedrich, and S. Schürmann, "Label□Free Multiphoton Endomicroscopy for Minimally Invasive In Vivo Imaging," *Advanced Science*, vol. 6, no. 8, apr 2019. [Online]. Available: https://onlinelibrary.wiley.com/doi/abs/10.1002/advs.201801735

[281] W. Zong, H. A. Obenhaus, E. R. Skytøen, M. R. Jorge, M.-b. Moser, E. I. Moser, W. Zong, H. A. Obenhaus, E. R. Skytøen, H. Eneqvist, N. L. D. Jong, and R. Vale, "Resource Large-scale two-photon calcium imaging in freely moving mice ll ll Large-scale two-photon calcium imaging in freely moving mice," *Cell*, vol. 185, no. 7, pp. 1240–1256.e30, 2022. [Online]. Available: https://doi.org/10.1016/j.cell.2022.02.017

[282] "Pt230 pt piezo scanner tubes." [Online]. Available: https://www.physikinstrumente.com/en/products/piezoelectric-transducers-actuators/pt230-pt-piezo-scanner-tubes-103150